

University of Strathclyde
Department of Bioengineering

**Fundamental Characterisation and Early
Functional Testing of Micromoulded
Piezocomposites**

Duncan MacLennan

A thesis presented in fulfilment of the requirements for the
degree of Engineering Doctorate in Medical Devices

2010

Preface

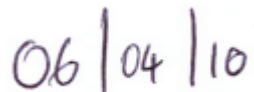
This thesis is the result of the author's original research. It has been composed by the author and has not been previously submitted for examination which has led to the award of a degree.

The copyright of this thesis belongs to the author under the terms of the United Kingdom Copyright Acts as qualified by the University of Strathclyde Regulation 3.50. Due acknowledgement must always be made of the use of any material contained in, or derived from, this thesis.

Signed:

A handwritten signature in dark ink, reading "Duncan MacLennan". The signature is written in a cursive style with a light blue background behind the text.

Date:

A handwritten date in dark ink, reading "06/04/10". The date is written in a simple, blocky style.

Acknowledgments

Firstly, I would like to thank my primary supervisor, Dr. Sandy Cochran, for his help, enthusiasm and support throughout the duration of my EngD. I also wish to thank my co-supervisor Prof. Geo Corner for his encouragement and in particular for his help at Ninewells. I learned a great deal during my EngD, much of which is was due to the first-rate supervision I received during this time.

I want to thank my colleagues from the Bioengineering department at University of Strathclyde, and in particular Prof. Trish Connolly for her support during my time with the department. Special mention must also go to Dr. Christine Démoré for her help and technical guidance during the project, for which I am incredibly grateful. Similarly, I wish to thank David Hughes for help in setting up the HFUS scanning system. I also acknowledge the support of AFM Ltd, Birmingham for providing the majority of devices used in this project; in particular Prof. Tim Button, Dr. Hana Hughes and Carl Meggs. I also wish to thank Dr. Rhiannon Webster and Dr. Tim Clipsham from the University of Birmingham.

From my time at University of Paisley I also wish to thank Gerry O'Hare, Geoff Moores and Jim Orr, whose technical skills were second to none. I also benefited greatly during my time at Paisley from the help and expertise of Jocelyn Elgoyhen, Kim McDonald, Dr. Anne Bernassau, Prof. Katherine Kirk and Dr. David Hutson; from Ninewells Hospital/University of Dundee: Patrick Carena, Duncan Kirkcaldy, and Dr. Stuart Brown. I am also indebted to Dr. Jeremy Brown of Dalhousie University for providing me with an excellent HFUS composite transducer.

I am incredibly grateful to my parents for their wide-ranging support during the production of this thesis, and in particular for their help with proof reading and printing.

Finally, a huge thank you to my wife, Helen.

Abstract

The development of high frequency ultrasound (HFUS) transducers offers new diagnostic opportunities afforded by micro-scale resolutions. 1-3 connectivity piezoceramic-polymer composites have highly advantageous properties such as high piezoelectric coupling and good acoustic matching to tissue, but the upper frequency possible with traditional fabrication techniques is limited due to the small piezoceramic structures required. Realisation of higher frequencies may be offered by new viscous polymer processing (VPP) techniques. However, characterisation of these materials by traditional methods is not possible.

This thesis presents results from characterisation of high frequency VPP micromoulded composite (MC) materials, based on electrical impedance spectroscopy and data fitting to a model based on the 1-D piezoelectric wave equation and well established homogenized piezocomposite model.

Results are presented from several VPP HFUS piezocomposites developed as part of a collaborative program. Effective piezoelectric properties were found to be in the following ranges c_{33}^E : 1.40 - 5.00 ($\times 10^{10}$ Nm²), e_{33} : 1.80 - 8.50 (Cm⁻¹), ϵ_R^S : 81.1 - 460, d_{33} : 8.70 - 12.5 ($\times 10^{11}$ mV⁻¹), h_{33} : 1.88 - 3.06 ($\times 10$ Vm⁻¹) and k_T : 0.45-0.51.

Single element transducers were fabricated with MCs, and results from basic characterisation of these are also presented. Transducers were found to have resolution and bandwidth commensurate with HFUS applications. Data generated from this work showed that VPP fabrication has good potential for production of HFUS piezocomposites.

Table of Contents

Preface.....	i
Acknowledgments.....	ii
Abstract.....	iii
Table of Contents.....	iv
List of Symbols and Abbreviations.....	vii
List of Figures.....	x
List of Tables.....	xvii
1. Introduction.....	1
1.1. History of Medical Ultrasound.....	1
1.2. High Frequency Ultrasound.....	3
1.3. Aims.....	3
1.4. Contributions to Knowledge.....	4
1.5. Outline of Thesis.....	5
1.6. Publications and conference submissions.....	6
1.7. References.....	10
2. Theory.....	11
2.1. Introduction.....	11
2.2. Medical imaging modalities.....	12
2.3. Ultrasound Waves.....	17
2.4. Wave propagation at boundaries.....	26
2.5. Basic ultrasound imaging.....	30
2.6. Background to piezoelectric materials.....	33
2.7. Piezoelectric materials commonly used for HFUS.....	38
2.8. Piezoelectric composite materials.....	44
2.9. Electrical impedance spectroscopy.....	48
2.10. Ultrasound Transducers.....	54
2.11. Ultrasound scanning systems.....	61
2.12. Summary.....	62
2.13. References.....	63
3. Historical development of HFUS transducers.....	68

3.1. Clinical Need.....	68
3.2. Piezoelectric Material Development.....	78
3.3. Transducer Development.....	91
3.4. Conclusion.....	91
3.5. References.....	92
4. Materials and methods.....	106
4.1. Piezoelectric Material Fabrication.....	108
4.2. Ultra Precision Grinding.....	114
4.3. Characterisation of passive materials.....	116
4.4. Design and fabrication of materials testing jig.....	125
4.5. Experimental Characterisation of Active Materials.....	132
4.6. Piezoelectric Modelling Techniques.....	134
4.7. Simulation using One Dimensional Modelling.....	139
4.8. Fabrication of single element transducers.....	155
4.9. Basic testing of transducers.....	159
4.10. Design of high frequency scanning system.....	160
4.11. Visualisation of collected data.....	163
4.12. Wires and tissue imaging.....	163
4.13. Summary.....	166
4.14. References.....	166
5. Results.....	170
5.1. Introduction.....	170
5.2. Transducer materials.....	171
5.3. Active materials: standard composite SC1.....	177
5.4. Active Materials: fibre composites.....	180
5.5. Active materials: micromoulded composites.....	190
5.6. Summary.....	205
5.7. References.....	206
6. Transducer testing and applications testing.....	207
6.1. Introduction.....	207
6.2. Basic testing: Transducers made with standard materials.....	208
6.3. Basic Testing: Unfocussed MC Transducers.....	213

6.4. Basic Testing: Focussed MC Transducers	218
6.5. Summary	234
6.6. References	234
7. Discussion	235
7.1. Transducer design and fabrication	236
7.2. Active materials: standard materials	237
7.3. Novel materials: fabrication and characterisation.....	239
7.4. Transducer applications results	245
7.5. Summary	248
7.6. References	248
8. Conclusions	250
8.1. Micromoulded piezocomposites provide a route to production of high resolution ultrasound transducers.....	250
8.2. Further conclusions	252
8.3. Further Work.....	254
8.4. References	256
9. Appendices.....	259
9.1. Appendix A: Calculation sheet for piezoelectric properties from electrical impedance spectroscopy measurements.....	259
9.2. Appendix B: Effect of varying ODM input parameters on calculated electrical impedance spectrum.....	260
9.3. Appendix C: Description of LabVIEW B-scan collection program	263

List of Symbols and Abbreviations

A	Area (m^2), Amplitude
a	Acceleration (ms^{-2})
c	Stiffness (Nm^{-2})
C	Capacitance (F)
d	Piezoelectric modulus or piezoelectric charge constant (mV^{-1})
D	Electric displacement (Cm^{-2})
DOF	Depth of field (m)
E	Young's Modulus (Nm^{-2}), Electric field (Vm^{-1})
e	Piezoelectric stress constant (Cm^{-1})
f	Frequency (Hz)
F	Force (N)
$\bar{F}_{F(i)}$	Forward travelling coefficient of force (N)
$\bar{F}_{B(i)}$	Backward travelling coefficient of force (N)
$f\#$	f-number
FC	Fibre composite
f_a	Antiresonant frequency or mechanical resonant frequency (Hz)
f_r	Resonant frequency or electrical resonant frequency (Hz)
f_s	Sampling frequency (Hz)
G	Transverse modulus (Nm^{-2})
g	Piezoelectric voltage constant (VmN^{-1})
h	Piezoelectric stiffness constant (Vm^{-1})
I	Acoustic intensity (Wm^{-2}), Current (A)
K	Modulus of compression (Nm^{-2}), Bulk elastic modulus (Nm^{-2})
k	Electromechanical coupling coefficient, Kerf width (m)
k_T	Electromechanical coupling coefficient of thickness expander plate
L	Inductance (H)
l	Length (m)

<i>LNO</i>	Lithium niobate
<i>m</i>	Mass (kg)
<i>MC</i>	Micromoulded composite
<i>N</i>	Near field length (m)
<i>PMN-PT</i>	Lead magnesium niobate – lead titanate
<i>PVDF</i>	Polyvinylidene fluoride
<i>PZT</i>	Lead Zirconate titanate
<i>PZT-PNN</i>	Lead Zirconate titanate – lead nickel niobate
<i>Q</i>	Charge (C)
<i>r</i>	Focal distance of transducer (m)
<i>R</i>	Resistance (Ω)
<i>R_A</i>	Axial resolution (m)
<i>R_L</i>	Lateral resolution (m)
<i>R_x</i>	Reflection coefficient
<i>S</i>	Strain
<i>s</i>	Compliance (m^2N^{-1}), Complex Laplacian operator
<i>T</i>	Thickness (m), Mechanical stress (Nm^{-2})
<i>t</i>	Time (s)
<i>t_p</i>	-6 dB pulse length (s)
<i>T_x</i>	Transmission coefficient
<i>U</i>	Particle velocity (ms^{-1})
<i>UPG</i>	Ultra precision grinding
<i>v</i>	Velocity (ms^{-1})
<i>V</i>	Voltage (V)
<i>VF</i>	Volume fraction
<i>v_l</i>	Longitudinal velocity (ms^{-1})
<i>VPP</i>	Viscous polymer processing
<i>v_t</i>	Transverse velocity (ms^{-1})
<i>w</i>	Pillar width (m)
<i>x</i>	Distance (m)
<i>X_c</i>	Capacitive reactance (Ω)
<i>X_L</i>	Inductive reactance (Ω)

Z	Acoustic impedance (Rayl), electrical impedance (Ω)
α	Attenuation coefficient (dBm^{-1})
β	Dielectric impermeability (mF^{-1})
γ	Strain tensor
δ_{ij}	Kronecker delta
ε	Permittivity (Fm^{-1})
ε_R	Relative permittivity
ε_R^S	Relative permittivity at constant strain
ε_R^T	Relative permittivity at constant stress
θ	Phase angle ($^\circ$)
θ_c	Critical angle ($^\circ$)
θ_i	Incident angle ($^\circ$)
θ_r	Reflection angle ($^\circ$)
θ_t	Transmission angle ($^\circ$)
λ	Wavelength (m), Lamé coefficient (Nm^{-2})
μ	Lamé Coefficient (Nm^{-2}), Modulus of rigidity (Nm^{-2})
ξ	Particle displacement (m)
ρ	Density (kgm^{-3})
σ	Stress tensor (Nm^{-2}), Poisson's ratio
ω	Angular frequency (rads^{-1})

List of Figures

Figure 2. 1: Micro-CT images of (a) bone and (b) kidney (from GE Healthcare).....	13
Figure 2. 2: MRI image of a mouse brain taken with a 7T magnetic field (Bock et al., 2005)	14
Figure 2. 3: OCT image of human eye, showing several structures including retina, sub-retinal fluid (SRF), retinal pigment epithelium (RPE), sclera and blood vessels (BV) (from Huang et al., 1991).	15
Figure 2. 4: (a) Sound wave travelling through a medium, with molecules undergoing compression and rarefaction. (b) Corresponding time-dependent pressure wave.	18
Figure 2. 5: Depiction of a wave incident on a boundary at an oblique angle, showing reflection and refraction.	26
Figure 2. 6: Wave at normal incidence to boundary.	28
Figure 2. 7: Wave incident on liquid-solid boundary and solid-liquid boundary where $0 < \theta_i < \theta_t$	29
Figure 2. 8: Wave incident on liquid-solid boundary and solid-liquid boundary, where $\theta_l < \theta_i < \theta_s$	30
Figure 2. 9: Principle of pulse-echo operation used to generate an A-scan, shown alongside typical received echo signals	32
Figure 2. 10: Illustration showing the indirect piezoelectric effect, mechanical deformation occurring in response to an applied electric field.....	33
Figure 2. 11: Simulated impedance magnitude and phase for Lithium Niobate single element and array element at 40 MHz.	39
Figure 2. 12: Simulated impedance magnitude and phase for PVDF single element and array element at 40 MHz.	39
Figure 2. 13: Simulated impedance magnitude and phase for PZT-5H (CTS3203HD) single element and array element at 40 MHz.....	40
Figure 2. 14: Simulated electrical impedance magnitude and phase for 30% VF CTS3203HD/RX771 Composite single element and array element at 40 MHz	40

Figure 2. 15: Simulated impedance magnitude and phase for PMN-PT (Ibule) single element and array element at 40 MHz.	40
Figure 2. 16: Simulated electrical impedance magnitude and phase for 30% VF PMN-PT/RX771 Composite single element and array element at 40 MHz.	40
Figure 2. 17: Simulation of k_T with volume fraction for a PZT-5H / RX771 composite.	43
Figure 2. 18: Stages in the fabrication of a 1-3 piezocomposite. Details are given in the text.	45
Figure 2. 19: Diagram of surface of 1-3 composite illustrating pillar width and inter-pillar kerf.	46
Figure 2. 20: Electrical impedance magnitude and phase versus frequency.	50
Figure 2. 21: Diagram showing a cross section of a typical single element transducer	55
Figure 2. 22: Transducers focused by (a) adding a lens and (b) curving the active material.	58
Figure 2. 23: Illustration of lateral resolution, R_L , and axial resolution, R_A , of an ultrasound transducer.	60
Figure 2. 24: Stages in processing involved in production of an ultrasound image ..	61
Figure 3. 1: Scan Image of ex-vivo bovine eye taking using 20 MHz annular array (from Ketterling and Silverman, 2006)	70
Figure 3. 2: Image showing structures within the skin: stratum corneum (SC), stratum granulosum (GR), stratum germinativum (GE), stratum papillare (SP), stratum reticulare (SR) and eccrine sweat glands (SG) (from Passmann and Emert, 1996)	72
Figure 3. 3: (a) Ultrasound image of diseased coronary artery showing intimal thickening (scale is 100 μm per division), alongside (b) corresponding histology. Also shown is (c) the integrated backscatter coefficient profile (Machado and Foster, 2001)	75
Figure 3. 4: (a) IVUS image of arterial tissue and (b) the same image with strain information overlaid (from Leung et al., 2006)	76

Figure 3. 5: Section image showing mouse liver and kidney (from Foster et al., 2000)	77
Figure 3. 6: Diagram showing process used to fabricate spherically focussed single element transducers from non flexible active materials, in this case PZT (from Lockwood et al., 2004)	83
Figure 3. 7: an example of a fabrication method for fibre composites (from Smith and Auld 1989)	88
Figure 4. 1: Flow chart showing the steps from a PZT powder to ultrasound image. Work reported in this thesis is indicated by a bold outline.	106
Figure 4. 2: Illustration of VPP, showing ceramic paste being milled and calendered to produce a green state ceramic sheet (picture adapted from Cochran et al. (2004)).	108
Figure 4. 3: Photographs of (a) lapping machine and (b) dicing saw	109
Figure 4. 4: Photograph of poling jig.	110
Figure 4. 5: Photographs of grain structure of PZT fibres from sol gel, extrusion, VPP and VSSP and corresponding piezoelectric properties (from Dent et al., 2005).	111
Figure 4. 6: Fibres composite after (a) collection of fibres into bunches, and (b) cutting into slices.	112
Figure 4. 7: Diagrams showing micro-moulding composite fabrication process (picture adapted from Cochran et al. (2004)).	113
Figure 4. 8: Schematic diagram of piezocomposite material, indicating height difference between phases.	114
Figure 4. 9: Photograph of PicoAce process chamber (picture from Loadpoint, Cricklade, UK).	115
Figure 4. 10: Diagram showing through-transmission of ultrasound through a sample.	118
Figure 4. 11: (a) Schematic of experimental set-up and (b) paths resulting from beam incident on sample at non-perpendicular angle $\theta_i < \theta_c$.	120
Figure 4. 12: Diagram showing ‘reference’ signal and ‘sample’ signal, for a sample of aluminium.	123

Figure 4. 13: Photographs of jig showing front view, with labels described below, and side view.....	127
Figure 4. 14: Graphs showing influence of incident angle on transmitted signal amplitude. Note voltage has been offset for clarity on individual plots. Voltages shown are relative.	130
Figure 4. 15: Photographs of (a) Agilent 4294A impedance analyser and (b) fixture used for testing of bare piezoelectric materials.....	133
Figure 4. 16: Pulse echo measurement set-up for bare composite samples.	134
Figure 4. 17: Mason's equivalent circuit for thickness expander plate (from Krimholtz et al., 1970).	135
Figure 4. 18: Equivalent circuit of a piezoelectric element, showing an RLC circuit in parallel with a capacitor	136
Figure 4. 19: KLM equivalent circuit for a plate in thickness mode. This also applies to a bar geometry (from Krimholtz et al., 1970).	137
Figure 4. 20: 3 port model devised by Jackson and Hayward (from Jackson & Hayward, 1984).....	139
Figure 4. 21: Layered structure as used in ODM (from Powell et al. (1998)).	141
Figure 4. 22: (a) Impedance magnitude and phase of a composite and (b) external and internal forces on front and back face over time.....	149
Figure 4. 23: 1-3 piezocomposite configuration, showing x, y and z axes referred to in main text.....	150
Figure 4. 24: Cross section of single element PZT /polymer composite transducer.	156
Figure 4. 25: Fabrication procedure for single element transducer. Photographs from Aristizábal and Turnbull (2003).....	158
Figure 4. 26: Photographs of (a) prototype high frequency single element transducer and (b) section of same transducer design (from Webster, 2008).....	158
Figure 4. 27: Example of (a) depth of field and (b) line spread function from a high frequency transducer (JB1).	160
Figure 4. 28: (a) Photograph of scanning system pulser receiver (A), transducer (B) and scanning stages (C) and (b) schematic of component connections with arrows showing direction of signals.....	162

Figure 4. 29: Example of a B-scan image of an eye, generated by MATLAB from data collected from A-scans with a 32MHz transducer.	163
Figure 4. 30: Diagram of (a) Tungsten wire holder and (b) photograph of holder being scanned using HFUS transducer.	164
Figure 4. 31: (a) Diagram of tooth samples encased in epoxy for imaging, showing enamel and dentine layers, with EDJ (enamel dentine junction) in between and (b) resulting 3D rendered HFUS image.	166
Figure 5. 1: Graph showing relationship between density and W-volume fraction in W-loaded epoxy.	172
Figure 5. 2: Graph showing change in attenuation of longitudinal waves in Tungsten-loaded epoxy with increasing volume fraction.	173
Figure 5. 3: Surface profile of LP1	175
Figure 5. 4: (a) SEM photomicrograph of boundary between ceramic pillar and polymer matrix in Sample LP2 and (b) corresponding surface profile.	176
Figure 5. 5: Surface profiles from LP3a (blue line) and LP3b (red line).....	177
Figure 5. 6: Electrical impedance spectroscopy measurement and simulation for SC1	179
Figure 5. 7: Electrical impedance spectroscopy experimental measurement and simulation for FC1	182
Figure 5. 8: Electrical impedance spectroscopy experimental measurement and simulation for FC2	184
Figure 5. 9: Electrical impedance spectroscopy experimental measurement and simulation for FC3a	187
Figure 5. 10: Electrical impedance spectroscopy measurement for FC3b.....	189
Figure 5. 11: Pulse-echo signal from FC3b in (a) time-domain and (b) frequency domain.....	189
Figure 5. 12: Photograph of piezocomposite sample MC1.....	191
Figure 5. 13: Electrical impedance spectroscopy experimental measurement and simulation for MC1	192
Figure 5. 14: Pulse-echo signal from MC1.	194

Figure 5. 15: Photographs of Composite MC2, including close up of small crack.	195
Figure 5. 16: Electrical impedance spectroscopy measurement and simulation for MC2	195
Figure 5. 17: Pulse-echo signal from MC2 in (a) time domain and (b) frequency domain.....	197
Figure 5. 18: Microscope photograph of MC3.....	198
Figure 5. 19: Electrical impedance spectroscopy experimental measurement and simulation for MC3	199
Figure 5. 20: Microscope photographs showing MC4 and close-up of a section of pillars.....	201
Figure 5. 21: Electrical impedance spectroscopy experimental measurement and simulation for MC4.....	201
Figure 5. 22: Microscope photographs of MC6.....	203
Figure 5. 23: Electrical impedance spectroscopy measurement and simulation for MC6	204
Figure 6. 1: Experimental measurement of impedance magnitude and phase of JB1	209
Figure 6. 2: Pulse-echo from stainless steel flat surface from JB1 in (a) time and (b) frequency domains.	209
Figure 6. 3: Line spread function from transducer JB1	209
Figure 6. 4: Depth of field measurement for JB1.....	209
Figure 6. 5: B-scan image of single 5 μm Tungsten wire at focus of JB1	210
Figure 6. 6: B-scan image of porcine eye from JB1.	211
Figure 6. 7: Impedance Magnitude and Phase of LNO60.....	212
Figure 6. 8: Pulse-echo measurement of LNO60 from stainless steel block at 20.5 mm	212
Figure 6. 9: FFT of pulse in Figure 6.8.....	212
Figure 6. 10: Line spread function from LNO 60 MHz transducer, taken using pulse-echo on 5 μm Tungsten wire.....	212
Figure 6. 11: Electrical impedance magnitude and phase measurement for TH10.	214

Figure 6. 12: Pulse shape from TH10 through-transmission (at 10 mm distance) in (a) time and (b) frequency domains.....	215
Figure 6. 13: Pulse-echo measurement from TH10 on stainless steel at distance of 11.5 mm, shown in time and frequency domains.....	216
Figure 6. 14: Single scan of 5 μ m Tungsten wire at distance of 11.5 mm from TH10.	217
Figure 6. 15: Surface profile of TH09 in 3D.....	218
Figure 6. 16: Surface profile of TH09 in 2D.....	218
Figure 6. 17: Electrical impedance magnitude and phase measurement for TH09, and associated piezoelectric properties.....	219
Figure 6. 18: Through measurement of pulse from TH09 from membrane hydrophone, taken at 11 mm, in time domain and frequency domain	220
Figure 6. 19: Pulse-echo from TH09, in time domain and frequency domain.....	220
Figure 6. 20: Line spread function of TH09 at focus, taken from pulse-echo measurements on 5 μ m Tungsten wire.	221
Figure 6. 21: Depth of field of Transducer TH09, taken by pulse-echo measurements from 5 μ m Tungsten wire.....	221
Figure 6. 22: B-scan image of single 5 μ m Tungsten wire at focus of TH09.....	222
Figure 6. 23: B-scans of single 5 μ m wire at varying distances from the transducer. Wire was at distances of (top row, l-r) 2 mm, 3 mm, 4 mm; (middle row, l-r) 5 mm, 6 mm, 7 mm and (bottom row, l-r) 8 mm, 9 mm, 10 mm from the transducer in 1 mm increments.....	224
Figure 6. 24: B-scan of ovine eye generated using TH09.....	225
Figure 6. 25: Impedance magnitude and phase measurement and 1D simulation from TH16	226
Figure 6. 26: Pulse-echo measurement from TH16 at focus in (a) time and (b) frequency domains.	227
Figure 6. 27: Line spread function for TH16 by pulse-echo from 5 μ m W wire at focus.	227
Figure 6. 28: Depth of field measurement of TH16 taken by pulse-echo on stainless steel.	227
Figure 6. 29: B-scan image of single 5 μ m Tungsten wire at focus of TH16.....	228

Figure 6. 30: B-scan of porcine eye generated by TH16	229
Figure 6. 31: Experimental measurements and 1D simulation of impedance magnitude and phase from TH13	230
Figure 6. 32: Pulse-echo measurement from TH13 on stainless steel at focus in (a) time and (b) frequency domains.....	231
Figure 6. 33: Line spread function from TH13 by pulse-echo from 5 μm W wire..	231
Figure 6. 34: Depth of field measurement for TH13.	231
Figure 6. 35: B-scan image of single 5 μm Tungsten wire at focus of TH13.....	232
Figure 6. 36: B-scan of porcine eye from TH13	233
Figure 6. 37: Mouse tumour imaged using (a) TH13 and (b) a Visualsonics Vevo system. Dimension markers are in mm.	233
Figure 7. 1: Summary showing ceramic volume fractions of all composites tested.	241
Figure 7. 2: Summary showing velocities of all composites tested.	241
Figure 7. 3: Summary showing acoustic impedance of all composites tested.	241
Figure 7. 4: Summary showing c_{33}^D of all composites tested.	241
Figure 7. 5: Summary showing c_{33}^E of all composites tested.	242
Figure 7. 6: Summary showing ϵ_R^S of all composites tested.	243
Figure 7. 7: Summary showing k_T of all composites tested.....	243
Figure 7. 8: Summary showing e_{33} of all composites tested.....	243
Figure 7. 9: Summary showing h_{33} of all composites tested.....	244
Figure 7. 10: Summary showing d_{33} of all composites tested.....	244
Figure 8. 1: Prototype linear array made with MC	255

List of Tables

TABLE 2. 1: ACOUSTIC IMPEDANCES OF VARIOUS MATERIALS	20
TABLE 2. 2: EQUATIONS FOR CALCULATION OF ELASTIC PROPERTIES OF PASSIVE MATERIALS	25
TABLE 2. 3: PIEZOELECTRIC PARAMETERS.....	36

TABLE 2. 4: SUMMARY TABLE OF PIEZOELECTRIC PROPERTIES OF MATERIALS SIMULATED IN FIGURES 2.11 – 2.16.....	41
TABLE 2. 5: RELATIONSHIPS BETWEEN PIEZOELECTRIC PROPERTIES AND ELECTRICAL IMPEDANCE	53
TABLE 4. 1: MECHANICAL, ELECTRICAL AND PIEZOELECTRIC PROPERTIES DETERMINED FOR PIEZOELECTRIC SAMPLES	132
TABLE 4. 2: MATERIAL PROPERTIES OF 50% VOLUME FRACTION CTS3203HD AND RX771 PIEZOCOMPOSITE	148
TABLE 5. 1: PHYSICAL CHARACTERISTICS OF SC1.....	178
TABLE 5. 2: CALCULATED PIEZOELECTRIC PARAMETERS OF SC1	179
TABLE 5. 3: PHYSICAL CHARACTERISTICS OF FC1.....	181
TABLE 5. 4: CALCULATED PIEZOELECTRIC PARAMETERS OF FC1	183
TABLE 5. 5: PHYSICAL CHARACTERISTICS OF FC2.....	184
TABLE 5. 6: CALCULATED PIEZOELECTRIC PARAMETERS OF FC2	185
TABLE 5. 7: PHYSICAL CHARACTERISTICS OF FC3a.....	186
TABLE 5. 8: CALCULATED PIEZOELECTRIC PARAMETERS OF FC3a	187
TABLE 5. 9: PHYSICAL CHARACTERISTICS OF FC3B	189
TABLE 5. 10: PHYSICAL CHARACTERISTICS OF MC1	191
TABLE 5. 11: CALCULATED PIEZOELECTRIC PARAMETERS OF MC1.....	193
TABLE 5. 12: PHYSICAL CHARACTERISTICS OF MC2	194
TABLE 5. 13: CALCULATED PIEZOELECTRIC PARAMETERS OF MC2.....	196
TABLE 5. 14: PHYSICAL CHARACTERISTICS OF MC3	198
TABLE 5. 15: CALCULATED PIEZOELECTRIC PARAMETERS OF MC3.....	199
TABLE 5. 16: PHYSICAL CHARACTERISTICS OF MC4	200
TABLE 5. 17: CALCULATED PIEZOELECTRIC PARAMETERS OF MC4.....	202
TABLE 5. 18: PHYSICAL CHARACTERISTICS OF MC6	203
TABLE 5. 19: CALCULATED PIEZOELECTRIC PARAMETERS OF MC6.....	204
TABLE 6. 1: PHYSICAL CHARACTERISTICS OF JB1	208
TABLE 6. 2: STATISTICS FOR JB1 PULSE-ECHO MODE	210

TABLE 6. 3: PHYSICAL CHARACTERISTICS OF LNO60	212
TABLE 6. 4: STATISTICS FOR LNO60 PULSE-ECHO MODE	212
TABLE 6. 5: PHYSICAL CHARACTERISTICS OF TH10	214
TABLE 6. 6: STATISTICS FOR TH10 THROUGH-TRANSMISSION MODE ..	215
TABLE 6. 7: STATISTICS FOR TH10 PULSE-ECHO MODE	216
TABLE 6. 8: PHYSICAL CHARACTERISTICS OF TH09	219
TABLE 6. 9: STATISTICS FOR TH09 THROUGH-TRANSMISSION MODE ..	220
TABLE 6. 10: STATISTICS FOR TH09 PULSE-ECHO MODE	221
TABLE 6. 11: PHYSICAL CHARACTERISTICS OF TH16	226
TABLE 6. 12: STATISTICS FOR TH16 PULSE-ECHO MODE	227
TABLE 6. 13: PHYSICAL CHARACTERISTICS OF TH13	230
TABLE 6. 14: STATISTICS FOR TH13 PULSE-ECHO MODE	231
TABLE 7. 1: LIST OF COMPOSITE SAMPLES TESTED.....	240
TABLE 7. 2: SUMMARY OF MEASURED PULSE-ECHO PERFORMANCE CHARACTERISTICS OF ALL TRANSDUCERS TESTED.....	246

1. Introduction

1.1. History of Medical Ultrasound

Ultrasound is a widely used imaging modality, with a variety of applications in sonar, non-destructive testing and medical diagnosis. The beginnings of ultrasound instrumentation can be traced back to the demonstration of the *piezoelectric effect* by Pierre and Jacques Curie in 1880, where applying an electric field to certain materials can cause high frequency mechanical vibrations (Cracknell, 1980). The converse is also true. One particular piezoelectric material, quartz, was then incorporated into the first ultrasound device, a *hydrophone* developed by Paul Langevin in the early 20th century, intended for sonar applications (Biquard, 1972).

The use of ultrasound for medical imaging was pioneered in the 1950s. Initially, ultrasound was used in *A-mode*, a path measurement used commonly in sonar, to detect pathology such as gallstones. The first medical, two-dimensional, *B-mode* images, similar to those used today, were generated by Wild and Reid (1952), using mechanical scanning apparatus to build up a 2D image based on a number of 1D measurements. This was mainly used to detect tumours within the stomach, brain and breast tissue and was seen as replacing needle biopsies. The spectrum of medical applications of ultrasound diagnosis widened, and by the 1960s ultrasound was being used in obstetrics, for *foetal cephalometry*: measuring of the foetal head size to determine growth.

The use of fixed focal depth, mechanical scanning continued, with various configurations proposed, until a significant technological advance in ultrasound imaging occurred with the development of arrays containing several independently operated elements. The first commercially available linear array, the Multi-scan system, was released in 1972 (Bom et al., 2004). The most straightforward array is a *flat linear array*, where subsets of elements are excited sequentially. Electronic scanning replaced mechanical scanning, frame-rates were significantly increased and real-time 2D scans imaging was now possible. *Curvilinear* arrays are similar in

operation to flat linear arrays but are convex shape, allowing the image width to be bigger than the array footprint. The most sophisticated arrays are *phased* arrays. Applying specific time delays to the excitation voltages used to drive array elements, known as *phasing*, allowed dynamic depth focusing and the ability to electronically focus and steer the ultrasound beam. Improvements in computing power and electronics have further increased the efficacy of ultrasound as a diagnostic tool.

In recent years, a number of other techniques have been introduced to ultrasound imaging, the most significant being contrast agents and Doppler imaging. Doppler flow imaging is used to detect movement of tissues, and most commonly blood flow. Colour Doppler flow imaging has now been introduced which allows real-time visualisation of blood flow, with the blood flow rate depicted by a colour scale on the grey-scale background of a standard ultrasound image (Kasai et al., 1985). Similarly, micron scale gas bubbles, *contrast agents*, are used to enhance contrast in both B-mode and Doppler imaging (Goldberg et al., 1990).

During this period, other imaging modalities have also been developed and improved, such as X-ray, X-ray computed tomography (CT), magnetic resonance imaging (MRI) positron emission tomography (PET) and, more recently, optical coherence tomography (OCT). Each modality has inherent advantages and disadvantages. X-ray is relatively low-cost and is the most frequently used medical imaging procedure but is a source of ionising radiation and does not show soft tissue. CT produces excellent images at high resolution but is expensive and subjects the patient to large doses of ionising radiation. MRI also can generate images at high resolution but is very expensive and metallic objects present a hazard. This can include pacemakers, implants and even shards of metal lodged in the body, ruling out use on many patients. Ultrasound, with resolution of around half a millimetre for a standard 3 MHz transducer, may be considered to produce images of poorer resolution than CT or MRI but it is second only to X-ray in terms of number of procedures undertaken per year (Szabo, 2004). This is due to certain attractive features: it is safe, systems are relatively inexpensive to buy and maintain, scanners are easily portable and they produce images in real time.

1.2. High Frequency Ultrasound

High frequency ultrasound (HFUS) research aims to improve the spatial resolution of ultrasound systems such that it is comparable to, or even better than, other imaging technologies. The resolution obtainable with an ultrasound transducer is dependent on the frequency of the device, with higher frequency devices generally allowing better resolution. This comes at a cost of reduced penetration depth. Research into HFUS for medical diagnostics has centred on applications where small anatomical structures are of interest and are accessible with a transducer probe. These applications include ophthalmology, dermatology, intra-vascular imaging and small animal imaging.

Commercial HFUS systems have existed for some years for ophthalmological imaging and small animal imaging as part of genetics research. Until very recently these systems used mechanically scanned, single element transducers. However, a high frequency array system has recently become available commercially: the VisualSonics Vevo 2100. Nevertheless, these arrays still require significant optimisation and there is significant scope for improvement in other aspects of the development of HFUS systems.

Although the historical development of HFUS devices has centred on applications, analysis of scientific literature concerning HFUS suggests that modest technological advances of transducers have always slowed the progress toward better resolution. At the root of this is the lack of availability of suitable piezoelectric materials and fabrication techniques. Development of superior high frequency piezoelectric materials is directly linked to potential improvement of imaging systems. This is the motivation behind the work of this thesis.

1.3. Aims

The aim of the work presented in this thesis is to establish whether a novel technique, viscous polymer process (VPP) micromoulding, provides a viable route to fabrication

of high frequency piezoelectric material. Two main bodies of work were undertaken: fundamental characterisation and early functional testing.

Fundamental characterisation in this case refers to testing of the piezoelectric properties of the VPP micromoulded composites (MCs). Performance data was generated from electrical impedance spectroscopy measurements and verified with computer models based on the one-dimensional wave equation and piezocomposite homogenisation principles of Smith and Auld (1991). Investigation of the high frequency properties of passive transducer materials was also undertaken. Prototype transducers fabricated with MCs were subjected to early functional testing of their ultrasonic properties. This included measurements of bandwidth, spatial resolution and depth of field and assessment of imaging performance in a basic mechanical scanning system.

1.4. Contributions to Knowledge

The work described in this thesis has contributed to knowledge in three areas:

The piezoelectric properties of micromoulded composites may be characterised using electrical impedance spectroscopy measurements and one-dimensional modelling

The process used to fabricate MCs does not allow characterisation to be carried out using standard IEEE methodology. Well-established testing procedures based on derivation of piezoelectric properties from electrical impedance spectroscopy measurements, and verification using one-dimensional modelling, have been applied to MCs and shown to be an effective method of characterisation.

Assessment of the fundamental piezoelectric properties of VPP micromoulded composites

MCs have been extensively characterised. The piezoelectric properties of MCs were shown to compare well with those of piezoelectric materials traditionally used for high frequency transducer manufacture. However, MCs appear to have poorer properties than those reported for recently developed single crystal composites.

Verification of micromoulded piezocomposite as a viable piezoelectric material for high frequency ultrasound transducer and array fabrication

Transducers fabricated with MC have been tested and shown to have resolution and sensitivity commensurate with high frequency imaging applications.

1.5. Outline of Thesis

Chapter 2 discusses the theoretical principles behind this work, primarily that concerning ultrasound waves, piezoelectric materials and ultrasound transducer design and fabrication. Chapter 3 reviews past and present research into HFUS, investigating the influence of clinical need, availability of piezoelectric materials and advancement of transducer technology on the field of HFUS.

Chapter 4 sets out the experimental methodology utilised in the work of this thesis, including fabrication, testing and analysis procedures. Chapter 5 presents results from fundamental characterisation of a number of piezocomposite samples, including a standard dice-and-fill PZT composite, VPP fibre composites and VPP MCs. Chapter 6 reports results from functional testing of a number of prototype MC transducers.

Chapter 7 discusses the results presented in Chapters 5 and 6. Finally, conclusions drawn from the work of this thesis are presented in Chapter 8, along with an overview of further work leading on from this thesis.

1.6. Publications and conference submissions

Journal Paper in preparation

1. MacLennan D., Bamber J.C., Bush N.L., Button T.W., Corner G., Démoré C.E.M., Elgoyhen J., Hughes H., Meggs C., Zhang D., Cochran S. (2009) Fundamental Performance Characterisation of High Frequency Piezocomposites made with Net-shape Viscous Polymer Processing for Medical Ultrasound Transducers. *For submission to IEEE Transactions on Ultrasonics, Ferroelectrics and Frequency Control.*

With Proceedings

1. T.W. Button, S. Cochran, K.J. Kirk, D. MacLennan, A. MacNeil, K. McDonald, C. Meggs, D. Rodriguez-Sanmartin, R. Webster and D. Zhang. *Net-Shape Ceramic Manufacturing as an Aid to Realize Ultrasonic Transducers for High-Resolution Medical Imaging* 2005 IEEE International Ultrasonics Symposium, Rotterdam.
2. D. MacLennan, S. Cochran, T.W. Button, H. Hughes, M. Ponting, J. Sweet. *Ultra Precision Grinding in the Fabrication of High Frequency Piezocomposite Ultrasonic Transducers.* 2006 IEEE International Ultrasonics Symposium, Vancouver.
3. D. MacLennan, J. Elgoyhen, T. W. Button, C. E. M. Démoré, H. Hughes, C. Meggs, S. Cochran. *Fundamental Properties and Application-oriented Performance Characterisation of High Frequency Piezocomposite Ultrasonic Transducers* 2007 IEEE International Ultrasonics Symposium, New York
4. R.A. Webster, S. Cochran, D. MacLennan, C. Meggs, T.W. Button, *Passive Materials for High Frequency Ultrasound Components* 2007 IEEE International Ultrasonics Symposium, New York
5. D. MacLennan, C. Démoré, G. Corner, T. Button, J. Elgoyhen, H. Hughes, C. Meggs, S. Cochran. *Fundamental Performance Characterisation of High*

Frequency Piezocomposites made with Net-shape Viscous Polymer Processing for Medical Ultrasound Transducers 2008 IEEE International Ultrasonics Symposium, Beijing

Without proceedings

1. S. Cochran, K.J. Kirk, D. MacLennan, T.W. Button, C. Meggs, D. Rodriguez-Sanmartin, R. Webster and K. McDonald. *Development of high frequency ultrasonic transducers*. 2005 Brit. Conf. on NDT, Harrogate.
2. K. McDonald, D. MacLennan, A. MacNeill, S. Cochran, T. Button, C. Meggs, D. Rodriguez-Sanmartin, R. Webster D. Zhang *High Frequency Ultrasonic Transducers for High Resolution Medical Imaging* 2005 IPEM Glasgow
3. D. MacLennan, D. Zhang, S. Cochran, T.W. Button, K. Kirk. *Piezofibre-Polymer Composite Material for High-frequency Ultrasound*, 2006 POLECER International Conference, Lillehammer.
4. D. MacLennan, S. Cochran, G.A. Corner. *Using an Edinburgh pipe phantom to quantify the performance of a range of ultrasound scanners*. 2006 IPEM Quality Assurance of Ultrasound Scanners Scientific Meeting, York.
5. M. Blair, S. Cochran, G.A. Corner, D.P. MacLennan. *A novel dynamic ultrasound test object using feedback to automate Quality Assurance*. 2006 IPEM Quality Assurance of Ultrasound Scanners Scientific Meeting, York.
6. D. MacLennan, S. Cochran, T. W. Button. *Real-time Ultrasonic Imaging: Towards the Cellular Level*. 2006 Scottish Sonoporation Symposium, Dundee.
7. D. MacLennan, S. Cochran, J-F Saillant, T.W. Button, H. Hughes, M. Ponting and J. Sweet. *A Role for Ultra Precision Grinding in the Fabrication*

of High Frequency Piezoelectric Transducer. 2007 Ultrasonics Industry Association, London,

8. C.E.M. Démoré, A.L. Bernassau, D. MacLennan, T.W. Button, S. Cochran *Investigation of Element Cross Talk in Arrays using 1-3 Piezocomposite Substrate*. 2007 Ultrasonic Transducer Engineering Conference, Los Angeles
9. S. Cochran, T. W. Button, A. Bernassau, T. Clipsham, C.E.M. Démoré, G. Dolman, H. Hughes, D. MacLennan, C. Meggs, G. O'Hare, and R.A. Webster. *A Holistic Approach to Ultrahigh Frequency Ultrasonic Arrays*. 2007 Ultrasonic Transducer Engineering Conference, Los Angeles
10. D. MacLennan, J. Elgoyhen, T. W. Button, C. E. M. Démoré, H. Hughes, C. Meggs, S. Cochran, L. Garcia-Gancedo. *Fundamental Properties and Performance of Piezocomposite for High Frequency Ultrasonic Transducers*. 2007 Ferroelectrics UK Conference
11. M.F. Wallace, P. Marin, H. Mulvana, M.P. Walsh, T.W. Button, H. Hughes, D. MacLennan, S. Cochran. *Applications of new Piezoelectric materials for high performance ultrasonic NDT Transducers*. 2007 Nondestructive Testing, Glasgow.
12. S. Cochran, J. Bamber, A. Bernassau, N. Bush, T. Button, C. Démoré, L. Garcia-Gancedo, D. Hutson, D. MacLennan, P. Maher, C. Meggs and R. Webster, *Progress towards transducers and arrays for real-time high frequency biomedical ultrasound imaging*. Acoustics 2008, Paris.
13. Cochran S., Bamber J., Bernassau A., Bush N., Button T.W., Démoré C., Garcia-Gancedo L., Hutson D., MacLennan D., Maher P., Meggs C., Webster R.A. *Utilisation of ceramic micromoulding techniques for high frequency ultrasound transducers and arrays*. UBM 2008 6th International Conference on Ultrasonic Biomedical Microscanning, Malibu.

14. T.W. Button, S. Cochran, G. Corner, C.E.M. Démoré, J. Elgoyhen, H. Hughes, D. MacLennan, C. Meggs, D. Zhang. *Material properties of piezocomposites made with viscous polymer processing for high frequency medical ultrasound transducers*. Piezo 2009, Electroceramics for End Users IV, Zakopane, Poland
15. D. Zhang, L.J. Nelson, A. Dent, D. MacLennan, C. Meggs, G. Dolman, B. Su, S. Cochran, K.J. Kirk, C.R. Bowen, and T.W. Button. *Fine Scale Lead Zirconate Titanate (PZT) Fibres and Composite Structures*. 2006 POLECER International Conference, Lillehammer.
16. D. MacLennan, D. Zhang, S. Cochran, K.J. Kirk and T.W. Button. *Piezofibre-Polymer Composite Material for Ultrasonic Transducers*, 2006 Ferroelectrics UK Conference, Birmingham.
17. D. MacLennan, S. Cochran, M. Ponting, J. Sweet. *Ultra precision grinding in High-Frequency Piezocomposite Ultrasonic Transducer Manufacture*. 2006 Ferroelectrics UK Conference, Birmingham.
18. D. Zhang, L.J. Nelson, A. Dent, D. MacLennan, C. Meggs, G. Dolman, B. Su, S. Cochran, K.J. Kirk, C.R. Bowen, and T.W. Button. *Fine Scale Lead Zirconate Titanate (PZT) Fibres and Composite Structures*. 2006 Ferroelectrics UK Conference, Birmingham.
19. Cochran S., Bamber J., Bernassau A., Bush N., Button T.W., Démoré C., Garcia-Gancedo L., Hutson D., MacLennan D., Maher P., Meggs C., Webster R.A. *Progress towards piezocomposite transducers and arrays for real-time high frequency biomedical ultrasound imaging* 2008 ONR Transducer Materials and Transducers Workshop.

1.7. References

Biquard P. (1972) *Paul Langevin Ultrasonics*, Vol. 10 pp. 213-214

Bom N., van der Steen A.F.W., de Jong N and Roelandt J.R.T.C. (2004) Early, recent and future applications of echocardiography. *Clin. Physiol.Funct. Imaging* **24**, pp141–146

Cracknell A.P., (1980) *Ultrasonics*, Wykeham Publications, London. pp. 62

Goldberg BB, Hilpert PL, Burns PN, Liu JB, Newman LM, Merton DA (1990) Hepatic tumors: Signal enhancement after intravenous injection of a contrast agent. *Radiology* **177**:713-7 17

Kasai C., Namekawa K., Koyano A., and Omoto R. (1985) “Real-Time Two-Dimensional Blood Flow Imaging Using an Autocorrelation Technique,” *IEEE Transactions on Sonics and Ultrasonics*, vol. 32, pp. 458-464.

Smith W.A. & Auld B.A. (1991) Modelling 1-3 composite piezoelectrics: thickness-mode oscillations. *IEEE Transactions on Ultrasonics, Ferroelectrics and Frequency Control*, **38** (1), pp. 40-47.

Szabo T.L. (2004) *Diagnostic Ultrasound Imaging: Inside Out*. Elsevier Academic Press. pp.22

Wild J.J. and Reid J.M. (1952) Application of Echo-Ranging Techniques to the Determination of Structure of Biological Tissues *Science* Vol. 115 pp. 226-230

2. Theory

2.1. Introduction

This thesis concerns demonstration of the viability of micromoulded piezocomposite materials for use in high frequency single element transducers and arrays. The content of this chapter is designed to reflect the physical and technical principles involved.

Section 2.2 reviews the most widely used medical imaging modalities to assess the place of ultrasound in medical imaging. The general physics of sound waves is discussed in Section 2.3, including key concepts such as speed, acoustic impedance and attenuation. A description of the influence of elastic behaviour of materials on wave propagation is also given, due to the importance of this to the behaviour of both the passive and piezoelectric materials used to construct ultrasound transducers. Wave propagation at boundaries is described in Section 2.4 and ultrasonic inspection and imaging procedures are discussed briefly in Section 2.5: although no new imaging procedures were developed in the work of this thesis, basic imaging procedures have been used as part of the device characterisation undertaken. An overview of piezoelectric materials is then presented in Section 2.6, including the principles of piezoelectricity, and relative advantages and disadvantages of the piezoelectric materials used commonly for HFUS devices are then discussed in Section 2.7. Section 2.8 extends this with a closer examination of piezocomposite materials. Section 2.9 then describes how electrical impedance spectroscopy may be used to characterise piezoelectric materials. The chapter closes by briefly describing the fabrication and operation of ultrasound transducers and systems in Sections 2.10 and 2.11 respectively.

2.2. Medical imaging modalities

A number of medical imaging modalities are available. The most widely used are X-ray, CT, MRI, PET and OCT. These systems have different advantages and disadvantages and can generally be considered to be complementary to one another.

2.2.1. X-ray and Computed Tomography

X-rays are a form of electromagnetic radiation discovered in 1895 by the German physicist W.K. Roentgen and adopted as a diagnostic tool shortly after, using rays of wavelength between 10 pm and 10 nm for diagnostic frequencies. X-ray procedures are currently the most commonly used imaging modality in the world (Szabo, 2004). The major disadvantage of X-rays is that they are ionising radiation and thus potentially harmful to patients. They are unable to differentiate soft tissue, will always produce a two dimensional image of what is in fact a three-dimensional structure and are relatively insensitive. However, despite the obvious limitations, X-ray imaging has the advantage of being a very cost-effective imaging modality.

X-ray technology was further advanced in the 1960s with the development of CT. CT uses X-rays to produce images, but is capable of producing three-dimensional, quantitative images. CT images or ‘slices’ are built up computationally from multiple projections of an object, taken from different positions. Computational reconstruction of these projections allows greater contrast than is possible with X-ray, and hence imaging of both bone and soft tissue is possible. The main uses of CT are in diagnosis of neural and spinal conditions, such as tumour or haemorrhage. The resolution of a CT scanner depends on the number of pixels, slice thickness, algorithms, data sampling and computer hardware.

High resolution imaging with CT is called *Micro-CT*. High resolution imaging systems are available commercially, for example the eXplore Locus SP (GE Healthcare, Giles, UK). This system has imaging resolution of down to 8 μm (if imaging contrast agents are used) and can image both soft tissue and bone. Some example images are shown in Figure 2.1.

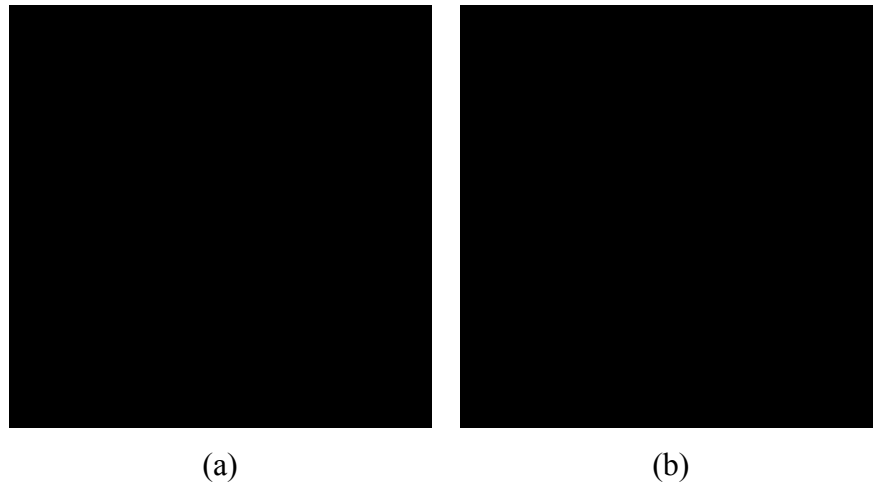


Figure 2. 1: images removed due to copyright restrictions.

The main disadvantage of CT is that ionising radiation is required to produce images, particularly as each CT scan subjects the patient to a radiation dose equivalent to over a hundred X-rays. High resolution images cannot be achieved without high X-ray dosages. This precludes micro-CT from being used on small animals *in vivo*. Further disadvantages are that CT systems can be expensive, and are not portable.

2.2.2. Magnetic Resonance Imaging

Nuclear magnetic resonance (NMR) was discovered in 1946 and adopted as a diagnostic tool, known more commonly as Magnetic Resonance Imaging (MRI) in the 1970s. The spatial resolution of an MRI system depends on the number of pixels generated for an image of a certain area. The number of pixels is itself limited by the signal sensitivity of the scanner because increasing the resolution of an MRI image, i.e. the number of pixels, results in significant degradation of signal-to-noise ratio. Ultimately, it is the strength of the magnet in the system which determines signal strength, and hence resolution. Bruker Biospin (Coventry, UK) produce a 9.4 T research scanner with spatial resolution of around 50 μm . However, a stronger magnet is accompanied by a significant increase in cost. Side-effects of MRI include dizziness and other sensory symptoms in the patient, and this is more marked with stronger magnetic fields (Weintraub et al., 2007). Normal medical imaging systems use magnetic fields of between 0.5 and 3.0 T and hence have poorer resolution.

Image quality is still subject to artefacts caused by movement of the patient. This is a particular problem for higher resolution images, which can take several hours to produce.



Figure 2. 2: MRI image of a mouse brain taken with a 7T magnetic field (Bock et al., 2005, ©Wiley)

A MR image of a contrast-perfused mouse brain is shown in Figure 2.2, taken with a 7 T magnetic field. It could be argued that MRI represents the gold standard for imaging. It is non-ionising, minimally invasive, can differentiate between soft tissue types extremely well and has excellent spatial resolution when high magnetic fields are used. However, MRI scanners are certainly not portable, and are also very expensive. Purchasing a scanner requires a large initial outlay (approximately £500k to £2M) for the machine and accompanying specialist accommodation and high maintenance costs (tens of thousands of pounds per year) will be incurred throughout the lifetime of the machine. A branch of MRI, functional MRI (fMRI), measures haemodynamic response in the brain, so can be used to monitor neural activity (Kwong et al., 1992).

2.2.3. Positron Emission Tomography

Positron emission tomography (PET) was developed for medical diagnostic use in the 1970s. A radionuclide is injected into the body, or swallowed, and positrons are emitted from the body when this radionuclide comes into contact with positron emitting radioisotopes that occur naturally in the body, such as ^{11}C , ^{15}O and ^{13}N . These are detected by ‘scintillation cameras’ which surround the patient. PET

scanners have relatively poor spatial resolution and signal to noise ratio (SNR) compared to other imaging modalities, and as such PET is primarily used to study metabolic functions, something which can be done much more effectively than with ultrasound, MRI or X-ray.

2.2.4. Optical Coherence Tomography

Optical Coherence Tomography (OCT) uses low-coherence interferometry to produce images of optical scattering from structures such as tissue (Huang et al., 1991). In this sense, it is an optical analogy of ultrasonic pulse-echo imaging. An image of an eye produced by an early OCT system is shown in Figure 2.3. OCT has excellent spatial resolution and has been adopted as a medical imaging tool, particularly for ophthalmology (Drexler and Fujimoto, 2007). Clinical systems are now available commercially, such as the Stratus OCT (Carl Zeiss Meditec, Inc, Welwyn Garden City, UK). This system is capable of cross-sectional imaging of the retina at axial and lateral resolutions of less than 10 μm in real-time. The depth of field of OCT systems is relatively small: 2 mm in the case of the Stratus OCT.

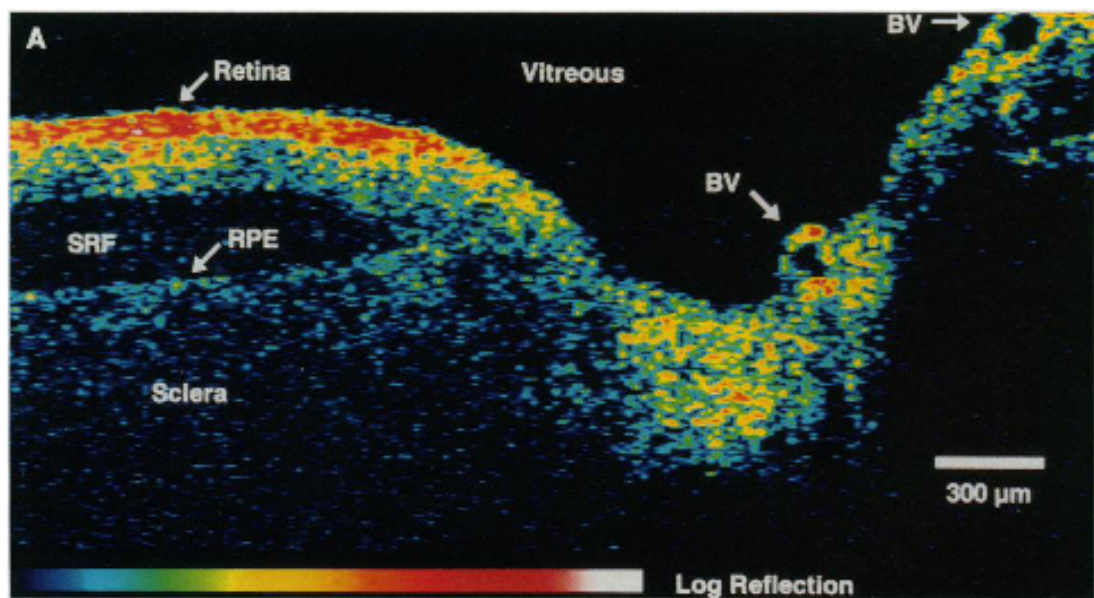


Figure 2. 3: OCT image of human eye, showing several structures including retina, sub-retinal fluid (SRF), retinal pigment epithelium (RPE), sclera and blood vessels (BV) (from Huang et al., 1991. Reprinted with permission from AAAS).

OCT also has high sensitivity, detecting signals of the order of 10^{-10} times the incident beam intensity (Huang et al., 1991). Recent systems, known as ultrahigh-resolution OCT, have reported imaging resolution of 2 μm , and can scan at sufficiently high speeds to allow three dimensional images to be generated (Wojtowski et al., 2005). Optical aberrations are common in OCT images but this can be countered using adaptive optics (Zawadzki et al., 2009).

2.2.5. High Frequency Ultrasound

Ultrasound is the second most commonly used medical imaging modality after X-ray (Szabo, 2004). This is attributed to the fact that it is low cost, non-invasive and non-ionising, systems are generally portable and they image in real-time. The development of ultrasound array devices, which facilitate electronic scanning and steering of the ultrasound beam, and dynamic depth focusing, has allowed high quality, real-time 2D images to be produced with high frame rates.

The operational frequency of an ultrasound system will depend on the application for which it is designed. It can be categorised, for example: “Lower frequencies of 2-5 MHz are employed for abdominal, obstetrical and cardiological studies, 5-7.5 MHz are used for paediatric, and peripheral vascular applications and higher frequencies from 10-30 MHz are utilized for intravascular, intra-cardiac and eye imaging” (Gururaja and Panda, 1998). For the purposes of this thesis, high frequency ultrasound (HFUS) is considered to be frequencies above 20 MHz. Ultrasound technology at lower frequencies (below 20 MHz) is well established and many systems are available. This is not the case with high frequency systems.

The propagation velocity of ultrasound is tissue dependent, varying with density and stiffness of the tissue, but has an average value of 1540 ms^{-1} . The resolution of an imaging device is strongly dependent on the wavelength of the ultrasound used. Wavelength, λ , is related to operational frequency, f , by:

$$\lambda = \frac{v}{f} \quad 2.1$$

where v is propagation velocity.

Thus for frequencies quoted above, the wavelength of a 2-5 MHz transducer is 800-300 μm , for a 10 MHz transducer it is around 150 μm and for a 30 MHz transducer the wavelength is approximately 50 μm .

From this it can be inferred that a HFUS system with sufficiently high frequency can be used to produce images with comparable resolution to the alternative modalities discussed in this section. Combining this with the well-known advantages of ultrasound systems, such as cost and patient safety, HFUS would be an extremely useful tool. HFUS systems have been available for some years, but using a single element transducer which is mechanically scanned. A commercial HFUS system using arrays has only very recently become available, and is still not optimally designed (Foster, 2008). This is primarily because of the difficulty of fabricating HFUS arrays due largely to a lack of suitable active materials. As described previously, the work reported in this thesis was undertaken with the objective of overcoming these problems.

2.3. Ultrasound Waves

The physical principles behind ultrasound imaging and ultrasound device fabrication are now discussed. The developmental history of ultrasound devices, and current state of the art, are discussed in detail in Chapter 3.

Ultrasound is a class of mechanical pressure waves of frequencies above 20 kHz, the upper limit of the audible range for human beings. These waves can propagate through a solid, liquid or, to a lesser extent, gaseous medium in the form of sinusoids of wavelength defined by the frequency and speed of sound of the wave as shown in Equation 2.1.

The propagation of ultrasound occurs because vibrating particles interact with neighbouring particles within a material, causing a periodic change in pressure. The

material alternately undergoes compression, an increase in the density of the material compared to the normal state, and rarefaction, a decompression or decrease in density of the material. When this occurs, energy is spread in all directions from this point. Assuming that the material has a succession of alternate compressed and decompressed areas, the distance between the start of successive compressed areas is equivalent to the wavelength of the sound wave. This pressure wave can be detected by an ultrasound transducer and recorded, as illustrated in Figure 2.4.

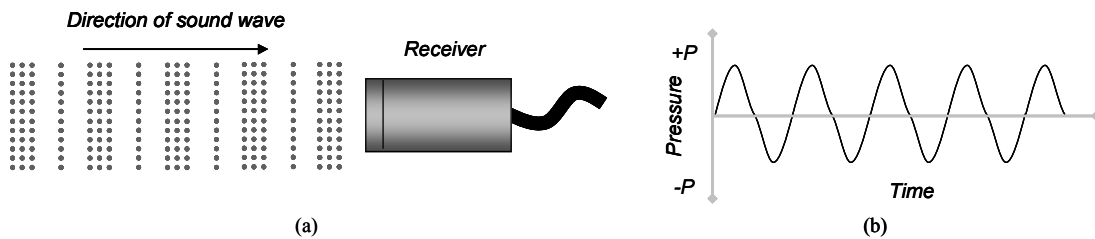


Figure 2. 4: (a) Sound wave travelling through a medium, with molecules undergoing compression and rarefaction. (b) Corresponding time-dependent pressure wave.

2.3.1. Types of wave

Several types of waves exist: the primary waves of interest in this thesis are longitudinal waves, where the pressure wave moves by compression and rarefaction in the direction of propagation, and transverse waves, where the pressure changes are perpendicular to the direction of propagation. Surface acoustic waves (SAW), known as Rayleigh waves, propagate along the surface of a material, within approximately one wavelength of that surface (Cheeke, 2002a). The final category of wave is plate waves, such as Lamb waves. Like longitudinal waves, these propagate by compression and rarefaction, but can do so only in thin plates of material. Plate waves occur when movement is bounded by the plate surface, causing the particles of the plate to move in elliptical paths on the surfaces of a material and as such they propagate through the entire thickness of the material. Within this thesis, only longitudinal and transverse waves are considered.

2.3.2. Acoustic Impedance

Acoustic impedance, Z , is defined as:

$$Z = \rho v \quad 2.2$$

where ρ is the density of the material. The units of acoustic impedance are *Rayl* ($\text{kg m}^{-2} \text{s}^{-1}$) but values are usually expressed in *MRayl*. Reflections of a sound wave occur in a subject when there is a change in acoustic impedance, for example at the interface between soft tissue and bone. This is known as an impedance *mismatch*. The intensity or energy reflection coefficient, R_x , i.e. the proportion of ultrasonic energy reflected at an interface between two materials of differing acoustic impedance is dependent on the acoustic impedance of both of the materials and is calculated by:

$$R_x = \left(\frac{Z_1 - Z_2}{Z_1 + Z_2} \right)^2 \quad 2.3$$

where Z_1 and Z_2 are the acoustic impedances of the two materials respectively. It should be noted that the intensity reflection coefficient will be the same whether going from higher impedance to lower or vice versa, and that all energy that is not reflected is considered to have been transmitted. Hence, it follows that the transmission coefficient, T_x , is given by:

$$T_x = 1 - R_x = \frac{4Z_1Z_2}{(Z_1 + Z_2)^2} \quad 2.4$$

Some example values of acoustic impedance in tissue are given below (Hedrick et al., 1995a, O'Leary et al., 2005) in Table 2.1, along with their reflection coefficients with respect to water.

TABLE 2. 1: ACOUSTIC IMPEDANCES OF VARIOUS MATERIALS

Material	ρ (kg m ⁻³)	v (ms ⁻¹)	Z (MRayl)	R_x w.r.t. Water
Water	1000	1480	1.48	0
Air	1.2	330	0.0004	0.99
Soft Tissue	1060	1540	1.63	0.002
Bone	1912	4080	7.8	0.46
Epoxy	1210	2700	3.25	0.14
Steel	7900	5900	46	0.88

2.3.3. Attenuation

As a sound wave travels through any medium, the intensity of the wave will decrease with distance, partly due to beam spreading, but also due to *attenuation*. Attenuation of a sound wave occurs because of two phenomena, absorption and scattering. Absorption occurs because the energy of the sound wave is converted into other forms of energy, mainly heat. The level of absorption is dependent on the material through which the sound wave is travelling, in particular the physical properties of the material (Cheeke, 2002). An attenuation coefficient, α , may be measured for any given material. In general, absorption will respect the following expression for the intensity, I , of a sound wave:

$$I = I_0 e^{-\alpha x} \quad 2.5$$

where I_0 is the initial intensity of the wave and x is the distance travelled through the medium. Absorption is also dependent on the frequency of the wave in an approximately linear fashion, with higher frequency waves subject to greater attenuation (Cheeke, 2002), so values for attenuation are always quoted at the frequency measured, usually 1 MHz.

Scattering occurs when the sound wave is reflected or refracted in directions other than the original direction of propagation. In general, any interface that is irregular at

a small (sub-wavelength) scale will cause scattering. Large amounts of energy are dissipated in the body due to scattering (Hill and Bamber, 2004a). This could generally be regarded as a hindrance, but can also be utilised to improve the quality of ultrasound images. For example, sub-wavelength diameter gas bubbles are used to improve contrast in diagnostic imaging, particularly echocardiography.

2.3.4. Influence of elastic properties of a material

Materials can be split into three categories: viscous, viscoelastic and elastic. Viscous materials are those that resist transverse flow and strain linearly with time on application of a stress, and include fluids. Elastic materials are instantaneously strained when placed under stress, but return to their original state on termination of the applied stress, and this includes most solids. Viscoelastic materials exhibit properties of both viscous and elastic materials, and exhibit time dependent strain on application of a stress.

Most types of tissue are viscoelastic though some, such as cartilage, are poroelastic (Konofagou et al., 1999). Poroelastic materials are solid materials permeated with a liquid or gas. Almost all materials making up components of ultrasound transducers are elastic. Viscous, viscoelastic and poroelastic materials are not considered in detail within this thesis. However, due to the importance of elastic properties of a material to ultrasound propagation, and hence, transducer design and fabrication, elasticity is now discussed.

The propagation of an ultrasound wave through any material is determined by the mechanical properties of that material. Most importantly, the speed of sound of a wave travelling through a material, on which the acoustic impedance and the concept of ultrasound imaging depend, is strongly influenced by the elastic moduli of the material. As the properties of both longitudinal waves and transverse waves are integral to parts of this thesis, an explanation of the elastic theory influencing these is now given.

To begin, one must consider the concept of strain and stress tensors in the context of Hooke's Law. A brief description of the key points is given below; a more in depth explanation is given in Cheeke (2002).

A solid obeys Hooke's law if the relationship

$$\sigma_{ij} = c_{ijkl} \gamma_{kl} \quad 2.6$$

is followed, for the stress tensor, σ_{ij} , the strain tensor, γ_{kl} , and a tensor of elastic constants, or moduli which are independent of stress or strain, c_{ijkl} . If the material is isotropic, it may be described using only two independent elastic constants (Fung, 1993, Ch. 2). This allows Hooke's law to be expressed as:

$$\sigma_{ij} = \lambda \gamma_{xx} \delta_{ij} + 2\mu \gamma_{ij} \quad 2.7$$

where δ is the *Kronecker delta*, and λ and μ are the *Lamé coefficients*. μ is also named the *modulus of rigidity*.

The stiffness matrix for a material may be described from Hooke's Law, in reduced notation, as follows:

$$c_{ij} = \begin{bmatrix} c_{11} & c_{12} & c_{13} & c_{14} & c_{15} & c_{16} \\ c_{21} & c_{22} & c_{23} & c_{24} & c_{25} & c_{26} \\ c_{31} & c_{32} & c_{33} & c_{34} & c_{35} & c_{36} \\ c_{41} & c_{42} & c_{43} & c_{44} & c_{45} & c_{46} \\ c_{51} & c_{52} & c_{53} & c_{54} & c_{55} & c_{56} \\ c_{61} & c_{62} & c_{63} & c_{64} & c_{65} & c_{66} \end{bmatrix} \quad 2.8$$

As the material is assumed to be isotropic, this matrix may be simplified using the Lamé coefficients and symmetry:

$$c_{ij} = \begin{bmatrix} \lambda + 2\mu & \lambda & \lambda & 0 & 0 & 0 \\ \lambda & \lambda + 2\mu & \lambda & 0 & 0 & 0 \\ \lambda & \lambda & \lambda + 2\mu & 0 & 0 & 0 \\ 0 & 0 & 0 & \mu & 0 & 0 \\ 0 & 0 & 0 & 0 & \mu & 0 \\ 0 & 0 & 0 & 0 & 0 & \mu \end{bmatrix} \quad 2.9$$

c_{11} ($= c_{22} = c_{33}$), the stiffness of a material for a wave propagating along its own direction of polarisation is equivalent to $\lambda + 2\mu$, while c_{44} ($= c_{55} = c_{66}$), the stiffness of a material with the wave travelling perpendicular to the direction of polarisation is equivalent to μ .

The Lamé coefficients may also be used to derive the following expression for K , the *modulus of compression*, or *bulk elastic modulus* (Cheeke, 2002):

$$K = \lambda + \frac{2}{3}\mu \quad 2.10$$

From this, expressions for the longitudinal and transverse velocity may be derived. The longitudinal velocity, v_l , of a material can be related to c_{11} by the equation (Auld, 1990):

$$c_{11} = \rho v_l^2 \quad 2.11$$

and transverse velocity, v_s , is related to c_{44} by:

$$c_{44} = \rho v_s^2 \quad 2.12$$

The importance of bulk and transverse elastic moduli in determining the longitudinal and transverse velocities of a material can then be demonstrated by combining Equations 2.9, 2.10 and 2.12 to derive:

$$v_l = \sqrt{\frac{c_{11}}{\rho}} = \sqrt{\frac{\lambda + 2\mu}{\rho}} = \sqrt{\frac{K - \frac{2}{3}\mu + 2\mu}{\rho}} = \sqrt{\frac{K + \frac{4}{3}\mu}{\rho}} \quad 2.13$$

$$v_s = \sqrt{\frac{c_{44}}{\rho}} = \sqrt{\frac{\mu}{\rho}} \quad 2.14$$

As most fluids have finite viscosity, they can theoretically support transverse waves. However, in practice this occurs only to a limited extent and they are generally considered not to have definable v_s .

Other important elastic properties for a material can also be derived from the Lamé coefficients. Young's Modulus, E , is defined as the ratio of axial stress, T_1 , to axial strain, S_1 , in a rod, hence:

$$E = \frac{T_1}{S_1} = \frac{\mu(3\lambda + 2\mu)}{\lambda + \mu} \quad 2.15$$

Similarly, an expression for Poisson's ratio, σ , the ratio of lateral strain, S_2 (or S_3) to S_1 , can be derived from:

$$\sigma = -\frac{S_3}{S_1} = -\frac{S_2}{S_1} = \frac{\lambda}{2(\lambda + \mu)} \quad 2.16$$

Finally, the transverse modulus, G , can also be defined. It is equivalent to the modulus of rigidity i.e.:

$$G = \mu \quad 2.17$$

These elastic properties are inter-related, and as such the elasticity of an isotropic material may be described fully with any two of these properties, as seen from

Equation 2.9. These definitions assume that constant environmental conditions prevail. Sound wave propagation in certain materials is very sensitive to changes in conditions, for example compression or changes in temperature, because of the close relationship between acoustic velocity and elastic moduli.

A number of the elastic properties described above can be derived from measurements of longitudinal acoustic velocity, transverse acoustic velocity and density of a material. Expressions for a selection of these are shown in Table 2.2.

TABLE 2. 2: EQUATIONS FOR CALCULATION OF ELASTIC PROPERTIES OF PASSIVE MATERIALS

Parameter	Equation	Equation Number
c_{11}, c_{22}, c_{33}	ρv_l^2	2. 18
σ	$\frac{0.5v_l^2 - v_t^2}{v_l^2 - v_t^2}$	2. 19
E	$\frac{\rho v_l^2 (3v_l^2 - 4v_t^2)}{v_l^2 - v_t^2}$	2. 20
K	$\rho \left(v_l^2 - \frac{4}{3} v_t^2 \right)$	2. 21
$G, \mu, c_{44}, c_{55}, c_{66}$	ρv_t^2	2. 22

Biological tissue, unlike the materials described above, is not isotropic. In fact, it is an anisotropic, heterogeneous medium (King, 1974) and hence propagation of a sound wave through tissue is an extremely complex process. As tissue is composed largely of fluid (water), transverse waves are not well supported and are highly attenuated.

2.4. Wave propagation at boundaries

The propagation of waves in a medium is dependent on both the properties of the medium and the type of wave. However, not only do different types of wave propagate differently, their behaviour changes when the angle of incidence upon the discontinuity changes: a wave with normal incidence behaves very differently to one not normal to that boundary. This is now discussed. First, however, the concepts of *Snell's law*, the *critical angle* and *mode conversion* are introduced.

2.4.1. Snell's Law

When a wave is incident at an oblique angle, θ_i , upon a boundary between two materials of differing acoustic velocity, part of the wave is reflected, at an angle θ_r , where $\theta_r = \theta_i$. A further portion of the wave is transmitted, and *refraction* occurs, as shown in Figure 2.5. This is essentially a redirection of the wave, and is also seen with electromagnetic waves.

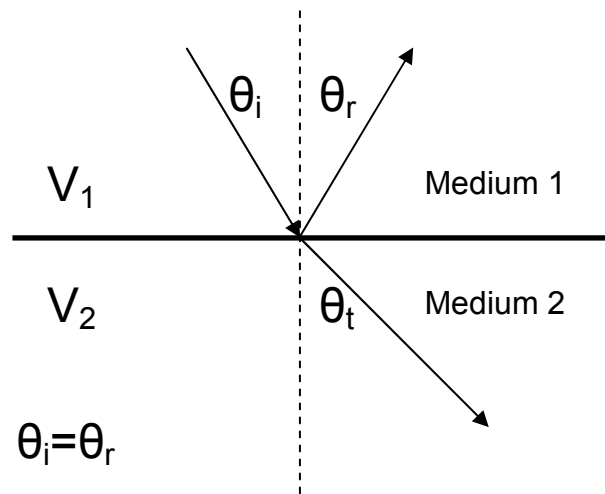


Figure 2. 5: Depiction of a wave incident on a boundary at an oblique angle, showing reflection and refraction.

Snell's Law describes the relationships between the velocities of two materials either side of a boundary, and the angle of refraction of the wave. Assume a wave with incident angle θ_i from the normal transmits from medium 1, which has propagation

velocity v_1 , to medium 2 with velocity v_2 . The angle with which the wave propagates in medium 2, θ_t , is governed by:

$$\frac{\sin \theta_i}{v_1} = \frac{\sin \theta_t}{v_2} \quad 2.23$$

2.4.2. The critical angle

Another concept relevant here is that of the critical angle, θ_c : the angle at which transmission is no longer possible, and a wave is completely reflected. Again, this is dependent on the ratio of the velocities of the two media in a boundary, defined by the relationship:

$$\theta_c = \sin^{-1}\left(\frac{v_1}{v_2}\right) \quad 2.24$$

When the incident angle of a wave reaches the critical angle, no transmission occurs. Instead, the wave energy is converted into a surface wave. This propagates along the boundary, with an energy entering the transmitted medium decaying to negligible value within 0.2λ (Cheeke, 2002). In the case where $v_1 > v_2$, no critical angle exists as $v_1/v_2 > 1$, and hence the concept of the critical angle applies only to transmission from a lower speed medium to a higher speed medium.

2.4.3. Mode conversion

When an incident wave encounters a boundary at an oblique angle less than the critical angle, refraction may be accompanied by *mode conversion*. The wave causes particles in the incident medium to compress and rarefact not only in the longitudinal direction, with propagation velocity v_l but also transversely, and hence transverse waves of velocity v_t are excited. As the angle of incidence increases, the energy converted into transverse waves increases while the proportion remaining as longitudinal waves lessens.

As described earlier, the propagation velocities of longitudinal and transverse waves in a material are constant (assuming constant environmental conditions) and dependent on the elastic properties of that material. Transverse waves are slower than longitudinal waves, so refract less and hence follow a different path. Similarly, the critical angle for transmission of longitudinal waves, θ_{v_l} , is smaller than that for transverse waves, θ_{v_t} .

Four cases are considered below: (i) a wave propagating normal to the boundary, $\theta_i = 0$ (ii) a wave with incident angle, θ_i , between zero and θ_{v_l} , (iii) a wave with incident angle between θ_{v_l} and θ_{v_t} , (iv) a wave with incident angle greater than θ_{v_t} . Only liquid-solid and solid-liquid transmission are relevant to the work described in this thesis.

i. Waves propagating normal to boundary

A wave approaching a boundary where the boundary is perpendicular to the direction of propagation is relatively simple to characterise. The wave energy is partially transmitted, and the remainder reflected. The reflected and transmitted proportions depend on the relative acoustic impedances of the media either side of the boundary. This is shown in Figure 2.6.

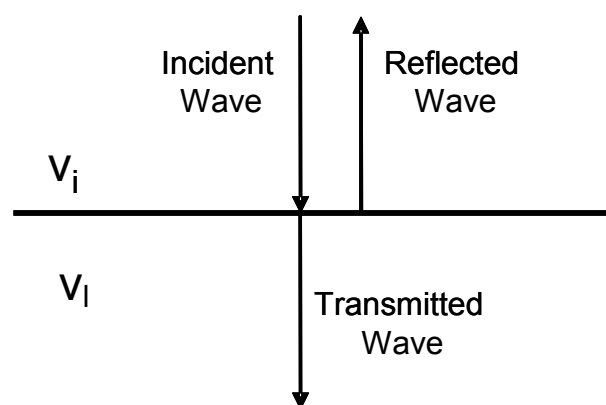


Figure 2. 6: Wave at normal incidence to boundary.

ii. Wave with incident angle $0 < \theta_i < \theta_c$

Firstly, consider a wave (which can only be longitudinal) incident at an oblique angle on a liquid-solid boundary. As before, part of the wave is reflected, while part is transmitted. The reflected part will propagate back into the liquid at an angle equal to the angle of incidence, as shown in Figure 2.7. The transmitted wave will undergo mode conversion, and both longitudinal and transverse waves will be transmitted, with angles θ_l and θ_t .

Consider now a wave with the same incident angle on a solid-liquid boundary. The incident wave may be longitudinal or transverse and the converse result occurs. Only longitudinal waves will be transmitted, as transverse waves are effectively not supported in liquid. Moreover, unlike the liquid-solid boundary, the reflected wave will be converted into both longitudinal and transverse waves (assuming that the angle of incidence is smaller than the critical angle for both longitudinal and transverse transmission). This occurs regardless of whether the incident wave is longitudinal or transverse. This is illustrated in Figure 2.7, for both the liquid-solid, and solid-liquid boundaries.

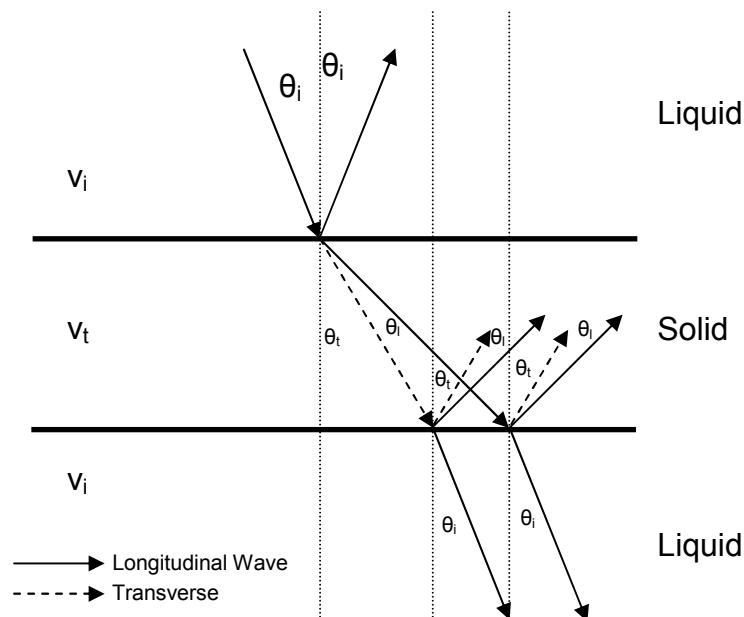


Figure 2. 7: Wave incident on liquid-solid boundary and solid-liquid boundary where $0 < \theta_i < \theta_c$.

iii. Wave with incident angle $\theta_i < \theta_i < \theta_s$

As in cases (i) and (ii), the incident wave will be both transmitted and reflected. As before, longitudinal waves will be reflected. However, in this case, only transverse waves will be transmitted, as the incident angle is greater than the critical angle for longitudinal waves. This is shown in Figure 2.8. A portion of the wave will also be converted to a surface wave.

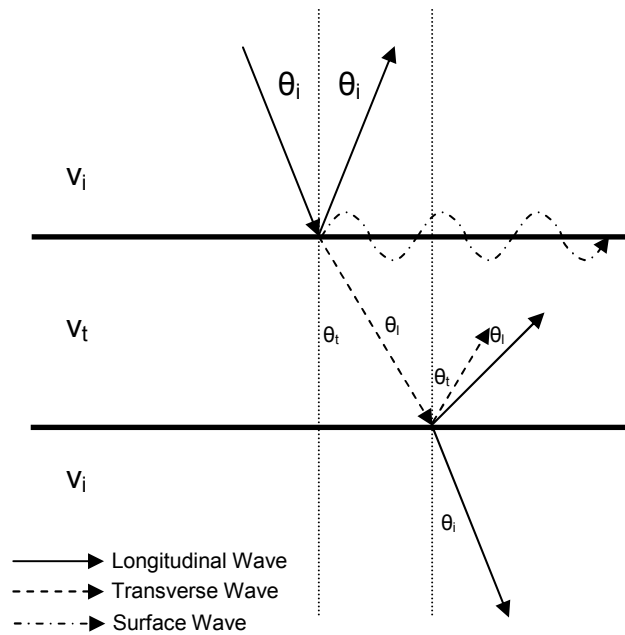


Figure 2. 8: Wave incident on liquid-solid boundary and solid-liquid boundary, where $\theta_i < \theta_i < \theta_s$,

iv. Wave with incident angle $\theta_i < \theta_i$

In this final case, as the incident angle is greater than both θ_i and θ_t , no transmission occurs. All of the energy of the wave is either reflected or converted to surface waves.

2.5. Basic ultrasound imaging

2.5.1. Pulse-echo operation

Ultrasound imaging is based on the principle of *echo ranging* (Hedrick et al., 1995b). An ultrasound beam is emitted from an ultrasound transducer into an object of

interest. The sound energy propagates through the object until a discontinuity in the acoustic impedance of the material is encountered, for example at an interface between two different materials. At this point, portions of the energy are reflected, diffracted or scattered. The transducer detects reflected energy and converts this into an electrical signal. The time of reception of the returned pulse can be used to calculate the distance, x , travelled by the pulse, using the equation:

$$x = \frac{vt}{2} \quad 2.25$$

where t is the time between emission and reception of a pulse. Hence spatial information can be determined.

2.5.2. A-scan

An amplitude scan, or *A-scan*, is a point measurement where an ultrasound wave is emitted by an ultrasound transducer. A reflection will occur at any point where there is an acoustic impedance mismatch, and these reflections can be recorded by the transducer over a short time interval, to give a trace, such as the one in Figure 2.9 where information on the times and amplitudes of reflections can be seen.

The amplitude of each reflection, or echo, is determined by a combination of the reflection coefficient of the media in question and the attenuation of the wave between transmission and reception. Spatial information can be determined from time information in an A-scan, using Equation 2.25. A-scans are commonly used in NDT for applications such as thickness measurements, and in medical applications for ophthalmology (King, 1974) and bladder volume measurement.

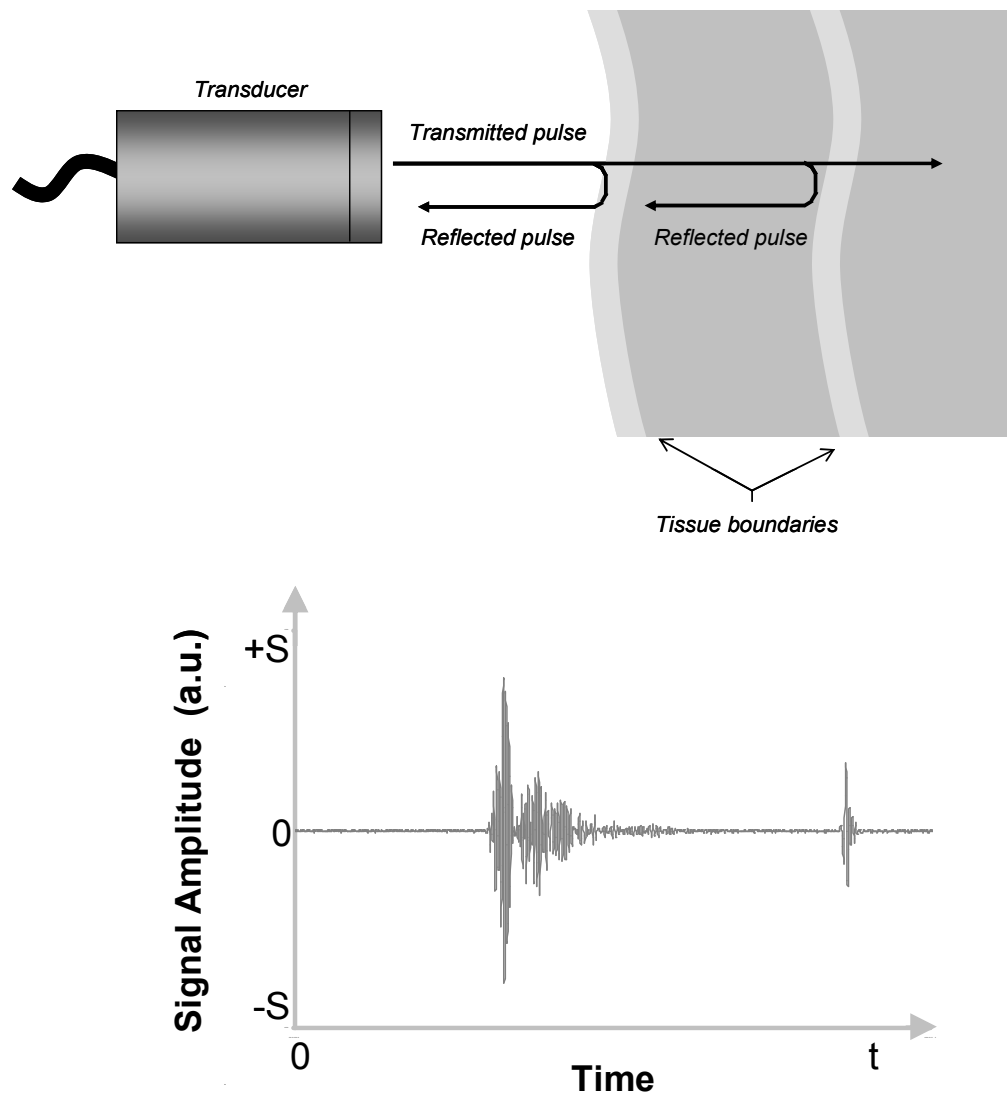


Figure 2. 9: Principle of pulse-echo operation used to generate an A-scan, shown alongside typical received echo signals

2.5.3. B-scan

A brightness scan, shortened to *B-scan*, is a series of A-scans, taken at several adjacent points and presented together with signal amplitude represented by brightness. Thus, a 2-D representation of spatial information is generated. This is the approach used most commonly in medical diagnostic ultrasound. A modern scanning system has sufficient computing speed to generate B-scans at a rate that allows real-time imaging to take place.

2.6. Background to piezoelectric materials

Generation of ultrasound relies on the ability of some materials to convert electrical energy into a mechanical vibration, which is emitted in the form of a sound wave, and a complementary conversion of a received mechanical vibration into electrical energy. A certain group of materials, known as *piezoelectric* materials, have this capability and as such are central to the development of most ultrasound transducers. Piezoelectric materials, and the principle of *piezoelectricity*, are discussed in this section.

2.6.1. Principles of piezoelectricity

Due to the polar crystalline nature of piezoelectric materials, application of an electrical current to a piezoelectric material results in a mechanical deformation (van Randerat and Settington, 1974). Depending on the polarity of the applied current, this deformation will take the form of the material becoming shorter (and fatter), or longer (and thinner) the extent to which will depend partly on the value of Poisson's ratio for the material, as illustrated in Figure 2.10. By applying an alternating current to the piezoelectric material, the material will rapidly contract and expand and hence a mechanical wave is generated. The nature of samples of piezoelectric materials is such that they will preferentially contract and expand at a specific frequency, the *resonant frequency*. When the material is mechanically deformed, for instance when excited by a mechanical wave, an electrical signal will be generated with the same frequency as the mechanical vibrations of the piezoelectric material. An oscilloscope or other device may be used to record this signal.

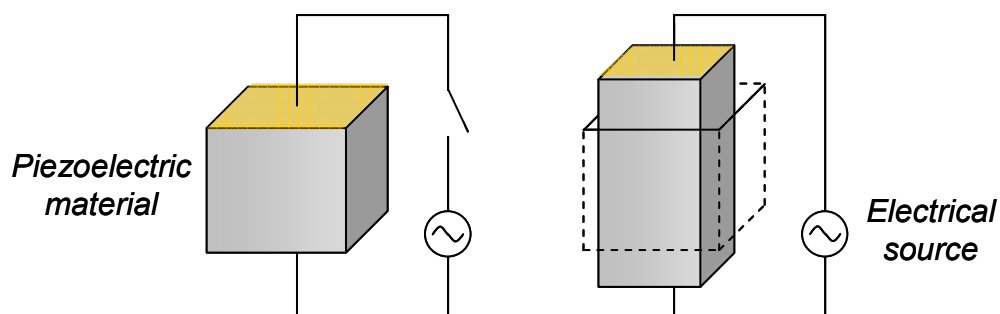


Figure 2. 10: Illustration showing the indirect piezoelectric effect, mechanical deformation occurring in response to an applied electric field

When a piezoelectric crystalline structure is put under stress, not only is a strain produced but also a potential difference between the opposing faces of the crystal. This is due to the lack of a centre of symmetry. The crystal is made up of a series of *dipoles*, positive and negative charges spaced a certain distance apart. When the crystal is deformed, the alignment of charges within the crystal is disturbed. This leads to an imbalance of positive and negative charges, and hence generation of a dipole moment and a corresponding polarisation, on which the potential difference is based. The polarity of this potential difference depends on whether the material has been compressed or expanded. This is governed by:

$$E = -gT \quad 2.26$$

where T is the mechanical stress applied, E is the electric field generated and g is the piezoelectric voltage constant (van Randeraat and Settrington, 1974).

Gabrielle Lippmann deduced the *converse* or *indirect* piezoelectric effect – application of electric field inducing mechanical deformation - mathematically in 1881 and the Curies verified this experimentally soon after. Application of an electric field across the crystal causes a torque to be induced in the dipole moments, the direction of which is dependent on the polarity of the electric field applied. This torque causes the material to expand or contract laterally and hence induces a complementary contraction and expansion in the longitudinal direction, i.e. the direction of polarity of the crystal (van Randeraat and Settrington, 1974). This is governed by the expression:

$$S = dE \quad 2.27$$

where S is the *strain* ($S = \Delta l/l$ where l is length) generated and d is the *piezoelectric modulus* of the material .

If an alternating charge is applied the crystal will, to a first approximation, alternately expand and contract, with the same frequency as the applied voltage (King, 1974).

2.6.2. Piezoelectric constitutive equations

As piezoelectric materials are electromechanical systems, they are governed by both electrical and mechanical conditions. A material subject to zero stress, but a finite electric field, E , can be described by the expression:

$$D = \epsilon E \quad 2.28$$

where D is the resultant *electric displacement* and ϵ is the permittivity of the material. In the mechanical case, where the material is subject to zero electric field but has a stress, T , applied:

$$S = sT \quad 2.29$$

where S is the resultant strain and s is the *compliance* of the material.

Combining Equations 2.26 and 2.28, and Equations 2.27 and 2.29, gives the interactions between the electrical and mechanical cases, known as the *Piezoelectric Constitutive Equations*:

$$S = s^E T + dE \quad 2.30$$

$$D = dT + \epsilon^T E \quad 2.31$$

The superscripts in Equations 2.30 and 2.31 denote the parameter being kept constant, in this case field strength, E , and stress T respectively.

Changing the independent variable allows derivation of the following formulae to incorporate a selection of commonly quoted piezoelectric properties:

$$E = -gT + \frac{D}{\epsilon^T} \quad 2.32$$

$$S = s^D T + g D \quad 2.33$$

$$E = -h S + \frac{D}{\epsilon^S} \quad 2.34$$

$$T = c^D S - h D \quad 2.35$$

$$D = e S + \epsilon^S E \quad 2.36$$

$$T = c^E S - e E \quad 2.37$$

The constants in these equations are important performance indicators of a piezoelectric material, and significant for the work in this thesis. Hence, they are summarised in Table 2.3.

TABLE 2.3: PIEZOELECTRIC PARAMETERS

Parameter	Name	Units
c	Elastic stiffness	Nm ⁻²
d	Piezoelectric charge constant	mV ⁻¹
e	Piezoelectric stress constant	Cm ⁻¹
g	Piezoelectric voltage constant	VmN ⁻¹
ε	Permittivity	Fm ⁻¹
h	Piezoelectric stiffness constant	Vm ⁻¹
s	Elastic compliance	m ² N ⁻¹

2.6.3. Directional dependence

When expressing a value for any of the piezoelectric parameters in Table 2.3, one must take into account directional dependence: the directions of the applied (or generated) electric field, displacement, stress or strain. To deal with this, the three-dimensional axes are defined 1, 2, 3 for x , y and z respectively. Transverse forces about the x , y and z axes are denoted by 4, 5, and 6 respectively. Take, for example, d , which relates electric field strength and strain developed. For strain measured in the x , or 1, direction in response to an electric field in the z , or 3, direction, the

notation will be d_{13} . Similarly, an electric field measured in the y , or 2, direction will be related to the stress applied in the z , or 3, direction, by g_{23} . It is important to note that due to symmetry $s_{12} = s_{21}$, $g_{23} = g_{32}$ and so on (van Randerat and Setterington, 1974).

2.6.4. Electromechanical coupling coefficient

A further useful parameter of a piezoelectric material is the electromechanical coupling coefficient, k , which describes the proportion of energy converted between mechanical and electrical forms in the material. The coupling coefficient is defined by:

$$k^2 = \left[\frac{\text{stored energy converted}}{\text{stored input energy}} \right] = \frac{d^2}{s^E \epsilon^T} \quad 2.38$$

The two most commonly expressed forms of k are k_{33} , the coupling coefficient of a thin rod, and k_T , the coupling coefficient of a large, thin plate. k_T is defined, from Equation 2.38, as:

$$k_T = \sqrt{\frac{e_{33}^2}{c_{33}^D \epsilon_{33}^S}} \quad 2.39$$

2.6.5. Material thickness and resonant frequency

The antiresonant frequency, f_a , also known as the mechanical resonant frequency, of a piezoelectric material is proportional to the longitudinal velocity of sound in the material, v_l , in the poled direction and inversely proportional to the thickness, T , of the material, according to the following equation:

$$f_a = \frac{v}{2T}$$

2. 40

It can be seen that $T = \lambda/2$. As such, piezoelectric elements are often referred to as half-wavelength resonators.

2.7. Piezoelectric materials commonly used for HFUS

Medical ultrasound applications today utilise a variety of materials: polymers such as PVDF (Foster et al., 2000), crystalline Lithium Niobate (LNO) (Cannata et al., 1999), piezoceramic materials such as PZT (Lockwood et al., 1994) and composites made from PZT (Smith, 1989) or PMN-PT (Jiang et al., 2008). The advantages and disadvantages of using each material for high frequency applications can be demonstrated by undertaking one dimensional electrical impedance spectroscopy simulations of basic transducers made using these materials. To aid discussion of materials properties, which is a central theme of this thesis, results of this are presented now. The modelling procedure used is discussed in detail in Section 4.7.

Single element transducer simulations were conducted with a 1.6 mm diameter circular element, with air loading on both faces (i.e. no other layers). Although not a primary focus of this thesis, it is worth considering arrays in this context, as it is almost certain these will replace single element HFUS transducers in the near future. As such, array-sized elements, of 30 μm x 2 mm were also simulated. This size was chosen because array elements should have width of no more than one wavelength (Foster, 2008) and 2 mm is a viable length. The properties used to simulate the piezoelectric materials here are summarised in Table 2.4.

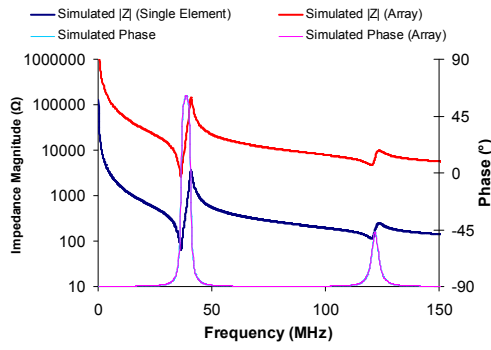


Figure 2. 11: Simulated impedance magnitude and phase for Lithium Niobate single element and array element at 40 MHz.

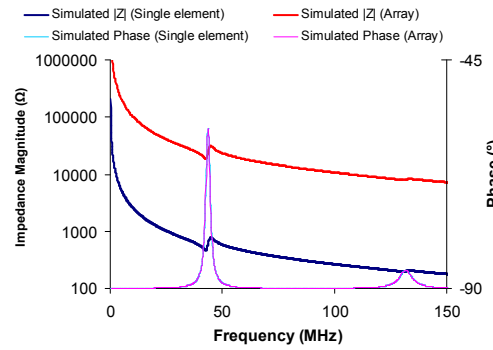


Figure 2. 12: Simulated impedance magnitude and phase for PVDF single element and array element at 40 MHz.

Consider firstly electrical impedance matching to standard 50 Ω drive electronics. Simulations of LNO, shown in Figure 2.11 show why it is a popular material for single element high frequency transducers, having relatively low high frequency (clamped) permittivity at constant strain, ϵ_R^S , which leads to an electrical impedance magnitude of close to 50 Ω for elements of this size. In this case, the electrical impedance magnitude is around 65 Ω at electrical resonance. Simulations of high permittivity monolithic PZT and PZT composite, given in Figures 2.13 and 2.14 respectively show that they have electrical impedance of 1 – 3 Ω , as is the case with PMN-PT and PMN-PT composite, shown in Figures 2.15 and 2.16 respectively. PVDF (shown in Figure 2.12) however, has very low permittivity and electrical impedance of over 500 Ω . It is worth noting that although composite materials are of significantly lower permittivity than monolithic materials, their electrical impedance is often similar because element thickness is less for a composite than monolithic material at a given frequency.

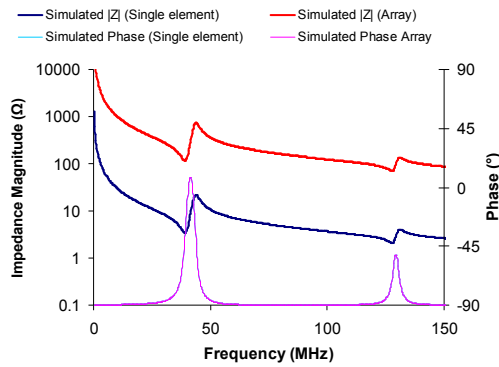


Figure 2. 13: Simulated impedance magnitude and phase for PZT-5H (CTS3203HD) single element and array element at 40 MHz

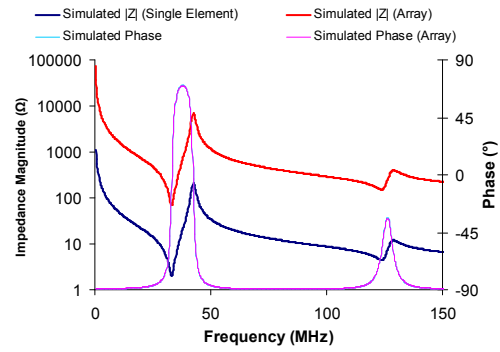


Figure 2. 14: Simulated electrical impedance magnitude and phase for 30% VF CTS3203HD/RX771 Composite single element and array element at 40 MHz

For a single transducer of this particular design, LNO is relatively easy to match electrically to standard 50 Ω equipment but when elements of the size required for a high frequency array are considered, LNO has very high electrical impedance. PVDF is also subject to prohibitively high electrical impedance, effectively limiting its practical use to large aperture devices. Work is being undertaken to fabricate PVDF arrays for medical imaging (Carey et al., 2004) but high drive voltages are required. It could be argued that this is offset by the well matched acoustic impedance of PVDF to tissue. Monolithic PZT and PZT composite are more suitable for small aperture devices, having electrical impedance of only around 100 Ω for the array elements simulated here, making matching to electronic circuitry more easily achievable

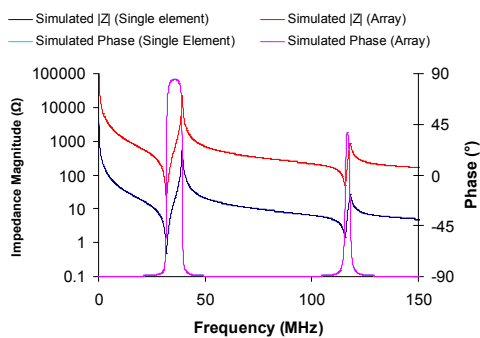


Figure 2. 15: Simulated impedance magnitude and phase for PMN-PT (Ibule) single element and array element at 40 MHz.

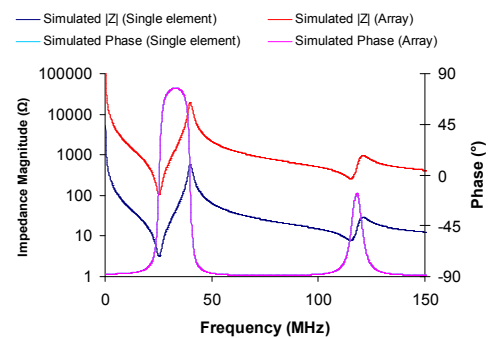


Figure 2. 16: Simulated electrical impedance magnitude and phase for 30% VF PMN-PT/RX771 Composite single element and array element at 40 MHz.

TABLE 2. 4: SUMMARY TABLE OF PIEZOELECTRIC PROPERTIES OF MATERIALS SIMULATED IN FIGURES 2.11 – 2.16.

Parameter	LNO (Cannata, 2007)	PVDF (Foster et al., 2000)	PZT-5H (CTS 3203HD) (Sherrit et al., 1997)	CTS 3203HD/ RX771 30% VF Composite	PMN-PT (Ibule) (Wallace, 2008)	PMN-PT/ RX771 30% VF Composite
Element Thickness (μm)	90	25	55	45	60	45
ρ (kg m^{-3})	462	1780	7800	3138	7843	3151
v (ms^{-1})	7360	2200	4767	3827	4713	3597
Z (MRayl)	33.9	3.92	37.18	12.0	36.96	11.33
c_{33}^D ($\times 10^9 \text{ Nm}^{-2}$)	250	8.61	177	46.0	174	40.7
c_{33}^E ($\times 10^9 \text{ Nm}^{-2}$)	191	8.30	144	25.9	107	14.5
ϵ_R^S	39.0	8.40	1300	428.5	741	227
e_{33} (Cm^{-1})	4.5	0.15	19.7	8.72	21	7.26
h_{33} ($\times 10^9 \text{ Vm}^{-1}$)	13.0	2.04	1.71	2.30	3.20	3.62
d_{33} ($\times 10^{-12} \text{ mV}^{-1}$)	18.0	17.6	111	190	120	178
k_T	0.49	0.19	0.44	0.66	0.62	0.80
α (dB cm^{-1} @ 1 MHz)	0.5	6.5	0.1	2.7	0.5	3.0

A second significant advantage of LNO is the thickness velocity of sound within the material. At 7360 ms^{-1} , it is significantly faster than the alternative materials, which range from 2200 ms^{-1} for PVDF to around 4800 ms^{-1} for monolithic PZT. For a material of thickness mode velocity, v , and thickness, T , the mechanical resonant frequency is given by the relationship $f_a = \frac{v}{2T}$. Materials with lower velocity require thinner active layers to achieve a given operational frequency, potentially making fabrication more difficult and expensive. As PVDF is produced as a film of the desired thickness, this is a less significant consideration. However, PVDF is generally only available at certain thicknesses, and hence frequencies and it is difficult to make thin enough to operate at very high frequencies.

An accompanying disadvantage of high thickness velocity in the context of medical transducers is high acoustic impedance. LNO is less suitable in this respect having acoustic impedance $Z > 30 \text{ MRayl}$. This is also the case with PZT and PMN-PT. PVDF provides a major advantage, having $Z \approx 4 \text{ MRayl}$ and thus inherently good matching to tissue. Piezocomposites, while not as well matched as PVDF, are still relatively well matched with $Z \approx 12 \text{ MRayl}$.

Finally, key aspects of piezoelectric performance should be considered. These are outlined in Table 2.4. Thickness mode electromechanical coupling, k_T , is a particularly significant property of a material because it indicates how efficiently a material converts mechanical energy to electrical energy and vice versa. It can be seen that PVDF has particularly poor $k_T \approx 0.2$. Other monolithic materials are more efficient, LNO having $k_T \approx 0.5$ and the examples of PZT (CTS3203HD) having $k_T \approx 0.44$. However, it is demonstrated that composite materials are of significantly higher k_T , at 0.66. The value of k_T for a piezocomposite is dependent on the volume fraction of ceramic, as shown in Figure 2.17 for a PZT/RX771 piezocomposite. Piezocomposites have higher values of k_T because the value of k_{33} , the coupling coefficient of a thin rod or bar, is higher than k_T , the coupling coefficient of a large plate. Combining a piezoelectric material with a polymer matrix allows this to be exploited in a composite material.

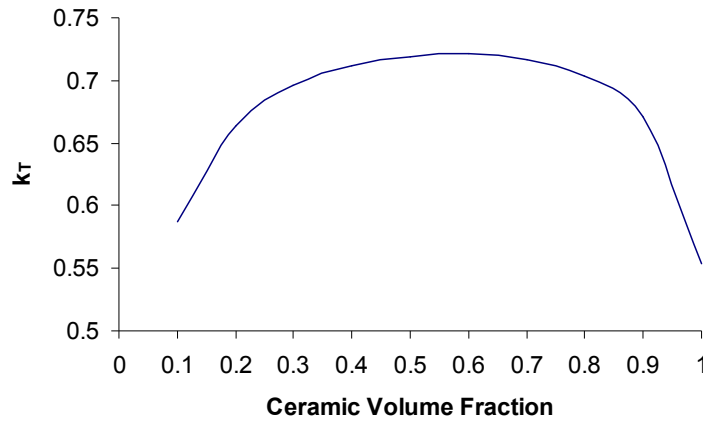


Figure 2. 17: Simulation of k_T with volume fraction for a PZT-5H / RX771 composite.

The leading material, in terms of k_T , of those investigated here, is PMN-PT-composite. Modern single crystal materials are known for their exceptionally efficient energy conversion: it can be seen from Table 2.4 that while monolithic PMN-PT has similar $k_T \approx 0.62$ to rather poor PZT-composite, PMN-PT composites have very high $k_T \approx 0.80$. The reason for this is that PMN-PT has very high $k_{33} \approx 0.90$, and as such converts energy very efficiently in pillar form i.e. as a 1-3 connectivity piezocomposite with tall narrow pillars. The brittle nature of PMN-PT makes fabrication of pillar structures small enough for HFUS composites difficult using mechanical dicing. This has limited the upper frequency to which these can be fabricated. However, recent work has shown that reactive ion etching may be used instead to produce piezocomposites from PMN-PT (Jiang et al., 2008) at higher frequencies than previously possible.

It can be seen from the discussion above that piezocomposite materials offer many advantages and as such they have become the material of choice for medical ultrasound applications at low (<20 MHz) frequencies. The work of this thesis concerns characterisation and testing of PZT composite materials for use in high frequency ultrasound. As such further explanation of the design and fabrication procedures used for standard piezocomposites are given in the next section.

2.8. Piezoelectric composite materials

Composites designs are generally characterised by the connectivity of the ceramic and polymer parts and given the name M-N composite, where M and N are the geometrical connectivity of the ceramic and polymer respectively. M and N can be between zero and three depending on the design. The most common design, due mainly to ease of fabrication, is the 1-3 composite, which consists of high aspect ratio ceramic pillars (i.e. pillar height is much greater than width) surrounded by a polymer matrix: thus the high k_{33} is utilised. The volume fraction of these composites can be controlled to allow the piezoelectric properties to be optimised to match the requirements of the ultrasound system.

For medical ultrasound applications, composites have a number of significant advantages. They exhibit high coupling coefficient, show reduced unwanted resonance modes, have low acoustic impedance and their flexibility allows them to be mechanically formed. Composites have lower permittivity than monolithic ceramic materials (although higher than e.g. LNO and PVDF) which is a disadvantage for array manufacture but could be considered an advantage for single element transducer manufacture. The main disadvantage of composites is that they are relatively costly to produce, essentially requiring production of a monolithic material that is used to manufacture the composite material, as discussed in the next paragraphs, followed by extra steps to produce the final composite.

The desired properties of a piezoelectric material are dependent on the application for which it is required, but the overall performance of composite could be argued to be better than other available materials – essentially providing the best compromise. It is for this reason that monolithic piezoelectric materials have been replaced by composites where this has become possible, just as single element transducers have historically been replaced by arrays.

2.8.1. Fabrication of 1-3 piezocomposites

1-3 connectivity piezocomposites are fabricated by a variety of means, the most common being known as dice-and-fill. The dice-and-fill method was initially developed by Savakus et al. (1981). This procedure involves a number of steps, which are illustrated in Figure 2.18. Firstly, a piece of monolithic active material is selected (a). A series of parallel channels is cut into this (b) using a precision dicing saw. The material is then rotated through 90° and a further set of parallel channels is cut to create a structure of square pillars (c). The height of the pillars will depend on the depth of cut. The gap between each pillar and its neighbouring pillars, the *kerf*, is dependent on the width of the saw blade. The width of the pillars themselves is determined by the centre-to-centre distance between each cut, the *pitch* of the composite, minus the kerf.

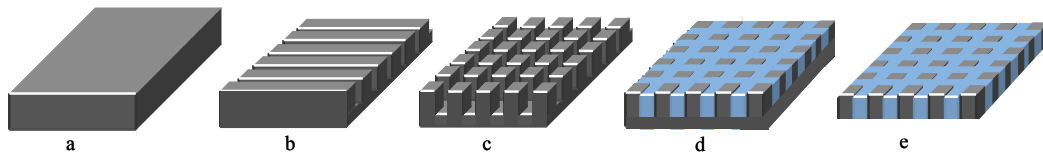


Figure 2. 18: Stages in the fabrication of a 1-3 piezocomposite. Details are given in the text.

After the pillar matrix has been diced from the monolithic material, a structure known as a bristle block remains. This is then filled, under vacuum, with a polymer (d). The polymer is given time to cure before the resultant composite material is thinned to the desired thickness and cut to the required shape (e). By electroding the major surfaces of the composite, working piezoelectric material results. Before use, the composite must be poled, unless a pre-poled ceramic is used.

Poling is a procedure where the dipole moments within the ceramic structure are aligned along one axis of a piezoelectric material. This does not occur naturally in most materials, although it does in some single crystal materials, such as quartz. Poling involves heating the material to a particular temperature, before applying a high DC field to metallised electrodes on the relevant surfaces of the material. The temperature to which the piezoelectric material must be heated relates to a property of the material itself, known as the *Curie temperature*. When the material is heated to

close to the Curie temperature, it assumes a centre of symmetry and hence can no longer have an electric dipole moment (Randeraat, 1974). The presence of an external electric field then aligns the dipoles within the material to the direction of that field as far as possible, consistent with the structure of the material. If the temperature is reduced back to room temperature with the field still applied, the dipoles stay aligned.

In addition to square pillars, the dicing procedure can produce hexagons made by cutting three channels at 60° rotation with respect to one another, or triangles also made by cutting three sets of channels at different angles to one another with the shape of the triangle dependent on the angles used (Brown, 2007). Research has been undertaken into various pillars shapes, although it has been shown that square pillars are satisfactory for most purposes (Hossack and Hayward, 1990).

2.8.2. Composite volume fraction

A key parameter of a piezocomposite is the ceramic volume fraction. This is defined as the percentage of the total composite volume made up of ceramic. In 1-3 composites with square pillars, the volume fraction is dependent on the ratio between the pillar width, w , and the kerf, k , as shown in Figure 2.19.

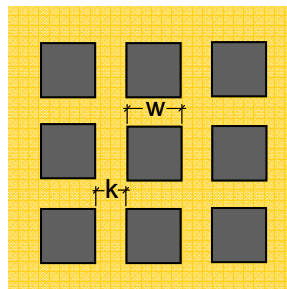


Figure 2. 19: Diagram of surface of 1-3 composite illustrating pillar width and inter-pillar kerf.

The composite is made up of repeating units cells of area $(w+k)^2$. Each contains a square of ceramic of area w^2 . From this, the ceramic volume fraction, VF , of a 1-3 composite with pillar width w and kerf k is given by:

$$VF = \left[\frac{w^2}{(w+k)^2} \right] \quad 2.41$$

2.8.3. Composite design requirements

To take full advantage of their performance benefits, 1-3 composite materials require to be fabricated according to certain design criteria. Work by Hossack and Hayward (1991) has suggested that the aspect ratio of pillar height over pillar width is desired to be at least four and that the volume fraction of the composite should be in the range 0.3-0.7 for optimal performance. In practice, it is considered that composites will work well for aspect ratios of three or more. Reduction in aspect ratio leads to degradation of performance, in particular a reduction in k_T (Hayward and Bennett, 1996).

Composite materials are now ubiquitous in low frequency applications, but their use at high frequency has been restricted by the limitations of the dice-and-fill technique. Assuming that the volume fraction of the composite and its pillar aspect ratio are required to be within sensible ranges, the smallest pillar size is dictated entirely by the kerf between pillars, which is, itself, dictated by the smallest saw blade available. Rearranging Equation 2.41 above allows calculation of the smallest possible pillar width, w , for a given volume fraction, VF , and kerf, k :

$$w = \frac{k\sqrt{VF}}{1-\sqrt{VF}} \quad 2.42$$

Presently, saw blades are unavailable thinner than 9 μm . Kerf width is at least 1.1 times the blade width, meaning the smallest possible kerf is around 11 μm .

To demonstrate the limitations this imposes on frequency of operation, it is useful to consider an example. Assuming that one wishes to keep volume fraction of at least 0.3, and aspect ratio of 3, Equation 2.42 above shows that the minimum pillar width possible is approximately 14 μm . This ultimately means that to produce a

piezocomposite with pillars of height to width aspect ratio of three, the thinnest possible layer thickness, T , is 40 μm . A composite with $\text{VF} = 30\%$ will have propagation speed, $v \approx 3700 \text{ ms}^{-1}$, and so the fundamental frequency of this composite will be $f \approx 45 \text{ MHz}$. It can be seen that if higher frequencies are desired from piezocomposite devices, either smaller saw blades or an alternative means of producing composite structures is required.

2.9. Electrical impedance spectroscopy

Having briefly considered fabrication of piezoelectric materials, the thesis now turns to the topic of characterisation.

2.9.1. Background

Any current flowing in a circuit is subject to a resistive force, or resistance. In DC circuits, the resistance, R , is determined purely by the amplitudes of the voltage, V , and current, I , in the circuit, following Ohm's Law:

$$R = \frac{V}{I} \quad 2.43$$

However, in an AC circuit the resistive force is also dependent on the phase of the voltage and current, and as such is a complex quantity, called *impedance*. Impedance is defined, according to Ohm's Law, as:

$$Z = |Z|e^{j\theta} = \frac{V}{I} = \frac{|V|e^{j(\omega t + \phi_V)}}{|I|e^{j(\omega t + \phi_I)}} \quad 2.44$$

where the units of Z are Ohm. Alternatively, electrical impedance can be thought of as a combination of a real part, the resistance, R , and an imaginary part, the reactance, X , where:

$$Z = R + jX \quad 2.45$$

The impedance of a sample of piezoelectric material has a magnitude, $|Z|$ and phase, θ :

$$|Z| = \sqrt{R^2 + X^2} \quad 2.46$$

$$\theta = \arctan\left(\frac{X}{R}\right) \quad 2.47$$

While resistance, R , is theoretically constant with varying frequency, the reactance, X , is frequency dependent. Two types of reactance exist: inductive reactance, X_L , and capacitive reactance, X_C . The total reactance, X , is the difference between these:

$$X = X_L - X_C \quad 2.48$$

where X_L and X_C are defined as:

$$X_L = 2\pi fL \quad 2.49$$

$$X_C = \frac{1}{2\pi fC} \quad 2.50$$

Electrical impedance is a key property of a sample of piezoelectric material. It may be measured using an electrical impedance analyser. When plotted against frequency, the impedance of a piezoelectric transducer typically follows a very distinctive pattern, as illustrated in Figure 2.20.

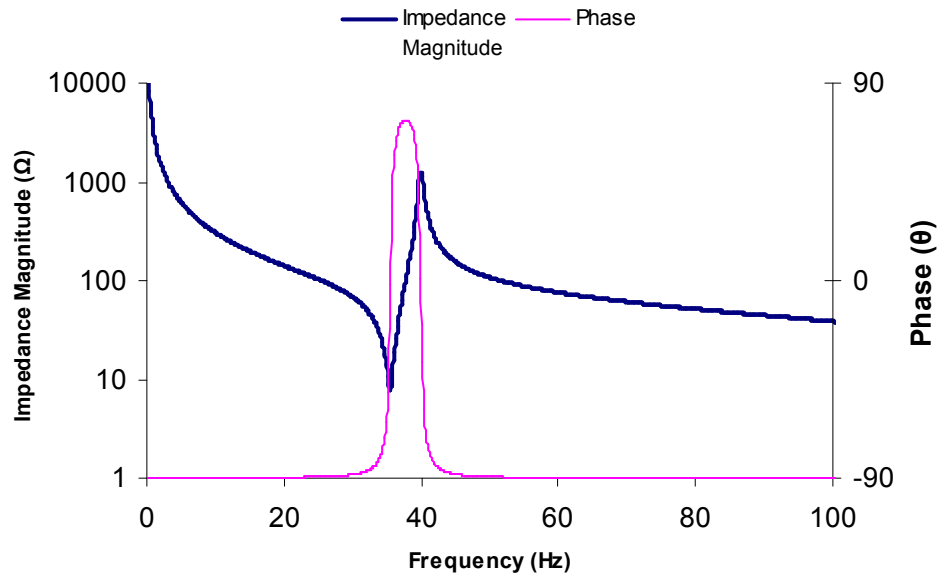


Figure 2. 20: Electrical impedance magnitude and phase versus frequency.

There are certain key points on this curve. Local minima and maxima show, respectively, resonant frequencies, f_r , and antiresonant frequencies, f_a , of the sample of piezoelectric material. These are also known as the electrical and mechanical resonant frequencies, or series and parallel resonant frequencies, respectively.

In a plate, the fundamental resonant, or electrical resonance frequency, is related to the fundamental antiresonant, or mechanical resonance frequency, by the coupling coefficient, k_T , via:

$$k_T = \sqrt{\frac{\frac{\pi f_r}{2 f_a}}{\tan\left(\frac{\pi f_r}{2 f_a}\right)}} \quad 2.51$$

2.9.2. Influence of capacitance on electrical impedance

A piezoelectric material, when not at resonance, acts much like a capacitor. The capacitance, C , of any dielectric material is given by:

$$C = \frac{\epsilon_0 \epsilon_r A}{T}$$

2. 52

where ϵ_0 is the permittivity of free space, ϵ_r is the relative permittivity of the material, A is the area of the dielectric material and T is the thickness of the material. Piezoelectric materials are more complex, given they are electromechanical systems, i.e. not purely electrical. However, from this equation, one can see the strong influence of the key geometrical parameters of a transducer – namely area and thickness. The material thickness is typically dictated by the operational frequency required. In cases such as single element transducers the area of the transducer can be altered to emit a desired ultrasound field. The area of the transducer element becomes highly significant in high frequency array design. Although a commercial system has now become available with 1.5λ pitch (Foster, 2008), the pitch of adjacent array elements should ideally be approximately less than the wavelength of the emitted ultrasound wave to avoid imaging artefacts. Hence, at high frequency, array element sizes must be very small and electrical impedance may be very high. This makes them difficult to use with standard instrumentation which generally has internal resistance of 50Ω . The permittivity of the piezoelectric material used becomes particularly important in this case because a piezoelectric material of higher permittivity will reduce the electrical impedance of the transducer. When designing a composite one can increase the ceramic volume fraction to increase permittivity, although this will come at a cost of increased acoustic impedance.

2.9.3. Determination of piezoelectric properties from impedance

With the exception of the piezoelectric charge and voltage constants, d and g , many of the significant piezoelectric properties discussed in Section 2.6 may be easily calculated from a few straightforward measurements, provided only the thickness mode is being considered.

Firstly, thickness, T , area, A , and density, ρ , of the piezoelectric sample must be measured. Secondly, resonant frequency, f_r , and antiresonance frequency, f_a , capacitances at low frequency (~ 1 kHz), C_L , and high frequency ($\sim 2f_a$), C_H , are

measured. These can all be found from the impedance curve of the material. d is measured using specialised equipment, and g can be calculated from d using $g = d / \epsilon^T$ where ϵ^T is the low frequency (unclamped) permittivity at constant stress. Table 2.5 summarises relationships that can then be used to determine various piezoelectric properties. These will be used later in the thesis to determine piezoelectric properties from electrical impedance spectroscopy measurements.

TABLE 2. 5: RELATIONSHIPS BETWEEN PIEZOELECTRIC PROPERTIES AND ELECTRICAL IMPEDANCE

Parameter	Measurements Required	Formula used	Equation reference
Speed	T, f_a	$v = 2f_a T$	2. 53
Acoustic Impedance	T, f_a, ρ	$Z = 2\rho f_a T$	2. 54
k_T	f_a, f_r	$k_T = \sqrt{\frac{\frac{\pi f_r}{2 f_a}}{\tan\left(\frac{\pi f_r}{2 f_a}\right)}}$	2. 55
ϵ^T	A, C_L, T	$\epsilon^T = \frac{C_L T}{A}$	2. 56
ϵ^S	A, C_H, T	$\epsilon^S = \frac{C_H T}{A}$	2. 57
c_{33}^D	T, f_a, ρ	$C_{33}^D = \rho(2f_a T)^2$	2. 58
C_{33}^E	$A, C_H, T, f_a, f_r, \rho$	$C_{33}^E = \rho(2f_a T)^2 \left(1 - \frac{\left(\frac{\pi f_r}{2f_a}\right)^2}{\tan\left(\frac{\pi f_r}{2f_a}\right)} \right) \left(\frac{C_H T}{A} \right)$	2. 59
e_{33}	$A, C_H, T, f_a, f_r, \rho$	$e_{33} = \left(\frac{\pi f_r}{\tan\left(\frac{\pi f_r}{2f_a}\right)} \right) \left(\frac{\rho C_H}{8TA} \right)$	2. 60

2.10. Ultrasound Transducers

Ultrasound imaging is conducted using a piezoelectric transducer or transducer array. Early transducers consisted of a single active element, with fixed focal point that was mechanically scanned to produce a 2D image. As a consequence, images were only focused at a single depth and frame rates were limited by the speed of mechanical scanning. However, multi-element linear arrays were then developed, which allowed electronic scanning and much improved frame rates. Following that, the introduction of phased linear arrays allowed dynamic depth focusing and beam-steering, improving the efficacy of diagnostic ultrasound imaging greatly. These techniques are now used with linear arrays. However, single element transducers are still widely used in medical ultrasound applications, particularly at high frequencies where the first commercial array system has only very recently become available. The work of this thesis focused primarily on single element transducers, the key components of which are discussed in this section.

A standard ultrasound transducer is a multi-component device, as shown in Figure 2.21. The key components are the active element, backing layer and matching layer. In some transducers the matching layer also doubles as a wear plate. Where required, a transducer may also have a lens cast on the front to allow focusing. These layers are discussed individually here.

2.10.1. Active Element

The active layer of an ultrasound transducer is almost always a piezoelectric material. These were discussed in detail in Sections 2.6-2.8.

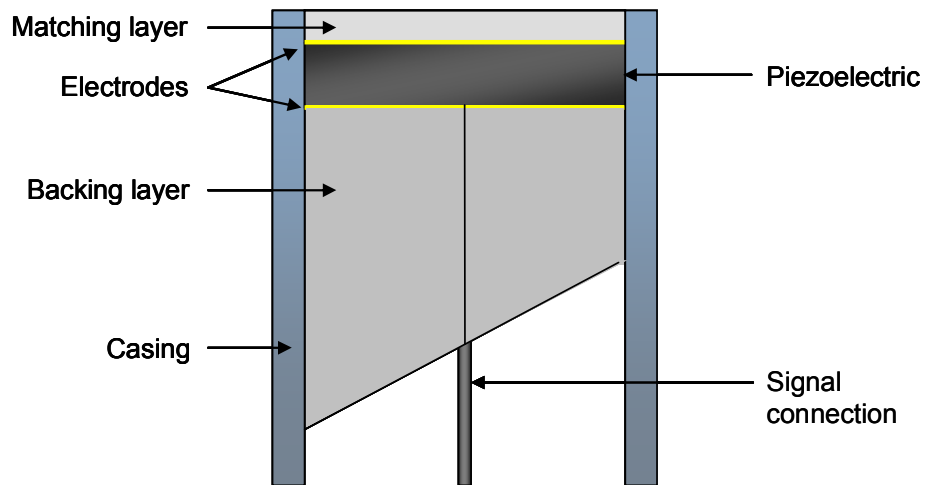


Figure 2. 21: Diagram showing a cross section of a typical single element transducer

2.10.2. Backing layers

Backing layers fill dual roles within a transducer. Firstly, they provide structural support for the active material, which can often be thin and fragile, especially for high frequency devices. Secondly, they help to control the pulse length produced by the transducer. By making the backing material acoustically lossy, energy transferred from the active material into the backing layer is absorbed. This stops reflection from the back of the backing layer reaching the active material and causing spurious signals from the transducer. The backing layer is often shaped, as shown in Figure 2.21, to further decrease internal reflections by ensuring there is not a surface with normal incidence at the back of the transducer.

Efficient damping gives better axial resolution and greater bandwidth. The optimal method of achieving this is to use a backing layer that has a value of acoustic impedance well matched to the active material. However, this results in a large portion of the ultrasonic energy from the transducer passing into the backing material, as opposed to the ultrasound medium. This reduces output signal amplitude, which degrades SNR. Hence, a compromise between signal sensitivity, axial resolution and bandwidth must be reached for optimal performance: this will depend on the application for which the transducer is designed.

In practice, a backing material with lower acoustic impedance than the active material is used, as this causes reflected pressure waves to undergo a 180° phase shift, and hence stay in phase with the primary resonance of the active element (Hill and Bamber, 2004b). Backing materials are often made of an epoxy filled with particles of a high-density material, such as tungsten. Acoustic impedance can be finely controlled by changing the volume fraction of filler (Webster et al., 2007).

2.10.3. Matching Layers

Matching layers also perform two functions within a transducer. Active layers in a transducer can be damaged over time, particularly by contact testing. Hence, the matching layer provides a protective barrier. This function is sometimes performed using an acoustically transparent layer. Matching layers have another function: to promote energy transfer into the ultrasonic medium.

As described earlier, any acoustic impedance mismatch between two media will result in a portion of a signal being reflected, and this is equally true for the interface between an active element in a transducer and the imaging medium. Not only will a significant proportion of the energy generated in the transducer not be transmitted into the imaging medium, but the bandwidth of the transducer will also be reduced because energy is trapped in the transducer for a longer time. A matching layer with acoustic impedance between that of the active material and the imaging medium bridges this gap.

In the case of medical imaging, matching layers are of particular importance. The acoustic impedance of soft tissue is approximately 1.5 MRayl. Most piezoelectric materials have significantly greater acoustic impedance than this. For example, PZT has acoustic impedance of 34 MRayl. A PZT-based composite of 0.3 volume fraction will have $Z \approx 11$ MRayl, which better matches tissue and is one reason why composites are commonly used. However, even then, the transmission coefficient between a PZT composite and tissue will be only around 0.3, meaning that 70% of the energy generated in the transducer does not transmit to the ultrasound medium.

This is undesirable for a number of reasons. The lack of energy entering the imaging object leads to reduced sensitivity, bandwidth can be reduced because of less instantaneous energy transfer; and it is likely that reflected energy will cause heating in the transducer.

A matching layer should be designed to have the value of acoustic impedance, Z_m , which maximises transmission between the active layer, of acoustic impedance Z_t and imaging medium, of acoustic impedance, Z_i . It can be calculated using the expression (McKeighen, 1998):

$$Z_m = \sqrt{Z_t^{\frac{1}{3}} Z_i^{\frac{2}{3}}} \quad 2.61$$

As there will still be some acoustic impedance mismatch between the matching layer and imaging medium, not all of the energy transmitted from active material to matching layer is immediately transmitted to the imaging medium: a portion of energy reverberates *within* the matching layer before transmitting. A situation then arises where waves generated a finite time later by the active material are transmitted to the imaging medium at the same time as waves that have reverberated within the matching layer. For optimal coherent energy transmission, these waves must be in phase with one another. The thickness of a matching layer is therefore important, and depends on the frequency of operation of the transducer. To ensure that waves transmitted to the imaging medium (i.e. those subject to reverberation in the matching layer and those not) are in phase the thickness of a matching layer is always $\lambda/4$. This is valid only at one frequency, which must be chosen accordingly.

A transducer may have one or more matching layers depending on the acoustic impedance mismatch between the active layer and imaging medium, the manufacturing effort and the desired performance. It has been shown that using multiple matching layers of graded acoustic impedances provides improved transmission between the active material and imaging medium (Goll and Auld, 1975). However, using more than one matching layer increases the difficulty in fabrication of a transducer.

2.10.4. Properties of a Transducer

The design of a transducer is optimised according to its intended usage. Transducers may be intended for only transmission, i.e. conversion of an electrical input to an acoustic output; only for reception, where an acoustic input is converted to an electrical output; or for both transmission and reception as in pulse-echo operation. Most medical diagnostic transducers will act in pulse-echo mode. The ultrasonic field generated by the transducer is important and any design will specify field parameters such as a specific focal point, high sensitivity or a certain resolution. These parameters are described below.

Focusing

Many commercially available single element transducers are focused, the focal point depending on the application of the transducer. Focusing can be done either by using a curved lens, or by curving the active material itself, as shown in Figure 2.22. Generally, the second approach gives better performance. Acoustic lenses have a number of disadvantages, in particular due to the path length travelled by emitted sound waves varying across the aperture, giving uneven losses.

The focus of a transducer will generally be described by the f-number ($f\#$) given by:

$$f\# = \frac{\text{focal length}}{\text{aperture diameter}} \quad 2.62$$

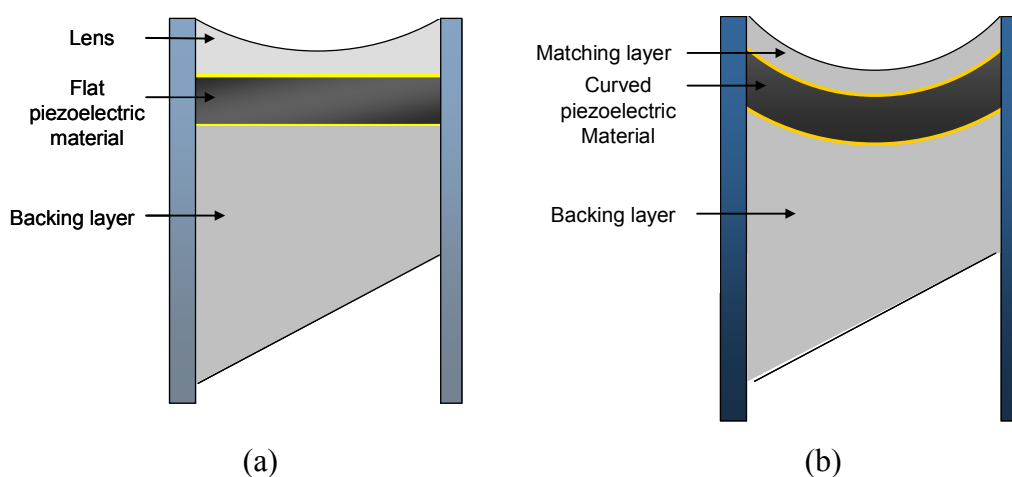


Figure 2. 22: Transducers focused by (a) adding a lens and (b) curving the active material.

Depth of field and beam width

An ultrasound beam is made up of two distinct regions: the *near field* between the transducer and the focal point, and the *far field* beyond the focal plane. Within the near field the beam will have several maxima and minima; as such it is difficult to take quantitative measurements in this region. When operating in continuous wave mode, the length of the near field, N , is given by the equation:

$$N = \frac{D^2}{4\lambda} \quad 2.63$$

for a transducer of diameter, D . This should be considered only as an approximation to the kind of pulsed system used in real echo-ranging techniques.

Within the near and far fields, there exists a focal zone. The focal zone is the region over which the pulse-echo signal strength is within -6 dB of the maximum, at the focal point, and is also known as the *depth of field*. The length of the focal zone, d_{FZ} , is given by (Lu et al., 1994):

$$d_{FZ} = 8 \frac{\lambda}{f} \left(\frac{r}{D} \right)^2 \sqrt{1 + 8 \left(\frac{2\lambda r}{\pi D^2} \right)^2} \quad 2.64$$

where r is the focal distance of the transducer. The beam width for a focused transducer is also dependent on the wavelength and diameter of the transducer, and can be calculated as follows (Kino, 1987):

$$d_{BW} = 1.02 \frac{r\lambda}{D} \quad 2.65$$

Resolution

The axial resolution, R_A , of a transducer is the smallest distance between two reflectors in the axial direction that the transducer can resolve, as shown in Figure 2.23. It is primarily dependent on the pulse length of the transducer, but is also

affected by frequency and speed of sound in the imaging medium. R_A can be determined, using the following relationship:

$$R_A = \frac{1}{2} v_l t_P \quad 2.66$$

where t_P is the time taken for the pulse amplitude to decay to -6 dB of its maximum amplitude. To optimise axial resolution, the pulse length must be minimised. This is generally done by using a highly damping backing layer, with closely matched acoustic impedance to the active material, and optimised matching layers.

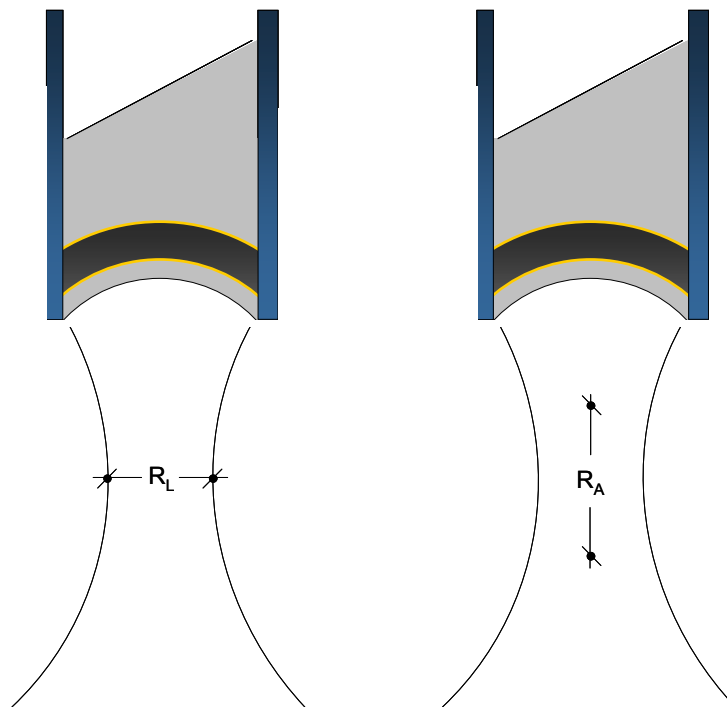


Figure 2. 23: Illustration of lateral resolution, R_L , and axial resolution, R_A , of an ultrasound transducer.

The smallest distance between two reflectors that a transducer can resolve in the lateral direction defines *lateral resolution*, R_L , as shown in Figure 2.23. Lateral

resolution improves with increasing frequency but is also dependent on the width of the sound beam emitted by the transducer. R_L of a transducer is given by:

$$R_L = \lambda \frac{r}{D} = \lambda f \# \quad 2.67$$

Sensitivity

The ability of a transducer to detect reflectors within an imaging medium is known as its sensitivity. A highly sensitive transducer will have increased penetration and lower SNR. The sensitivity of a transducer will depend on a number of factors. Improvements can be made, for example, by using a piezoelectric material with high k_T and an optimal matching layer. A backing layer that has acoustic impedance poorly matched to the active material will increase sensitivity, but this will be at the cost of axial resolution. In practice, a trade-off between sensitivity and resolution is made.

2.11. Ultrasound scanning systems

An ultrasound scanning system uses a number of components to form a B-scan image, following the steps shown in Figure 2.24. The key steps in this process are now described.

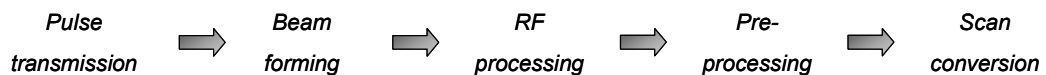


Figure 2. 24: Stages in processing involved in production of an ultrasound image

Pulse Transmission and Beam Forming

Pulse transmission and beam forming for single element transducers have been discussed previously in Section 2.10.

RF processing

To improve the quality of a B-scan image, received signals are usually subjected to pre-processing before being displayed in the form of an image. The most common of these are logarithmic compression and time-gain compensation.

Logarithmic compression of echo data is used to improve image quality due to the fact that returned signals may have a large dynamic range: for example, reflections from tissue boundaries are much greater than those caused by diffuse scattering from smaller tissue structures. Returned signals are usually amplified but attempting to over-amplify returned signals tends to lead to degradation of the final image.

Ultrasound beams decrease in intensity with depth due to attenuation of the beam, causing the reflected signal from two similar targets to be different if they are at different depths in the imaging medium. To offset this, the level of amplification which the receiving device applies to the return signal can be increased with time, which is proportional to the depth from which the echo is originated. This process is called time-gain compensation.

Scan Converter

The scan converter is used to transform received signals into a two-dimensional, or sometimes three-dimensional, image. At this point echo data will still be in the form of a time-domain signal, but this is converted to a spatial form and displayed as a range of brightness on a rectangular coordinate output.

2.12. Summary

This chapter has covered three main topics: acoustic waves, piezoelectric materials and ultrasound transducers. A particular emphasis was placed on the propagation of two types of waves: longitudinal and transverse. Understanding of these waves is crucial to parts of this thesis, as this is required for characterisation of materials used in the fabrication of transducers. Similarly, the electromechanical properties of piezoelectric materials were discussed because of work for this thesis on the

characterisation of piezoelectric materials, in particular piezocomposites. Finally, the basic principles of ultrasound transducer operation and design were discussed, as work for this thesis focused on testing and characterisation of prototype transducers. The next chapter describes the historical development of HFUS transducers, with particular emphasis on two key driving forces: clinical need and piezoelectric material development.

2.13. References

Auld, B.A. (1990) *Acoustic Fields and Waves in Solids*. Florida: Krieger Publishing Company.

Bock N A., Nieman B.J., Bishop J.B., Henkelman R.M. (2005) In Vivo Multiple-Mouse MRI at 7 Tesla *Magnetic Resonance in Medicine* Vol. 54 pp.1311–1316

Cannata J., University of Southern California. Piezoelectric Properties of Lithium Niobate y36°: personal communication.

Brown J. A, Chérin E., Yin J., Foster F.S. (2007) Fabrication and Performance of a High-Frequency Geometrically Focussed Composite Transducer with Triangular Pillar Geometry. *Proceedings of 2007 IEEE Ultrasonics Symposium* pp. 80-83

Cannata J.M., Zhao J.Z., Ayyappan S., Ritter T. A., Chen W., Shung K.K.(1999) Fabrication of High Frequency (25-75 MHz) Single Element Ultrasonic Transducers. *Proceedings of IEEE Ultrasonics Symposium*. pp. 1099-1103

Cheeke, J.D.N. (2002a) *Fundamentals and Applications of Ultrasonic Waves*.Ch.8 Boca Raton: CRC Press.

Drexler W., Fujimoto J.G. (2007) Optical Coherence Tomography in Ophthalmology. *Journal of Biomedical Optics* July/August 2007 Vol. 12(4)

Duker J.S. (2005) Three-dimensional Retinal Imaging with High-Speed Ultrahigh-Resolution Optical Coherence Tomography. *Ophthalmology*, pp. 1734-1746

Foster F.S. (2008) Micro-ultrasound Takes Off (In the Biological Sciences). *Proceedings of 2008 IEEE Ultrasonics Symposium*. pp. 120-125

Foster F.S., Harasiewicz K.A., Sherar M.D. (2000) A History of Medical and Biological Imaging With Polyvinylidene Fluoride (PVDF) Transducers. *IEEE Transactions on Ultrasonics, Ferroelectrics, and Frequency Control*, Vol. 47, No. 6, pp. 1363-1371

Foster F.S., Harasiewicz K.A., Sherar M.D. (2000) A History of Medical and Biological Imaging With Polyvinylidene Fluoride (PVDF) Transducers. *IEEE Transactions on Ultrasonics, Ferroelectrics, and Frequency Control*, Vol. 47, No. 6, pp. 1363-1371

Goll J.H. and Auld, B.A. (1975) Multilayer Impedance Matching Schemes for Broadbanding of Water Loaded Piezoelectric Transducers and High Q Electric Resonators *IEEE Transactions on Sonics and Ultrasonics* Vol. SU-22, No.1. pp.52-53

Hayward G, Bennett J (1996) Assessing the Influence of Pillar Aspect Ratio on the Behavior of 1-3 Connectivity Composite Transducers. *IEEE Transactions on Ultrasonics, Ferroelectrics, and Frequency Control*, Vol. 43, No.1 pp.98-108

Hedrick, W.R., Hykes, D.L., Starchman, D.E. (1995a) *Ultrasound Physics and Instrumentation* pp.7, Mosby-Year Book: St. Louis. Third Edition

Hedrick, W.R., Hykes, D.L., Starchman, D.E. (1995b) *Ultrasound Physics and Instrumentation* pp.27, Mosby-Year Book: St. Louis. Third Edition

Hill, CR, Bamber J.C., ter Haar, G.R. (2004a) *Physical Principles of Medical Ultrasonics*. pp.93 Wiley, Chichester

Hill, CR, Bamber J.C., ter Haar, G.R. (2004b) *Physical Principles of Medical Ultrasonics*. pp. 27 Wiley, Chichester

Hossack, J.A., Hayward, G. (1990) Assessment of Different Pillar Geometries for 1-3 Composite Transducers Using Finite Element Analysis *Proceedings of IEEE Ultrasonics Symposium*. pp. 389-392

Hussey, M. *Diagnostic Ultrasound: An Introduction to the Interactions between Ultrasound and Biological tissues*. Bishopbriggs: Blackie 1975 (pg. 23)

Huang D., Swanson E.A, Lin C.P., Schuman J.S., Stinson W.G., Chang W., Hee M.R., Flotte T., Gregory K., Puliafito C. A, Fujimoto J.G. (1991) Optical Coherence Tomography *Science, New Series*, Vol. 254, No. 5035 pp. 1178-1181

Jiang X., Snook K., Cheng A., Hackenberger W., Geng X. (2008) Micromachined PMN-PT Single Crystal Composite Transducers - 15-75 MHz PC-MUT *Proceedings of 2008 IEEE Ultrasonics Symposium* pp. 164-167

King, D.L. (Ed) (1974). *Diagnostic Ultrasound*. Saint Louis: CV Mosby Company

Kino, G.S. (1987) *Acoustic Waves: Devices, Imaging and Analogue Signal Processing* pp.189. Englewood Cliffs, New Jersey: Prentice Hall

Konofagou E.E., Harrigan T., Ophir J., and Krouskop T. (1999) Poroelastography: Estimating and Imaging the Poroelastic Properties of Tissues. *Proceedings of 1999 IEEE Ultrasonics Symposium* pp. 1627-1630

Kwong KK, Belliveau JW, Chesler DA, Goldberg IE, Weisskoff RM, Poncelet BP, Kennedy DN, Hoppel BE, Cohen MS, Turner R, Cheng HM, Brady TJ, and Rosen BR (1992) Dynamic Magnetic-Resonance-Imaging Of Human Brain Activity During

Primary Sensory Stimulation. *Proceedings of the National Academy of Sciences of the United States of America* Vol.89 No.12 pp. 5675-5679

Lockwood G.R., Turnbull D.H., Foster F.S. (1994) Fabrication of High Frequency Spherically Shaped Ceramic Transducers. *IEEE Transactions on Ultrasonics, Ferroelectrics and Frequency Control*. Vol. 41, No. 2 pp. 231-235

Lu, J.Y., Zou, H., Greenleaf, J.F. (1994) Biomedical Ultrasound Beamforming. *Ultrasound in Medicine and Biology*, Vol. 20, pp.403-428

McGehee, D., Jaffe, J.S. (1992) A Spatially Shaded PVDF Acoustic Transducer. *IEEE Ultrasonics Symposium Proceedings* pp. 589-562

McKeighen, R.E. (1998) Design Guidelines for Medical Ultrasonic Arrays. *SPIE International Symposium on Medical Imaging* Vol. 3341 pp.2-18

O'Leary R L, Hayward G, Smillie G and Parr A C S (2005) *CUE Materials Database, Version 1.2*. Centre for Ultrasonic Engineering, University of Strathclyde, Glasgow.

Savakus, H. P., Klicker K. A., and Newnham R. E. (1981) PZT-Epoxy Piezoelectric Transducers: A Simplified Fabrication Procedure. *Materials Research Bulletin*, Vol. 18, pp. 677-680

Sherrit S., Wiederick H.D., Mukherjee B.K. (1997) A complete characterization of the piezoelectric, dielectric, and elastic properties of Motorola PZT 3203 HD including losses and dispersion. *SPIE Medical Imaging* Vol. 3037 pp.158-169

Smith WA (1989). The Role of Piezocomposites in Ultrasonic Transducers. *Proceeding of 1989 IEEE Ultrasonics Symposium* pp. 755-766

Szabo T.L. (2004) *Diagnostic Ultrasound Imaging: Inside Out*. Elsevier Academic Press. pp.22

van Randerat, J., Setterington R.E. (Ed) (1974). *Piezoelectric Ceramics*. London: Mullard Ltd

Wallace M., University of Paisley. Piezoelectric Properties of PMN-PT (Ibule): personal communication.

Webster R.A., Cochran S., MacLennan D., Meggs C., Button T.W. (2007) Passive Materials for High Frequency Ultrasound Components *Proceedings of 2007 IEEE International Ultrasonics Symposium* pp. 1925-1928

Weintraub M.I., Khoury A., Cole S.P. (2007) Biological effects of 3 Tesla (T) MR imaging comparing traditional 1.5 T and 0.6 T in 1023 consecutive outpatients *Journal of Neuroimaging*. Vol.17 No.3 pp.241-245

Wojtkowski M., Srinivasan V., Fujimoto, J.G., Ko T., Schuman, J.S., Kowalczyk A., Zawadzki R. J., Choi S.S., Fuller A.R., Evans J.W., Hamann B., and Werner J.S. (2009) Cellular resolution volumetric in vivo retinal imaging with adaptive optics–optical coherence tomography. *Optics Express* Vol. 17 No.5 pp.4084-4094

3. Historical development of HFUS transducers

3.1. Clinical Need

A major driver of ultrasound transducer development is always clinical need. This is also true with HFUS. The particular applications relevant to HFUS are discussed below. Naturally, much of the technology implemented has been used in more than one of these applications.

3.1.1. Ophthalmology

Many of the important structures of the eye are located in the anterior segment, at a depth of a few millimetres, and as such HFUS is highly suitable to image them. The relatively safe output of ultrasound scanners, compared to e.g. X-ray, is a further advantage as the delicate structures of the eye are susceptible to damage from ionising radiation.

Initial research into uses of ultrasound in ophthalmology can be dated back to 1956-65 (Erikson, 1974). Baum et al. (1956) studied the effect of ultrasound radiation on the eye while Ossoining (1965) later saw the potential for ultrasound to be used as a tool for diagnosis of eye tumours. Measurements of eye length using ultrasound had been reported previously by Purnell and Sokollu (1962).

The A-scan, as discussed in Chapter 2, was widely adopted as a tool for inspection of the eye, as reported by Bronson (1966). Where injury had occurred due to the presence of a foreign object, it was noted that ultrasound could easily pick up reflections from the object, for example a metal shard where clouding of the eye had made optical detection difficult (Erikson, 1974). B-scan imaging was later used to map the eye. This could be used to detect conditions such as retinal detachment (Sutherland and Forrester, 1974).

Chapter 3. Historical development of HFUS transducers

HFUS has been used in ophthalmology for some time. The first HFUS instrumentation for ophthalmic imaging was developed by Foster et al. (1990), who reported clinical examination of forty patients with a variety of pathological conditions using an ultrasound backscatter microscope, operating at 50-100 MHz. Such instrumentation was used to characterise ocular tissue in this frequency range, with measurements of speed, attenuation and backscatter from the eye taken by Ye et al. (1992). The first commercial single element imaging system designed for the eye was released in 1994 by Carl Zeiss Ltd (Lockwood et al., 1996).

In the mid 1990s, commercial medical imaging probes were available that operated at around 10 MHz. However, this corresponds to a resolution of only around 150 μm in tissue. Larger structures within the eye, such as the 500 μm thick cornea, would be visible at this frequency, but visualising detailed anatomy would be difficult. Often in ophthalmology, clinicians are interested in measuring precise thicknesses of a structure. To do this accurately would require better resolution, and hence higher frequency.

A further application of high frequency imaging of the eye may be to acquire biometric data. Lizzi et al. (1999) used a 50 MHz centre frequency transducer to scan anterior chambers of both rabbit and human eyes. This research was undertaken with the intention of measuring individual-specific data such as the volume or surface area of the ciliary body. Accompanying software was then developed by Lizzi et al. (2000) to produce three-dimensional images of the eye.

A 200 MHz ultrasound biomicroscope was then developed by Knapik et al. (2000), capable of imaging at resolutions of down to 14 μm and 12 μm in the lateral and axial directions respectively, and was used to collect high resolution images of ocular tissues amongst others.

HFUS is now well established in ophthalmic imaging, but commercial systems generally use single element transducers. More recently, however, prototype arrays have been developed for use in ophthalmology. Ketterling and Silverman (2006)

have reported a 20 MHz annular array, showing an axial resolution of 0.25 mm over a depth-of-field to around 18 mm, four times the depth-of-field expected of a single element transducer. This allows the transducer to image the entire cross-section of an eye in focus, as shown in Figure 3.1.

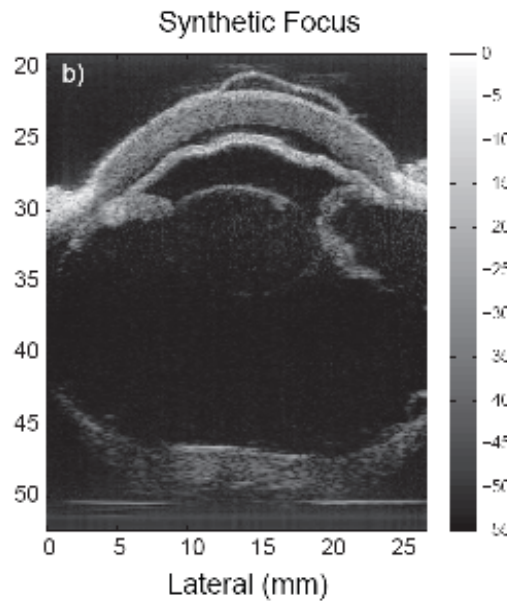


Figure 3. 1: Scan Image of ex-vivo bovine eye taking using 20 MHz annular array (from Ketterling and Silverman, 2006. © IEEE)

3.1.2. Dermatology

A second clinically beneficial application of HFUS is in skin imaging. Once again, the skin is suitable for HFUS because it is easily accessible. Skin consists of two layers. The epidermis (outer layer), varies in thickness from 80 – 500 μm and contains five distinct sub-layers: stratum corneum, stratum lucidum, stratum granulosum, stratum spinosum and stratum germinativum (Martini, 2004a). The dermis consists of two sub-layers, the papillary layer and the reticular layer below which is a layer of subcutaneous fat and connective tissue (also known as the hypodermis) that varies in thickness and constitution between individuals. Within the skin there are a number of accessory structures, such as hair follicles and sweat glands. This anatomy is too small to be resolved by ultrasound at traditional medical frequencies.

Similar to the beginnings of ophthalmology, ultrasound A-scans were initially employed to measure skin dimensions (Lockwood et al., 1996), before B-scan technology was used to generate images of skin pathology. More recently, dermatological diagnosis with ultrasound has concentrated on detection, staging and boundary definition of tumours (Lockwood et al., 1996), in particular *cutaneous melanoma*.

A 40 MHz diagnostic system was developed by Yano et al. (1987) that generated B-scan images by mechanical scanning of a single element transducer, incorporating a quartz lens. This was tested for detection of melanoma, and also benign conditions such as seborrheic keratosis. Sustained research into skin imaging was undertaken from the later 1980s, starting with Hoess et al. (1989), who developed a 50 MHz system for skin imaging. This could be mechanically scanned in two directions allowing both B-scans and C-scans to be generated.

The system developed for use in ophthalmology by Foster et al. (1991) was also adaptable to use in skin imaging. Passman et al. (1993) later used a focussed 30 - 130 MHz transducer to generate B-scans of the skin at several depths for multi-layer images. This was known as the B/D (Brightness/Depth) concept. Producing a transducer with sufficient resolution for useful diagnostic images came at the cost of reduced depth of field and early attempts to characterise tumours with ultrasound were restricted by the limited resolution of transducers available at the time.

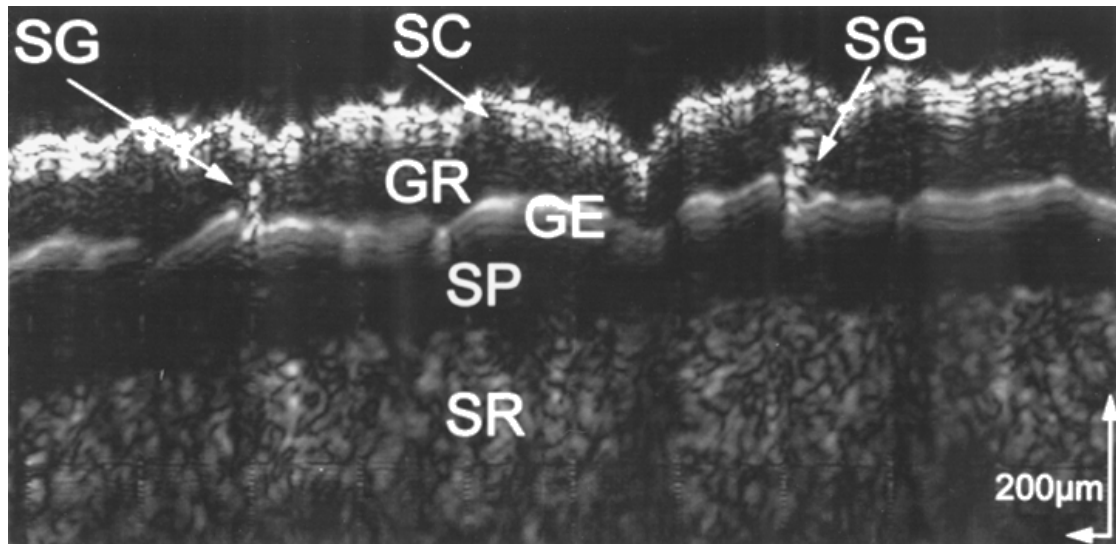


Figure 3. 2: Image showing structures within the skin: stratum corneum (SC), stratum granulosum (GR), stratum germinativum (GE), stratum papillare (SP), stratum reticulare (SR) and eccrine sweat glands (SG) (from Passmann and Emert, 1996. © IEEE)

Passmann et al. (1994) continued working with broadband single element transducers, this time in the 20 - 150 MHz range, but further developed the imaging techniques and also introduced signal processing to compensate for the loss of depth of field which came with improved resolution. Further improvement of SNR, and hence image quality and homogeneity was accomplished by using *synthetic aperture focusing* and coded signals, such as *chirps* (Passmann and Ermert, 1995 & 1996). A scan showing distinct skin layers is shown in Figure 3.2.

Concurrent research was undertaken by Turnbull et al. (1993), who developed an ultrasound backscatter microscopy system operating at 40 - 100 MHz, capable of resolution of 30 μm . It was demonstrated that such a system could be used for detection and characterisation of both malignant melanoma and benign skin features.

Structural examination of the skin was carried out by Vogt et al. (1998), again using single element transducers and the B/D concept. Procedures were used to differentiate between structural features such as separate skin layers, and attenuation was estimated. Pathological changes could also be recorded using this technique.

Studies by Raju et al. (2000) used ultrasound in the frequency range 10 – 55 MHz to characterise skin from the fingertip and forearm of human subjects by measuring attenuation coefficients rather than traditional B-scan techniques. The aim was to provide a quantitative method of skin characterisation, as it was thought such a method could be used to detect changes to structure or tension in the skin indicative of the presence of disease.

Dermatological research using HFUS has diversified more recently, incorporating other techniques in ultrasound. Vogt and Ermert (1997) looked at blood flow, due to the clinical interest in microcirculation in skin. High resolution is required for visualisation of the micro-scale vessels within skin, which are of the order of 100 μm in diameter. This technique incorporates Pulsed Wave Doppler systems at high frequency. Strain imaging using HFUS has also been studied (Vogt et al. 2002) as a method of determining the effects of ageing, environmental or pathological effects on skin.

Vogt et al. have continued work on high frequency systems designed for imaging of skin, using frequencies of 20-100 MHz. This work still incorporates single element transducers, so improvements in accompanying systems have been the main advance in skin imaging for example through optimisation of signals using techniques such as network analysis (Vogt et al., 2003) and improved filtering (Vogt et al., 2005). As with most high frequency imaging applications, it is anticipated that major developments in imaging will be possible with the introduction of high frequency arrays.

3.1.3. Intravascular Ultrasound

Intravascular ultrasound (IVUS) is imaging of the vasculature from within. A great challenge in modern medicine comes from problems caused by plaque build-up in the arteries as this can lead to a number of cardiological health problems, due to a weakening of the lumen and thromboses. Such problems may be treated, but accurate visualisation and characterisation of damaged or unhealthy vasculature is required to

Chapter 3. Historical development of HFUS transducers

maximise the chances of a successful outcome. Ultrasound may offer a relatively non-invasive method of doing this. Probes may be made very small, for example to fit on a catheter of diameter 1.5 Fr (0.5 mm) (Ritter and Shung, 2000), which may be inserted into the vasculature to allow study of blood flow or the lumen.

Ultrasound emerged as a method for characterisation of plaque build up within the vasculature and for guidance during vascular surgery. Differentiation between different layers of the lumen is also possible due to the different scattering and reflection properties of these layers. The walls of vasculature are of the order of 1 mm thick or less (Martini, 2004b), so the penetration possible with HFUS is enough for this modality, including frequencies above 30 MHz.

Early work by Ryan (1992) et al. tested for changes in elasticity of arterial tissue due to atherosclerosis, by measuring the displacement of a vessel wall under pressure. The small scale of displacements was such that a HFUS transducer was required; in this case a 42 MHz probe was used. It was concluded that this technique could feasibly detect changes to tissue elasticity, and as such had potential for use as a tool for assessment of arterial diseases.

Machado et al. (1997) used ultrasound at 50 MHz to characterise vascular tissue, measuring speed of sound, attenuation coefficient and integrated backscattering coefficient in an artery wall in vitro. It was found that there was no significant difference in speed of sound or attenuation between diseased and healthy arteries, but that backscatter could be used to differentiate the two tissues. As such this work was continued by Machado and Foster (2001), who used an improved measurement profiling technique for backscatter and were able to show that there were differences between backscatter measurements from different tissue types, as shown in Figure 3.3. It was thought that this technique could also differentiate between early, mid and advanced stage atherosclerotic build-up.

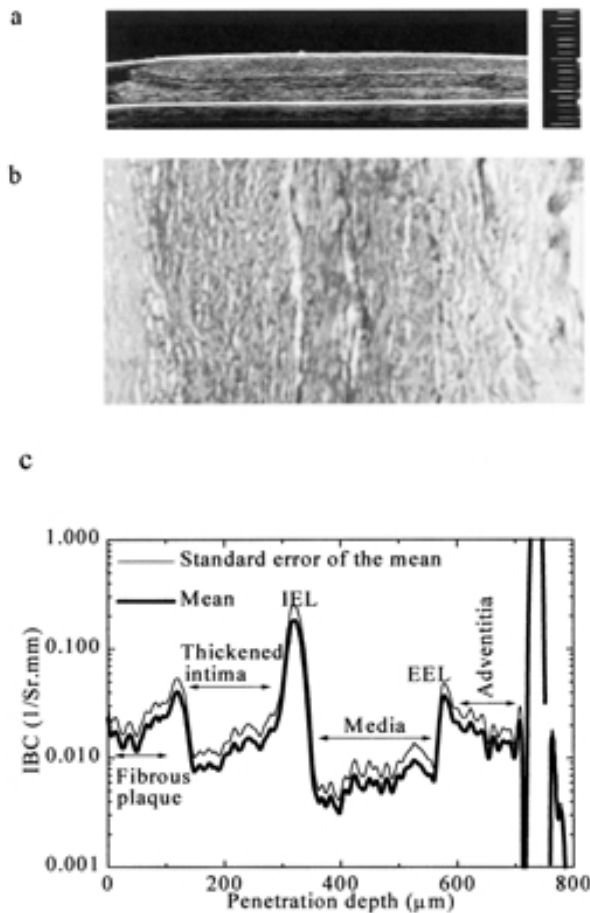


Figure 3. 3: (a) Ultrasound image of diseased coronary artery showing intimal thickening (scale is 100 μm per division), alongside (b) corresponding histology. Also shown is (c) the integrated backscatter coefficient profile (Machado and Foster, 2001. © IEEE)

An alternative method used for detection of atherosclerotic plaques is a technique developed from elastography, IVUS palpography (Leung et al., 2006). This uses a HFUS array, in this case with operating frequency 20 MHz, to produce a high resolution image but also records strain measurements of arterial tissue, as shown in Figure 3.4. This gives an indication of both the presence and the stability of an arterial plaque. A plaque in itself is not necessarily damaging to health, but becomes much more dangerous when it ruptures; this means information on the stability of the plaque is very useful. Accurate strain measurements can be difficult due to cardiac activity causing movement of both IVUS transducers and tissue. Danilouchkine et al. (2008) have introduced reconstruction using normalized convolution algorithms to reconstruct measurements and counteract this problem.

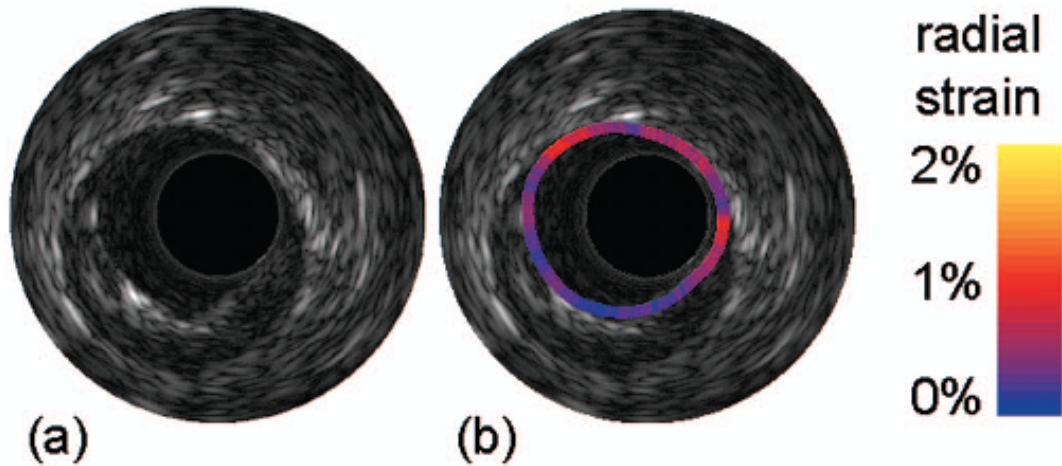


Figure 3. 4: (a) IVUS image of arterial tissue and (b) the same image with strain information overlaid (from Leung et al., 2006. © IEEE)

Work has been undertaken to combine imaging technologies. An example of this is a device reported by Yang et al. (2008) which incorporates an OCT probe and a 35 MHz ultrasound probe, for intravascular imaging. This is designed to take advantage of the high resolution available with OCT and increased penetration of ultrasound.

3.1.4. Small animal imaging

Use of ultrasound in small animal imaging has also developed greatly in recent times. The mouse model is increasingly used to monitor genetic manipulations in research into diseases such as cystic fibrosis (Lockwood, 1996). A traditional method of studying mouse models is by examination of histology. However, ultrasound has several major advantages over this. Ultrasound is real-time and multiple 2D images can be acquired in a short time to give 3D data. Histological examination is inherently 2D and can be time consuming. Ultrasound examination is therefore a relatively inexpensive way of monitoring mouse models. The animal does not need to be sacrificed for examination, so cutting down on the number of animals required in each study, which has a further cost benefit and is ethically desirable.

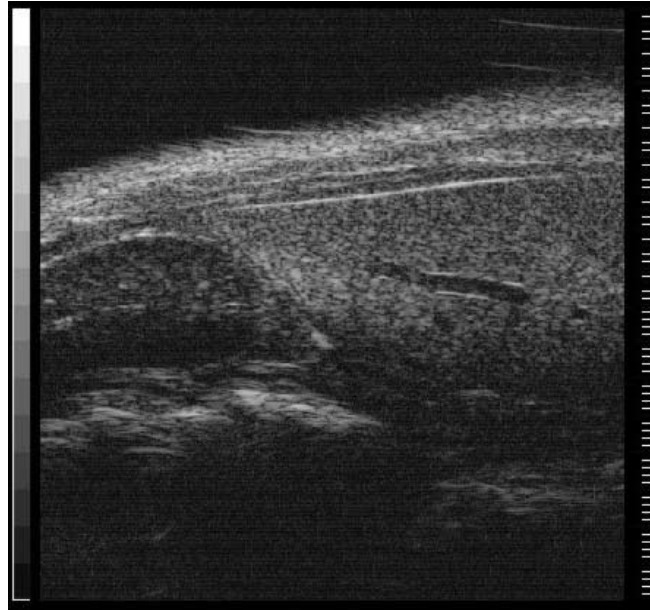


Figure 3. 5: Section image showing mouse liver and kidney (from Foster et al., 2000. © IEEE)

Foster et al. (2000) developed a system to assess development of tissue within a mouse model, using ultrasound biomicroscopy transducers. This system incorporated broadband 25 – 70 MHz single element probes. Images, such as the one shown in Figure 3.5, could be produced over wider depth of field computationally, by imaging at different frequencies in the near and far fields then producing a composite image. Due to the high rate at which the mouse heart beats, systems for imaging of the mouse also require fast frame rates, and this particular system could not generate true real time images.

Currently, there is significant interest in imaging of mouse embryo development and volumetric rendering of data but this can be difficult with fixed focus, single element transducers because of their very limited depth of field. As such arrays have been developed for mouse embryo imaging. Brown et al. (2004) generated images of a mouse anatomy with a depth of field of approximately 5 mm using a 45 MHz annular array while Aristizábal et al. (2005) reported a 40 MHz annular array with depth of field of approximately 10 mm, as compared to the 1 – 2 mm expected with single element devices used in the study for comparison.

The latter transducer allowed visualisation and three-dimensional recreation of structures such as limbs, cerebral ventricles and spinal cord, which could not be fully visualised previously. This was particularly true in later stage embryos, which are often too large for the field of view of a single element transducer. Further testing of this array (Aristizábal et al., 2006) confirmed the improvements in depth of field, but also showed much improved SNR compared with single element systems, allowing volumetric reconstruction of images of far larger structures than previously possible with fixed focus transducers.

Recent developments have seen HFUS combined with other ultrasound technologies. There is significant interest in the vascular development of embryos, and hence this is studied in mouse models. Turnbull et al. (2005) studied the fine structural detail of mouse embryo vascular system using an ultrasound biomicroscopy system, with images enhanced with use of a micro-bubble contrast agent, producing a 35% increase in signal intensity. HFUS has also been combined with Doppler techniques, in the work of Needles et al. (2006).

3.2. Piezoelectric Material Development

It is clear that HFUS has proved important in a number of applications, particularly in recent years. This chapter has thus far focused on the clinical perspective of HFUS development. However, the sophistication of ultrasound imaging systems has always been limited by the capabilities of the transducers around which the system is built, particularly in recent years where computing power and electronics have improved dramatically. However, transducer development is itself reliant on the central component, the active material. As such the development of imaging systems can be intrinsically linked to the appearance of new materials, from the first systems using piezoceramics, to the development of ceramic-composites and polymers, and now potentially new composites using high-performance single crystal materials.

Section 2.7 discussed the features of the main materials used in HFUS applications, and compared their attributes to one another. This discussion is continued in this

section with a review of the historical development of these materials. As this thesis concentrates primarily on piezocomposite transducers, piezoceramic composite materials will be covered in greatest detail.

3.2.1. Polyvinylidene Fluoride and Co-polymer

The piezoelectric nature of Polyvinylidene fluoride (PVDF) was first reported by Kawai (1969). PVDF has two major advantages: firstly, it is highly flexible and can easily be shaped for focussing and secondly, it has acoustic impedance much closer to tissue than other piezoelectric materials. PVDF also has relatively high internal losses, which further increases spatial resolution (Snook et al. 2002).

PVDF was first proposed for use in medical imaging by Ohigashi et al. (1979) and Foster et al. (1979). The initial application for which PVDF transducers were intended was breast imaging, at 13 MHz, as reported by Foster et al. (1984). The early devices were hybrids of PZT transmitters and PVDF receivers, but PVDF was phased out as arrays became more common as it does not have a sufficiently high dielectric constant to be used for arrays. However, the excellent acoustic impedance match and mechanical flexibility of PVDF led to widespread use in the developing HFUS field.

Sherar and Foster (1989) published the first images generated at high frequency by PVDF transducers, operating at 100 MHz. The fabrication of transducers at very high frequencies came relatively quickly, mainly due to the fact that the desired thickness of the PVDF active layer can be achieved easily and it is very flexible, hence easy to handle and to focus mechanically. Single element PVDF transducers were soon adopted for clinical B-mode imaging, in the ranges 40 - 60 MHz for ophthalmology and 20 MHz for dermatology (Foster et al., 2000). PVDF transducers have now been incorporated into commercial systems and are routinely used for skin imaging, ophthalmologic examination and small animal research (Foster et al., 2000).

PVDF does have some disadvantages as a piezoelectric material: primarily it has poor coupling coefficient, as noted in Section 2.7. It also needs to be very thin for high effective frequency because backing reduces the effective frequency (Snook et al., 2002). It is, however, the most widely used piezoelectric polymer material (Brown, 2001). In recent years, PVDF has been used to fabricate annular arrays, in particular through the work of Ketterling et al. (2005).

Other piezoelectric polymers have been studied in recent times, most commonly P(VDF-TrFE). Increasing the polymer TrFE percentage leads to an improved piezoelectric response, but also makes the film more brittle so less capable of tight focusing (Brown, 2001). Unlike PVDF, P(VDF-TrFE) does not have to be stretched to be piezoelectric, so can be more easily incorporated into a transducer structure directly, through coating, casting or moulding (Brown, 1992).

P(VDF-TrFE) was used by Snook et al. (2002) to develop a 100 MHz transducer. The co-polymer was spin-coated directly onto a spherically curved aluminium substrate, and a carbon substrate. This allowed the transducers to be fabricated without backing layers, which can reduce operating frequency. The carbon substrate was particularly useful for this reason, as it had a closer acoustic impedance match to co-polymer than had aluminium. It was also noted that, compared with traditional press-focusing, this proved an easier method of producing low f-number transducers.

Studies were also undertaken into piezoelectric polyurea by Nakazawa et al. (2006). In this case, vapour deposition was used to produce multiple layers of polyurea to make up the final transducer. Using a multi-layer approach increased the coupling co-efficient and sensitivity of the transducer.

3.2.2. Lithium Niobate

One of the early materials used in ultrasonic transducers was LiNbO_3 (LNO). When LNO was introduced in the 1960s, it was found to have a coupling coefficient which was superior to most available materials and was also thermally and electrically

Chapter 3. Historical development of HFUS transducers

stable (Warner, 1965). It was also noted to be a single crystal material that must be grown; hence it was considered expensive to produce at the time.

LNO has been used for high frequency transducer development in the work of Cannata. LNO (Y-36° cut) transducers were fabricated to operate in the 25-75 MHz range (Cannata, 1999), with the primary intention of being used as ultrasound biomicroscopy (UBM) devices for ophthalmology. The transducers were capable of imaging detailed anatomy in the eye and could be impedance matched to 50 Ω electronics relatively easily despite their large apertures, due to the low permittivity of the material (Cannata, 1999). Further work on LNO transducers centred on fabrication of focused devices, both using lenses and by spherically curving the piezoelectric material (Cannata, 2000). It was noted that the high acoustic impedance of LNO makes acoustic matching more problematic, hence a double matching layer was utilised. A flexible supportive layer of silver-loaded epoxy was used to maintain the mechanical integrity of the active material, using a method published by Lockwood et al. (1994), described in the next section (3.2.3). The press-focusing technique used to curve the active material was proved to produce transducers at around 50 MHz, capable of generating good quality images of the eye. However, it was noticed that the focal point of the transducer could be affected when the transducer was exposed to elevated temperatures.

The advantages of LNO as a material are succinctly discussed by Cannata et al. (2003). It has fast longitudinal speed of sound, so active layers can reach high frequency without being prohibitively thin. It has low permittivity, which is required if high sensitivity is to be achieved in large aperture devices. Its drawbacks are high acoustic impedance, and high Q factor, which limits the bandwidth of the transducer. Cannata et al. (2003) also noted that broadband transducers could be made by addition of carefully designed matching and backing layers. High sensitivity was possible, particularly when the active element was curved, as opposed to a lens being added for focusing. The transducers were susceptible to failure due to electrical shorts, however, because of small cracks developing within the active material.

More recently, LNO has been used to fabricate a dual element annular array for use in harmonic imaging, at fundamental frequency 20 MHz. It is noted, once more, that the main advantage of using LNO is that it has suitable permittivity for larger aperture devices (Kim et al., 2006). LNO transducers have also been used for Doppler imaging (Aristizábal and Turnbull, 2003)

While LNO is a useful material for single element transducers, it is not suitable for linear or phased arrays because its low dielectric constant makes electrical impedance prohibitively high. Research into high frequency LNO arrays is therefore not widely reported in the literature.

3.2.3. Lead Zirconate Titanate

Lead zirconate titanate (PZT) was developed in the 1950s and soon became the active material of choice for ultrasonic transducers. PZT was not, however, used in early fabrication of high frequency transducers. This was dominated by polymer materials, such as PVDF. PZT was first studied for use in high frequency transducers by Foster et al. (1990). Transducers were developed to operate in the 30-80 MHz range using PZTs of varying grain sizes. PZT was shown to have higher coupling coefficient and greater sensitivity than piezoelectric polymers more commonly studied at that point. Although coupling coefficients were reduced in PZT when operational frequency was increased, with particular drop-off in performance above 60 MHz, Foster et al. (1991) later found k_T was still at least 0.3, so higher than in polymer, and as high as 0.44 in an 80 MHz transducer made with fine grain ceramic. Bandwidth, though not as great as in polymer, was also found to be an acceptable 50%.

In order to improve the performance of PZT transducers for B-mode imaging, focusing is required. The layers of active material required are very thin, around 40 μm , and as such a spherical shape cannot be machined. However, a method of mechanically shaping PZT, for the purposes of focusing, was developed by

Lockwood et al. (1993). Although PZT is in itself brittle, it was found that addition of a malleable backing layer to the PZT and shaping under heat stopped the formation of ‘macroscopic cracks’ that would prevent functional operation of the transducer. After bonding the PZT to the backing layer, the structure can be shaped by heating and pressing it into a spherical well with a ball bearing, as shown in Figure 3.6. A 53 MHz transducer was successfully produced using this method with a focal length of 4 mm, and aperture of 2 mm (Lockwood et al., 1994).

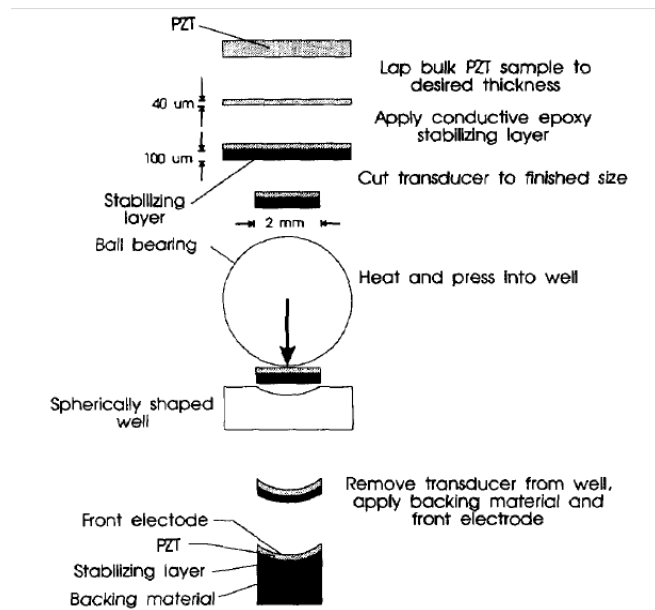


Figure 3. 6: Diagram showing process used to fabricate spherically focussed single element transducers from non flexible active materials, in this case PZT (from Lockwood et al., 2004. © IEEE)

An alternative method for producing high frequency PZT transducers was proposed by Lukacs et al. (1996), using thick film processes to produce active layers operating at UBM frequencies, around 80 – 200 MHz. These frequencies correspond to active layer thicknesses of 5 – 27 μm, which is too thin to be machined. Films made by traditional sol gel techniques are limited to around 3 – 4 μm in thickness. In this case, a modified process was used to produce a composite made up of multiple coated layers, each of thickness around 3 – 4 μm which produced active layers of thickness up to 100 μm, between that of traditional bulk material and thin films. Extensive

characterisation of these devices by Lukacs et al. (2000) found that the piezoelectric properties of the thick film PZT layers were poor compared to conventional PZT, particularly k_T , which was around 0.25. This was due to the greater porosity of the films and the fact that the substrates on which the films are deposited cannot stand high temperatures. This prohibits normal sintering of the film, a process that is essential for ceramic to have optimal parameters. However, devices of frequency 70 - 160 MHz were successfully fabricated and images of corneal segments were acquired.

Levassort et al. (2000) used a tape casting technique to produce thick films of PZT-PNN between 60 and 90 μm thicknesses. Again, this process has the major advantage that no lapping or polishing of the material is required to produce high frequency active layers, as they are cast to final thickness. It was reported that PZT-PNN had comparable k_T to PZT, at 0.43, and high relative permittivity, $\epsilon_R > 1900$. Further work by Levassort et al. (2003) reported that tape casting could produce a range of ceramic active layers with similar properties to bulk materials made by the same composition, and that these materials had suitable properties for integration into HFUS single element and array devices.

PZT has relatively high acoustic impedance, which makes acoustic matching to tissue difficult. Porous ceramics, as reported by Lethiecq et al. (2004), can reduce this problem. These are air-ceramic composites, with ceramic volume 25%, and can be of 3-0 or 3-3 geometries. These materials are cost-effective to produce and maintain comparable electromechanical coupling to bulk PZT, but with increased sensitivity and bandwidth in medical applications due to the reduced acoustic impedance mismatch. However, this material showed a drop-off in performance at frequencies above approximately 6-7 MHz, and as such may not be useful for HFUS applications.

A different technique for producing PZT films was proposed by Xu et al. (2003). This process used a combination of screen printing and laser lift-off, capable of producing films of thickness 20 - 100 μm . The film is first screen printed on a

substrate that can withstand the high temperatures of sintering, then, using laser lift-off, transferred to a second substrate, such as silicon, which has been metallised. As a result, PZT films produced using this technique have significantly greater piezoelectric properties than films produced using the sol-gel composite technique, including high dielectric constant and k_T of 0.49.

Investigation of screen printed PZT was also undertaken by Maréchal et al. (2005, 2006). In this case the film was printed onto a porous PZT substrate, allowing a very wideband response because of the well matched acoustic impedances of the active layer and supportive substrate. The PZT film and substrate were integrated into a transducer structure from which human dermatology images were successfully generated. The quality of these images was then maximised by varying the thickness and acoustic impedance of both the active element and barrier layer to produce optimal piezoelectric response from the transducer.

PZT sheets of thickness commensurate with high frequency operation have recently been developed by Button et al. (2005). The technique of net-shape processing, calenders PZT, while in a plastically formable green state into a tape of the desired thickness. This tape is then sintered. The resultant ceramic has favourable piezoelectric properties. This material has $k_T > 0.5$.

In recent years, PZT has been used to build high frequency arrays, due in part to its high permittivity. The work of Cannata et al. (2001, 2002) focused on mechanical dicing of fine grain, high density PZT to produce linear arrays of operating frequency 35 MHz, while later work by Lukacs et al. (2005) took advantage of the fact that PZT may be laser-machined to produce small scale linear array elements, operating at 30 MHz. Concurrently, work being undertaken by Brown et al. (2003, 2004) used monolithic PZT to produce annular arrays in the 40 – 60 MHz range, the array electrodes being patterned onto the PZT rather than using dicing or machining.

3.2.4. Single Crystal Materials

Although the piezoelectric nature of single crystal materials, such as LNO, has been known for some time, ultrasound transducer development has been dominated by ceramic materials, particularly PZT. However, in the 1990's the excellent piezoelectric properties of lead zirconate niobate doped with lead titanate (PZN-PT) and lead magnesium niobate doped with lead titanate (PMN-PT) were noted by Park and Shrout (1997) and Saitoh et al. (1998). In recent years, single crystal materials have been incorporated into high frequency devices.

The work of Gottlieb et al. (2005) used PMN-PT to produce a miniature high frequency needle transducer for intra-ocular Doppler imaging, at 44 MHz, for detection of blood flow in the microcirculation of the eye. This device successfully detected blood flow in the 1 mm diameter vessels of the retina. This work was continued by Xu et al. (2006), in this case further developing the needle transducer and also producing a 35 MHz linear array.

The work of Yuan et al. (2006) has incorporated PMN-PT into composite, which is widely regarded as the most effective use of single crystal material, in this case for use as an IVUS transducer. It was reported that the sensitivity and bandwidth of the device were approximately double that of a similar device fabricated from ceramic material, as expected theoretically (Yuan et al., 2006).

3.2.5. Composite Materials

Since their development in the 1970s, piezocomposites have become ubiquitous in commercial medical ultrasound devices, due to their excellent piezoelectric properties, flexible nature, and favourable acoustic impedance (Smith et al., 1985). As described previously, piezocomposite is a combination of a piezoelectric material, usually a ceramic, and a passive polymer. The relative volume fractions of the passive and active phases may be tailored to fit certain parameters defined by a transducer designer, such as electrical impedance, acoustic impedance, speed, or coupling coefficient (Smith, 1989). In reality, optimising one aspect of the

performance of a composite will lead to a decrease in another aspect, so a ‘trade-off’ design is required. However, composite can be regarded as having excellent all-round performance, explaining the ubiquity of adoption of this material.

There are many composite design geometries. However, in this section the focus will be on the development of 1-3 composites, with some brief discussion of 2-2 composites which have been used to develop high frequency transducers. A number of techniques have been employed for production of 1-3 composites, as discussed below.

Fibre composites

Also known as rod composites, fibre composites are made by producing fibres, or rods, of PZT which are much longer than they are wide. The fibres are then bundled together such that they run parallel to one another and bonded using a passive polymer. The resultant structure can be cut into slices perpendicular to the rods, each of which can be poled and used as an active piezoelectric material. This procedure is illustrated in Figure 3.7.

This technique was first developed by Klicker et al. (1980). This method was capable of producing composites with active pillars of around 200 μm in diameter, which is not commensurate with high frequency operation, where active layers must have thickness of the order of 50 μm or less, suggesting pillar diameter should be less than 20 μm . Later work by Card (1988) could produce finer scale fibre composites, with pillars under 50 μm in diameter, which is still not sufficiently fine-scale for high frequency transducers.

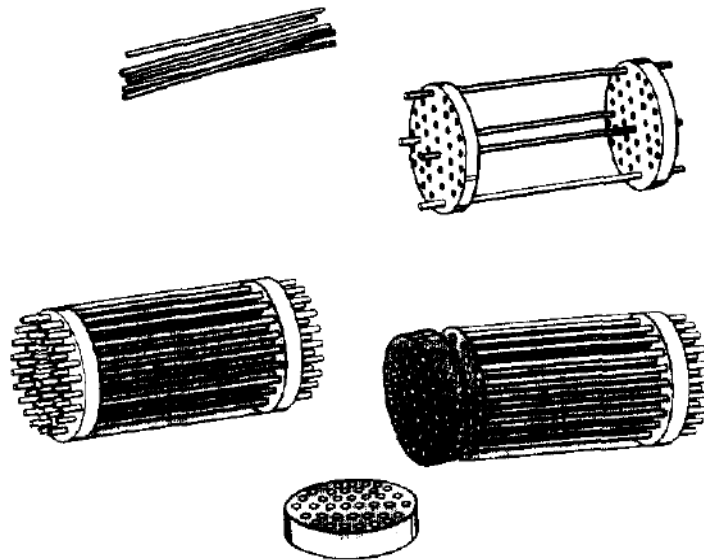


Figure 3. 7: an example of a fabrication method for fibre composites (from Smith and Auld 1989. © IEEE)

Recently, fibre composites have been developed specifically for HFUS using extrusion procedures such as sol-gel (Meyer et al., 1997). This procedure is capable of producing composite with rods of diameter between 10 – 60 μm , and operating at frequencies of 15 – 40 MHz while maintaining coupling co-efficient up to 0.7.

It was noted that the semi-random nature of the pillars in a fibre composite aids in the reduction of lateral modes. Snook et al. (2002) used fibre composite, incorporating 17 μm fibres, to build a 50 MHz single element transducer, but found that although the composite had high k_T , approximately 0.6, the sensitivity and bandwidth of the transducer were actually poorer than a similar LNO or lead titanate transducer.

Net shape processing can also be used to produce smaller rod structures, and is discussed in more detail below. Although not widely used to produce composites at present, this method does have the major advantage that it is potentially very economical. However, handling issues become more prominent in fine fibre structures.

Dice-and-fill composites

The most commonly used method for production of composites is the ‘dice-and-fill’ technique, as discussed in Section 2.8. It is desirable that a volume fraction of 30% or greater active material is maintained, although piezocomposite devices of lower volume fraction have been reported (Brown et al., 2007). Limitations of early fabrication procedures meant early composites (Savakus et al., 1981) had pillars of width approximately 50 μm : this would not have allowed high frequency composites to be produced while maintaining sufficient volume fraction and pillar aspect ratio. Recently, however, saw blade technology has improved such that small enough pillar structures may be produced for composites to operate at high frequency.

More recent research has seen composite materials incorporated into arrays with a number of designs proposed in the 1990s, including Nyugen-Dinh et al. (1996), using 1-3 PZT composite and Ritter et al. (1998), which used 2-2 composite material. The latter noted that composite appeared to have superior performance to a similar device made with monolithic ceramic. Work on arrays made using 1-3 composites was reprised by Brown et al. (2006). In this case a 40 MHz linear array was fabricated. The composite design was, naturally, limited by the availability of fine-scale saw blades. Brown et al. (2007) continued work on 1-3 composite transducers, switching from traditional square pillars to triangular pillars to minimise pillar width in the composite structure.

Interdigital pair bonding was proposed as a fabrication method for high frequency composites by Liu et al. (2001). This process can be used to fabricate high volume fraction 1-3 composites with small kerf, by dicing two or even four separate pieces of ceramic material and bonding them together, with the pillars of each ceramic layer intercalated with that of the other. These composites were shown to operate at up to 50 MHz. A variation of this process, known as interdigital phase bonding, was reported by Yin et al. (2004). This is a more complex procedure which involves pairing of two diced composites, which are lapped, then further diced and paired once more. It is capable of producing composites operating at up to 85 MHz, although in this case the composites are of the 2-2 geometry.

Alternative approaches to ceramic shaping

It is clear that the upper limits of operational frequency to which composite materials can be fabricated is dictated by blade thickness if a sawing process is used. As saw blades become thinner, they are both more difficult to make and more fragile to use, so producing smaller and smaller saw blades is unlikely to be the solution to increasing the frequency of composite transducers. Some alternative procedures are now briefly discussed.

Lukacs et al. used laser micromachining to shape bulk PZT. Both linear arrays (Lukacs et al., 1996) and annular arrays (Lukacs et al., 1999) have been fabricated in monolithic PZT, operating at high frequencies. Laser machining was carried out in the former case using a copper vapour laser (CVL) and the latter with an excimer laser. It was also noted that structures of aspect ratios of 1:4 could be fabricated this way (Lukacs et al., 1999). Lukacs et al. (2005) later reported that a 30 MHz 64-element array had been fabricated with laser machined kerfs of only 8 μm . It is believed the first commercial HFUS arrays were based on this work.

Farlow et al. (2001) also used a CVL, in this case to 'micro-machine' PZT into a 1-3 composite structure. Although the composite produced was not specifically designed for use at high frequency, i.e. above 30 MHz, the composite had kerf of 13 μm , which is commensurate with high frequency operation.

A final technique is that of net-shape processing, as reported by Cochran et al. (2004). This technique uses a 'lost mould' process such as that reported by Wersing et al. (1986). A defect free ceramic paste is embossed into a sacrificial mould, before being dried, sintered and filled with low-viscosity epoxy and lapped to thickness, similarly to standard dice-and-fill composites. Using this procedure, 1-3 piezocomposites were fabricated with pillar diameter down to 12 μm , sizes that would be suitable for use in high frequency composite transducers. As such it is hypothesised that the upper frequency of composite transducers may be extended beyond that achievable by standard procedures.

3.3. Transducer Development

As previously discussed, the development of ultrasonic transducers has always been linked to the availability of materials. In the case of single element devices, the fundamental design of the transducer has changed little in over fifty years. However, the operational frequencies and performance capabilities of transducers have improved significantly with the progress in materials technology, as covered in earlier sections of this chapter. As such, much of the work on development of high frequency transducers and arrays has been covered in previous sections of this chapter.

3.4. Conclusion

This chapter examined the state of the art in HFUS. This technology has been primarily driven by emerging clinical need for ultrasound systems with improved resolution. Modern medicine demands systems capable of imaging microscopic-scale anatomical structures such as the eyes, skin or vascular system, while the emergence of genetic research and study of mouse models has also created a demand for non-invasive high resolution imaging systems.

This chapter also reviewed the development of piezoelectric materials, which is intrinsically linked to the development of better transducers. Computing power and electronics have reached extraordinary levels, yet it can be argued that ultrasound systems cannot progress significantly without better transducers. Similarly, developments in transducer technology are often held back by a dearth of suitable materials. While systems based on mechanical scanning of single element transducers can now produce images of impressive contrast and resolution, they have limited depth of field. However, it is hoped that new approaches to material production, for example micro-scale composite materials will overcome this problem, allowing systems to make further significant improvements.

3.5. References

- Aristizábal O., Turnbull D.H. (2003) 44-MHz LiNbO₃ Transducers for UBM-Guided Doppler Ultrasound. *IEEE Transactions on Ultrasonics, Ferroelectrics, and Frequency Control*, vol. 50, no. 6 pp. 623-630
- Aristizábal O., Turnbull D.H., Ketterling J.A. (2005) Mouse Embryo Imaging with a 40 MHz Annular Array. *Proceedings of 2005 IEEE Ultrasonics Symposium* pp. 361-364
- Aristizábal O., Turnbull D.H., Ketterling J.A. (2006) Analysis of 40 MHz Annular Array Imaging Performance In Mouse Embryos *Proceedings of 2006 IEEE Ultrasonics Symposium* pp. 872-875
- Baum, G. (1956) "Effect of Ultrasonic Radiation U on the Eye and Ocular Adnexa," *Am. J. Ophthal.* Vol. 42:5
- Bernassau A.L., McKay S., Hutson D., Démoré C.E.M., Garcia-Gancedo L., Button T.W., McAneny J.J. and Cochran S. (2007) Surface Preparation of 1-3 Piezocomposite Material for Microfabrication of High Frequency Transducer Arrays. *Proceedings of 2007 IEEE Ultrasonics Symposium* pp. 96-99
- Bronson, N. (1965) Techniques of Ultrasonic Localization and Extraction. *Am. J. Ophthal.* 60-OKT, 8696-603.
- Brown J. A, Chérin E., Yin J., Foster F.S. (2007) Fabrication and Performance of a High-Frequency Geometrically Focussed Composite Transducer with Triangular Pillar Geometry. *Proceedings of 2007 IEEE Ultrasonics Symposium* pp. 80-83
- Brown J. A., Foster F.S., Needles A., Lockwood G. R. (2006) A 40 MHz Linear Array based on a 1-3 Composite with Geometric Elevation Focussing. *Proceedings of 2006 IEEE Ultrasonics Symposium* pp. 256-259
- Brown J.A., Lockwood G.R. (2005) Design of Sparse Annular Arrays for High-Frequency Imaging. *Proceedings of 2005 IEEE Ultrasonics Symposium* pp. 125-128

Chapter 3. Historical development of HFUS transducers

Brown J.A., Morton C.E., Lockwood G.R. (2003) Fabrication and Performance Of 40-60 MHz Annular Arrays. *Proceedings of 2003 IEEE Ultrasonics Symposium* pp.869-872

Brown J.A., Morton-Démoré C., Foster F.S., Lockwood G.R. (2004) Performance of a 50 MHz Annular Array Based Imaging System. *Proceedings of 2004 IEEE Ultrasonics Symposium* pp.760-763

Brown L.F. (1992) Ferroelectric Polymers: Current and Future Ultrasound Applications. *Proceedings of 1992 IEEE Ultrasonics Symposium* pp.539-550

Brown L.F. (2001) Design Considerations for Piezoelectric Polymer Ultrasound Transducers. *Proceedings of 2001 IEEE Ultrasonics Symposium* pp. 265-270

Button T.W., Cochran S., Kirk K.J., MacLennan D., MacNeil A., McDonald K., Meggs C., Rodriguez-Sanmartin D., Webster R., Zhang D. (2005) Net-Shape Ceramic Manufacturing as an Aid to Realize Ultrasonic Transducers For High-Resolution Medical Imaging. *Proceedings of 2005 IEEE Ultrasonics Symposium* pp.1625-1628

Cannata J. M., Ritter T.A., Chen W., and Shung K.K. (2000) Design of Focused Single Element (50 – 100 MHz) Transducers using Lithium Niobate *Proceedings of 2000 IEEE Ultrasonics Symposium*

Cannata J. M., Williams J. A. and Shung K. K. (2005) A Kerfless 30 MHz Linear Ultrasonic Array. *Proceedings of 2005 IEEE Ultrasonics Symposium* pp. 109-112

Cannata J. M., Zhou Q. F., and Shung K. K. (2004) Development of a High Frequency (35 MHz) Linear Ultrasonic Array using 2-2 Composite. *Proceedings of 2004 IEEE Ultrasonics Symposium* pp.894-897

Cannata J.M. and Shung K.K. (2002) Development of a High Frequency (>20 MHz) Linear Ultrasonic Array Using Fine Grain Ceramic Elements. *Proceedings of 2002 IEEE Ultrasonics Symposium* pp.1243-1247

Chapter 3. Historical development of HFUS transducers

Cannata J.M., Ritter T.A., Chen. W., Silverman R.H., Shung K.K. (2003) Design of Efficient, Broadband Single-Element (20–80 MHz) Ultrasonic Transducers for Medical Imaging Applications. *IEEE Transactions on Ultrasonics, Ferroelectrics, and Frequency Control*, Vol. 50 No.11, pp. 1548-1557

Cannata J.M., Ritter T.A., Shung K.K (2001) A 35 MHz Linear Array for Medical Imaging. *Proceedings of 2001 IEEE Ultrasonics Symposium* pp. 1157-1160

Cannata J.M., ShROUT T.R., Shung K.K (2002) A 35 MHz Linear Array for Medical Imaging. *Proceedings of 2002 IEEE Ultrasonics Symposium* pp. 343-346

Cannata J.M., Zhao J.Z., Ayyappan S., Ritter T. A., Chen W., Shung K.K.(1999) Fabrication of High Frequency (25-75 MHz) Single Element Ultrasonic Transducers. *Proceedings of 1999 IEEE Ultrasonics Symposium* pp. 1099-1103

Card, R. J. (1988) Preparation of Hollow Ceramic Fibers. *Advanced Ceramic Materials*, Vol.3, pp. 29-31

Cladé O., Palczewska G., Lewandowski J.J., Krakovitz P., Dinet D. (2006) Development and evaluation of a 20MHz array for ultrasonic detection of middle ear effusion. *Proceedings of 2006 IEEE Ultrasonics Symposium* pp. 2357-2360

Cochran S., Abrar A., Kirk K.J., Zhang D., Button T.W., Su B., Meggs C., Porch N. (2004) Net-Shape Ceramic Processing as a Route to Ultrafine Scale 1-3 Connectivity Piezoelectric Ceramic-Polymer Composite Transducers. *Proceedings of 2004 IEEE Ultrasonics Symposium* pp.1682-1685

Danilouchkine M., Mastik F., van der Steen, A. (2008) An Algorithm for Strain Reconstruction from Irregularly Sampled, Incomplete Measurements. *Proceedings of 2008 IEEE Ultrasonics Symposium* pp. 329-332

Duckett A.S., Reid A., Leamen L., Cucevic V., Foster F.S. (2003) Ultrasound Biomicroscopy for Mouse Imaging and Doppler: Assessment of Potential for Biological Effects in the Embryo and at Soft Tissue-Bone Interfaces. *Proceedings of 2003 IEEE Ultrasonics Symposium* pp. 246-249

Chapter 3. Historical development of HFUS transducers

Erikson K.R., Fry F.J. Jones J.P. (1974) Ultrasound in Medicine: A Review. *IEEE Transactions on Sonics and Ultrasonics*, Vol. Su-21, No. 3

Farlow R., Galbraith W., Knowles M, and Hayward G. (2001) Micromachining of a Piezocomposite Transducer Using a Copper Vapor Laser *IEEE Transactions on Ultrasonics, Ferroelectrics, and Frequency Control*, Vol.48, No. 3. pp.639-640

Foster F. S., Hunt J.W., (1979) "Improved Ultrasonography by Means of Cylindrical Transducers," in *Proc. World Fed. Ultrasound Med. Biol.* pp. 402

Foster F. S., Liu G., Mehi J., Starkoski B. S., Adamson L., Zhou Y., Harasiewicz K. A., and Zan L. (2000) High Frequency Ultrasound Imaging: From Man to Mouse *Proceedings of 2000 IEEE Ultrasonics Symposium*

Foster F. S., Pavlin C. J., Lockwood G. R., Ryan L.K., Harasiewicz K.A., Berube L., and Rauth A.M. (1993) Principles and Applications of Ultrasound Backscatter Microscopy *IEEE Transactions on Ultrasonics, Ferroelectrics, and Frequency Control*, Vol. 40, No. 5 pp. 608-617

Foster F. S., Ryan L. K., Turnbull D.H. (1991) Characterization of Lead Zirconate Titanate Ceramics for Use in Miniature High-Frequency (20-80 MHz) Transducers. *IEEE Transactions on Ultrasonics, Ferroelectrics and Frequency Control*, Vol. 38. No. 5 pp. 446-453

Foster F. S., Strban M., Austin G. (1984) The Ultrasound Macroscope: Initial Studies Of Breast Tissue, *Ultrason. Imag.*, Vol. 6, pp. 243–261

Foster F.S. (2008) Micro-ultrasound Takes Off (In the Biological Sciences). *Proceedings of IEEE Ultrasonics Symposium* pp. 120-125

Foster F.S., Harasiewicz K.A., Sherar M.D. (2000) A History of Medical and Biological Imaging With Polyvinylidene Fluoride (PVDF) Transducers. *IEEE Transactions on Ultrasonics, Ferroelectrics, and Frequency Control*, Vol. 47 No.6 pp. 1363-1371

Chapter 3. Historical development of HFUS transducers

Foster F.S., Pavlin C.J., Lockwood G.R., Ryan L.K., Harasiewicz K., Berube L., Rauth A.M. (1991) High Frequency Ultrasound Backscatter. *Proceedings of 1991 IEEE Ultrasonics Symposium* pp. 1161-1170

Foster F.S., Pavlin C.J., Starkoski B. and Harasiewicz K. (1990) Ultrasound Backscatter Microscopy Of The Eye In Vivo *Proceedings of 1990 IEEE Ultrasonics Symposium* pp. 1481-1484

Foster F.S., Ryan L.K., Turnbull D.H. (1990) Design and Fabrication of Non-Polymer Transducers in the Frequency Range from 30 to 80 MHz *Proceedings of 1990 IEEE Ultrasonics Symposium* pp. 375-378

Gottlieb E. J., Lai B., Xu X., Cannata J., Yen J., Zhou Q, Han P, Ameri H., Ratanapakorn T, Barnes A, Humayun M, Shung K.K. (2005) PMN-PT High Frequency Ultrasonic Needle Transducers for Pulsed Wave Doppler in the Eye. *Proceedings of 2005 IEEE Ultrasonics Symposium* pp. 2227-2230

Gottlieb E.J., Cannata J.M., Hu C.H., Shung K.K. (2005) High Frequency Copolymer Annular Array Ultrasound Transducer Fabrication Technology. *Proceedings of 2005 IEEE Ultrasonics Symposium* pp. 121-124

Gururaja T.R., and Panda R.K. (1998) Current Status and Future Trends in Ultrasonic Transducers for Medical Imaging Applications. *Proceedings of 1998 IEEE Ultrasonics Symposium* pp. 223-228

Hoess A., Ermert H., El-Gammal S., Altmeyer P. (1989) A 50 MHz Ultrasonic Imaging System For Dermatologic Application *Proceedings of 1989 IEEE Ultrasonics Symposium* pp. 849-852

Ito Y., Kushida K., Sugawara K., Takeuchi H. (1995) A 100-MHz Ultrasonic Transducer Array Using ZnO Thin Films. *IEEE Transactions on Ultrasonics, Ferroelectrics, and Frequency Control*, Vol. 42, No. 2, pp.316-324

Kawai H., (1969) "The Piezoelectricity of Polyvinylidene Fluoride", *Jpn. J. Appl. Phys.* 8, pp. 975-976.

Chapter 3. Historical development of HFUS transducers

Ketterling J.A. and Silverman R H. (2006) 20-MHz Annular Arrays for Ophthalmic Imaging. *Proceedings of 2006 IEEE Ultrasonics Symposium* pp.252-255

Ketterling J.A., Aristizábal O., Turnbull D.H. (2005) Polyimide Backed 40-MHz PVDF Transducers. *Proceedings of IEEE Ultrasonics Symposium* pp. 117-120

Kim H. H., Cannata J. M., Liu R., Sun L., Shung K. K., Silverman R. H., Babar S. (2006) Dual Element Transducers for High Frequency Harmonic Imaging. *Proceedings of IEEE Ultrasonics Symposium* pp. 2325-2328

Klicker, K. A., "Piezoelectric Composites with 3-1 Connectivity for Transducer Applications," Ph. D. Thesis, Solid State Science, The Pennsylvania State University, May 1980

Knapik D. A., Starkoski B., Pavlin C. J., and Foster F. S. (2000) A 100-200 MHz Ultrasound Biomicroscope. *IEEE Transactions on Ultrasonics, Ferroelectrics, and Frequency Control*, vol. 47, no. 6 pp.1540-1549

Knapik D.A., Starkoski B., Pavlin C.J., Foster F.S. (1997) A Realtime 200 MHz Ultrasound B-scan Imager. *Proceedings of IEEE Ultrasonics Symposium* pp. 1457-1460

Lethiecq M., Feuillard G., Ratsimandresy L., Nguyen-Dinh A., Pardo L., Ricote J., Andersen B., Millar C. (1994) Miniature High Frequency Array Transducers Based On New Fine Grain Ceramics. *Proceedings of IEEE Ultrasonics Symposium* pp. 1009-1013

Lethiecq M., Levassort F., Tran-Huu-Hue L.P. Rabelais F. Alguero M, Pardo L., Bove T., Ringgaard E., Wolny W (2004) New Low Acoustic Impedance Piezoelectric Material for Broadband Transducer Applications. *Proceedings of IEEE Ultrasonics Symposium* pp. 1153-1156

Leung K.Y.E, Baldewsing R.A., Mastik F., Schaar J.A., Gisolf A., and van der Steen A.F.W (2006) Motion Compensation for Intravascular Ultrasound Palpography. *IEEE Transactions on Ultrasonics, Ferroelectrics, and Frequency Control*, Vol. 53 no.7 pp.1269-1280

Chapter 3. Historical development of HFUS transducers

Levassort F., Bove T., Ringgaard E., Tran-Huu-Hue L. P., Holc J., Lethiecq M. (2003) A Complete Range Of Tape-Cast Piezoelectric Thick Films For High Frequency Ultrasonic Transducers. *Proceedings of IEEE Ultrasonics Symposium* pp. 2003-2006

Levassort F., Trarl-Huu-Huel L.P., Lethiecq M. (2000) New Piezoceramic Films for High Resolution Medical Imaging Applications. *Proceedings of IEEE Ultrasonics Symposium*

Liu R., Harasiewicz K.A., Foster F. S. (2001) Interdigital Pair Bonding for High Frequency (20–50 MHz) Ultrasonic Composite Transducers *IEEE Transactions on Ultrasonics, Ferroelectrics, and Frequency Control*, Vol. 48, No. 1, pp. 299-306

Lizzi F.L. (1997) Ultrasonic Scatterer-Property Images of the Eye and Prostate. *Proceedings of IEEE Ultrasonics Symposium* pp.1109-1117

Lizzi F.L., Deng C.X. and Feleppa E.J. (1999) Three-dimensional Biometric Images of Ocular Structures Using Very-high-frequency Ultrasound. *Proceedings of IEEE Ultrasonics Symposium* pp. 1581-1583

Lizzi F.L., Feleppa E.J. and Kalisz A. (2000) High-resolution, Three-dimensional Visualization and Morphology Assays of the In-vivo Ciliary Body. *Proceedings of IEEE Ultrasonics Symposium*

Lockwood G.R., Turnbull D.H., Christopher D.A., and Foster F.S. (1996) Beyond 30 MHz: Applications of High Frequency Ultrasound Imaging. *IEEE Engineering in Medicine and Biology* Vol. 15, pp. 60-71

Lockwood G.R., Turnbull D.H., Foster F. S. (1993) High Frequency (> 20 MHz) Spherically Shaped Ceramic Transducers *Proceedings of IEEE Ultrasonics Symposium* pp. 495-498

Lockwood G.R., Turnbull D.H., Foster F.S. (1994) Fabrication of High Frequency Spherically Shaped Ceramic Transducers *IEEE Transactions on Ultrasonics, Ferroelectrics, and Frequency Control*, Vol. 41, No. 2 pp. 231-235

Chapter 3. Historical development of HFUS transducers

Lukacs M., Sayer M., Foster S. (2000) Single Element High Frequency (>50 MHz) PZT Sol Gel Composite Ultrasound Transducers *IEEE Transactions on Ultrasonics, Ferroelectrics, and Frequency Control*, Vol. 47, No. 1 pp. 148-159

Lukacs M., Sayer M., Knapik D., Candela R., and Foster F.S. (1996) Novel PZT Films for Ultrasound Biomicroscopy *Proceedings of IEEE Ultrasonics Symposium* pp. 901-904

Lukacs M., Sayer M., Lockwood G., Foster F.S. (1999) Laser Micromachined High Frequency Ultrasonic Arrays. *Proceedings of IEEE Ultrasonics Symposium* pp. 1209-1212

Lukacs M., Yin J., Pang G., Garcia R., Cherin E., Williams R., Foster F.S., Mehi J. (2005) Performance and Characterization of High Frequency Linear Arrays. *Proceedings of IEEE Ultrasonics Symposium* pp. 105-108

Machado J.C., Foster F.S. (2001) Ultrasonic Integrated Backscatter Coefficient Profiling of Human Coronary Arteries In Vitro. *IEEE Transactions on Ultrasonics, Ferroelectrics, and Frequency Control*, Vol. 48, No. 1

Machado J.C., Foster F.S., and Gottlieb A.I. (1997) In Vitro Ultrasound Characterization of Coronary Arteries at 50 MHz. *Proceedings of IEEE Ultrasonics Symposium* pp. 1067-1070

Maréchal P., Levassort F., Holc F., Tran-Huu-Hue L.P., Kosec M., Lethiecq M. (2005) High Frequency Transducer Based on Integrated Piezoelectric Thick Films for Medical Imaging. *Proceedings of IEEE Ultrasonics Symposium* pp. 2223-2226

Maréchal P., Levassort F., Holc J., Tran-Huu-Hue L.P., Kosec M., and Lethiecq M. (2006) High-Frequency Transducers Based on Integrated Piezoelectric Thick Films for Medical Imaging. *IEEE Transactions on Ultrasonics, Ferroelectrics, and Frequency Control*, Vol. 53, no. 8, pp.1524-1533

Maréchal P., Levassort F., Tran-Huu-Hue L.-P., Holc J., Kosec M., Lethiecq M. (2006) Optimization of an integrated structure including a screen-printed

Chapter 3. Historical development of HFUS transducers

piezoelectric thick film for high frequency transducers. *Proceedings of IEEE Ultrasonics Symposium* pp. 260-263

Martini F.H. (2004a) *Fundamentals of Anatomy and Physiology* pp.156-164 6th Ed. Benjamin Cummings, San Francisco, CA, USA.

Martini F.H. (2004b) *Fundamentals of Anatomy and Physiology* pp.722-723 6th Ed. Benjamin Cummings, San Francisco, CA, USA.

Meyer R. J., Jr., Lopath P., Yoshikawd S., Shrout T. R. (1997) High Frequency 1-3 Composite Transducers Fabricated From Alkoxide-Derived PZT Fibers. *Proceedings of IEEE Ultrasonics Symposium* pp. 915-918

Nakazawa M., Maezawa A., Nakamura K., Ueha S. (2006) A 100 MHz Multi-layered High Performance Transducer Using Polyurea Thin Film. *Proceedings of IEEE Ultrasonics Symposium* pp. 2421-2424

Needles A., Cheung A.M., Foster F.S., Goertz D.E. (2006) High Frequency Colour Flow Imaging of Mouse Tumours using Inter-Frame Clutter Filtering. *Proceedings of IEEE Ultrasonics Symposium* pp. 971-974

Nguyen-Dinh A., Ratsimandresy L., Mauchamp P., Dufait R., Flesch A, Lethiecq M. (1996) High Frequency Piezo-Composite Transducer Array Designed For Ultrasound Scanning Applications. *Proceedings of IEEE Ultrasonics Symposium* pp. 943-947

Oakley C.G., Zipparo M.J. (2000) Single Crystal Piezoelectrics: A Revolutionary Development for Transducers. *Proceedings of IEEE Ultrasonics Symposium*

Ohigashi H., Nakanishi T., Itoh T., Suzuki M., Omoto R., (1979) "Study on piezoelectric polymer transducers for high resolution ultrasound imaging," *World Fed. Ultrasound Med. Biol. Proceedings*, pp. 376.

Ossoining, K (1965) On the ultrasonic diagnosis of eye tumors (Clinical and Experimental studies with saw-tooth recordings) *Klin. Monatsbl. Augenheilk* 146, pp.321-337

Chapter 3. Historical development of HFUS transducers

Park S.E., ShROUT T.R. (1997) Characteristics of Relaxor-Based Piezoelectric Single Crystals for Ultrasonic Transducers. *IEEE Transactions on Ultrasonics, Ferroelectrics, and Frequency Control*, Vol. 44, No. 5, pp. 1140–1147

Passmann C., Ermert H. (1994) 150 MHz In Vivo Ultrasound of the Skin: Imaging Techniques and Signal Processing Procedures Targeting Homogeneous Resolution. *Proceedings of IEEE Ultrasonics Symposium* pp. 1661-1664

Passmann C., Ermert H. (1995) Adaptive 150 MHz Ultrasound Imaging of the Skin and the Eye using an Optimal Combination of Short Pulse Mode and Pulse Compression Mode. *Proceedings of IEEE Ultrasonics Symposium* pp.1291-1294

Passmann C., Ermert H. (1996) A 100-MHz Ultrasound Imaging System for Dermatologic and Ophthalmologic Diagnostics. *IEEE Transactions on Ultrasonics, Ferroelectrics, and Frequency Control*, Vol. 43, No. 4, pp. 545-552

Passmann C., Ermert H., Auer T., Kaspar K., El-Gammal S., Altmeyer P. (1993) In Vivo Ultrasound Biomicroscopy. *Proceedings of IEEE Ultrasonics Symposium* pp. 1015-1018

Pazol B. G., Bowen L. I., Gentilman R. L., Pham H. T., Serwatka W. J., Oakley C. G., Dietz D. R. (1995) Ultrafine Scale Piezoelectric Composite Materials for High Frequency Ultrasonic Imaging Arrays. *Proceedings of IEEE Ultrasonics Symposium* pp. 1263-1268

Purnell E and Sokollu A (1962) Ultrasonic measurements of Eye Length. *Acta Ophthalmologica* 40, pp. 218-222.

Raju B.I., Srinivasan M.A. (2000) In Vivo Characterization of Human Fingertip and Forearm Skin Using Attenuation of High Frequency Ultrasound. *Proceedings of IEEE Ultrasonics Symposium*

Ritter T. A. and Shung K.K. (2000) Catheter Mounted Doppler Ultrasound Transducers. *Proceedings of IEEE Ultrasonics Symposium*.

Chapter 3. Historical development of HFUS transducers

Ritter T. A., Shung K. K., Cannata J., and Shrout T. R. (2000) High Frequency Ultrasound Arrays for Medical Imaging. *Proceedings of IEEE Ultrasonics Symposium*.

Ritter T., Shung K.K., Geng X., Wang H., Shrout T.R. (1998) 30 MHz Medical Imaging Arrays Incorporating 2 -2 Composites. *Proceedings of IEEE Ultrasonics Symposium*. pp. 1851-1856

Ryan L.K., Lockwood G.R., Starkoski B.G., Holdsworth D.W., Rickey D.W., Drangova M., Fenster A., Foster F.S. (1992) A High Frequency Intravascular Ultrasound Imaging System For Investigation Of Vessel Wall Properties. *Proceedings of IEEE Ultrasonics Symposium*. pp.1101-1106

Saitoh S., Kobayashi T., Shimanuki S., Hashimoto S., Yamashita Y. (1998) Phased array ultrasonic probe using $\text{Pb}(\text{Zn } 1/3 \text{ Nb } 2/3)\text{O}_3\text{-PbTiO}_3$ single crystal. *Proc. SPIE 3341*, pp. 264 – 271

Savakus, H. P., Klicker K. A., and Newnham R. E. (1981) PZT-Epoxy Piezoelectric Transducers: A Simplified Fabrication Procedure. *Materials Research Bulletin*, Vol. 18, pp. 677-680

Sherar M. D., Foster F.S.T. (1989) The design and fabrication of high frequency poly(vinylidene fluoride) transducers. *Ultrasonic Imaging*., vol. 11, pp. 75–94.

Smith W.A., Shaulov A., Auld B.A. (1985) Tailoring the Properties of Composite Piezoelectric Materials for Medical Ultrasonic Transducers. *Proceedings of IEEE Ultrasonics Symposium*. pp. 642-647

Smith WA (1989). The Role of Piezocomposites in Ultrasonic Transducers. *Proceedings of IEEE Ultrasonics Symposium*. pp. 755-766

Snook K., Rhee S., Robert M., Gottlieb E. and Shung K.K. (2002) Development Of P(VDF-TRFE) Ultrasonic Transducers Operating At 50-120 MHz. *Proceedings of IEEE Ultrasonics Symposium*. pp. 1249-1252

Chapter 3. Historical development of HFUS transducers

Snook K.A., Ritter T.A., ShROUT T.R., Shung K.K. (2001) Design of a High Frequency Annular Array for Medical Ultrasound. *Proceedings of IEEE Ultrasonics Symposium*. pp. 1161-1164

Snook K.A., Zhao J.Z., Alves C.H.F., Cannata J.M., Chen W.H., Meyer, R.J., Ritter T.A., Shung K.K. (2002) Design, Fabrication, and Evaluation of High Frequency, Single Element Transducers Incorporating Different Materials. *IEEE Transactions on Ultrasonics, Ferroelectrics, and Frequency Control*, Vol. 49, No. 2. pp. 169-176

Sutherland G.R. and Forrester J.V. (1974) B Scan Ultrasonography in Ophthalmology, *British Journal of Radiology* Vol.47 pp.383-386.

Turnbull D.H., Aristizábal O., Ketterling J.A. (2005) In Vivo Contrast-Enhanced Imaging of Mouse Vascular Development. *Proceedings of IEEE Ultrasonics Symposium*.pp. 747-750

Turnbull D.H., Starkoski B.G., Harasiewicz K.A., Lockwood G.R. and Foster F.S. (1993) Ultrasound Backscatter Microscope for Skin Imaging *Proceedings of IEEE Ultrasonics Symposium*. pp. 985-988

Vogt M., Ermert H. (1997) Application of High Frequency Broadband Ultrasound for High Resolution Blood Flow Measurement. *Proceedings of IEEE Ultrasonics Symposium*. pp.1243-1246

Vogt M., Ermert H., El Gammal S., Kaspar K., Hoffmann K., Altmeyer P. (1998) Structural Analysis of the Skin using High Frequency, Broadband Ultrasound in the Range from 30 to 140 MHz *Proceedings of IEEE Ultrasonics Symposium*.pp. 1685-1688

Vogt M., Paul B., Scharenberg S., Scharenberg R., and Ermert H. (2005) In Vivo Ultrasound Biomicroscopy Of Skin With 20 MHz and 100 MHz Range Ultrasound: Inverse Echo Signal Filtering Optimization. *Proceedings of IEEE Ultrasonics Symposium*. pp. 508-511

Vogt M., Paul B., Scharenberg S., Scharenberg R., Ermert H. (2003) Development Of A High Frequency Ultrasound Skin Imaging System: Optimization Utilizing

Chapter 3. Historical development of HFUS transducers

Time Domain Reflectometry and Network Analysis. *Proceedings of IEEE Ultrasonics Symposium*. pp. 744-747

Vogt M., Scharenberg S., Scharenberg R., Hoffmann K., Altmeyer P., Ermert H. (2002) In Vivo Evaluation and Imaging of Skin Elasticity Applying High Frequency (22 MHz) Ultrasound. *Proceedings of IEEE Ultrasonics Symposium*. pp. 1863-1866

Warner A.W. (1965) New Piezoelectric Materials. *Proceedings of 19th Annual Symposium on Frequency Control* pp. 5-21

Wersing, W. (1986) Composite Piezoelectrics for Ultrasonic Transducers. *Proceedings of IEEE International Symposium on Applications of Ferroelectrics*, pp. 212-223.

Xu B., Buhler S., White D., Zesch J., and Wong W. (2003) Fabrication of Piezoelectric Thick Films for High Frequency Transducers. *Proceedings of IEEE Ultrasonics Symposium*. pp. 1999-2002

Xu X., Zhou Q., Ameri H., Gottlieb E.J., Lai B., Yen J.T., Cannata J.M., Han P., Humayun M.S., Shung K.K. (2006) High-frequency Pulsed-wave Ultrasound Doppler System for Biomedical Applications with PMN-PT Needle Transducer and 30 MHz Linear Array. *Proceedings of IEEE Ultrasonics Symposium*. pp. 2234-2237

Yang H.C., Yin. J., Hu. C, Zhou Q., Cannata. J, Chen Z., and Shung K.K (2008) Novel biomedical imaging that combines intravascular ultrasound (IVUS) and optical coherence tomography (OCT). *Proceedings of IEEE Ultrasonics Symposium*. pp. 1769-1772

Yano T., Fukukita H., Ueno S. and Fukumoto A. (1987) 40 MHz Ultrasound Diagnostic System for Dermatologic Examination. *Proceedings of IEEE Ultrasonics Symposium*. pp. 875-878

Ye S.G., Harasiewicz K. A, Pavlin C. J., and Foster F. S. (1992) Ultrasound Characterization Of Ocular Tissue In The Frequency Range From 50 MHz To 100 MHz. *Proceedings of IEEE Ultrasonics Symposium*. pp. 1107-1112

Chapter 3. Historical development of HFUS transducers

Ye S.G., Harasiewicz K. A., Pavlin C. J., and Foster F. S. (1995) Ultrasound Characterization of Normal Ocular Tissue in the Frequency Range from 50 MHz to 100 MHz. *IEEE Transactions on Ultrasonics, Ferroelectrics, and Frequency Control*, Vol. 42, No. 1 pp.8-14

Yin J., Lukacs M., Harasiewicz K., Foster S. (2004) Ultra-Fine Piezoelectric Composites for High Frequency Ultrasonic Transducers. *Proceedings of IEEE Ultrasonics Symposium*. pp. 1962-1965

Yuan J.R., Jiang X., Cao P.J., Sadaka A., Bautista R., Snook K., Rehrig P. W. (2006) High Frequency Piezo Composites Microfabricated Ultrasound Transducers for Intravascular Imaging. *Proceedings of IEEE Ultrasonics Symposium*. pp. 264-268

Zipparo M., Oakley C., Hackenberger W., Hackenberger L. (1999) Single Crystal Composites, Transducers, and Arrays. *Proceedings of IEEE Ultrasonics Symposium*. pp. 965-968

Zipparo M.J., Shung K.K., Shrout T.R. (1997) Piezoceramics for High-Frequency (20 to 100 MHz) Single-Element Imaging Transducers. *IEEE Transactions on Ultrasonics, Ferroelectrics, and Frequency Control*, Vol. 44, No. 5, pp. 1038-1048.

4. Materials and methods

To produce an ultrasound imaging system, an active material must first be produced with suitable properties for the application intended, in this case medical diagnostic imaging. This material must then be prepared such that it operates well at a desired frequency and incorporated into a suitable transducer casing along with other components such as backing and matching layers. The transducer is then integrated into an imaging system. The aims of the work reported here centred on several issues within this process: development of high performance piezoelectric materials, characterisation of the material and optimisation of material preparation procedures; characterisation of the electromechanical and acoustic properties of transducers made with new piezocomposite material, and testing of the potential uses for this material in diagnostic imaging. The steps are illustrated in Figure 4.1.

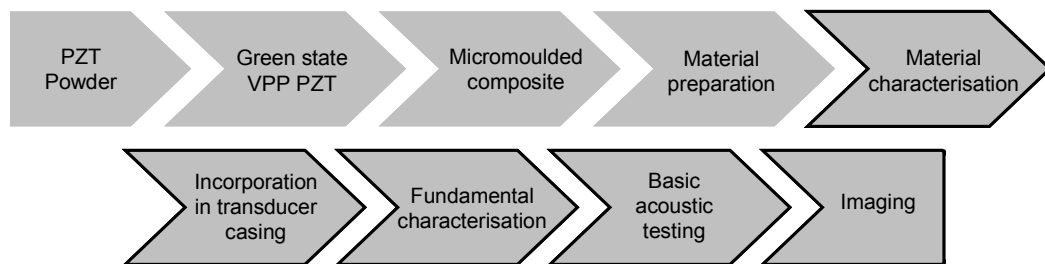


Figure 4. 1: Flow chart showing the steps from a PZT powder to ultrasound image. Work reported in this thesis is indicated by a bold outline.

The work reported in this thesis focused on the latter steps in this process: from characterisation of micromoulded composite (MC) material through to investigation of the potential for these materials to be used in diagnostic medical imaging systems. Fundamental characterisation of MC was undertaken to determine piezoelectric properties of the material. Passive materials used for transducer construction were also characterised at high frequencies. Transducers made from MC were then characterised, both to assess the fundamental properties of the transducers and their acoustic performance. This was then extended to some basic imaging procedures to test the potential for MC to be used in imaging devices. This chapter describes the materials and experimental methodology used.

The chapter begins by describing initial studies done on piezoelectric material fabrication and preparation and the procedure for fabrication of the MC that form the basis for the majority of work for this thesis, in Section 4.1. Section 4.2 describes initial studies undertaken to assess a novel technique of material preparation, ultra precision grinding.

The next sections concentrate on characterisation of transducer materials. Producing a well-designed ultrasound transducer requires thorough knowledge of the properties of the active material used, but also the properties of passive materials used to make other components of the transducer, such as backing or matching layers. The relevant literature contains very little documentation of the properties of passive materials at high frequencies. Work was therefore carried out on characterisation of passive materials at high frequencies, as described in Section 4.3 and 4.4.

The focus of this chapter then returns to active materials. The procedures used to determine the piezoelectric properties of the MC from experimental measurements are described in Section 4.5. These results required verification against theory. There are a number of widely used modelling procedures suitable for this purpose and these are briefly described in Section 4.6. A one-dimensional model, based on the wave equation and piezocomposite homogenisation as presented by Smith and Auld (1991), was chosen for characterisation of the MC, and this is analysed in detail in Section 4.7. A manual parameter fitting procedure was used to verify experimental measurements taken for the MC: this is also outlined.

Once the piezoelectric properties of the MC had been ascertained, determination of the acoustic performance of the MC was required. This is most conveniently done by packaging the MC in a casing which can be connected to suitable instrumentation. The fabrication process used for incorporation of piezocomposites, and other active materials, into casings is described in Section 4.8. Section 4.9 then describes the procedures used to determine some of the fundamental properties of the transducers: bandwidth, axial and lateral resolution, and depth of field.

Ultimately, these transducers are being developed for use in diagnostic medical imaging systems so testing to determine whether these transducers could potentially be used for imaging systems was also carried out. An automated 2D scanning system was developed to facilitate more sophisticated performance testing, including basic 2D imaging. The design of the system, components used and procedure for visualisation of recorded data is outlined in Sections 4.10 and 4.11 respectively. Imaging tests were carried out using a specially designed tungsten wire target and ex-vivo tissue samples: this is described in Section 4.12.

4.1. Piezoelectric Material Fabrication

4.1.1. Fabrication of PZT samples

Initial investigation of monolithic PZT was undertaken. The PZT used was modified TRS600FG (TRS Technologies, State College, PA, USA), a form of PZT-5H, produced using the viscous polymer processing (VPP) method, as described by Cochran et al. (2004).

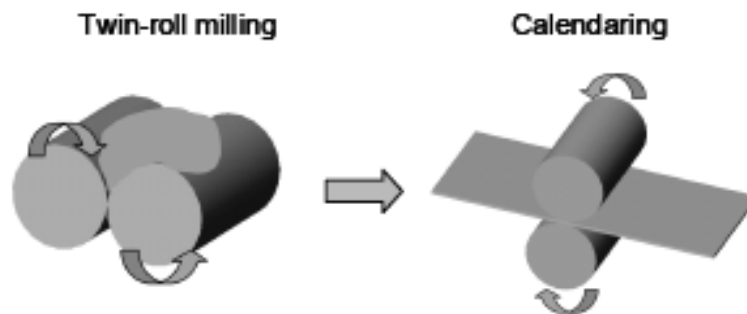


Figure 4. 2: Illustration of VPP, showing ceramic paste being milled and calendered to produce a green state ceramic sheet (picture adapted from Cochran et al. (2004). © IEEE).

Figure 4.2 illustrates the key stages of VPP. The first stage involves high shear mixing of PZT powder, polymeric binder, solvents and flow modifier using a twin-roll mill to produce a low defect, high green strength ceramic paste. This paste is then calendered into sheets of a desired thickness which are sintered in a lead-rich environment at approximately 1200 °C. The VPP samples must then be poled and

lapped to thickness. Alternatively, the material may be lapped to thickness before being poled.

To provide mechanical strength and damping for a piezoelectric material, a backing material should be used. The transducers studied here had backing materials made from either Ag-loaded epoxy (Part No.186-3616, RS Components, Corby, UK) or W-loaded epoxy, fabricated in-house. The advantage of using W-loaded epoxy is that acoustic impedance of the backing can be tailored to optimise transducer performance. Unlike the proprietary Ag-loaded epoxy product, W-loaded is not electrically conductive if the volume fraction of Tungsten is below 0.4. W-loaded epoxy is discussed more in Section 5.2.1. The ceramic was first thoroughly cleaned using an ultrasonic bath with acetone, isopropanol and distilled water successively. After adhesion to the ceramic material, the epoxy was allowed to cure for 24 hours then lapped to an even thickness of 1mm. At this point the ceramic samples were cut into 3 mm squares, to allow incorporation into transducer casings.

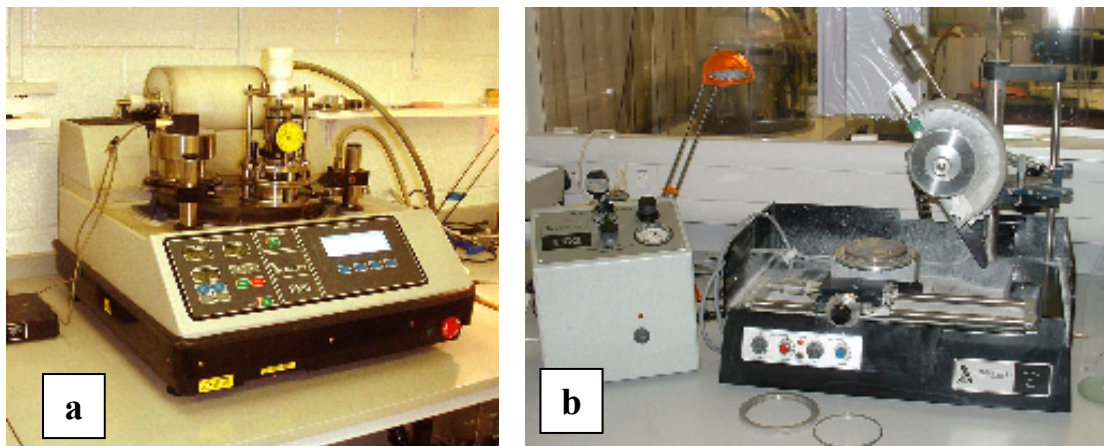


Figure 4. 3: Photographs of (a) lapping machine and (b) dicing saw

Lapping and Dicing

To obtain the required thickness of PZT for high frequency operation, a precision lapping and polishing machine (Logitech PM 5, Logitech Ltd, Glasgow, UK) was used in conjunction with alumina powder in slurry. Three grades of alumina slurry were used: 9 μm , 3 μm and 1 μm . The 9 μm powder is used to remove larger

thicknesses of bulk material, while the 3 μm and 1 μm solutions remove material more slowly but provide a better surface finish.

Where samples required to be cut to a specific shape, a Logitech Model 15 Dicing Saw was used. The lapping machine and dicing saw are shown in Figures 4.3a and 4.3b respectively.

Poling

Many of the piezoelectric samples fabricated for this work used PZT that had not been poled. This was generally the first procedure carried out with new samples. The poling procedure was as follows. Each sample was immersed in silicon oil, and placed on a bespoke jig, shown in Figure 4.4, with electrical contacts either side. The oil was then heated to 120 $^{\circ}\text{C}$ using a hot plate. An electric field of 2kV/mm was applied to the samples, with the field gradually increased from zero. This was maintained for around 15 minutes, after which the temperature of the oil was reduced to 20 $^{\circ}\text{C}$, with the field still applied. At this point, the field was then reduced to zero and the newly-poled ceramic sample was removed from the silicon oil and cleaned.

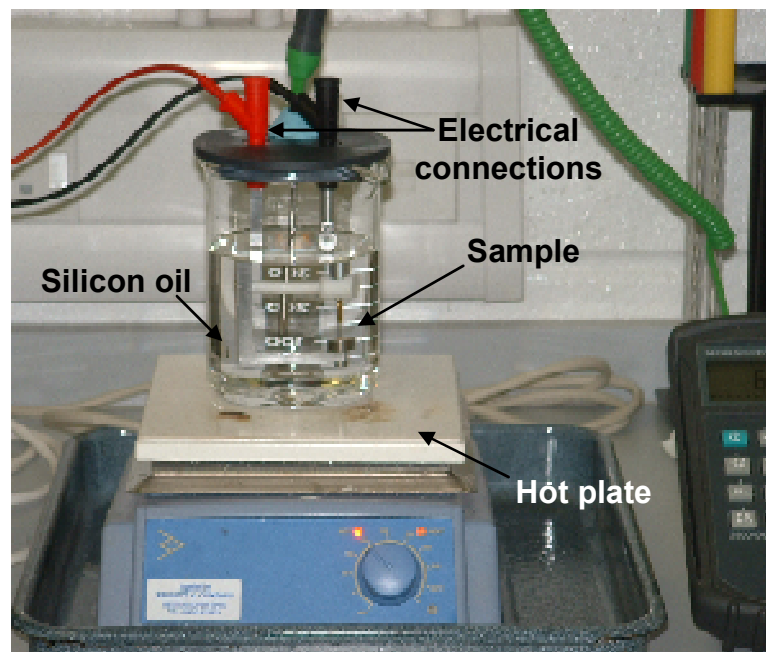


Figure 4. 4: Photograph of poling jig.

4.1.2. Fabrication of fibre composite

Fibre composites are 1-3 connectivity composites made from extruded PZT fibres and a passive polymer, as described in Chapter 3. The fabrication procedure is as follows:

PZT fibres are made by extrusion of PZT made with VPP. This process can produce fibres of a variety of diameters.

VPP fibres were compared by Nelson et al. (2003) and Dent et al. (2005) to fibres made by three alternative processes: sol gel, extrusion and viscose suspension spinning (VSSP). Results of this comparison are shown in Figure 4.5. It was found that VPP fibres have a more uniform grain structure and higher piezoelectric properties, d_{33} , e_{33} , k_{33} and s_{33} .

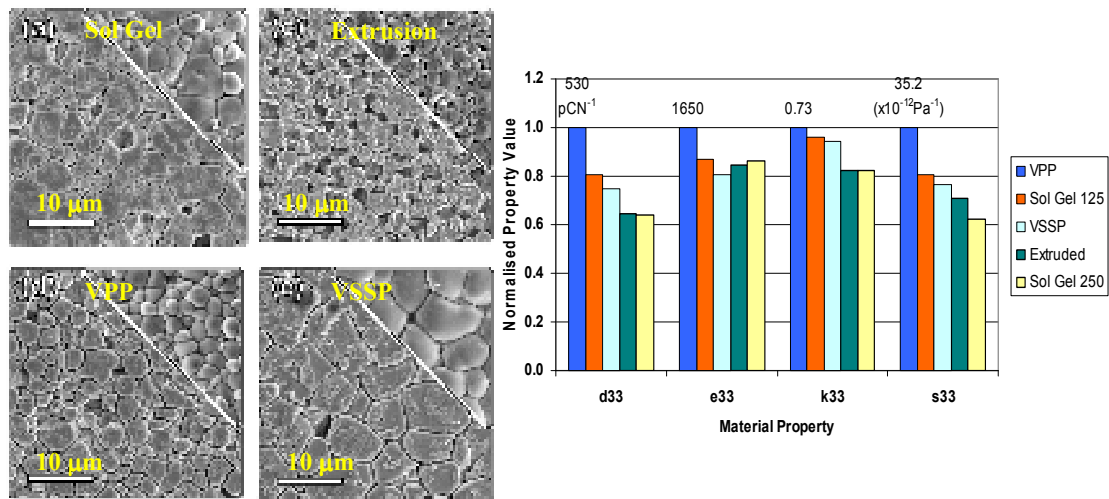


Figure 4. 5: Photographs of grain structure of PZT fibres from sol gel, extrusion, VPP and VSSP and corresponding piezoelectric properties (from Dent et al., 2005. Reprinted with permission© IEEE).

In this work, fibres were of diameter 350 μm . To make 1-3 composites from PZT fibres, the fibres were collected into bunches with the fibres positioned randomly and bonded together with a RX771/HY1300 polymer matrix (Robnor Resins, Swindon, UK) to form lengths of piezofibre-polymer composite material with 1-3 connectivity (Figure 4.6a). The lengths are sliced, lapped and polished to a suitable thickness for

ultrasound (Figure 4.6b). After poling, these are ready to be used as the piezocomposite component in an ultrasonic transducer.

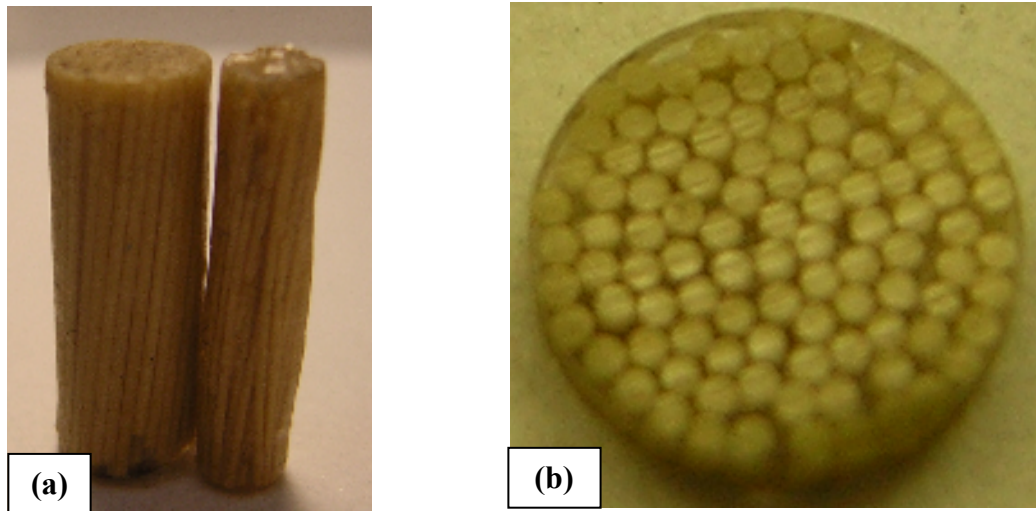


Figure 4. 6: Fibres composite after (a) collection of fibres into bunches, and (b) cutting into slices.

4.1.3. Fabrication of Micromoulded Piezocomposites

The most important material for the work for this thesis was piezocomposite made with micromoulded PZT. The piezocomposites in question were fabricated using a *lost mould* process to shape ceramic paste, made using the VPP process, into fine scale bristle blocks suitable for high frequency composite. The fabrication process for these composites is outlined in detail by Cochran et al. (2004). Due to the importance of micromoulded piezocomposites to the work for this thesis, a brief description is also given here. The lost mould composite fabrication process is shown diagrammatically in Figure 4.7.

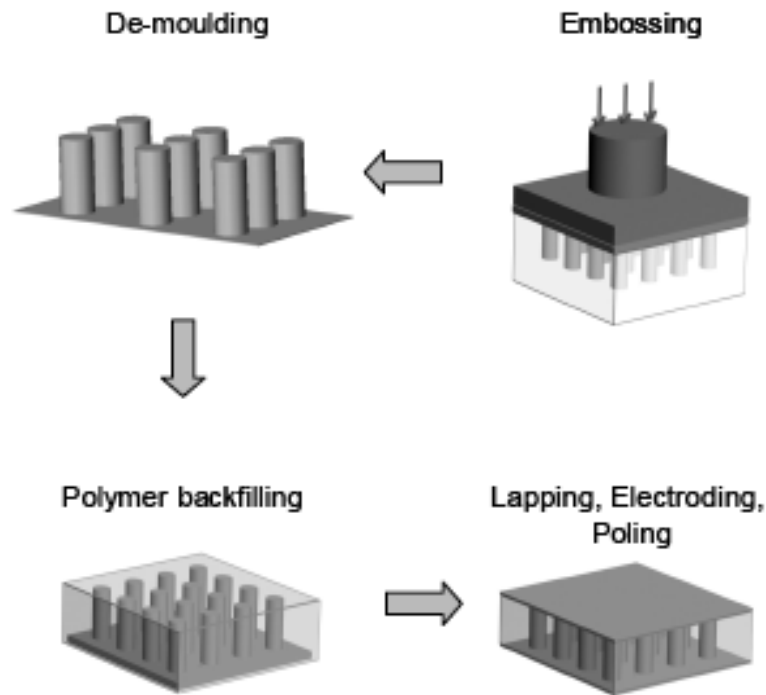


Figure 4. 7: Diagrams showing micro-moulding composite fabrication process (picture adapted from Cochran et al. (2004) © IEEE)

The procedure for production of MC begins with production of a green state ceramic sheet, formed using the VPP process described in Section 4.1.1. However, rather than sintering the ceramic at this point, it is embossed into a mould, with pillar shapes of suitable scale for high frequency composite manufacture, and dried. The mould used is then sacrificed. Chemical dissolution removes the mould, but as green state ceramic produced by VPP has high mechanical strength, the remaining pillar structure is not damaged. The pillar structure is now sintered in a lead rich environment. The ceramic structure is backfilled with polymer, generally RX771/CY1301 in the present work. This is then lapped to the desired thickness, electroded by deposition of gold, and poled to produce an active piezocomposite material suitable for incorporation into an ultrasound transducer.

4.2. Ultra Precision Grinding

As discussed previously in this thesis, piezocomposites are the material of choice in high performance transducers at standard medical frequencies, and the performance benefits of piezocomposites may also be realised in high frequency applications. Achieving the thin layers required for high frequency operation in piezocomposite is challenging, as layer thicknesses must be in the range 35 – 45 μm for a frequency of 50 MHz. Conventional lapping or grinding used in commercial piezocomposite fabrication is insufficiently precise for high frequency operation and is subject to undesirable intra-process variation.

1-3 connectivity piezocomposites incorporate two constituent materials, in this case PZT and polymer, which have differing mechanical properties. Typically, when conventional lapping and grinding processes are used, the pillars of the active ceramic or crystal material abrade faster than the polymer (Schmarje, 2005) as the polymer is more able to compress during the material removal process and subsequently to expand. This leads to height differences and physical discontinuities at the boundaries between the different phases and hence to an uneven surface, as shown schematically in Figure 4.8.

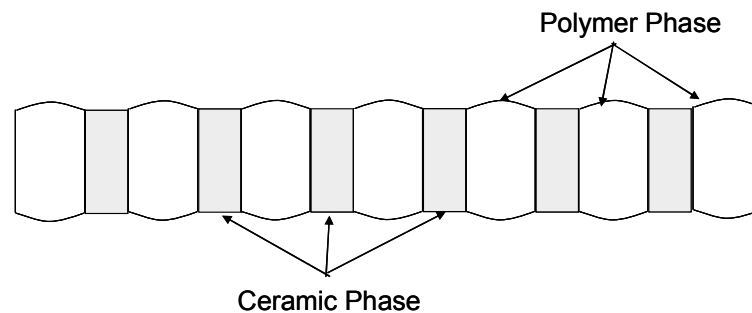


Figure 4. 8: Schematic diagram of piezocomposite material, indicating height difference between phases.

If lapping procedures are optimised, it is possible to produce surface finishes of sufficient quality for high frequency transducers, particularly when chemical processes are incorporated (Bernassau et al. 2007). However, it is slow and may be prohibitively expensive to produce large numbers of piezoelectric elements.

4.2.1. Background to Ultra Precision Grinding

A potential alternative procedure for production of piezoelectric active layers is *ultra precision grinding (UPG)*. This is a generic name given to surface finishing processes where a high quality finish is to be achieved on a fixed size sample. To test whether UPG could be used to produce high frequency active layers, UPG was carried out using a PicoAce NanoGrinder (Loadpoint, Cricklade, UK). The general arrangement of this machine is shown in Figure 4.9, including (a) the cup-wheel grinding spindle, (b) the rotary work table and (c) X- and Z-slideways mounted in a closed loop structure.

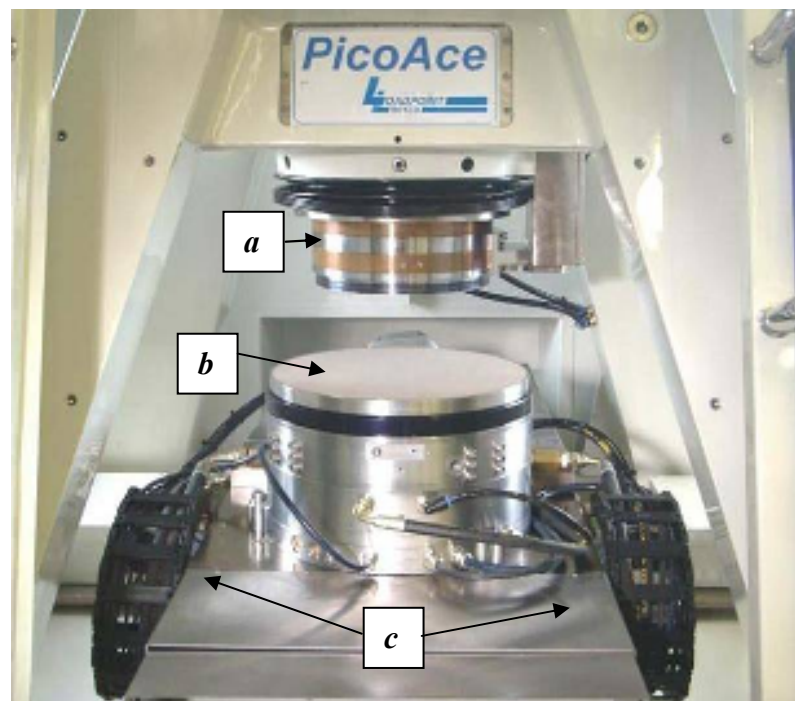


Figure 4. 9: Photograph of PicoAce process chamber (picture from Loadpoint, Cricklade, UK).

4.2.2. Piezocomposite Samples Tested with UPG

To test the capabilities of UPG in the processing of piezocomposites, 1-3 connectivity composite materials made with both electromechanically hard and soft piezoceramics were investigated after being thinned to approximately 50 μm . In both cases, the ceramic pillars were bound in RX771/HY1301 hard polymer matrices. The

first was a PZT 4D piezocomposite made with standard dice-and-fill methods. Two samples of MC were also investigated.

Two samples of PZT-4D piezocomposite and two samples of micromoulded composites were thinned. In each case one was prepared with standard precision lapping, using a PM5 lapping/polishing machine (Logitech, Glasgow, UK), and another with UPG using the Loadpoint PicoAce. The quality of surface finish produced by the two methods was then compared for both composite types.

4.3. Characterisation of passive materials

As well as active materials, passive material characterisation was studied for high frequency application. The modelling procedure used in the work for this thesis allowed the contribution of a passive material to a transducer structure to be assessed, whether this is a polymer matrix in a composite or a passive backing or matching layer. Knowledge of the following parameters was required: c_{33} , σ , ϵ_R , ρ and α , where σ is Poisson's ratio.

ρ is found by measuring the physical dimensions, i.e. thickness T and area A , and mass of the sample, as would be expected. ϵ_R is derived from the expression for a capacitor:

$$\epsilon_R = \frac{TC}{\epsilon_0 A} \quad 4.1$$

C can be measured directly using an impedance analyser. For this work, capacitance measurements of samples were undertaken using an Agilent 4294A Precision Impedance Analyzer with a contact jig, made in-house. The 4294A has a frequency range of 40 Hz – 110 MHz, and accuracy of $\pm 0.08\%$.

As described in Section 2.3.4, c_{33} and σ are calculated from measurements of longitudinal wave velocity, v_l , and transverse wave velocity, v_t . α is calculated from

measurements of transmission signal through the material. The methodology used to determine v_l , v_t , and α is described in the following sections. Isotropic material is assumed.

4.3.1. Measuring longitudinal and transverse wave velocities

Measurement of longitudinal and transverse wave velocities in passive material is done by measuring the time taken for an ultrasound wave, of each mode, to propagate through a known thickness of material. This can be done by placing two contact ultrasound transducers on opposing faces of the material and measuring the time between transmission of a pulse from the first transducer and reception of that pulse by the second. An alternative method, which was preferred in this work, is to immerse two transducers, operating in ‘through-transmission’ mode, in water. A sample of the material of interest is placed between them and the time taken to propagate through the sample is measured, as described in the next section.

4.3.2. Underwater through measurement

The underwater method of measuring transmission velocities does not require the transmitter and receiver to be in contact with a sample; they are in fact positioned facing opposite one another, a known distance, x , apart, with x greater than the sample thickness, T , as illustrated in Figure 4.10. Two measurements are then taken. Firstly, the time taken for an ultrasound pulse to propagate from the transmitter to the receiver is recorded with only water between, denoted here as the *reference measurement*, t_i . Secondly, the sample is placed in the gap between the transmitter and receiver and the propagation time (through water and the sample) is recorded again, denoted here as the *sample measurement* t_j . The difference between these two propagation times, Δt_i , can be used to calculate both longitudinal and transverse wave velocities in a sample, using the procedures now described.

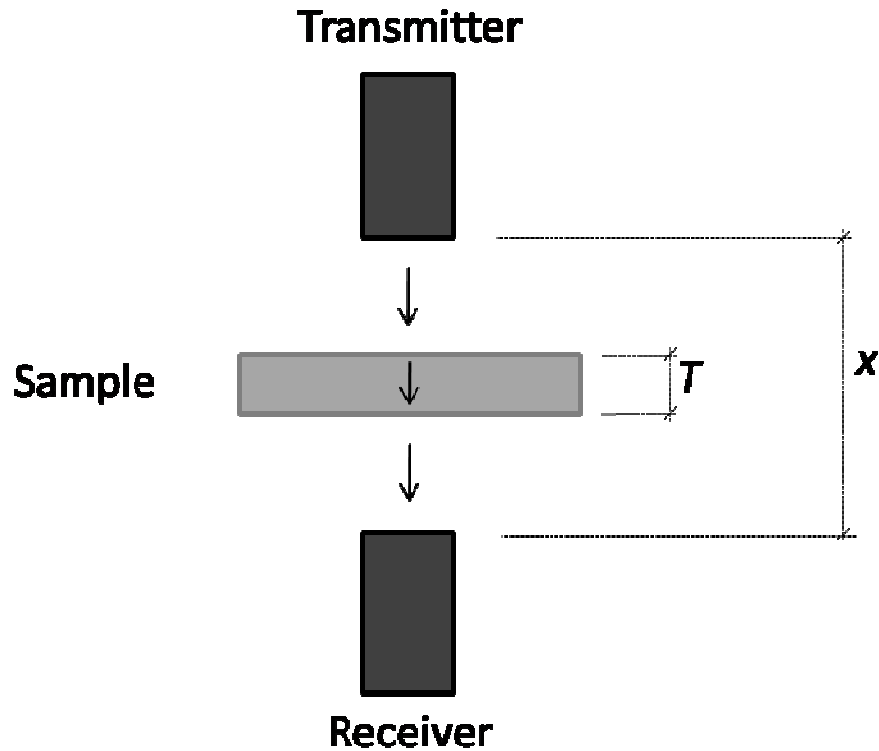


Figure 4. 10: Diagram showing through-transmission of ultrasound through a sample.

4.3.3. Taking a reference measurement

The transmitter and receiver are placed in a water bath and positioned facing one another, on the same axis, a known distance, x , apart. For the work of this thesis, the transmitter used was a prototype MC transducer, denoted AFMTH09, of centre frequency 36 MHz, -6dB bandwidth of 29 MHz, and f-number 3.8. AFMTH09 is described in detail in Section 6.4.1. The receiver was a 16 μm PVDF Membrane Hydrophone (Precision Acoustics, Dorchester, UK) with active element of diameter 0.4 mm and bandwidth 80 MHz.

The position of the receiver is adjusted to obtain the maximum signal from the transmitter, at which point it may be accepted that the active area of the receiver is aligned with the ultrasound beam. A measurement is taken of the time, t_i , for signals to travel between the transmitter and receiver. The velocity of sound in water, v_i , in the water bath may then be determined from:

$$v_i = \frac{x}{t_i} \quad 4.2$$

It is important to determine the propagation velocity of water initially, as it is subject to variation because of environmental conditions.

4.3.4. Measuring longitudinal wave velocity

To measure v_l , the sample is placed between the transmitter and receiver, without disturbing the position of either. Again, alignment is crucial. The sample must be of uniform thickness, and must be placed such that it is exactly perpendicular to the ultrasound beam. This can be checked by adjusting the sample until the received signal amplitude is maximised. The time, t_l , taken for the ultrasound signal to travel through the water and sample is now measured. If the thickness of the sample is known, v_l may be calculated using the equation:

$$v_l = \frac{T}{\left(\frac{T}{v_i}\right) - \Delta t_l} \quad 4.3$$

An alternative technique was proposed by Wu (1996). Time domain measurements are transformed to the frequency domain. Instead of Δt_l being the parameter of interest, the difference between the phase of the reference pulse, ϕ_r , and that of the sample pulse, ϕ_l , is now used to calculate longitudinal wave velocity using the expression:

$$v_l = \frac{v_i}{1 + v_i(\phi_l - \phi_r \pm 2n\pi)(2\pi fT)} \quad 4.4$$

where f is the frequency of interest, and n is an integer

Wu's method has a major advantage over time domain techniques in that velocity information may be calculated over a frequency band with only one measurement taken. Thus, velocity information at several frequencies can be generated by one measurement. The frequency range will be determined by the bandwidth of the transmitter and receiver.

4.3.5. Measuring Transverse Wave Velocity

Measurement of transverse wave velocity, v_t , uses a similar method. As described in Section 2.4, if a longitudinal wave, travelling in a liquid, is incident upon a liquid-solid boundary at a non-perpendicular angle, less than θ_c , mode conversion may lead to propagation of both longitudinal and transverse waves. Therefore the sample must be rotated with respect to the ultrasound beam (i.e. the axes of transmitter and receiver) as shown in Figure 4.11.

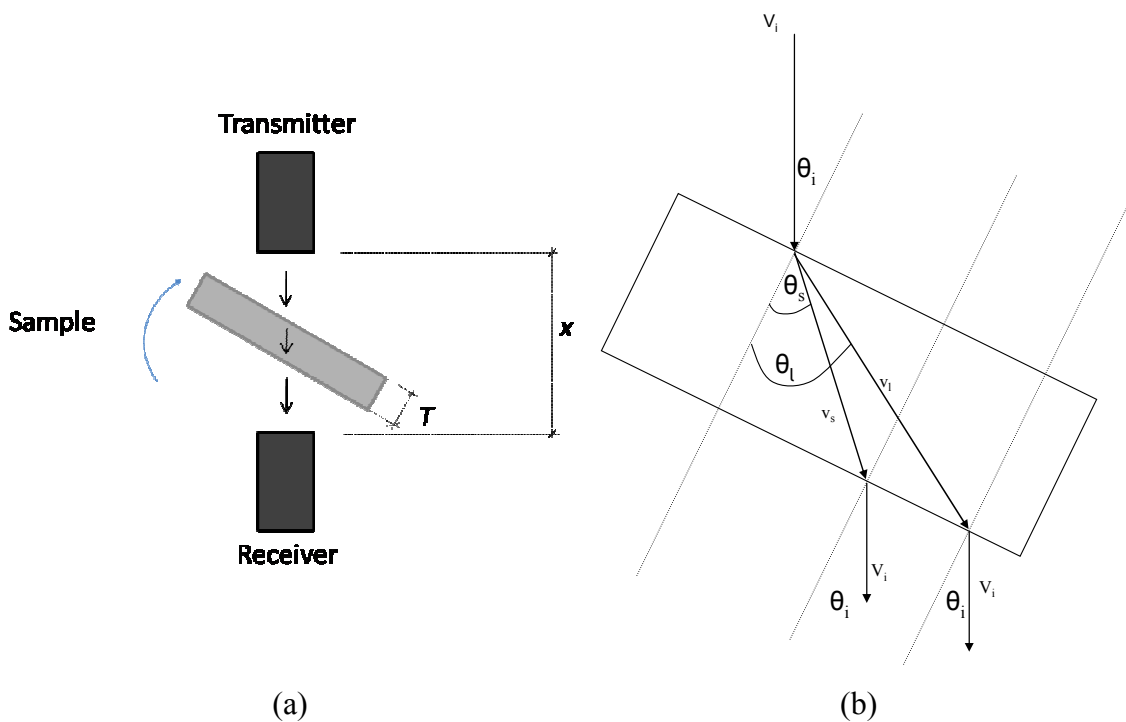


Figure 4. 11: (a) Schematic of experimental set-up and (b) paths resulting from beam incident on sample at non-perpendicular angle $\theta_i < \theta_c$.

This will result in transmission of both longitudinal and transverse waves through the sample, as shown in Figure 4.11. The time taken for the two waves to travel through the sample may then be measured. However, when the sample is rotated, the ultrasound beam is refracted when propagating through the sample. The distance travelled through the sample is therefore not known, so that a different expression is required to calculate transverse wave velocity, as reported by O’Leary (2003):

$$\Delta t_t = T \left[\frac{\cos \theta_i \sqrt{1 - \frac{v_t^2 \sin^2 \theta_i}{v_i^2}} + \frac{v_t \sin^2 \theta_i}{v_i}}{v_i \cos \theta_i} - \frac{1}{v_t \sqrt{1 - \frac{v_t^2 \sin^2 \theta_i}{v_i^2}}} \right] \quad 4.5$$

In this case there are two unknowns, Δt_t , the difference between reference, t_i , and sample, t_t , signal arrival times, and v_t . Transverse wave velocity is determined by progressive estimation of v_t , which is then fitted to measurements of Δt . This can be done easily with a simple computer algorithm. This method gives reliable results and has the advantage of being relatively straightforward. If Δt is measured at a variety of incident angles, then curve fitting can be used to minimise the error in the value of v_t calculated.

Wu (1996) also described a method of determining transverse wave velocity from measurements of phase difference, in this case using the equation:

$$v_t = \frac{v_i}{\sqrt{\sin^2 \theta_i + \left[\frac{(\phi_s - \phi_i \pm 2n\pi)v_i}{2\pi f T} + \cos \theta_i \right]^2}} \quad 4.6$$

where θ_i is the incident angle of the ultrasound beam.

This expression can be modified to work in the time domain. If one substitutes:

$$-\Delta t = \frac{(\phi_s - \phi_w \pm 2n\pi)}{2\pi f} \quad 4.7$$

into Equation 4.6, the expression for v_i may be re-written as:

$$v_i = \frac{v_i}{\sqrt{\sin^2 \theta_i + \left[\frac{-\Delta t v_i}{T} + \cos \theta_i \right]^2}} \quad 4.8$$

Errors in these measurements may occur from transducer misalignment, sample shape and signal detection. Issues with transmitter and receiver alignment are more prevalent at high frequencies where wavelengths are particularly small. To minimise this as far as practicable, a bespoke high frequency ultrasonic characterisation jig was constructed using optics instrumentation, including precision micrometers and goniometers and a planar spirit level. The jig is described in detail in Section 4.4. In all cases the transducer position was adjusted to achieve the maximum signal at the receiver, indicating the transducer is well aligned. When samples are rotated the path of the ultrasonic wave will change: the characterisation jig allows the relative positions of the transmitter and receiver to be adjusted to ensure maximised signals are recorded.

Sample thickness is measured using a precision micrometer (Mitutoyo Digimatic, Mitutoyo, Andover UK), with accuracy of $\pm 1 \mu\text{m}$. To ensure samples are of uniform thickness they are prepared using a precision lapping machine (Logitech PM 5, Logitech Ltd, Glasgow, UK). The temporal resolution of the oscilloscope used to collect arrival time data is 0.5 ns.

Using contact techniques rather than immersion techniques can reduce the likelihood of transducer misalignment, but it was not possible to do this with the prototype transducers used for the work described here, as they did not have contact wear plate front layers and could have been damaged by contact with samples.

4.3.6. Cross correlation

Where time domain techniques are used, values for t_i , t_l and t_r may be found simply by inspecting received pulses on an oscilloscope, and noting the arrival time of each pulse. Δt is then found by taking the difference between t_i , and t_l or t_r . An example of the difference between reference and sample signals is shown in Figure 4.12. Figure 4.12 shows a recorded reference signal, i.e. a signal from transmitter to a receiver through water. Figure 4.12 also shows the signal recorded after a 500 μm thick sample of aluminium is placed between the transmitter and receiver. As aluminium is of faster propagation velocity than water, the sample pulse is received earlier. As a large proportion of energy is reflected at the boundaries between aluminium and water, the recorded signal is of smaller amplitude.

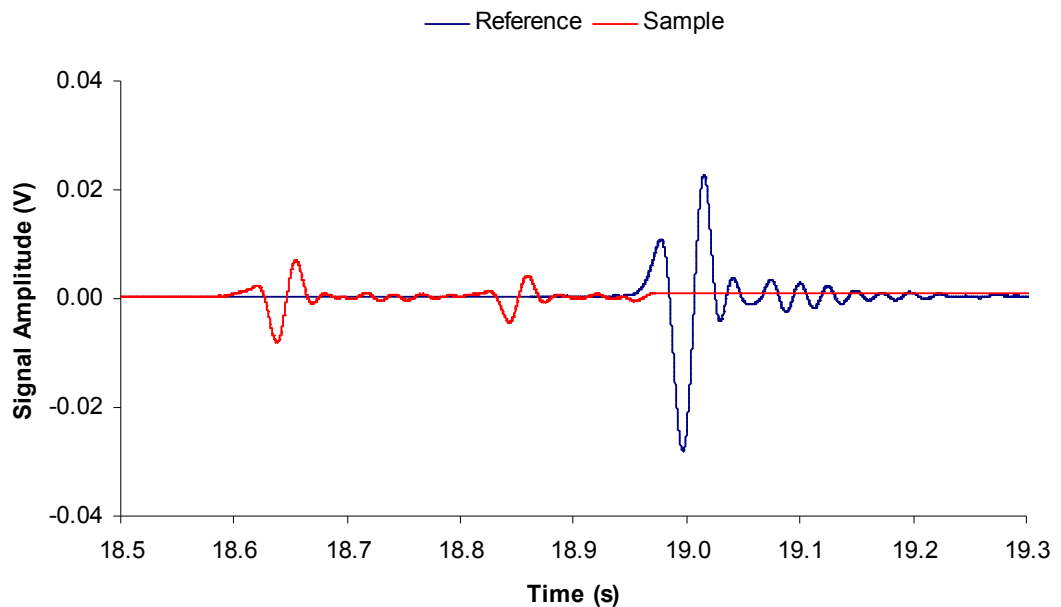


Figure 4. 12: Diagram showing ‘reference’ signal and ‘sample’ signal, for a sample of aluminium.

Pulse shapes are subject to change when travelling through highly attenuative material, for example epoxies, which can cause errors when attempting to compare reference and sample measurements. A more reliable and accurate method for determination of Δt is to record the entire received pulse from both reference and

sample measurements and use *cross correlation* to compare reference measurements with sample measurements mathematically (O’Leary, 2003).

Cross correlation involves the following steps: both reference and sample measurements are subjected to a Hilbert transform to find the envelope of the received pulse. They are then normalised and compared using the MATLAB function *xcorr*. The *xcorr* function treats the two pulse envelopes as matrices of dimensions $1 \times n$, e.g. $[a_1 \ a_2 \ \dots \ a_n]$ and $[b_1 \ b_2 \ \dots \ b_n]$. The sum of the product of these matrices is calculated, i.e. $a_1.b_1 + a_2.b_2 + \dots + a_n.b_n$. The matrices are then adjusted with respect to one another by one index step and the sum of their products calculated again: i.e. the sum becomes $a_1.b_2 + a_2.b_3 + \dots + a_n.0$ (or $a_1.0 + a_2.b_1 + \dots + a_n.b_{n-1}$). This procedure is repeated until all combinations are exhausted. The matrices are adjusted by a number of indices, i , until the point at which the two measurements maximally coincide. One index step is equivalent to $1/f_s$ where f_s is the sampling frequency of the reference and sample measurements. The time difference, Δt , between the reference arrival time t_r and the sample arrival time, t_l or t_i is therefore:

$$\Delta t = \frac{n_d}{f_s} \quad 4.9$$

where n_d is the number of discretisation points.

4.3.7. Measuring Attenuation

The attenuation coefficient of a material also has a significant effect on its behaviour. A highly attenuative material will absorb energy readily. This means that large amounts of energy will have to be output to detect reflections from deep within the structure to image such a material in pulse-echo mode. The attenuation coefficients of a transducer’s constituent materials also affect the performance of that transducer, and this is used to optimise the transducer design. For example, using a highly attenuative backing material reduces the risk of internal reflections propagating within the transducer. The attenuation coefficient can also be determined from the through-transmission measurements described previously.

Longitudinal Wave Attenuation

The attenuation coefficient of water is known to be $0.0022 \text{ dBMHz}^{-1}\text{cm}^{-1}$ (Hedrick et al., 1995) so as with velocity, attenuation is calculated using comparison of transmitted pulses through water and through a sample. Using time domain techniques, the amplitude of the ‘sample’ pulse, A_s is directly compared to the amplitude of the received reference pulse, A_w , to obtain a value for the attenuation coefficient, α_l . The transmission coefficient, T , for the water/material boundary is also taken into account, giving the expression:

$$\alpha_l = \frac{\ln\left(\frac{T^2 A_w}{A}\right)}{d} \quad 4.10$$

where $T = \frac{4Z_w Z_l}{(Z_w + Z_l)^2}$, $Z_w = \rho_w v_w$ and $Z_l = \rho_s v_l$.

Z_w and Z_l are the acoustic impedances of water and the sample respectively and ρ_w and ρ_s the densities of the water and sample respectively.

A frequency domain method for calculating attenuation is also described by Wu (2003). In this case, the amplitudes of the frequency spectra are compared. If A_w and A_s are the amplitudes of the spectra from reference and sample pulses respectively, and α_w is the attenuation coefficient of water, the longitudinal wave attenuation coefficient of the sample, α_l , may be calculated using:

$$\alpha_l = \alpha_w + \frac{\ln\left(\frac{T_l A_w}{A_s}\right)}{T} \quad 4.11$$

4.4. Design and fabrication of materials testing jig

Measuring transmission velocity of ultrasound at high frequency is difficult. Due to the very small wavelengths involved, physical misalignment between transmitter,

sample and receiver greatly compromises any measurement. As such, there is very little reported in the literature on the velocity of sound in materials at high frequency. Information on attenuation coefficients of passive materials is rare at conventional ultrasound frequencies, and virtually non-existent at high frequency. To surmount these problems, a high frequency measurement jig was designed and fabricated. Certain design criteria were noted:

- The jig had to align the transmitter, sample and receiver very precisely with respect to one another, so the positions of all three needed to be adjustable
- The jig had to incorporate a transducer as transmitter and either a transducer or a membrane hydrophone as receiver.
- The sample needed to be rotated precisely, with respect to the transmitter and receiver.
- The sound wave is refracted when the sample is rotated. The transmitter therefore needed to be able to move such that the sound beam remains directly incident on the receiver.
- As many of the transducers to be used as transmitters in these measurements were made using experimental fabrication procedures, misalignment of the element with respect to the transducer barrel was possible. The jig had to allow compensation for this.
- High frequency waves are also highly attenuated so distances between transmitter and receiver needed to be small.
- Samples needed to be thin, in order that attenuation was not prohibitively high to allow through-transmission measurements. However, they should also be sufficiently thick that internal reflections within the sample do not cause received pulses to be distorted. This dictates that:

$$\text{sample thickness} > \frac{1}{2} t_p v_l$$

where t_p is pulse length.

- The jig will be almost entirely submerged in water so needed to be made from a material resistant to corrosion.

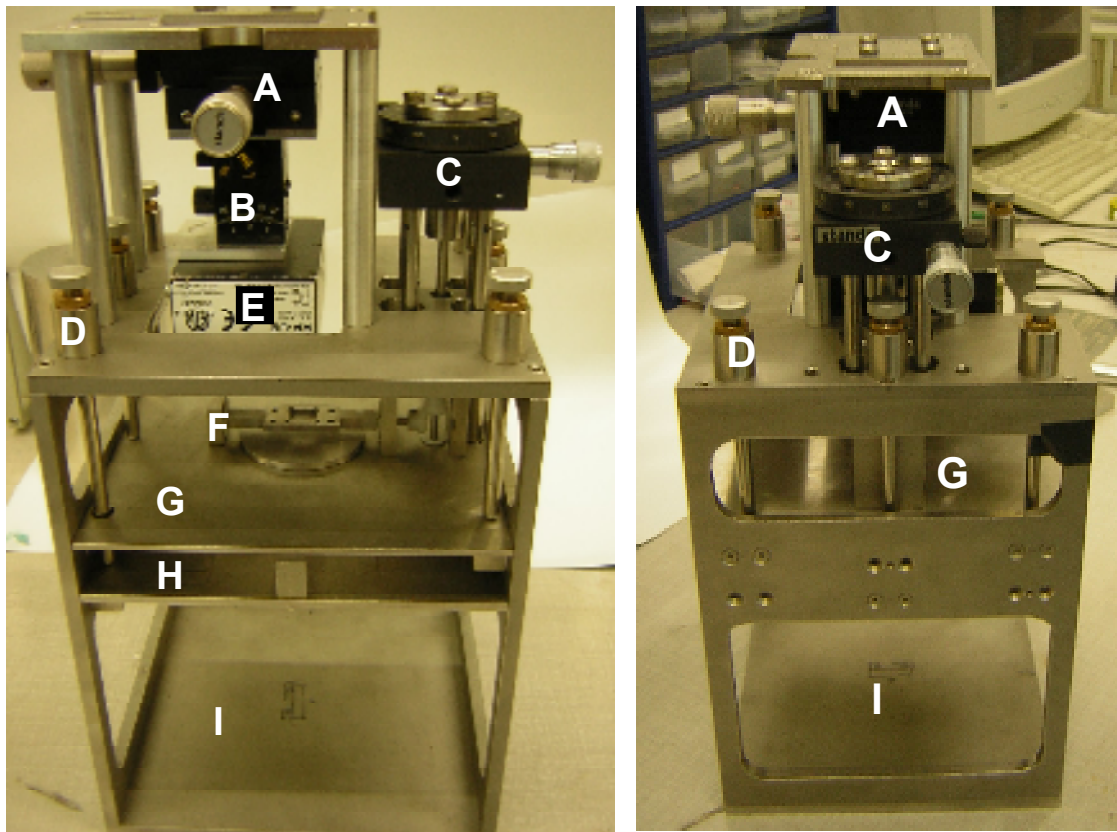


Figure 4.13: Photographs of jig showing front view, with labels described below, and side view.

The final design of the jig to meet these requirements is shown in Figure 4.13. The labels A-I correspond to the following parts:

A: X-Y optical stages (Standa, Vilnius, Lithuania), to allow initial alignment of transmitter and receiver and movement to account for refraction of the ultrasound beam after sample rotation

B: Goniometer (Melles Griot, Cambridge, UK), to adjust the angle of the transmitter in *pitch* and *yaw*

C: Optical rotation stage (Standa, Vilnius, Lithuania), to precisely rotate the sample when required.

D: Fine-pitch lead screws (Standa, Vilnius, Lithuania) Three are attached to the sample holder and receiver holder. These can be adjusted to ensure correct alignment.

E: Remote pulser receiver box, with transmitter attached

F: Sample holder, which can be rotated perpendicular to the plane of the sample with respect to transmitter and receiver. This is controlled by the optical rotation stage (C).

G: Platform for sample holder. This also doubles as a protective cover for the hydrophone, with only a small hole in the centre to allow transmission of ultrasound. When not in use, a removable cover is put in place to protect the hydrophone from accidental damage. Aligned by three fine pitch lead screws (D)

H: Platform for hydrophone, also aligned by three lead screws (D)

I: Base. There is a large gap between the platforms and base to reduce influence of reflections from bottom of jig or water tank floor. Acoustic absorber may be placed here to reduce reflections further.

Procedure for use of materials testing jig

The following procedure assumes a prototype high frequency transducer (Applied Functional Materials, Birmingham, UK) is used as transmitter and a membrane hydrophone is used as receiver.

Step 1: Sample Preparation

Samples are cut to size 1 cm x 1 cm, to fit in the sample holder, and lapped to a uniform thickness. Thickness is dependent on the material itself, as described previously. For example, epoxies have longitudinal wave propagation velocity of up to 3000 ms^{-1} . The transducer used in this case had a pulse length of approx $0.2 \mu\text{s}$, therefore thickness $> 300 \mu\text{m}$ is suitable.

Step 2: Alignment of transducer, sample holder and receiver

Before putting the sample in the sample holder, Platforms G and H are adjusted, using the lead screws and referring to a spirit level, until they are exactly planar with one another. This ensures that any tilting of the bench on which the jig is placed does not affect the jig. The hydrophone (or other receiver) and transducer are then put into place and the jig is submerged in water.

Alignment of the transducer must first be undertaken in pitch and yaw with respect to platforms G and H. This is done by leaving the removable cover in place, operating the transmitter in pulse-echo-mode and observing echoes from the cover. When the transducer is accurately aligned to the sample cover in pitch and yaw (and hence to platforms G and H), the received echo will have maximum amplitude and minimum pulse length.

Once satisfactory pitch and yaw alignment are achieved, the transducer beam must be well aligned with the active area of the hydrophone in the x and y directions. This is done by observing a pulse received by the hydrophone, from the transducer. Again, when the received pulse is maximised in amplitude the transducer beam can be assumed to be directly incident on the hydrophone active area.

Step 3: Reference measurement

At this point, a reference pulse measurement must be taken with no sample in place. This serves two purposes as described previously: measurement of pulse arrival time with no sample in place, t_i , and calibration of the water velocity.

Step 3a: 'With sample' measurements

After a reference measurement has been taken, the sample is placed in the sample holder (F). At this point it is important to ensure that the sample is aligned such that it is exactly normal to the ultrasound beam propagating through it. This can be done by once again observing the pulse received by the hydrophone and adjusting the sample holder until it is of maximum amplitude.

When satisfactory alignment of the sample normal to the ultrasound beam has been achieved, the time taken for the ultrasound beam to propagate through the water and sample, t_l , can be measured. At this point, only longitudinal waves will propagate through the sample, and longitudinal wave propagation velocity may be calculated using Equation 4.3.

Step 3b: 'With sample' measurements: non-normal incidence of beam

The next step is to rotate the sample with respect to the ultrasound beam as outlined above. The material characterisation jig includes an optical rotation stage for this purpose, which allows the sample to be precisely rotated by small increments with respect to the ultrasound beam. Recordings of the received pulse are taken over a range of angles.

As the sample is rotated, mode conversion will lead to two separate pulses being received by the hydrophone: one due to longitudinal waves and one due to transverse waves. The amplitude of the longitudinal wave signal will diminish, eventually disappearing at the longitudinal wave critical angle, θ_{cl} , as described in Section 2.4. Simultaneously, the amplitude of the transverse wave signal will increase, before diminishing rapidly to zero at θ_{cl} , then increasing once again before diminishing to zero at the transverse critical angle, θ_{ct} . At this point enough information is available to determine v_t from Equation 4.8. Figure 4.14 shows an example of this behaviour, for an aluminium sample.

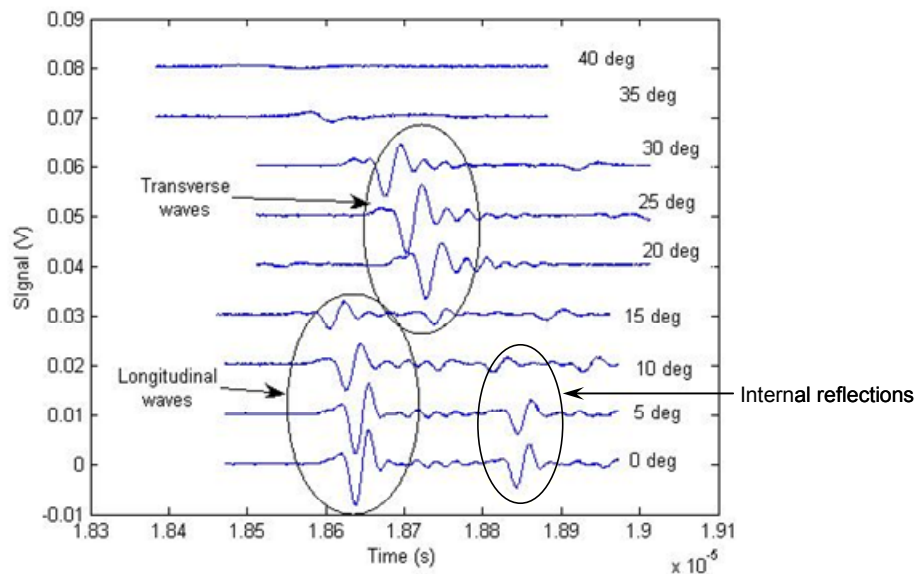


Figure 4. 14: Graphs showing influence of incident angle on transmitted signal amplitude. Note voltage has been offset for clarity on individual plots. Voltages shown are relative.

In each case the arrival time of the pulse is important for calculating longitudinal and transverse wave velocity, and the amplitude of the received pulses is also important as this is used to calculate longitudinal and transverse wave attenuation coefficients for the material.

As noted previously, refraction of the wave means that the transducer position should be adjusted to align the ultrasound beam correctly with the active area of the hydrophone. This is done by adjusting the x-y stage to maximise the amplitude of the received signal as before. As the longitudinal and transverse waves follow different paths through the sample, the position of the transducer has to be adjusted twice to maximise both pulses, with separate recordings of the received signal.

4.5. Experimental Characterisation of Active Materials

When characterising active materials, a range of fundamental material parameters was determined to provide indicators of the mechanical, electrical and piezoelectric properties of the material, and allow modelling of the material to verify data. These are listed in Table 4.1:

TABLE 4. 1: MECHANICAL, ELECTRICAL AND PIEZOELECTRIC PROPERTIES DETERMINED FOR PIEZOELECTRIC SAMPLES

Parameter	Symbol
Density	ρ
Longitudinal propagation speed	v_l
Acoustic impedance	Z
Stiffness at constant electric displacement	c_{33}^D
Stiffness at constant electric field	c_{33}^E
Relative permittivity at constant stress	ϵ_R^T
Relative permittivity at constant strain	ϵ_R^S
Piezoelectric stress constant	e_{33}
Piezoelectric stiffness constant	h_{33}
Piezoelectric modulus	d_{33}
Electromechanical coupling coefficient	k_T
Attenuation coefficient	α

To determine the material properties outlined in Table 4.1 for a given sample, one first measures physical properties of the sample: i.e. width and length, thickness, and mass. All of the subsequent data may be obtained from electrical impedance spectroscopy.

Impedance measurements of samples were undertaken using an Agilent 4294A Precision Impedance Analyzer with a contact jig, made in-house. These are shown in Figure 4.15. For each sample, impedance magnitude and phase, resistance and

reactance, and parallel capacitance and susceptance were measured. The frequency range chosen was generally at least $2f_a$, and greater than $3f_a$ where possible, to show 3rd harmonic resonance data, where f_a is the anti-resonant or mechanical resonant frequency. The Agilent 4294A has a measurement range of 40 Hz to 110 MHz: this dictated what could be measured. A measurement of capacitance is also taken at 1 kHz and $2f_a$. The following data is then entered into a spreadsheet, as shown in Appendix A: device area, thickness and mass, electrical and mechanical resonant frequencies, and capacitance at 1 kHz and $2f_a$. From this, the complete set of piezoelectric properties required for a one dimensional model may be calculated.

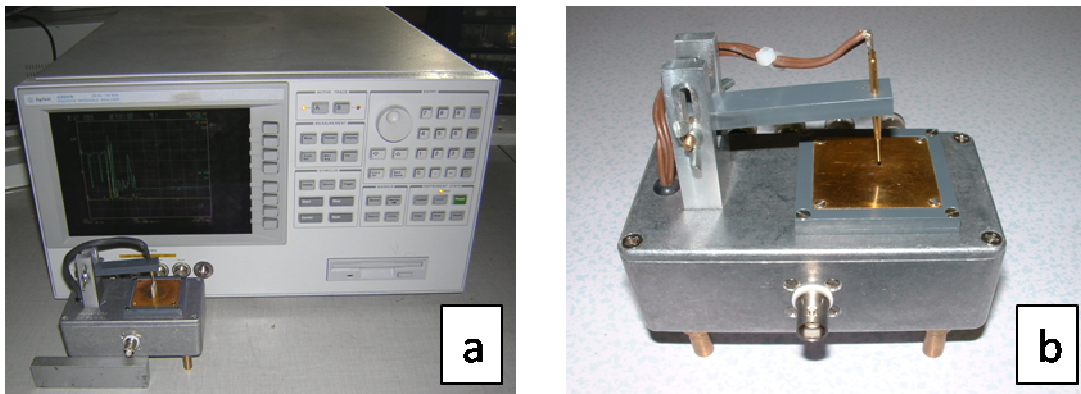


Figure 4. 15: Photographs of (a) Agilent 4294A impedance analyser and (b) fixture used for testing of bare piezoelectric materials

Where possible, pulse echo measurements were also taken from the bare composite samples, using the set-up shown in Figure 4.16. The sample was placed on a 1 cm thick stainless steel block, which was electrically grounded. A signal pin, connected to a DPR500 Pulser Receiver (JSR, Pittsford, NY, USA) with remote pulser, was used to excite the sample and amplify any received echoes from the back face of the steel block, which were recorded on an Agilent 54641A digital oscilloscope (Agilent Technologies, South Queensferry, UK). Ultrasound transmission gel was used to ensure good contact between the steel block and samples.

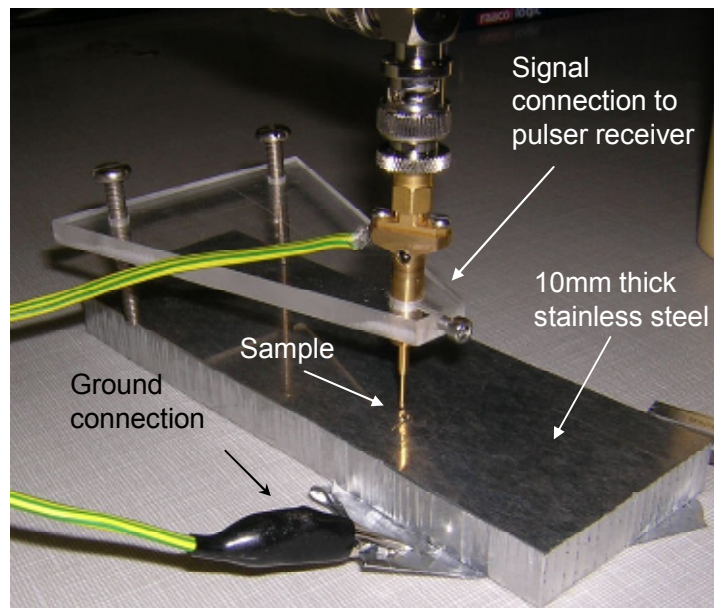


Figure 4. 16: Pulse echo measurement set-up for bare composite samples.

4.6. Piezoelectric Modelling Techniques

A number of modelling methodologies may be used for piezoelectric materials. Three common ones are the Mason equivalent circuit, the KLM model and linear systems modelling (LSM). Some aspects of modelling methodologies are now considered briefly.

4.6.1. Mason equivalent circuit

To bypass the complexities of finding solutions to the wave equation for piezoelectric materials analytically, Mason designed an equivalent circuit which represented, in a purely electrical form, the one-dimensional case and could be solved using network theory. A piezoelectric material is represented as two acoustic ports and one electrical port, with the acoustic ports in turn represented by an ideal electromechanical transformer (Berlincourt et al., 1964). Thus the circuit is described completely in terms of electrical components, with mechanical terms represented by electrical terms such as impedance or admittance. This is demonstrated by the diagram of the Mason equivalent circuit shown in Figure 4.17.

For the acoustic ports of the equivalent circuits, 1 V represents unit force and 1 A represents unit velocity. In this figure, F_1 and F_2 represent the forces exerted on the transducer by adjacent media, U_1 and U_2 the particle velocities, I and V the current and potential applied, respectively, and w , l and t the width, length and thickness of the transducer respectively. The direction of poling is represented by x_3 .

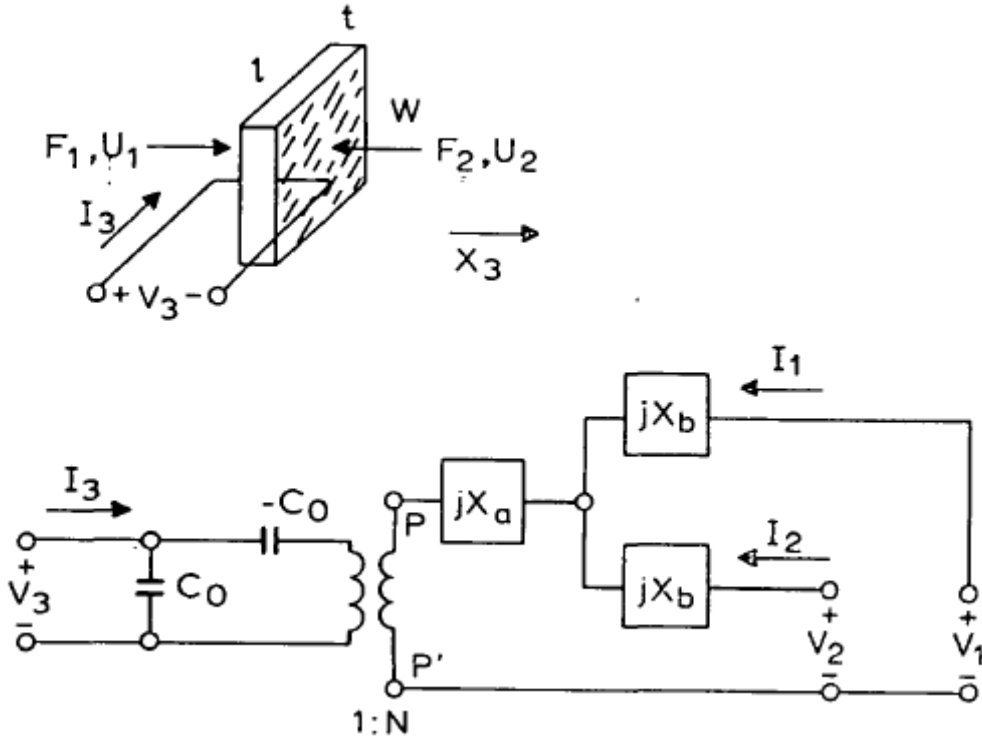


Figure 4. 17: Mason's equivalent circuit for thickness expander plate (from Krimholtz et al., 1970 © IET).

This is associated with the following expressions for the components shown in Figure 4.17:

$$C_0 = \frac{lw}{\beta_{11}^s t} \quad 4.12$$

$$N = C_0 h_{33} \quad 4.13$$

$$X_a = -Z_0 \cos ec \left(\frac{t\omega}{v_t^D} \right) \quad 4.14$$

$$X_b = -Z_0 \tan\left(\frac{t\omega}{2v_t^D}\right) \quad 4.15$$

$$v_t^D = \sqrt{\frac{c_{33}^D}{\rho}} \quad 4.16$$

where characteristic impedance, Z_0 , is given by:

$$Z_0 = \rho l w v_t^D \quad 4.17$$

and ω is the angular frequency, v_t^D is the acoustic wave velocity, C_0 is capacitance, jX complex impedance, β is the dielectric impermeability and N the ratio of turns of the transformer. Z_0 is the characteristic impedance associated with the acoustic transmission line of length l equal to the transducer dimension in the direction of wave propagation.

The Mason equivalent circuit, may be further simplified for an unloaded piezoelectric element as an RLC circuit in parallel with a further capacitor (Mason, 1964), as shown in Figure 4.18. It should be noted that this is only valid around the resonant and anti-resonant frequencies.

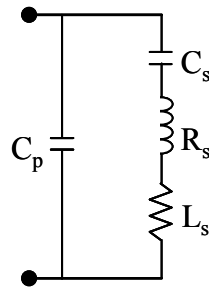


Figure 4. 18: Equivalent circuit of a piezoelectric element, showing an RLC circuit in parallel with a capacitor

4.6.2. KLM model

The Mason equivalent circuits were generally regarded to be flawed in that they required a negative capacitance at the electrical port of the circuit, as shown in Figure 4.18. Krimholtz, Lee and Matthaei (1970) designed alternative circuits for piezoelectric transducers, also in the form of thickness-expander plates, end-electroded bars and side-electroded bars, which could incorporate the effects of acoustic transmission lines. The model for the thickness-expander plate has since become more commonly known as the *KLM model* and has been used to design HFUS transducers for medical imaging (Foster et al., 1991; Zipparo et al., 1997). The KLM equivalent circuit for a thickness expander plate is shown in Figure 4.19.

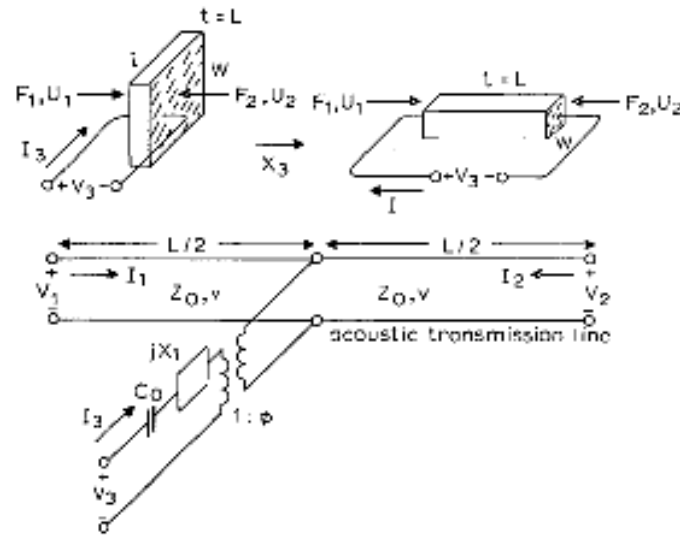


Figure 4. 19: KLM equivalent circuit for a plate in thickness mode. This also applies to a bar geometry (from Krimholtz et al., 1970. © IET).

In this case, the corresponding equations are as follows:

$$C_0 = \frac{lw}{\beta_{11}^S t} \quad 4.18$$

$$v = v_t^D = \sqrt{\frac{c_{33}^D}{\rho}} \quad 4.19$$

$$Z_0 = \rho l w v_t^D \quad 4.20$$

$$\phi = \left(\frac{1}{2M} \right) \cos ec \left(\frac{t\omega}{2v_t^D} \right) \quad 4.21$$

$$X_1 = Z_0 M^2 \sin \left(\frac{t\omega}{v_t^D} \right) \quad 4.22$$

where

$$M = \frac{h_{33}}{\omega Z_0} \quad 4.23$$

for angular frequency, ω .

4.6.3. Linear systems modelling

Jackson and Hayward (1983) devised a modelling system for piezoelectric transducers using *linear system theory*, where mathematical problems are simplified by treating properties of the system as linear. It is also a 3-port model and uses much of the same mathematical approaches as Powell et al. (1998) described in the next section. However, the approach of Jackson and Hayward was designed to provide greater intuitive insight into the mechanisms causing secondary effects (e.g. the electrical stimulation caused by the mechanical response to an initial electrical excitation and vice versa) than can be found using other modelling approaches. Voltage-charge feedback is used to model the secondary actions of the transducer. The transmission and reception cases are considered separately.

In transmission, the transducer will be subjected to no incident force, only an applied voltage which will generate internal forces. Secondary effects are then produced because the internal forces generate a voltage across the transducer, and modify the total charge in the structure. The converse is true in reception, where no external voltage is applied, but a voltage will be generated by the internal forces experienced by the transducer structure. From this, further internal forces will be generated: i.e. secondary effects. A series of ‘feedback loops’ is incorporated into the model, to include secondary effects in final calculations.

Both mechanical and electrical secondary effects are present in the general three-port case, and incorporated into the model. A diagram of these is given in Figure 4.20, showing the front and rear acoustic ports and the electrical port, and the relevant feedback loops. The model can be extended for multilayer structures, but analysis becomes more complex as reverberations from additional layers are incorporated.

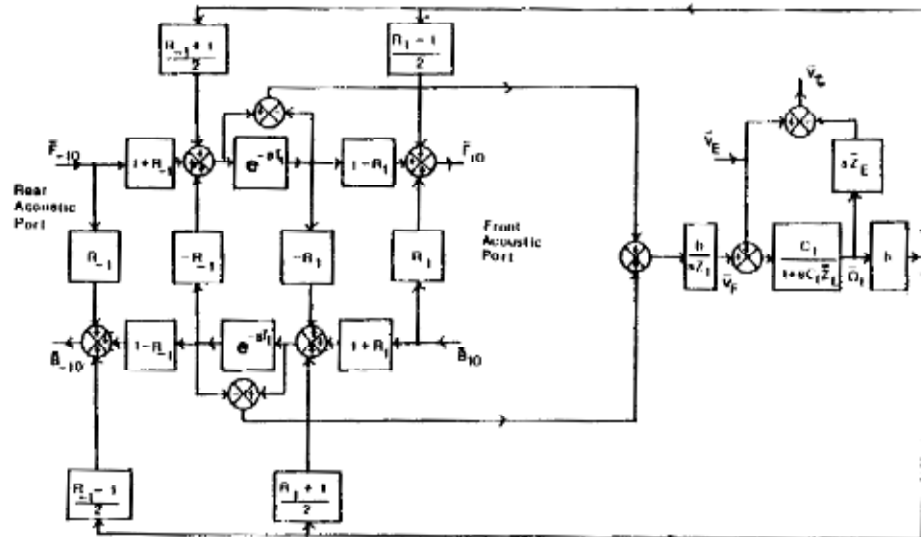


Figure 4. 20: 3 port model devised by Jackson and Hayward (from Jackson & Hayward, 1984. © IEEE).

Comparisons such as that of Sherrit et al. (1999) have shown that the various approaches lead to similar solutions, and have equal validity.

4.7. Simulation using One Dimensional Modelling

The Mason and KLM models have their basis in electrical engineering theory, while LSM has its basis in systems engineering and electronics. These methodologies were developed to remove the need to use lengthy repeated calculations when generating data on transducer performance. For example, the KLM modelling methodology is incorporated into commercially available PiezoCAD software (Sonic Concept Inc., Woodinville, WA). However, using these models requires understanding of electrical engineering concepts. The approach of the work for this thesis was more based in

physics theory, and as such a modelling approach less abstract from physical reality was considered more appropriate. Physical models are available, based on well established mathematics (Powell et al, 1998; Smith and Auld, 1991), that generate equivalent data to the other modelling techniques discussed above. The potential difficulties of undertaking repeated calculations were overcome by incorporating the physical model into a software modelling package for ultrasonic transducers, known as *ODM* (Cochran, Internal report, University of Strathclyde, 1997) which generates solutions to piezoelectric equations iteratively.

This program takes user-input transducer parameters including element dimensions and material properties and performs mathematical operations based on solving the 1D wave equation to produce simulations both of electrical output, in particular electrical impedance spectra, and also acoustic output, such as pressure. The multilayer transducer is the key technical structure of *ODM*. The mathematical approach to modelling such structures is based on the work of Powell et al. (1998). Each layer can be passive or active, and active layers can be piezoceramic, piezocomposite or piezopolymer.

Physical Properties of the Transducers

The shape (circular or rectangular) and lateral dimensions (width and length) are defined for the transducer structure as a whole. The characteristics of the individual layers are then defined: the thickness of each layer is specified, followed by piezoelectric properties of the material from which it is made. In the case of piezocomposites, the material properties for both active and passive phases of the composite are input and, treating the layer as a homogenised medium, effective properties of the composite are calculated, as described by Smith and Auld (1991). This is discussed further in this section.

Electrical and Acoustic Definitions

The acoustic connections between layers are defined by the ordering of the layers themselves. In the case of the front and back faces of the transducer, acoustic loading conditions are defined. Mechanical inputs for both faces must also be defined. In the

case of modelling transmission, these will be zero. For modelling of reception, these will be descriptions of transient inputs, or zero.

The electrical connections within the transducer may also be defined when preparing the model. Only active layers can be connected to an electrical circuit. Layers may be connected in a combination of parallel or series configurations, as specified by the user.

Mathematical Principles of ODM

The mathematical principles of ODM are based on multilayer transducers. More information can be found in Powell et al. (1998), but the main points are discussed below due to the importance to this thesis.

The approach of Powell et al. (1998) produces a system of equations which may be solved to describe the forces present within each layer, and the radiated force from the front and back layers of the complete transducer structure. Loading effects of external circuitry may also be included to improve the validity of the model. It is always assumed that lateral dimensions of the transducer are much greater than the thickness dimension.

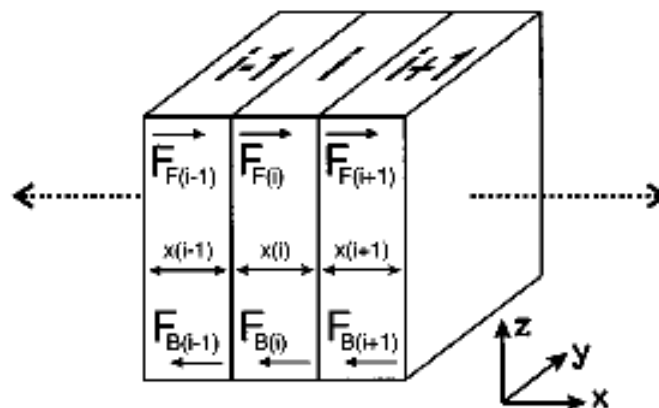


Figure 4. 21: Layered structure as used in ODM (from Powell et al. (1998) © IEEE).

A layered structure, such as that shown in Figure 4.21 is assumed. The behaviour of any layer will be governed not only by the electrical and mechanical stimuli of that

layer, but also by the electromechanical behaviour of neighbouring layers. The structures modelled for the work described in this thesis contained only one active layer. However, passive layers will impart mechanical loading, which must be considered.

Powell et al. (1998) described the behaviour of a layered structure in terms of force and voltage.

Force

Consideration of this multi-layered approach starts with the constitutive equations, as discussed in Section 2.6, namely:

$$T = c^D S - hD \quad 4.24 \quad E = -hS + \frac{D}{\epsilon^S} \quad 4.25$$

Hooke's Law states that $T = cS$ and S may be expressed in the form $S = \frac{\partial \xi}{\partial x}$, where x is layer thickness and ξ is the particle displacement. Hence:

$$T = c \frac{\partial \xi}{\partial x} \quad 4.26$$

$T = \frac{F}{A}$ for a given force, F , and area, A . From Newton's Second Law, $F = ma$ for mass, m , and acceleration, a . Thus:

$$T = \frac{ma}{A} = \left(\frac{Ax\rho}{A} \right) \left(\frac{\partial^2 \xi}{\partial t^2} \right) = x\rho \frac{\partial^2 \xi}{\partial t^2} \quad 4.27$$

Differentiating Equations 4.26 and 4.27 with respect to x yields:

$$\frac{\partial T}{\partial x} = c \frac{\partial^2 \xi}{\partial x^2} \quad 4.28$$

$$\frac{\partial T}{\partial x} = \rho \frac{\partial^2 \xi}{\partial t^2} \quad 4.29$$

Therefore:

$$\rho \frac{\partial^2 \xi}{\partial t^2} = c \frac{\partial^2 \xi}{\partial x^2} \quad \Rightarrow \quad \frac{\partial^2 \xi}{\partial t^2} = v_l^2 \frac{\partial^2 \xi}{\partial x^2} \quad 4.30$$

for
$$v_l = \sqrt{\frac{c}{\rho}}. \quad 4.31$$

This is the wave equation for plane compressional waves travelling in a plate.

Equation 4.30 is more conveniently solved in the Laplace domain, i.e. setting:

$$\frac{\partial^2 \bar{\xi}}{\partial x^2} = \frac{s^2}{v_l^2} \bar{\xi} \quad 4.32$$

for $\bar{\xi}$, the equivalent of ξ in the Laplace domain and s the complex Laplacian operator.

The relevant solution to this is:

$$\bar{\xi} = \Phi e^{-st} + \Psi e^{st} = \Phi e^{-\frac{sx}{v}} + \Psi e^{\frac{sx}{v}} \quad 4.33$$

where the first and second terms represent the forward and backward travelling waves. Φ and Ψ are the complex amplitude functions of these waves respectively, dependent on the relevant boundary conditions.

The build up of charge on each layer must also be taken into account. In the Laplace domain, for a transducer of cross sectional area, A , the surface charge, \bar{Q} is given by:

$$\bar{Q} = \bar{D}A \quad 4.34$$

The layer in question has no free charge, so application of Gauss's Law and the previous assumption of unidimensional resonance in the x-direction means:

$$\frac{\partial D_x}{\partial x} = 0 \quad 4.35$$

Combining Equations 4.32 and 4.33 gives an expression for $\frac{\partial \bar{\xi}}{\partial x}$ as follows:

$$\begin{aligned} \frac{\partial \bar{\xi}}{\partial x} &= \int \frac{\partial^2 \bar{\xi}}{\partial x^2} = \int \frac{s^2}{v_l^2} \left(\Phi e^{\frac{-sx}{v_l}} + \Psi e^{\frac{sx}{v_l}} \right) \\ &= \frac{s^2}{v_l^2} \left[\frac{v_l}{s} \left(-\Phi e^{\frac{-sx}{v_l}} + \Psi e^{\frac{sx}{v_l}} \right) \right] = \frac{s}{v_l} \left(-\Phi e^{\frac{-sx}{v_l}} + \Psi e^{\frac{sx}{v_l}} \right) \end{aligned} \quad 4.36$$

D and S in Equation 4.24 can be substituted with expressions from Equations 4.34 and 4.36 respectively, to form an expression for T :

$$T = c_{(i)} \frac{s}{v_{l(i)}} \left(-\Phi_{(i)} e^{\frac{-sx(i)}{v_{l(i)}}} + \Psi_{(i)} e^{\frac{sx(i)}{v_{l(i)}}} \right) - h_{(i)} \frac{\bar{Q}_{(i)}}{A} \quad 4.37$$

This expression for stress can be rewritten to express the force on a transducer, of area A :

$$F = sZ_{c(i)} \left[-\Phi_{(i)} e^{\frac{-sx(i)}{v_{l(i)}}} + \Psi_{(i)} e^{\frac{-sx(i)}{v_{l(i)}}} \right] - h_{(i)} \bar{Q}_{(i)} \quad 4.38$$

where $Z_{c(i)}$ is the characteristic acoustic impedance of the transducer layer (i) with density $\rho(i)$ and velocity $v_l(i)$ such that:

$$Z_{c(i)} = \rho(i)v_l(i)A$$

4. 39

Voltage

The voltage across each layer is found by substituting the expressions for S and D, in Equations 4.34 and 4.36 respectively, and integrating the equation for electric field, Equation 4.25, from $x = 0$ to $x = x(i)$:

$$\bar{V}_{(i)} = \int -h \frac{S}{v} \left(-\Phi e^{-\frac{sx}{v_l}} + \Psi e^{\frac{sx}{v_l}} \right) + \frac{D}{\varepsilon} = -h \frac{S}{v} \left[\Phi e^{-\frac{sx}{v_l}} + \Psi e^{\frac{sx}{v_l}} \right]_0^{x(i)} + \left[\frac{Q}{A\varepsilon} x \right]_0^{x(i)} \quad 4.40$$

$$\bar{V}_{(i)} = -h_{(i)} \left[\Phi_{(i)} \left(e^{-\frac{sx(i)}{v_l(i)}} - 1 \right) + \Psi_{(i)} \left(e^{\frac{sx(i)}{v_l(i)}} - 1 \right) \right] + \frac{\bar{Q}_{(i)}}{C_{0(i)}} \quad 4.41$$

where $\bar{V}_{(i)}$ is the voltage across layer (i), $h_{(i)}$ is the piezoelectric stiffness constant of layer (i), $\bar{Q}_{(i)}$ is the charge stored on layer (i), $C_{0(i)}$ is the static capacitance of layer (i), $v_{l(i)}$ is the velocity of layer (i) and $\Phi_{(i)}$ and $\Psi_{(i)}$ are amplitude functions associated with layer (i).

The consideration of voltage across each layer can take into account the amplitude factors of the forward and backward travelling waves of force:

$$\Phi_{(i)} = \frac{-\bar{F}_{F(i)}}{sZ_{c(i)}} \quad 4.42$$

$$\Psi_{(i)} = \frac{-\bar{F}_{B(i)}}{sZ_{c(i)}} e^{-st(i)} \quad 4.43$$

where $\bar{F}_{F(i)}$ and $\bar{F}_{B(i)}$ are the forward travelling component referenced to $x = 0$ and the backward travelling component referenced to $x = x(i)$ respectively, and $t(i)$ is the time taken to travel across layer (i).

The following boundary conditions may be set, based on continuity of particle displacement and force at interfaces between layers:

$$\bar{F}_i \Big|_{x=x(i)} = \bar{F}_{(i+1)} \Big|_{x=0} \quad \mathbf{4.44}$$

$$\bar{\xi}_i \Big|_{x=x(i)} = \bar{\xi}_{(i+1)} \Big|_{x=0} \quad \mathbf{4.45}$$

The forward component can now be written in terms of both electrical and mechanical parameters:

$$\bar{F}_{F(i)} = T_{(i-1)}^{(i)} \bar{F}_{F(i-1)} e^{-st(i-1)} + R_{(i)}^{(i-1)} \bar{F}_{B(i)} e^{-st(i)} + T_{(i-1)}^{(i)} \frac{h_{(i)} \bar{Q}_{(i)}}{2} - T_{(i-1)}^{(i)} \frac{h_{(i-1)} \bar{Q}_{(i-1)}}{2} \quad \mathbf{4.46}$$

as can be the backward component:

$$\bar{F}_{B(i)} = T_{(i+1)}^{(i)} \bar{F}_{B(i+1)} e^{-st(i+1)} + R_{(i)}^{(i+1)} \bar{F}_{F(i)} e^{-st(i)} + T_{(i+1)}^{(i)} \frac{h_{(i)} \bar{Q}_{(i)}}{2} - T_{(i+1)}^{(i)} \frac{h_{(i+1)} \bar{Q}_{(i+1)}}{2} \quad \mathbf{4.47}$$

where T_x^y and R_x^y are the transmission and reflection coefficients for waves of force travelling from x to y, given by:

$$T_x^y = \frac{2Z_{c(y)}}{Z_{c(x)} + Z_{c(y)}} \quad \mathbf{4.48}$$

$$R_x^y = \frac{Z_{c(y)} - Z_{c(x)}}{Z_{c(x)} + Z_{c(y)}} \quad \mathbf{4.49}$$

Substitution of the expressions for $\Phi_{(i)}$ and $\Psi_{(i)}$, given in Equations 4.42 and 4.43, into Equation 4.41 gives the voltage across each layer as:

$$\bar{V}_{(i)} = -\frac{h_{(i)}}{sZ_{c(i)}} \left[\left(\bar{F}_{F(i)} + \bar{F}_{B(i)} \right) \left(1 - e^{-st(i)} \right) \right] + \frac{\bar{Q}_{(i)}}{C_{0(i)}} \quad \mathbf{4.50}$$

With Equations 4.46, 4.47 and 4.50, the forces and voltages present in the active layer of the structure are fully described.

The modelling approach of Powell et al. (1998) was designed for multi-layer structures, and as such is extended to include the influence of neighbouring layers to the force and voltage present in a specific layer. However, in this thesis, only single active layers are considered. For simplicity, passive layers were modelled as

mechanical loads rather than distinct layers. ODM remains suitable for this situation. Mechanical loading conditions i.e. the acoustic impedance of the front and back face loads, are input into the programme, and it is from this that the reflection and transmission coefficient of waves generated in the active material are determined. Where modelling was carried out for bare composite, the acoustic impedance of air, 4.13×10^{-4} MRayl was used for back and front face loading. For modelling of transducers in casing, acoustic impedance of 7 MRayl, representing tungsten loaded epoxy of volume fraction 0.2, was used for the back face and either air (4.13×10^{-4} MRayl) or water (1.48 MRayl) was used for the front face depending on which of these front face loading conditions was being investigated.

As there are no mechanical or electrical contributions to the composite from neighbouring layers, Equation 4.46 for the forward wave component may be rewritten as:

$$\bar{F}_{F(i)} = R_{(i)}^{(i-1)} \bar{F}_{B(i)} e^{-st(i)} + T_{(i-1)}^{(i)} \frac{h_{(i)} \bar{Q}_{(i)}}{2} \quad 4.51$$

and Equation 4.47 for the backward wave component as:

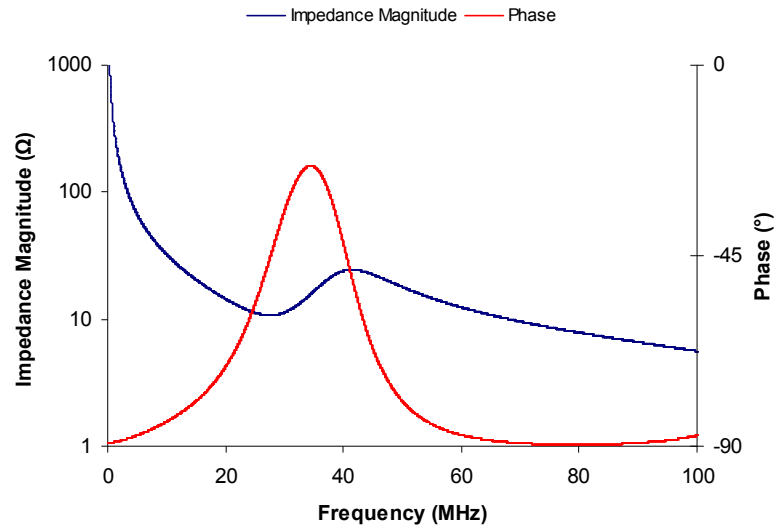
$$\bar{F}_{B(i)} = R_{(i)}^{(i+1)} \bar{F}_{F(i)} e^{-st(i)} + T_{(i+1)}^{(i)} \frac{h_{(i)} \bar{Q}_{(i)}}{2} \quad 4.52$$

As an example, consider a piezocomposite, with 50% volume fraction, made from PZT (CTS3203HD, CTS Corp, Albuquerque, NM, USA) and RX771/HY1300 (Robnor Resins Ltd, Swindon, UK). The material properties of this composite are given in Table 4.2. The front face loading is water and the back face is tungsten loaded epoxy of 20% tungsten volume fraction.

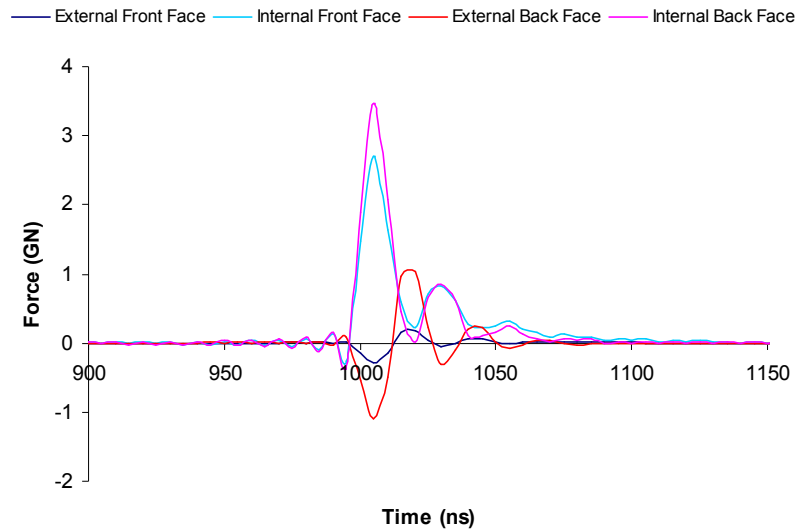
TABLE 4. 2: MATERIAL PROPERTIES OF 50% VOLUME FRACTION CTS3203HD AND RX771 PIEZOCOMPOSITE

Parameter	Value
v_l (ms^{-1})	3980
c_{33}^E (Nm^{-2})	3.81×10^{10}
e_{33} (Vm^{-1})	14.4
ε_R^S	712
ρ (kg m^{-3})	4470
Z (MRayl)	17.8
c_{33}^D (Nm^{-2})	7.09×10^{10}
h_{33} (Vm^{-1})	2.28×10^9
k_T	0.68

ODM simulation data for the frequency-dependent electrical impedance is shown in Figure 4.22(a) and internal and external forces generated on each composite are shown in Figure 4.22(b). The applied voltage in this case is a 100 V amplitude impulse. Note that an arbitrary time delay has been added in Figure 4.23(b) for illustration purposes.



(a)



(b)

Figure 4. 22: (a) Impedance magnitude and phase of a composite and (b) external and internal forces on front and back face over time.

It can be seen that the amplitudes of internal forces are larger than the external forces on both faces: more energy is reflected than transmitted at the layer boundary. This is to be expected because of the significant acoustic mismatch on both faces. From Equations 4.51 and 4.52, forces generated are dependent on the transmission coefficient between the active material and its neighbouring layer. Similarly, the external force generated at the back face is larger than at the front face as the mismatch at the back face is less than at the front. This demonstrates the importance of having matching layers on the front face of a transducer. It also shows that a significant proportion of energy is transmitted through the back face into the contacting medium.

Smith and Auld modelling of piezocomposite

ODM treats all layers of the transducer structure being modelled as homogeneous and, working in only one-dimension, accepts only thickness mode parameters. However, piezocomposites such as MC characterised in the work for this thesis are not homogeneous, consisting of two phases: ceramic pillars and polymer matrix with significantly different material properties. For ODM to calculate solutions for a

piezocomposite material, homogenised thickness mode parameters are required. ODM therefore includes the ability to calculate thickness mode properties for a piezocomposite based on user-input parameters for the two phases, based on the method of Smith and Auld (1991).

The Smith and Auld method of modelling 1-3 piezocomposites as a homogeneous medium applies in the case where the ceramic pillars are sufficiently tall and narrow. The physical principles behind this model are described in detail in Smith and Auld (1991); a brief description is given here. Put simply, the material parameters of a composite are described in terms of the material properties of the constituent ceramic and polymer materials, and the volume fraction of each. The geometric configuration and axes of the piezocomposite are as shown in Figure 4.23.

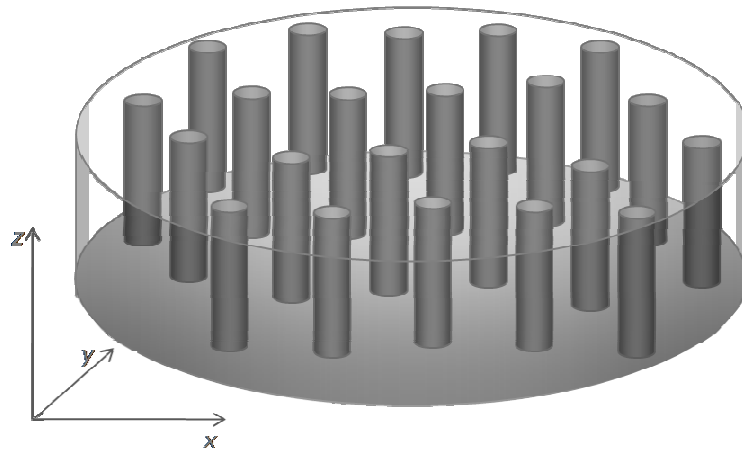


Figure 4. 23: 1-3 piezocomposite configuration, showing x, y and z axes referred to in main text.

Certain approximations are used as follows:

- Firstly, key parameters, such as stress, strain, electric field and displacement are assumed to be constant along the x and y axes of the composite. This is not true in reality, but the averaging of these properties across the composite structure allows this assumption to hold.

- Secondly, it is assumed that the composite is a large, thin electroded plate (i.e. length and width are much greater than thickness) and that there is symmetry in the x-y plane, with zero electric field in the x and y directions. This is valid for the work reported here.
- Thirdly, it is assumed that the thickness mode resonance leads to the ceramic and polymer phases oscillating exactly together. Strain in the ceramic and polymer phases are thus always equal. It is reasonable to assume this when the pillars are of sufficiently fine scale, but other behaviour is possible.
- The fourth approximation is that the electric field through the thickness of each phase is equal. This is justified by the fact that the entire major composite faces are electroded, and hence equipotentials, and also because the dielectric constant of the ceramic material dominates the structure so completely, one can disregard the polymer phase in this respect. In the present work, ceramic has $\epsilon_R^S > 1300$ and polymer has $\epsilon_R = 3.5$.
- The fifth approximation is that lateral stresses in both phases are equal, while the lateral strain of the ceramic phase is compensated by a complementary strain in the polymer. This approximation allows lateral clamping of the whole composite to be assumed. The actual strain of each phase is dependent on the volume fraction of the composite. Lateral strains can be expressed in terms of vertical (thickness) strain and electric field, so eliminating lateral parameters from the constitutive equations used to describe the composite.
- Finally, approximations are made for the dependent coordinates. Again, the contributions of each phase are averaged across the whole composite, allowing expressions for the effective total stress and electric displacement to be defined.

The constitutive equations for a composite are then defined as:

$$\bar{T}_3 = \bar{c}_{33}^E \bar{S}_3 - \bar{e}_{33} \bar{E}_3 \quad 4.53$$

$$\bar{D}_3 = \bar{e}_{33} \bar{S}_3 + \bar{\varepsilon}_{33}^S \bar{E}_3 \quad 4.54$$

where:

$$\bar{c}_{33}^E = VF \left[c_{33}^E - \frac{2\tilde{V}(c_{13}^E - c_{12}^E)^2}{VF(c_{11} + c_{12}) + \tilde{V}(c_{11}^E + c_{12}^E)} \right] + \tilde{V}F c_{11} \quad 4.55$$

$$\bar{e}_{33} = VF \left[e_{33} - \frac{2\tilde{V}F e_{31} (c_{13}^E - c_{12}^E)}{VF(c_{11} + c_{12}) + \tilde{V}(c_{11}^E + c_{12}^E)} \right] \quad 4.56$$

$$\bar{\varepsilon}_{33}^S = VF \left[\varepsilon_{33}^E - \frac{2\tilde{V}F (e_{31})^2}{VF(c_{11} + c_{12}) + \tilde{V}(c_{11}^E + c_{12}^E)} \right] + \tilde{V}F \varepsilon_{11} \quad 4.57$$

VF is volume fraction and $\tilde{V}F = (1 - VF)$.

In practice, it is easier to solve the constitutive equations with S_3 and D_3 as the independent variables. Rearranging Equations 4.69 and 4.70 for this gives:

$$\bar{T}_3 = \bar{c}_{33}^D \bar{S}_3 - \bar{h}_{33} \bar{D}_3 \quad 4.58$$

$$\bar{E}_3 = \bar{h}_{33} \bar{S}_3 + \bar{\beta}_{33}^S \bar{D}_3 \quad 4.59$$

where:

$$\bar{c}_{33}^D = \bar{c}_{33}^E + \frac{(\bar{e}_{33})^2}{\bar{\varepsilon}_{33}^S} \quad 4.60$$

$$\bar{h}_{33} = \frac{\bar{e}_{33}}{\bar{\varepsilon}_{33}^S} \quad 4.61$$

$$\bar{\beta}_{33}^S = \frac{1}{\bar{\epsilon}_{33}^S} \quad 4.62$$

The required material parameters for a full analysis are then completed by the following definitions for density, $\bar{\rho}$:

$$\bar{\rho} = VF\rho^c + \tilde{V}F\rho^p \quad 4.63$$

where the superscripts c and p indicate *ceramic* and *polymer* respectively. This gives expressions for the key parameters velocity, \bar{v} , acoustic impedance, \bar{Z} , and thickness mode coupling coefficient, \bar{k}_T .

$$\bar{v} = \sqrt{\left(\frac{c_{33}^D}{\rho}\right)} \quad 4.64 \quad \bar{Z} = \sqrt{\left(\frac{-D}{c_{33}^D \rho}\right)} \quad 4.65 \quad \bar{k}_T = \frac{\bar{h}_{33}}{\sqrt{c_{33}^D \bar{\beta}_{33}^S}} = \frac{\bar{e}_{33}}{\sqrt{c_{33}^D \epsilon_{33}^S}} \quad 4.66$$

Using ODM to verify experimental measurements

The primary reason for modelling the MC is to verify material properties measured experimentally. This is an unusual, but not unknown, approach previously used by e.g. Maréchal et al. (2006).

For a standard dice-and-fill piezocomposite, the material properties are not determined fundamentally from measurements taken from the piezocomposite. Instead, the constituent materials are characterised individually, and the properties of the piezocomposites are then calculated using a method such as Smith and Auld (1991). This is acceptable because the active phase of a dice-and-fill composite is made directly from a sheet of piezoelectric material whose material properties can be assumed the same before and after the composite fabrication process. However, the PZT bristle block used to make MC is moulded before the PZT is sintered. The influence of parameters such as material surface area on the

sintering process is significant, meaning there is no certainty that the piezoelectric properties of e.g. a PZT sheet, or bar, made by VPP are the same as those of a micromoulded PZT bristle block made by VPP. MC must therefore be treated as homogeneous material and characterised by direct measurement.

Experimental measurements were taken from piezoelectric samples, either in the form of bare composite or after inclusion in a casing. The procedure for taking experimental impedance measurements was as described in Section 4.5 for both cases.

Piezoelectric properties determined from experimental measurements were then entered into ODM and theoretical impedance data calculated from these for each composite. These were then compared with the impedance data measured experimentally. From the piezoelectric parameters listed in Table 4.1, only c_{33}^E , e_{33} , ϵ_R^T , ϵ_R^S , ρ and attenuation, α , are needed for ODM. These parameters were then adjusted until a good match was obtained between experimental and simulated impedance spectra. Results of properties determined with both experimental measurements and those used in simulation are given in Chapter 5. Fitting of simulations to experimental data using this approach requires good understanding of the influence of various material parameters on impedance spectra. As such, a number of simulations were undertaken to elucidate the results of variation of c_{33}^E , e_{33} , ϵ_R^T , and ϵ_R^S , as illustrated in Appendix B.

The process for determination of piezoelectric properties could have been extended to mathematical parameter optimisation (Wu, 2005). This has potential disadvantages however. Several parameters are used to generate solutions, meaning it is possible that more than one solution can exist and erroneous results may be generated with an automated process. Experimental data may also be influenced by unwanted modes, for example intra-pillar modes, which are common in HFUS piezocomposites which may not be optimally designed. This would cause difficulty using a computational approach. It is easier to make allowance for these problems with the empirical approach described here.

It would not be essential to use ODM as the simulation tool in the material characterisation process as described here. A similar approach to determination of material properties is reported by Maréchal et al. (2006), using a unidimensional KLM equivalent circuit model. As with the work reported here, frequency dependent electrical impedance is recorded and then compared with a theoretically generated impedance plot. The piezoelectric material being characterised was a PZT thick film. The film was incorporated in a structure with five layers: gold front electrode, PZT thick film, gold back electrode, PZT/PGO barrier layer (where PGO is lead germanate) and porous PZT substrate. The KLM model of this structure could potentially have a large number of unknown input variables. This could compromise the accuracy of the material properties generated for the PZT film. To reduce the number of variables and simplify the model, v_l and ρ (and hence, Z) were first determined for each layer. Other parameters (v_l , k_T , ε_R^S and mechanical losses, δ_m) were then found by fitting the theoretical electrical impedance to experimental data, in a similar manner to the work reported here.

4.8. Fabrication of single element transducers

When characterising piezoelectric materials, it is essential not only to determine the electrical properties of the material but also the ultrasonic performance. The most practical way to do this is to make a prototype transducer by incorporating the sample into a casing which can be easily connected to instrumentation designed for ultrasonic testing. This was done for the micromoulded composites studied in the work for this thesis.

4.8.1. Transducer components

The key components of this type of transducer design are described in the following sections: the casing, active element, backing layer and filler. These are shown in Figure 4.24.

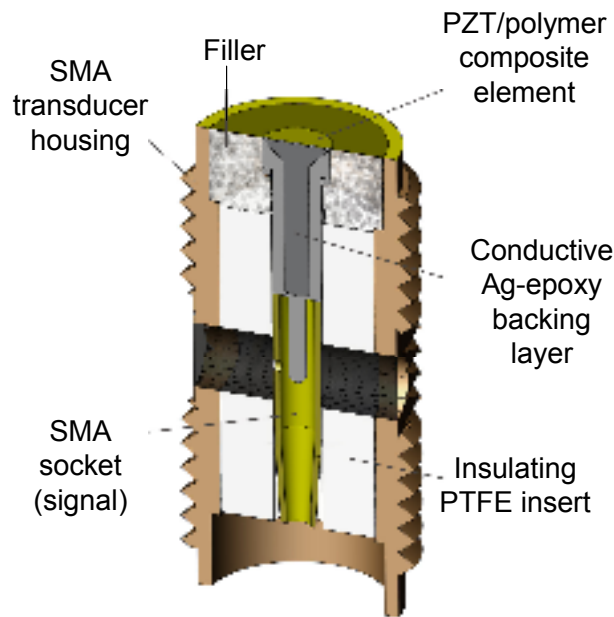


Figure 4. 24: Cross section of single element PZT /polymer composite transducer.

Casing: SMA Barrel

The barrel used is an SMA Jack (F) – Jack (F) adapter. The outer barrel is made from gold-coated stainless steel. Inside, there is a conductive contact for signal connection. This is insulated from the rest of the barrel (i.e. electrical ground) by PTFE inserts.

Active element

The active elements of the transducers reported in this thesis are mostly PZT/polymer piezocomposite, but can be other active materials, for example LNO and monolithic PZT. A number of the transducers tested here were spherically focussed using the process described by Lockwood et al. (1993) and discussed in Section 3.2.

Backing layer

The backing layer is typically made from silver loaded conductive epoxy (e.g. Part No. 186-3616, RS Components, Corby, UK). This provides mechanical support and damping for the active layer, plus electrical connection to the signal pin of the SMA barrel.

Filler

The filler material provides mechanical support for the piezocomposite/backing layer structure. It is made from an insulating microballoon-filled epoxy potting compound.

4.8.2. Fabrication Process

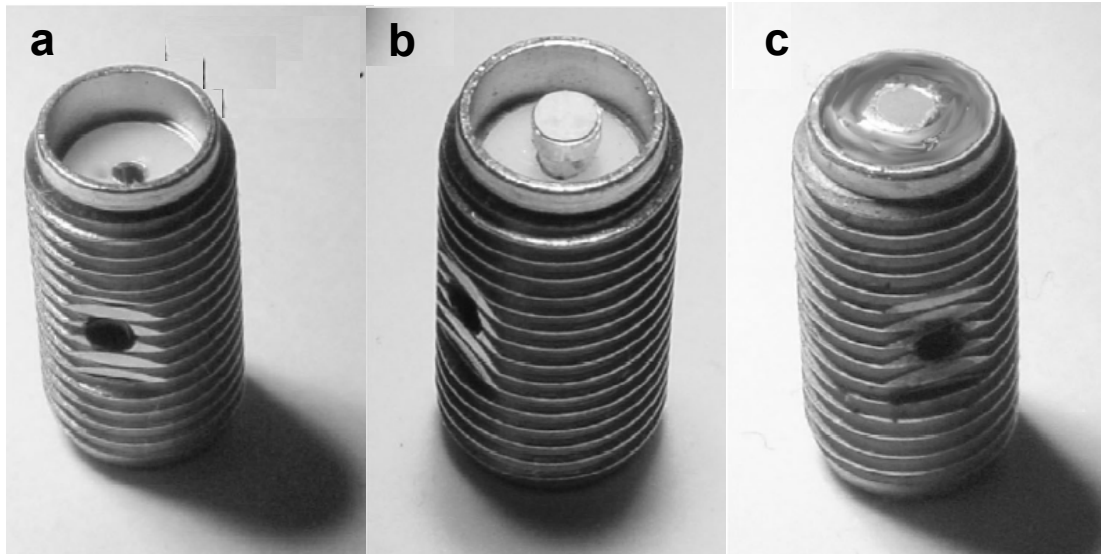


Figure 4. 25: Fabrication procedure for single element transducer. Photographs from Aristizábal and Turnbull (2003 © IEEE)

The fabrication process is illustrated in Figure 4.25. Starting with an SMA barrel (a), the active layer, with conductive backing layer already attached, and element shaping completed if required, is bonded to a signal pin and inserted into the socket of the SMA barrel (b). The barrel is then filled with insulating epoxy potting compound. Finally a gold ground electrode is deposited over the entire front face of the transducer.

An example of a finished transducer is shown in Figure 4.26:

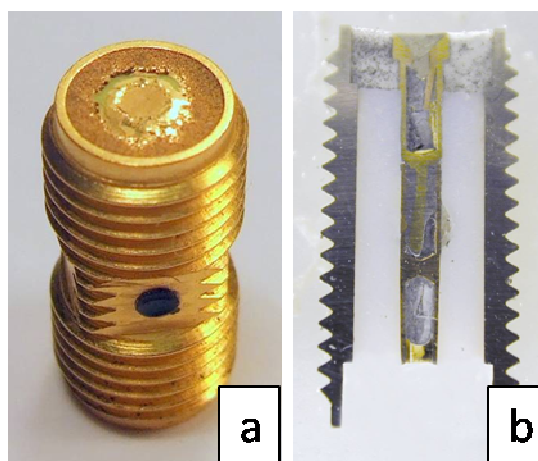


Figure 4. 26: Photographs of (a) prototype high frequency single element transducer and (b) section of same transducer design (from Webster, 2009).

4.9. Basic testing of transducers

4.9.1. Pulse shape

Pulse shapes were taken in *pulse-echo* mode for all transducers studied in this thesis. Echoes were collected by reflection from a planar stainless steel surface. For focussed transducers, the transducer was positioned such that the steel surface coincided with the focal point of the transducer. This was achieved by observing the amplitude of the received signal and recording this at the point at which the signal was maximised. For unfocussed transducers, measurements were taken at a predetermined point beyond the *near field* boundary. Axial resolutions were calculated from pulse data using Equation 2.66.

Where possible *through-transmission* measurements were also recorded, using a PVDF Membrane Hydrophone (Precision Acoustics, Dorset, UK) as a receiver.

In all cases the transducer was driven by a DPR500 Pulser Receiver (JSR, Pittsford, NY, USA) with remote pulser. The load impedance of the remote pulser was 100 Ω . The transducer is connected directly to the remote pulser so no cable effects need be considered. Signals were collected using an oscilloscope: signals from transducer TH09 were recorded with an Agilent 54641A digital oscilloscope (Agilent Technologies, South Queensferry, UK) and for all other transducers with a Tektronix TDS2024B digital oscilloscope (Tektronix, Bracknell, UK).

Experimental pulse shapes were then compared with data generated by ODM models, in both the time and frequency domains. Parameters for the ODM models were determined from impedance spectroscopy measurements, as before and the excitation pulse from the DPR500 pulser receiver was recorded and used as the electrical input for ODM models. The acoustic properties of the backing layer used were known and the resultant loading effects incorporated in the ODM model. Pulse amplitudes were normalised in all cases. Measurements expressed in dB are calculated from signal amplitude measurements using:

$$dB = 20\log_{10}(\text{normalised signal amplitude})$$

4. 67

for pulse-echo measurements.

4.9.2. Line Spread Function and Depth of Field

Depth of field was measured for transducers which were focussed. This was done by recording echoes from the stainless steel surface at a range of axial distances from the steel, and plotting amplitude against axial position. An example is shown in Figure 4.27a.

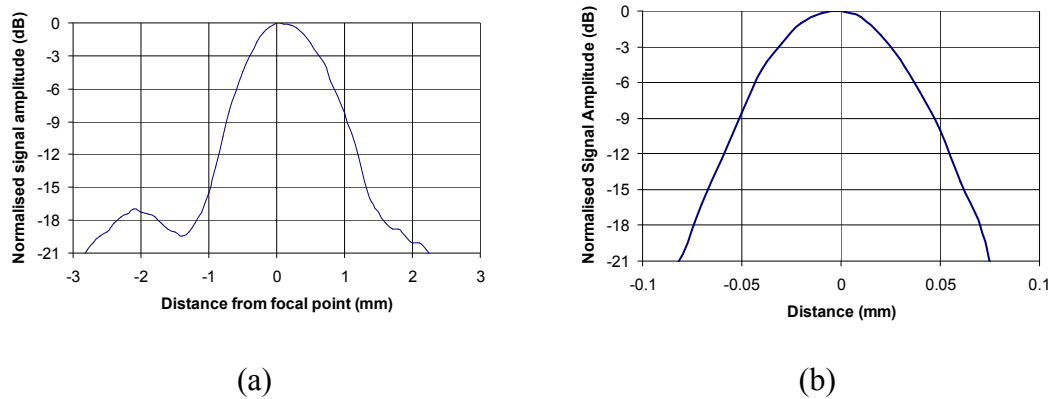


Figure 4. 27: Example of (a) depth of field and (b) line spread function from a high frequency transducer (JB1).

The line spread function for each transducer was also measured. Data for this was collected by operating the transducer in pulse-echo mode and recording the received signals from a 5 μm diameter tungsten wire in water. Each transducer was once again positioned such that the focal point coincided with the wire. The transducer was then moved laterally in positive and negative directions, in steps of 10 μm until no signal was detectable. The amplitude of echoes received was then plotted against position. An example is shown in Figure 4.27b. The line spread function provides a useful measure of the lateral resolution of the transducer.

4.10. Design of high frequency scanning system

A 2D scanning system was developed to allow automated collection of B and C-scans. The components of this included: JSR DPR500 High-frequency Pulser

receiver, Picoscope 5204 PC oscilloscope (Pico Technology, St Neots, UK), SG-SP-26-100 XY automatic scanning stages with SHOT-602 stage controller (Sigma Koki, Tokyo, Japan), and LabVIEW control software (National Instruments, Newbury, UK). The LabVIEW programme used is described in Appendix C. These scan system components are now described in further detail.

Pulser Receiver: The pulser receiver is connected via an RS232 port to a PC, from which control parameters for transducer excitation and reception are set using JSR software. These remained fixed at the following values: *Trigger:* internal; *Pulse repetition frequency:* 1.9 kHz; *Pulse Energy:* Low; *Damping:* 100 Ω ; *Receiver Bandwidth:* 5–300 MHz. Receiver gain was adjusted according to the sensitivity of the transducer between 10 and 20 dB.

Scanning stages: The scanning stages consist of two orthogonal (X and Y), motorized stages with a stage controller, connected via an RS232 connection to the PC. The stages move in 2 μm ‘steps’ in both directions and can be controlled either by manufacturer-provided software (for single movements) or programmed to set routines using a LabVIEW script.

Picoscope: The Picoscope is a software driven oscilloscope, which may also be programmed, via LabVIEW, to collect data automatically. The Picoscope connects directly to a PC using a USB connection. The sampling rate can be set to a maximum of 500 MHz.

The other components of this set-up are controlled by LabVIEW software. A photograph of the scan system components is shown in Figure 4.28a along with a schematic showing how the components were interconnected in Figure 4.28b.

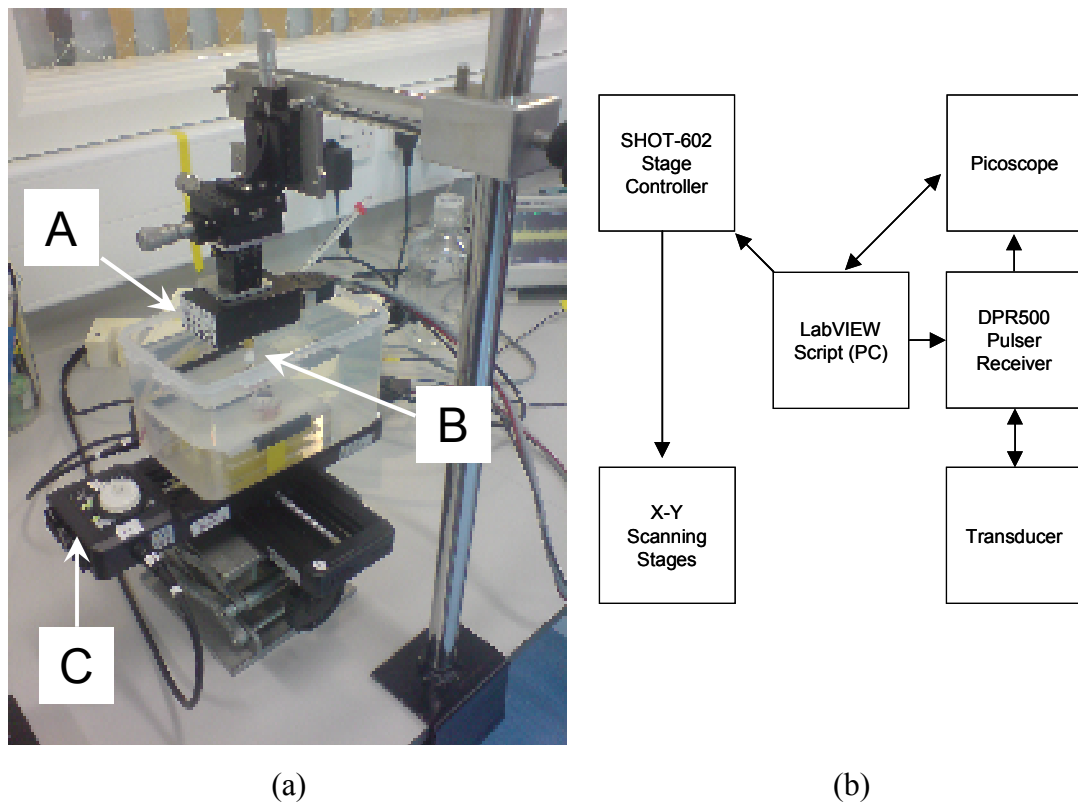


Figure 4.28: (a) Photograph of scanning system pulser receiver (A), transducer (B) and scanning stages (C) and (b) schematic of component connections with arrows showing direction of signals.

Other components: To ensure correct positioning of the transducer relative to the object being scanned, the transducer is connected to a set of three micrometers (Standa, Vilnius, Lithuania), allowing x, y and z adjustment and two goniometers to adjust pitch and yaw (Melles Griot, Cambridge, UK). The height of the scanning stage ensemble may also be adjusted using a lab jack.

Scanning system for TH9

Scans conducted using transducer TH9 were carried out with a different earlier scanning system. An automated three-dimensional scanning stage (Physik Instrumente, Karlsruhe, Germany) was used in conjunction with a Gagescope PC oscilloscope (Gage, Lockport, IL) and was operated by a script written in MATLAB (The Mathworks, Cambridge, UK). The system used the same JSR pulser receiver. This system allowed automated scanning in the x, y and z dimensions.

4.11. Visualisation of collected data

Data is saved in the form of an $m \times n$ array, where m corresponds to the number of individual A-scans collected, n to the number of points in each A-scan, and each individual point represents a voltage measurement from the Picoscope. This data was studied either by plotting individual A-scans, or by using the MATLAB function *imagesc(data)* to generate B-scan images, where voltages are represented as a colour scale. For the latter case, Hilbert transforms are performed on each individual A-scan to find the envelope of each pulse. This data is then converted to a dB scale before being represented as a colour map, an example of which is shown in Figure 4.29.

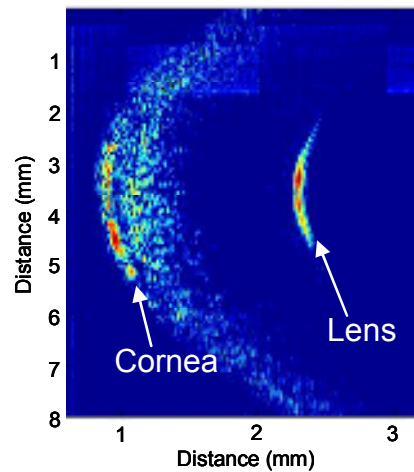


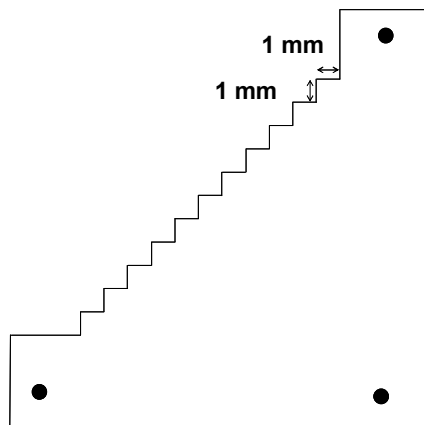
Figure 4. 29: Example of a B-scan image of an eye, generated by MATLAB from data collected from A-scans with a 32MHz transducer.

4.12. Wires and tissue imaging

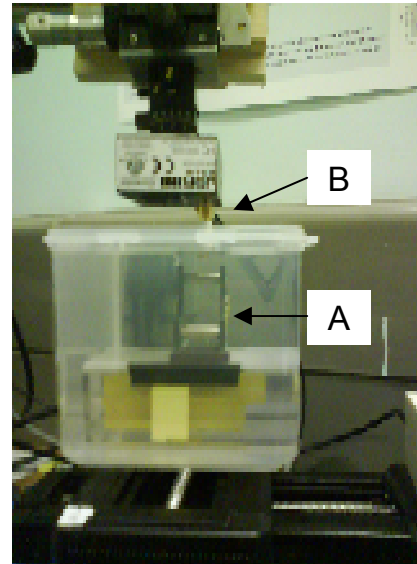
For purposes of further characterisation some imaging was also done using the prototype HFUS transducers. The goal of this was to show that the transducers could potentially be used for diagnostic imaging. Improving the quality of resulting images was not within the scope of this work, and as such the scanning system set-up was not extensively optimised. RF data recorded was subjected only to averaging and logarithmic compression.

4.12.1. Tungsten wire scanning

For the work reported here, a bespoke wire target was made using 5 μ m tungsten wire. Tungsten wire was chosen because it has very high acoustic impedance and therefore is highly reflective. The wires were loaded onto a holder, in a stepped fashion, designed such that wires were separated by 1 mm laterally and axially. A diagram and photographs of the wire holder are given in Figures 4.30(a) and (b) respectively.



(a)



(b)

Figure 4. 30: Diagram of (a) Tungsten wire holder and (b) photograph of holder being scanned using HFUS transducer.

This holder was designed to make beam profiling easier, as one can perform a simple B-scan across the wire and detect reflections of the beam from wires over an axial range of 12 mm, which is typically large enough to cover the depth of field of a transducer.

To scan the tungsten wires, the target was submerged in water and a B-scan was performed across several of the wires, at a fixed height determined by the characteristics of the individual transducer. Wire scans were performed for all transducers studied in this thesis.

4.12.2. Ex-vivo tissue scanning

Initial investigation of the efficacy of the transducer as a medical diagnostic tool was also undertaken. A number of applications were investigated.

Eye scanning. This was undertaken using either ovine or porcine eyes, sourced from a local abattoir according to availability. In each case, an eye was placed in a small water container and scanned using the automated set-up. To stop movement of the eye during a scan a small holder was made from wire. As part of the work of this thesis, eye scans were undertaken using several transducers, both focussed and unfocussed. This was to assess the potential of these transducers for use in HFUS systems.

Tooth scanning. Although not part of the work of this thesis, one of the MC transducers described in this thesis, AFMTH09, was also used for three-dimensional imaging of the enamel layer and dentine junction in ex-vivo tooth samples. This work was carried out by D. Hughes at University of Strathclyde and reported in Hughes et al. (2007). Tooth imaging is usually done using X-ray procedures. X-ray images are limited to two-dimensions and subject patients to doses of ionising radiation. Ex-vivo tooth samples were prepared to expose both enamel and dentine layers and encased in epoxy, as shown in Figure 4.31(a) before being imaged using the system described in Section 4.10. An example of a 3D rendering of a tooth sample is shown in Figure 4.31(b). It was concluded by Hughes et al. (2007) that this technique showed promise for use in diagnosis of caries.

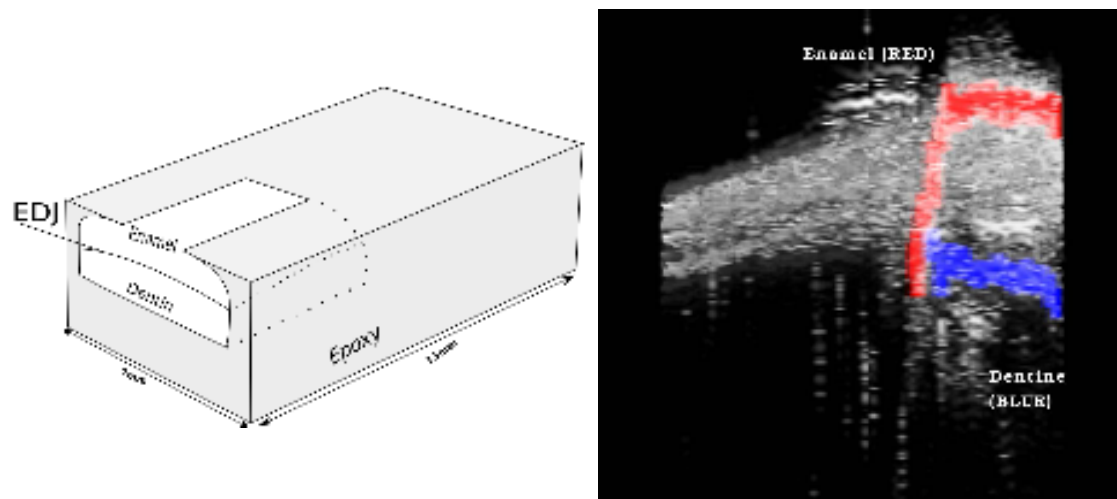


Figure 4. 31: (a) Diagram of tooth samples encased in epoxy for imaging, showing enamel and dentine layers, with EDJ (enamel dentine junction) in between and (b) resulting 3D rendered HFUS image.

4.13. Summary

This chapter described the materials and experimental methods used for work described in this thesis. Results and some discussion of these are presented for material characterisation work in Chapter 5 and transducer testing in Chapter 6. Further discussion is presented in Chapter 7 and conclusions drawn from these in Chapter 8.

4.14. References

Abrar A., Zhang D., Su B., Button T.W., Kirk K.J. & Cochran S. (2004) 1-3 connectivity piezoelectric ceramic-polymer composite transducers made with viscous polymer processing for high frequency ultrasound. *Ultrasonics* Vol.42 pp. 479-484.

Arai, S. (2004) *Surface Integrity Control of Piezoelectric Materials in Ultra Precision Grinding on the basis of Machine Design Assessment* PhD Thesis, University of Cranfield.

Aristizábal O., Turnbull D.H. (2003) 44-MHz LiNbO₃ Transducers for UBM-Guided Doppler Ultrasound. *IEEE Transactions on Ultrasonics, Ferroelectrics, and Frequency Control*, vol. 50, no. 6 pp. 623-630

Berlincourt D. A., Curran D.R., Jaffe H., "Chapter 3- Piezoelectric and Piezomagnetic Material and their Function in Transducers, pp. 169-270,

Button T.W., Cochran S., Kirk K.J., MacLennan D., MacNeil A., McDonald K., Meggs C., Rodriguez-Sanmartin D., Webster R., Zhang D. (2005) Net-Shape Ceramic Manufacturing as an Aid to Realize Ultrasonic Transducers For High-Resolution Medical Imaging IEEE Ultrasonics Symposium Proceedings pp. 1625-1628

Dent A.C. Nelson L.J., Bowen C.R., Stevens R., Cain M., Stewart M. (2005) Characterisation and properties of fine scale PZT fibres. *J. Euro. Ceram. Soc.*, 25, pp.2387-91

Devaney A.J. & Levine H. (1980) Effective elastic parameters of random composites *Applied . Physics Letters.*, Vol.37 No.4, pp. 377-379.

Foster F. S., Ryan L. K., Turnbull D.H. (1991) Characterization of Lead Zirconate Titanate Ceramics for Use in Miniature High-Frequency (20-80 MHz) Transducers. *IEEE Transactions on Ultrasonics, Ferroelectrics and Frequency Control*, Vol. 38. No. 5 pp. 446-453

Hayward G., Jackson M. N. (1984) A Lattice Model for the Discrete Time Simulation of a Multi-layered Piezoelectric Transducer System. *Proceedings of 1984 IEEE Ultrasonics Symposium* pp. 888-891

Hedrick, W.R., Hykes, D.L., Starchman, D.E. (1995) *Ultrasound Physics and Instrumentation* pp.24, Mosby-Year Book: St. Louis. Third Edition

Hughes D.A., Button T.W., Cochran S., Elgoyhen J., Girkin J.M., Hughes H. Longbottom C., Meggs C. and Poland S. (2007) 3D Imaging of Teeth using High

Frequency Ultrasound *Proceedings of 2007 IEEE Ultrasonics Symposium* pp. 327-330

Jackson M. N., Hayward G. (1983) A New Three-Port Model of the Thickness Mode Piezoelectric Transducer. *Proceedings of 1983 IEEE Ultrasonics Symposium* pp. 878-882

Krimholtz, R., Leedom, D. A., Matthaei, G. L. (1970) New equivalent circuits for elementary piezoelectric transducers. *Electronics Letters*. Vol. 6 No. 13 pp. 398-399

Lockwood G.R., Turnbull D.H., Foster F. S. (1993) High Frequency (> 20 MHz) Spherically Shaped Ceramic Transducers *IEEE Ultrasonics Symposium Proceedings* pp. 495-498

Maréchal P., Levassort F., Holc J., Tran-Huu-Hue L.P., Kosec M., and Lethiecq M. (2006) High-Frequency Transducers Based on Integrated Piezoelectric Thick Films for Medical Imaging. *IEEE Transactions on Ultrasonics, Ferroelectrics and Frequency Control*, Vol. 53, no. 8, pp.1524-1533

Mason W.P. (1964) *Physical Acoustics- Principles and Methods*. Volume I-Part A, ed. Academic Press, New York.

O'Leary R.L. (2003) *An investigation into the passive polymer materials utilised in the construction of piezoelectric composite transducers*. pp. 78-154 Ph.D. Thesis, University of Strathclyde, Glasgow, UK.

Powell, D.J., Hayward, G., Ting R.Y. (1998) Unidimensional Modelling of Multi-Layered Piezoelectric Transducer Structures. *IEEE Transactions on Ultrasonics, Ferroelectrics, and Frequency Control*, Vol. 45, No. 3 pp.667-677

S. Cochran, A. Abrar, K. J. Kirk, D. Zhang, T. W. Button, B. Su, C. Meggs and N. Porch (2004) Net-Shape Ceramic Processing as a Route to Ultrafine Scale 1-3 Connectivity Piezoelectric Ceramic-Polymer Composite Transducers *Proceedings of 2004 IEEE Ultrasonics Symposium*. pp. 1682-1685

Schmarje, N. (2005) *Lithium Niobate Piezocomposite for High Temperature Applications in Non-destructive Testing* PhD Thesis (pp.54), University of Paisley, Paisley, UK.

Smith W. A. & Auld B.A. (1991) Modeling 1-3 composite piezoelectrics: thickness-mode oscillations. *IEEE Transactions on Ultrasonics, Ferroelectrics and Frequency Control*, **38** (1), pp. 40-47.

Webster, R (2009) PhD Thesis, University of Birmingham. To be published.

Wu J. (1996) Determination of velocity and attenuation of shear waves using ultrasonic spectroscopy *Journal Acoustic. Society of America*, Vol.99 No.5 pp. 2871-2875.

Wu Z., “Bondlines in piezoelectric ultrasonic transducers”, PhD Thesis, University of the West of Scotland, pp. 69 – 73, 2005.

Zipparo M.J., Shung K.K., Shrout T.R. (1997) Piezoceramics for High-Frequency (20 to 100 MHz) Single-Element Imaging Transducers *IEEE Transactions on Ultrasonics, Ferroelectrics, and Frequency Control*, vol. 44, No. 5, pp. 1038-1048

5. Results

5.1. Introduction

The chapter details results of characterisation of transducer materials. This starts in Section 5.2 by presenting results of W-loaded epoxy, as used in transducer backing layers. An investigation of a novel method for piezocomposite fabrication is also presented, ultra precision grinding.

The remainder of the chapter concerns results of characterisation of a variety of piezoelectric materials. Section 5.3 contains results from preliminary experimental studies on a PZT-5A/polymer composite, made from commercially available materials using standard dice-and-fill techniques.

Sections 5.4 and 5.5 contain results of characterisation of piezocomposites made using the PZT produced by viscous polymer processing (VPP). Results are presented from piezocomposites made using extruded PZT fibres contained in a polymer matrix in Section 5.4. Results from piezocomposites fabricated by applying the novel micromoulding technique discussed in Section 4.1 to VPP ceramic are then presented in Section 5.5. It is these composites that form the main focus of this thesis.

For each sample in Section 5.4-5.5, a table describing the physical characteristics of the sample is given, followed by graphs showing simulated and experimentally measured electrical impedance spectroscopy data. A table of key piezoelectric parameters derived from electrical impedance data is then presented. In each case, the values calculated from simulation and direct measurements are given, along with the percentage difference between them. Where they exist, pulse-echo data are also presented, but this was not generated for all samples.

5.2. Transducer materials

5.2.1. Characterisation of passive materials: W-loaded epoxy

The passive materials used for fabrication of transducers significantly influence the performance of that transducer. As such it is important to know the mechanical properties of these materials, particularly at the intended frequency of operation of the transducer. The most recently fabricated MC transducers used backing layers made from W-loaded epoxy. Work was undertaken, in collaboration with R. Webster of University of Birmingham, to characterise W-loaded epoxy at high frequencies to aid in design of backing layers for HFUS transducers. Measurements were collected and data analysed by R Webster, using a specially designed and manufactured jig, designed by the author and described in detail in Section 4.3. The results were presented in Webster et al. (2007). Due to their relevance to the work of this thesis, results are also reported here.

Several samples of W-loaded epoxy were fabricated, with a range of tungsten volume fractions. The maximum tungsten volume fraction that was tested was 0.4; above this volume fraction the W-loaded epoxy becomes electrically conductive. While this is not a problem for single element transducers it is not suitable for arrays where elements must be electrically isolated, It is therefore not appropriate to study W-loaded epoxy of volume fractions greater than 0.4. The density of each sample was calculated, and shown in Figure 5.1. As expected, the density of the sample increases linearly with increased tungsten volume fraction.

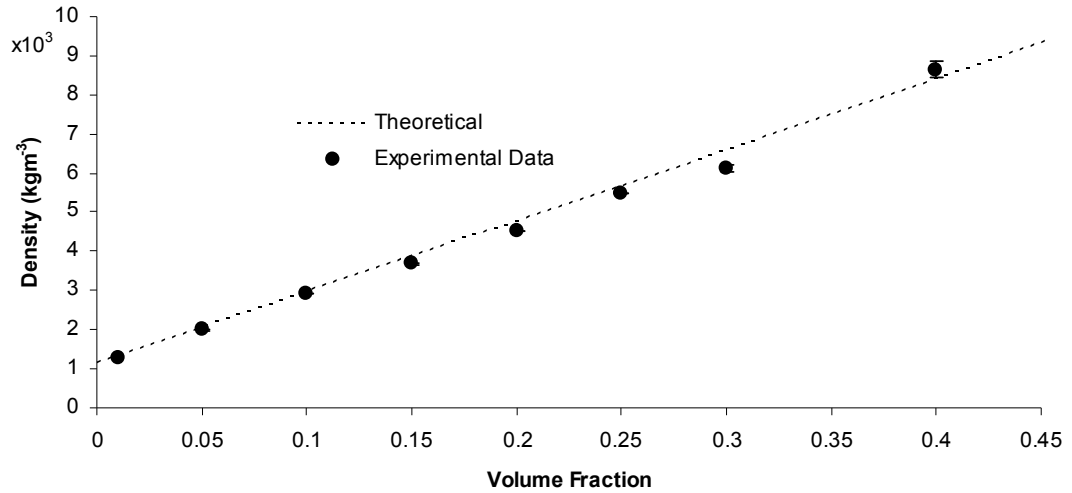


Figure 5. 1: Graph showing relationship between density and W-volume fraction in W-loaded epoxy.

Propagation velocity, acoustic impedance and attenuation were then determined for longitudinal and transverse propagation within each sample. Time-of-flight and signal intensity of longitudinal and transverse waves were measured using the high frequency materials characterisation jig, following the procedure described in Section 4.4. Three measurements were taken for each tungsten volume fraction of tungsten loaded epoxy. From these measurements, longitudinal and transverse propagation velocities are calculated using Equations 4.3 and 4.8 respectively, while longitudinal attenuation coefficients are calculated using Equation 4.10. For epoxy with zero tungsten content the longitudinal velocity was 2503m/s with standard deviation of 101m/s and the transverse velocity was 1160m/s with standard deviation 20m/s. Transverse wave attenuation coefficients were not measured for these particular samples. The one dimensional modelling techniques used for the work of this thesis only requires information on the longitudinal wave attenuation of materials. It was therefore not considered necessary to obtain transverse wave attenuation information for this study.

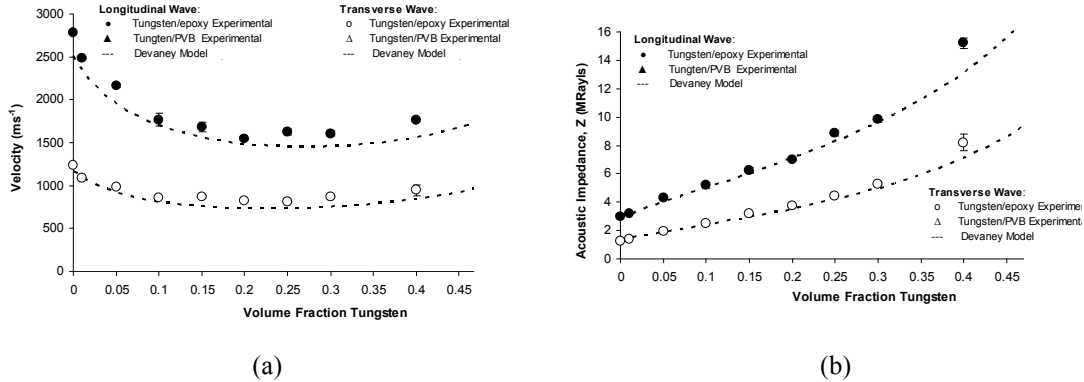


Figure 5.: Graph showing (a) longitudinal and transverse velocities and (b) longitudinal and transverse wave acoustic impedances of Tungsten-loaded epoxy samples with increasing volume fraction, measured at 36MHz

Graphs of the change in longitudinal and transverse velocities are shown in Figure 5.2a and corresponding acoustic impedances in Figure 5.2b. The calculated attenuation coefficients for longitudinal wave propagation are also shown for each sample, in Figure 5.3.

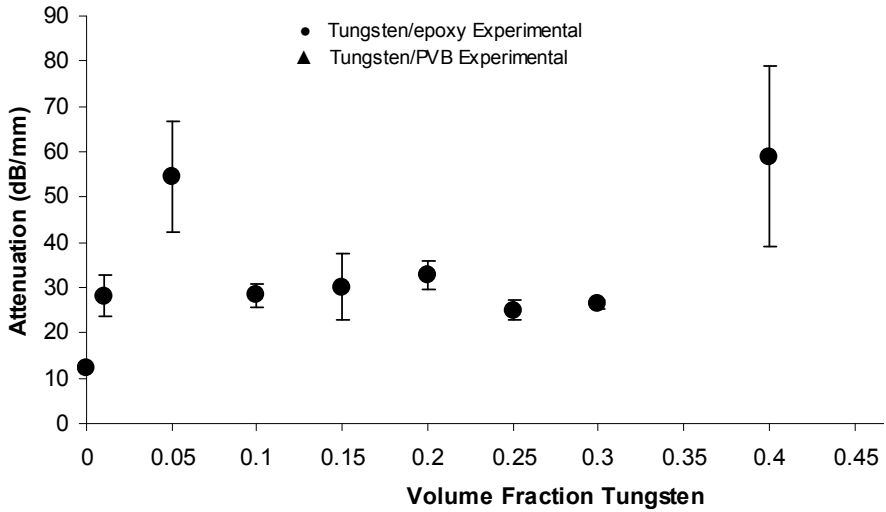


Figure 5. 2: Graph showing change in attenuation of longitudinal waves in Tungsten-loaded epoxy with increasing volume fraction.

The calculated values for longitudinal velocity for volume fractions of tungsten between zero and 0.4 are in the range $v_l = 1500 - 2800 \text{ ms}^{-1}$, corresponding to a

specific acoustic impedance range of $Z_l = 3 - 15$ MRayl. For transverse waves, velocities are in the range $v_t = 800 - 1200$ ms⁻¹, corresponding to a specific acoustic impedance range of approximately $Z_t = 1 - 8$ MRayl. The results show close correspondence with the theoretical model published by Devaney and Levine (1980). The acoustic impedance range described is suitable for use as a backing layer for piezocomposite active layers, which generally have longitudinal acoustic impedances of $Z_l = 12 - 22$ MRayl in the case of PZT-polymer composites of volume fractions of $VF = 0.3 - 0.7$.

The range of values of longitudinal wave attenuation coefficients shown in Figure 5.3 does not appear to show any distinct relationship with volume fraction. However, it can be seen that tungsten loaded epoxy is approximately twice as attenuative, at 30 dB/mm, as the unfilled epoxy, at 15 dB/mm. This shows the advantage of adding a filler material to a transducer backing layer.

5.2.2. Ultra Precision Grinding

A novel method for finishing of piezocomposites for HFUS applications, ultra precision grinding, was investigated as described in Section 4.2. Samples of standard dice and fill composites and also MC were prepared for high frequency operation, and the surface finish compared to that of standard lapping procedures. Surface finishes were assessed using a Dektak 3ST surface profiler (Veeco Instruments Limited, Cambridge). The Dektak is a stylus-based metrology system specifically designed for surface roughness measurements on microelectronics components, including polymers, with step height down to 10 Å, and scan lengths of up to 30 mm. As such, it is highly suited to measurements on the piezocomposite samples studied here. Results are now presented.

LP1: Lapping of standard composite

The DekTak surface profiler was used to record the surface profile of a conventional 1-3 connectivity piezoceramic composite (denoted LP1). This is shown in Figure 5.4. The piezocomposite was made, using conventional dice-and-fill techniques, from PZT 5A (Morgan Electroceramics, Ruabon, UK) and RX771/HY1301 (Robnor

Resins, Cambridge, UK), and thinned using conventional lapping to a thickness of 400 μm , corresponding to operational frequency of close to 5 MHz.

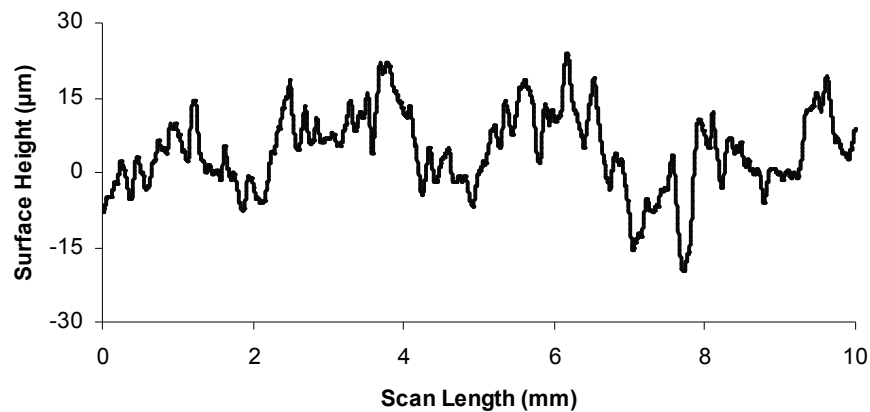


Figure 5. 3: Surface profile of LP1

The surface height shows more than $\pm 15 \mu\text{m}$ variation, equivalent to about 80% of the active layer thickness of 35 – 45 μm required for a 50 MHz transducer made with piezocomposite. This is insufficiently precise to produce the thin layers required for satisfactory high frequency operation

LP2: UPG of Standard Dice-and-fill Composite

A second sample of PZT5A composite, LP2, was then thinned using UPG. The sample was coated with a very thin layer (10 nm) of gold to facilitate scanning with a field emission scanning electron microscope (SEM). Figure 5.5(a) shows a SEM photomicrograph of LP2 after this process. The surface of the ceramic is relatively rough at a microscopic scale while the surface of the polymer is smoother, indicating that grain pull-out may be occurring from the ceramic. However, there is little evidence of any physical discontinuity at the ceramic-polymer boundary.

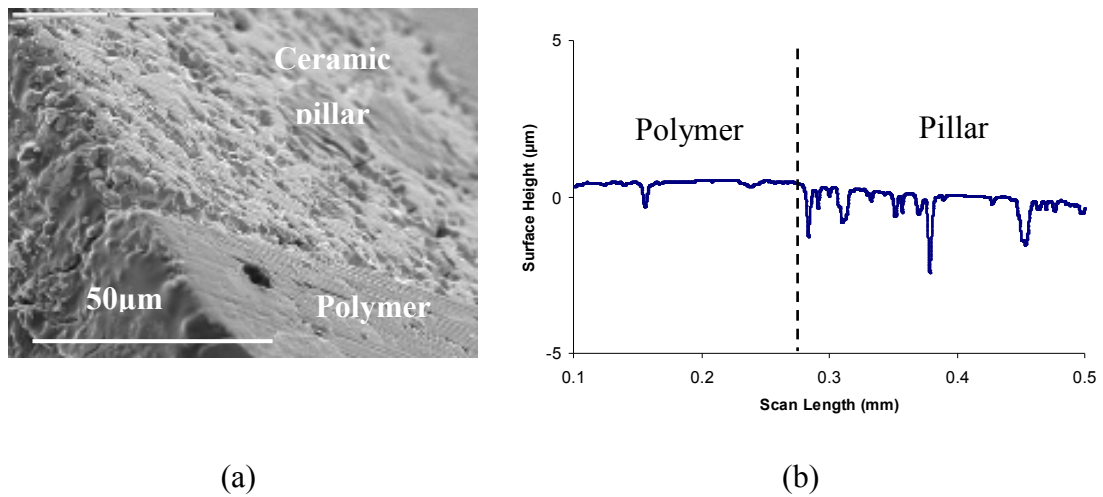


Figure 5. 4: (a) SEM photomicrograph of boundary between ceramic pillar and polymer matrix in Sample LP2 and (b) corresponding surface profile.

Further investigation of surface quality of LP2 was undertaken using the DekTak 3ST surface profiler. A scan of length 500 μm was taken including the boundary between ceramic pillar and polymer matrix. This is shown in Figure 5.5(b).

The height difference between the pillar and polymer is limited to less than 1 μm and is therefore small enough to be suitable for high frequency devices. In addition, the overall surface roughness is significantly better than that in Figure 5.4, produced with conventional lapping, with deviation not exceeding 3 μm.

Lapping vs. UPG for micromoulded composites

As micromoulded composites are central to the work of this thesis, UPG was also tested on a sample of micromoulded composite, and compared to a micromoulded composite prepared by traditional lapping. Sample LP3a was thinned using standard lapping and Sample LP3b was thinned using UPG. Surface profiles from LP3a after lapping and LP3b after UPG are shown in Figure 5.6. Both samples show good surface flatness compared to measurements taken from the standard dice-and-fill piezocomposite. This is attributed in part to the smaller grain size and increased density of VPP PZT giving less grain pull-out. This has been shown to be an advantage of the VPP process. It can be seen that UPG produces a slightly better surface finish than conventional lapping. The surface deviation on sample LP3a is

almost $\pm 2 \mu\text{m}$ compared to around $\pm 1 \mu\text{m}$ for LP3b. Clear periodicity can also be seen on the lapped sample, LP3a, suggesting less discontinuity between ceramic pillars and binding polymer in LP3b than in LP3a.

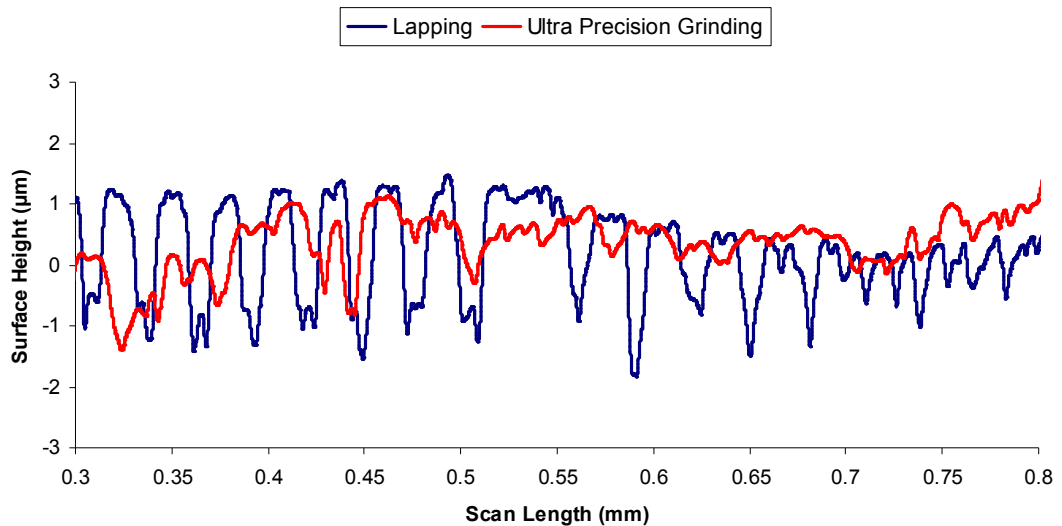


Figure 5. 5: Surface profiles from LP3a (blue line) and LP3b (red line).

5.3. Active materials: standard composite SC1

A composite material of volume fraction 0.3 was fabricated from PZ27 (PZT-5A) (Ferroperm, Kvistgaard, Denmark) and epoxy (RX771) using the dice-and-fill process. This was characterised using an impedance analyser and measured piezoelectric properties were verified using a one-dimensional model. The characterisation procedure used for piezocomposites in this work is described in more detail in Sections 4.5 and 4.7. The key objective of this specific investigation was to confirm, using a well-understood piezoelectric material, that the one dimensional model could be used to accurately characterise composite transducer materials. This would allow measurements of piezoelectric properties of micromoulded composites measured experimentally to be verified. Experimental measurements were therefore compared with simulations derived by two means. The first simulation used parameters derived directly from electrical impedance measurements made on the composite. The second used parameters calculated using

Smith and Auld composite homogenisation calculations, from parameters for the two constituent materials, PZ27 and RX771.

The physical characteristics of this sample are given in Table 5.1, electrical impedance spectroscopy simulation and experimentally measured results are shown in Figure 5.7, and piezoelectric parameters derived from these measurements are given in Table 5.2.

TABLE 5. 1: PHYSICAL CHARACTERISTICS OF SC1

Parameter	Value
Area (m ²) / shape	2.31 x 10 ⁻⁵ / square
Thickness (μm)	320
Piezoelectric Material	PZ27
Polymer	RX771
Volume fraction	0.3
Pillar shape	Square
Pillar width (μm) / Aspect Ratio	200 / 1.5
Electrodes	Silver paint

The main thickness mode resonance of this sample occurs at approximately 5 MHz. As can be seen, the one-dimensional model derived from impedance measurements fits extremely closely, while the simulation of impedance from Smith and Auld composite homogeneity calculations also matches well

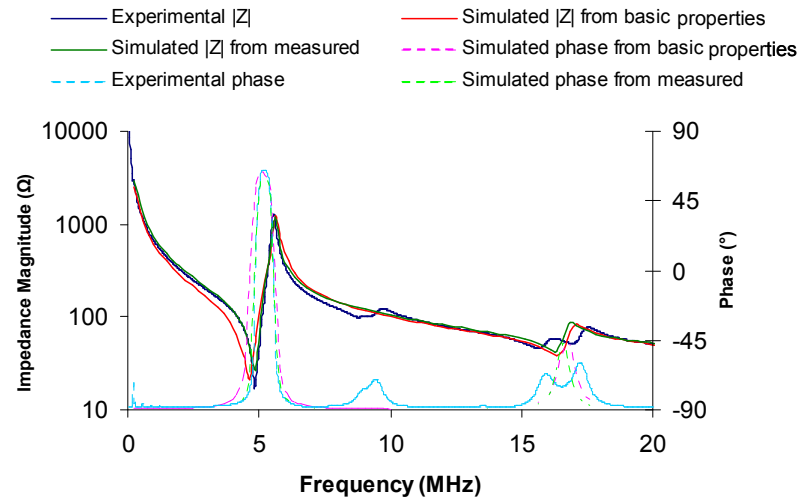


Figure 5. 6: Electrical impedance spectroscopy measurement and simulation for SC1

TABLE 5. 2: CALCULATED PIEZOELECTRIC PARAMETERS OF SC1

Parameter	Measured value	Fitted value	% difference	Nominal value	% difference
ρ (kg m ⁻³)	3240	3240	0	3120	+4
v (ms ⁻¹)	3560	3560	0	3600	-1
Z (MRayl)	11.55	11.55	0	11.25	+3
c_{33}^D (Nm ⁻²)	4.11×10^{10}	4.11×10^{10}	0	4.05×10^{10}	+2
c_{33}^E (Nm ⁻²)	2.95×10^{10}	2.95×10^{10}	0	2.55×10^{10}	+14
ϵ_R^S	246	246	0	259	-5
e_{33} (Cm ⁻¹)	5.04	5.04	0	5.86	-16
h_{33} (Vm ⁻¹)	2.31×10^9	2.31×10^9	0	2.56×10^9	-11
d_{33} (mV ⁻¹)	[#] N/M	N/M	0	1.45×10^{-10}	N/M
k_T	0.53	0.53	0	0.61	-14
α at 1 MHz (dB cm ⁻¹)	N/M	N/M	N/M	3.13	N/M

[#] N/M = Not measured

Most of the experimentally derived properties listed in Table 5.2 match nominal values to within a few percent, the notable exceptions being c_{33}^E , e_{33} and k_T . The discrepancies in these parameters may be explained by further inspection of the experimental impedance measurements. A spurious resonance occurs at around 10 MHz: the cause is a lateral intra-pillar mode. The pillars within the composite do not have sufficiently great height-width aspect ratio. This may contribute to poorer energy conversion, because pillars with low aspect ratio have reduced value of k_{33} , hence the composite has lower k_T . This could also be due to other factors e.g. some depoling during fabrication, or non-ideal properties of that particular sample of PZ27. The values of c_{33}^E and e_{33} are not independent of k_T so all are altered. However, it is reasonable to state that the two objectives have been satisfied. Firstly, piezoelectric parameters measured experimentally are well matched to those produced theoretically by simulations from nominal properties of PZ27 and RX771. Secondly, simulations produced from direct measurements of composite materials are reasonably well matched to models produced from Smith and Auld equations for composite homogeneity.

This is particularly useful when characterisation of novel micromoulded composites for this thesis is considered. As discussed previously, traditional characterisation of the active phase of these materials is impossible. The alternative method described here will allow these composites to be characterised.

5.4. Active Materials: fibre composites

A novel design for composite manufacture is to use extruded small diameter fibres, which are then packed together and bonded in a polymer matrix, as described in Section 4.1. Fibre composites have intrinsically high volume fraction if packed carefully. PZT fibres were produced with the VPP process and used to fabricate composites, which were subsequently characterised experimentally. The fibre composites tested were low frequency and made by a different process to micromoulded VPP composites. However, VPP fibre composite performance is a useful indicator of the performance of micromoulded VPP composites. Fibre

composites used in these experiments have been fabricated by bonding of PZT fibres in a RX771 polymer matrix. The PZT fibres used were made by extrusion of green state PZT, made using viscous polymer processing (VPP). Circular fibres of diameter 250 μm and 100 μm were available from which three active piezocomposites, all of volume fraction 0.3, were fabricated. Piezocomposites of thickness 990 μm and 240 μm were made from 250 μm fibres, with the intention of comparing piezocomposites with ideal pillar aspect ratio (i.e. greater than three) and non-ideal aspect ratio. A piezocomposite of thickness 200 μm was made from 100 μm fibres to allow operational frequency to be increased without greatly compromising pillar aspect ratio.

5.4.1. Results from FC1

The first sample tested, *FC1*, was lapped to a thickness of 990 μm . The physical characteristics of *FC1* are given in Table 5.3, electrical impedance spectroscopy simulation and experimentally measured results are shown in Figure 5.8, and piezoelectric parameters derived from these measurements are given in Table 5.4.

TABLE 5. 3: PHYSICAL CHARACTERISTICS OF FC1

Parameter	Value
Area (m^2) / Shape	2.27×10^{-6} / Circle
Thickness (μm)	990
Piezoelectric Material	PZT 5H (TRS600FG)
Polymer	RX771
Volume Fraction	0.3
Pillar shape	Circular
Pillar diameter (μm) / Aspect ratio	250 / 3.96
Electrodes	Cr-Au thin film

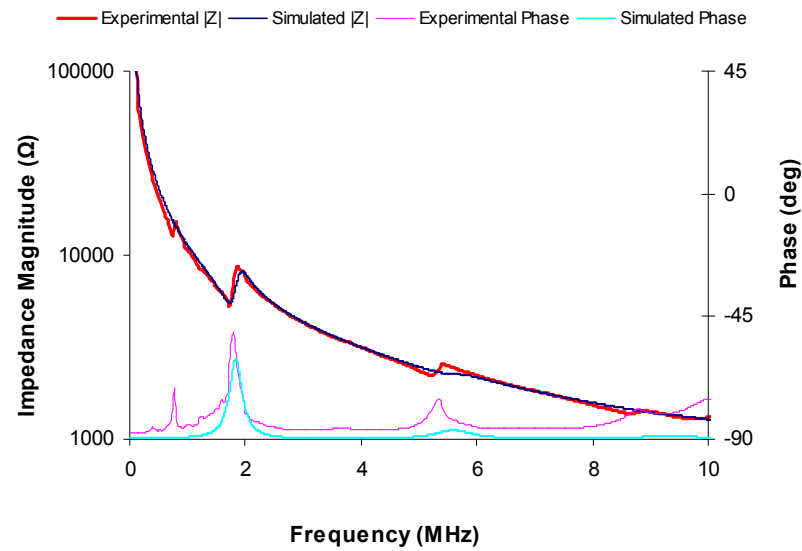


Figure 5. 7: Electrical impedance spectroscopy experimental measurement and simulation for FC1

Clear resonant activity can be seen at approximately 2 MHz. Simulated impedance magnitude and phase from fitted data show a close fit to experimental data. Fitted values correspond well to measured values with the exception of e_{33} , h_{33} and k_T . These are all within 20% of the measured value however.

TABLE 5. 4: CALCULATED PIEZOELECTRIC PARAMETERS OF FC1

Parameter	Measured Value	Fitted Value	% difference
ρ (kg m ⁻³)	3160	3160	0
v (ms ⁻¹)	3710	3719	<1
Z (MRayl)	11.7	11.8	1
c_{33}^D (Nm ⁻²)	4.36×10^{10}	4.37×10^{10}	<1
c_{33}^E (Nm ⁻²)	3.81×10^{10}	4.00×10^{10}	5
ϵ_R^S	617	617	0
e_{33} (Cm ⁻¹)	5.5	4.5	20
h_{33} (Vm ⁻¹)	9.98×10^8	8.24×10^8	18
d_{33} (mV ⁻¹)	1.26×10^{-10}	1.03×10^{-10}	18
k_T	0.35	0.29	18
α (dB cm ⁻¹ @ 1 MHz)	N/M	10	N/M

The piezoelectric properties of this fibre composite are comparable with standard composites, in the case of Z and c_{33} . k_T is significantly lower than expected in a composite material, as are e_{33} and h_{33} , but ϵ_R^S is higher than would be expected in a similar dice-and-fill composite, making this material useful for smaller area devices. The attenuation coefficient of this sample could not be measured experimentally. The value of attenuation used for modelling is higher than might be expected, however. Spurious resonances in this composite do exist e.g. at approximately 1 MHz, but these are of significantly smaller amplitude than the main thickness mode resonance.

5.4.2. Results from FC2

A second fibre composite sample was lapped to a thickness of 240 μm . This sample was denoted FC2. The physical characteristics are given in Table 5.5, electrical impedance spectroscopy simulation and experimentally measured results are shown in Figure 5.9, and piezoelectric parameters derived from these measurements are given in Table 5.6.

TABLE 5. 5: PHYSICAL CHARACTERISTICS OF FC2

Parameter	Value
Area (m ²) / Shape	2.27 x10 ⁻⁶ / Circle
Thickness (μm)	240
Piezoelectric Material	PZT 5H (TRS600FG)
Polymer	RX771
Volume Fraction	0.3
Pillar shape	Circular
Pillar diameter (μm) / Aspect ratio	250 / 0.96
Electrodes	Cr-Au thin film

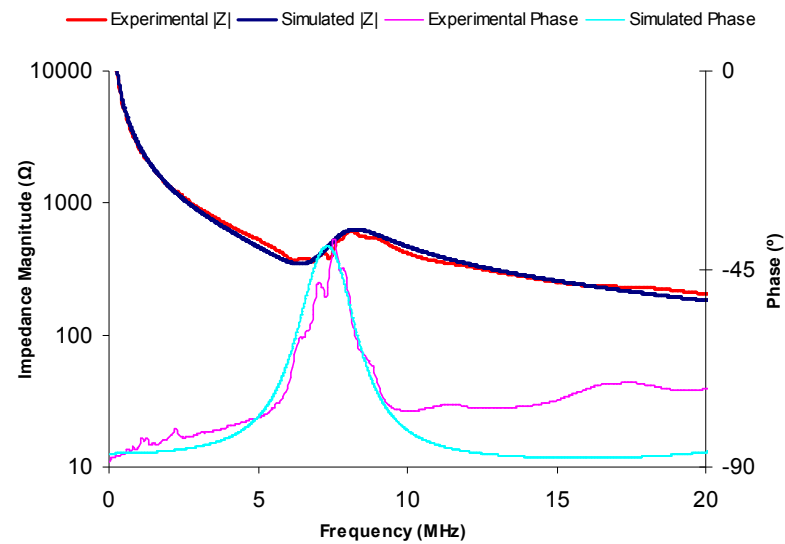


Figure 5. 8: Electrical impedance spectroscopy experimental measurement and simulation for FC2

TABLE 5. 6: CALCULATED PIEZOELECTRIC PARAMETERS OF FC2

Parameter	Measured Value	Fitted Value	% difference
ρ (kg m ⁻³)	3160	3160	0
v (ms ⁻¹)	3890	3830	-2
Z (MRayl)	12.1	11.9	-2
c_{33}^D (Nm ⁻²)	4.72×10^{10}	4.57×10^{10}	-3
c_{33}^E (Nm ⁻²)	3.18×10^{10}	3.30×10^{10}	+4
ϵ_R^S	473	500	+6
e_{33} (Cm ⁻¹)	8.03	7.50	-7
h_{33} (Vm ⁻¹)	1.91×10^9	1.65×10^9	-14
d_{33} (mV ⁻¹)	1.70×10^{-10}	1.64×10^{-10}	4
k_T	0.57	0.53	-8
α (dB cm ⁻¹ @ 1 MHz)	N/A	20	N/A

FC2 showed a resonant frequency of approximately 8 MHz. The simulated data fits well to the experimental data and piezoelectric properties are also reasonably close to those expected for a composite of this sort, more so than *FC1* in the case of k_T , e_{33} and ϵ_R^S . As before h_{33} is again lower than a standard composite. The values of piezoelectric properties generated by the theoretical model are within a few percent of the experimentally determined properties, apart from the case of h_{33} . This is because the calculated value of h_{33} is derived from several other parameters, leading to an intrinsically greater error.

The pillars in this sample are of approximately the same height as width, meaning that lateral modes will certainly be present but will not be detected in the impedance measurements because they are of the same frequency as the thickness mode. They also cannot be predicted using the one-dimensional model. Similarly, it is not possible to accurately compare the performance of *FC1* with *FC2* as had been hoped. This is a limitation of the one-dimensional model: the losses due to lateral modes cannot be assessed. Ideally, use of one-dimensional modelling should be limited to cases where the aspect ratio is large enough to separate thickness mode and lateral

mode resonances. In cases where the aspect ratio is less, finite element analysis should be used.

5.4.3. Results from FC3

A further fibre composite, sample *FC3*, was fabricated using smaller diameter fibres: 100 μm rather than 250 μm . It was initially lapped to a thickness of 200 μm , and tested: at this point it was denoted *FC3a*. Physical characteristics of *FC3a* are given in Table 5.7. Electrical impedance spectroscopy simulation and experimentally measured results are shown in Figure 5.10, and piezoelectric parameters derived from these measurements are given in Table 5.8.

TABLE 5. 7: PHYSICAL CHARACTERISTICS OF FC3a

Parameter	Value
Area (m^2) / Shape	2.27×10^{-6} / Circle
Thickness (μm)	200
Piezoelectric Material	PZT 5H (TRS600FG)
Polymer	RX771
Volume Fraction	0.3
Pillar shape	Circular
Pillar diameter (μm) / Aspect ratio	100 / 2
Electrodes	Cr-Au thin film

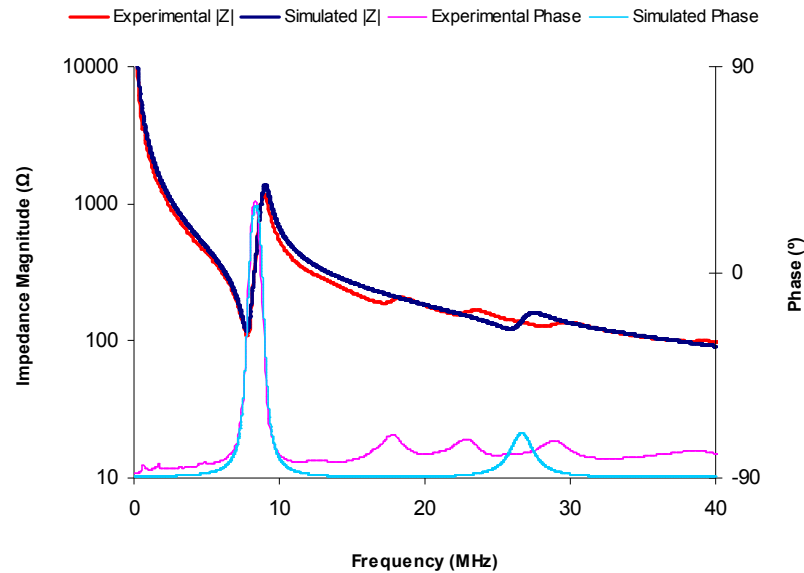


Figure 5. 9: Electrical impedance spectroscopy experimental measurement and simulation for FC3a

TABLE 5. 8: CALCULATED PIEZOELECTRIC PARAMETERS OF FC3a

Parameter	Measured Value	Fitted Value	% difference
ρ (kg m ⁻³)	3170	3170	0
v (ms ⁻¹)	3610	3580	-1
Z (MRayl)	11.5	11.4	-1
c_{33}^D (Nm ⁻²)	4.14×10^{10}	4.06×10^{10}	-2
c_{33}^E (Nm ⁻²)	2.96×10^{10}	2.96×10^{10}	< +1
ϵ_R^S	391	420	+7
e_{33} (Cm ⁻¹)	6.40	6.40	< +1
h_{33} (Vm ⁻¹)	1.85×10^9	1.72×10^9	-7
d_{33} (mV ⁻¹)	1.55×10^{-10}	1.58×10^{-10}	2
k_T	0.53	0.52	-3
α (dB cm ⁻¹ @ 1 MHz)	N/M	5.5	N/M

As with other samples, the fit of theoretical data to experimental data is good, and the piezoelectric properties measured and used for simulation are matched to within a few percent. The values are also very close to what would be expected for a comparable dice-and-fill composite, apart from h_{33} which is lower, as seen in

previous samples. Unlike previous samples, the resonant variations in impedance of this sample are much less attenuated than before.

Finally, sample *FC3* was lapped further to a thickness of 55 μm , and denoted *FC3b*. The physical characteristics of *FC3b* are given in Table 5.9 and experimentally measured electrical impedance spectroscopy results are shown in Figure 5.11. The aspect ratio of pillars in this sample is well below that normally required for a 1-3 composite. Clear pulse echo signals were detected, as shown in Figure 5.12, with frequency around 17 MHz which corresponds with the electrical impedance spectroscopy measurement. For a composite of this thickness and composition, the resonant frequency would be expected to be around 33 MHz, and resonance can be seen at this frequency in the electrical impedance spectroscopy and pulse echo measurements. As discussed earlier in this section, one-dimensional models cannot simulate the influence of non-ideal pillar aspect ratios, so it is difficult to verify the source of the resonant activity shown and hence explain the dominant resonance at 17 MHz. No table of properties is given for this sample for the same reason. Pulse-echo measurement data was obtained; this is shown in Figure 5.12.

This particular composite sample would not work effectively due to the pillars having greater width than height. For fibre composites to be used in high frequency transducers, fibres of significantly smaller diameter than those used in the work reported here would have to be fabricated, e.g. 10 μm for 50 MHz. Fibre composites are a cost effective way of producing active piezocomposite layers for HFUS transducers and absolute impedance magnitudes are of the order of 100 Ω , hence convenient for use with instrumentation, indicating further work to reduce fibre diameter would be beneficial.

TABLE 5. 9: PHYSICAL CHARACTERISTICS OF FC3B

Parameter	Value
Area (m ²) / Shape	2.27 x 10 ⁻⁶ / Circle
Thickness (μm)	55
Piezoelectric Material	PZT 5H (TRS600FG)
Polymer	RX771
Volume Fraction	0.3
Pillar shape	Circular
Pillar diameter (μm) / Aspect ratio	100 / 0.55
Electrodes	Cr-Au Thin film

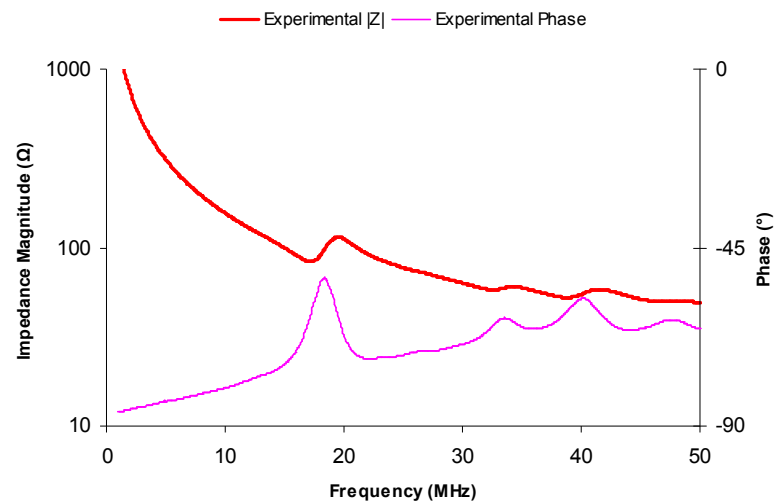


Figure 5. 10: Electrical impedance spectroscopy measurement for FC3b

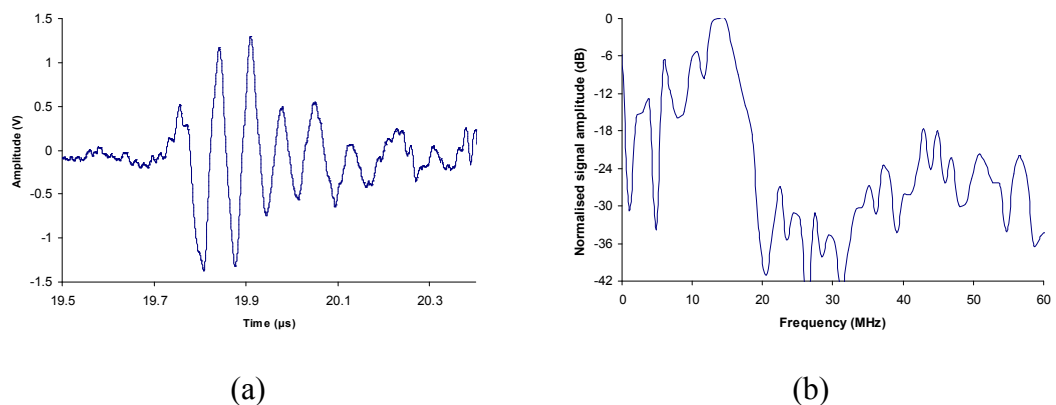


Figure 5. 11: Pulse-echo signal from FC3b in (a) time-domain and (b) frequency domain.

5.5. Active materials: micromoulded composites

The main aim of this thesis is determination of the potential for composites made by micromoulding of VPP PZT to be used as active materials for HFUS transducers. Several micromoulded composite samples were tested to determine piezoelectric properties of the material. Results from six of these samples are given in this section.

For each sample, the following information is provided: a table of physical characteristics; a figure showing electrical impedance spectroscopy measurement and fitted simulation of electrical impedance; a table listing piezoelectric properties measured directly from the composite sample, piezoelectric properties used in the fitted simulation and theoretical piezoelectric properties of a standard PZT-5H (TRS600) of similar volume fraction to the composite sample for purposes of comparison. The percentage difference between measured property and fitted property, or nominal property is also given. Where available, a measurement of pulse-echo response from the composite is also provided.

5.5.1. Results from MC1

The first, very early, MC tested was denoted MC1 and is shown in Figure 5.13. This composite was made with only 18 pillars of width around 90 μm , and had a very low volume fraction, of less than 10% ceramic. The physical characteristics of MC1 are given in Table 5.10, simulated and experimentally measured electrical impedance magnitude and phase data are shown in Figure 5.14 and corresponding piezoelectric properties are given in Table 5.11.

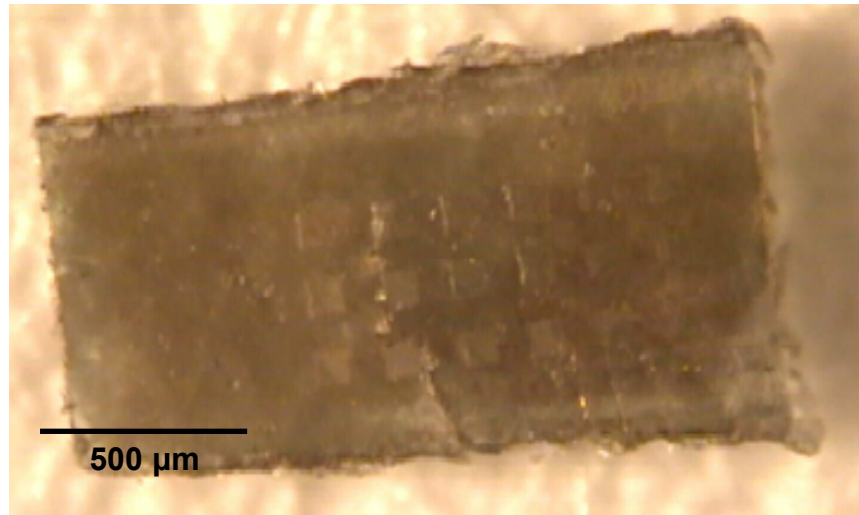


Figure 5. 12: Photograph of piezocomposite sample MC1.

TABLE 5. 10: PHYSICAL CHARACTERISTICS OF MC1

Parameter	Value
Area (m ²) / Dimensions (mm)	1.70 x 10 ⁻⁶ / 1.0 x 1.7
Thickness (μm)	140
Piezoelectric Material	PZT 5H (TRS600FG)
Polymer	RX771
Volume Fraction	0.08
Pillar shape	Square
Pillar Size (μm) / Aspect ratio	90 / 1.55
Electrodes	Cr-Au Thin film

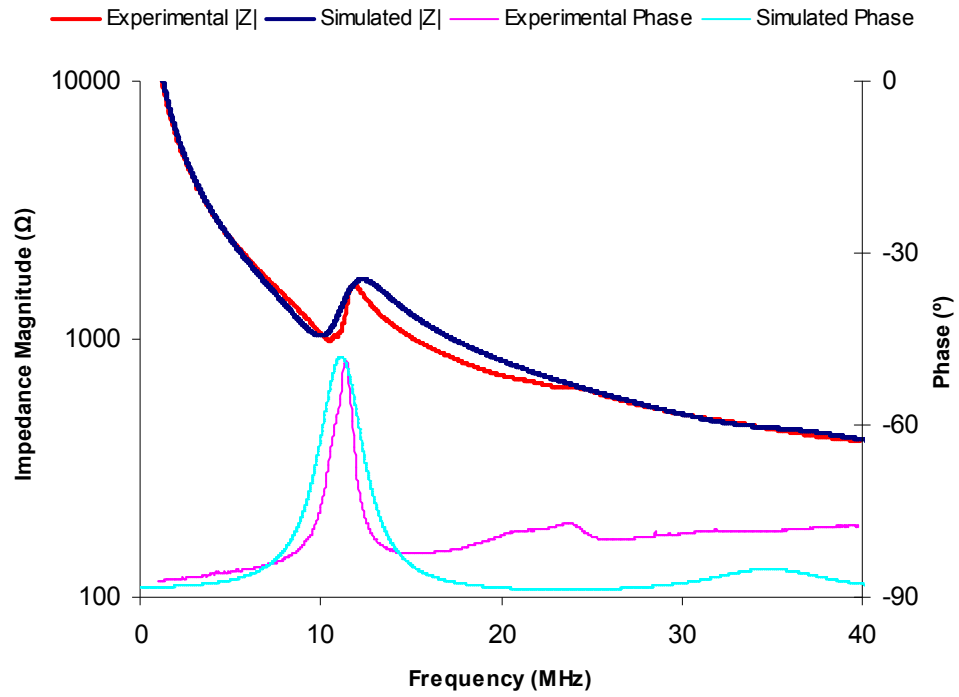


Figure 5. 13: Electrical impedance spectroscopy experimental measurement and simulation for MC1

TABLE 5. 11: CALCULATED PIEZOELECTRIC PARAMETERS OF MC1

Parameter	Measured Value	Fitted Value	% difference	Nominal Value (TRS600 8%)	% difference
ρ (kg m ⁻³)	1610	1610	0	1680	4
v (ms ⁻¹)	3340	3310	1	3380	1
Z (MRayl)	5.36	5.31	1	5.67	6
c_{33}^D (Nm ⁻²)	1.79×10^{10}	1.76×10^{10}	2	1.92×10^{10}	7
c_{33}^E (Nm ⁻²)	1.32×10^{10}	1.4×10^{10}	6	1.32×10^{10}	0
ϵ_R^S	101	101	<1	111	10
e_{33} (Cm ⁻¹)	2.04	1.80	12	2.42	19
h_{33} (Vm ⁻¹)	2.28×10^9	2.01×10^9	12	2.45×10^9	7
d_{33} (mV ⁻¹)	1.14×10^{-10}	1.02×10^{-10}	11	1.26×10^{-10}	11
k_T	0.51	0.45	12	0.56	10
α (dB cm ⁻¹ @ 1 MHz)	N/M	20	N/M	4.0	N/M

It can be seen that the theoretical data is a reasonably good fit to experimental data, and that most of the piezoelectric properties measured correspond to within a few percent of values used in the theoretical fitted models, and within 10% of nominal values predicted for this composite. There are discrepancies between measured values of e_{33} , h_{33} , and k_T and theoretical values; in each case the measured value is around 25% less than the nominal value and 12% less than the fitted value. The value of attenuation is significantly higher than expected, as seen in a number of previously studied composites. A pulse-echo signal was obtained from MC1; this is shown in Figure 5.15.

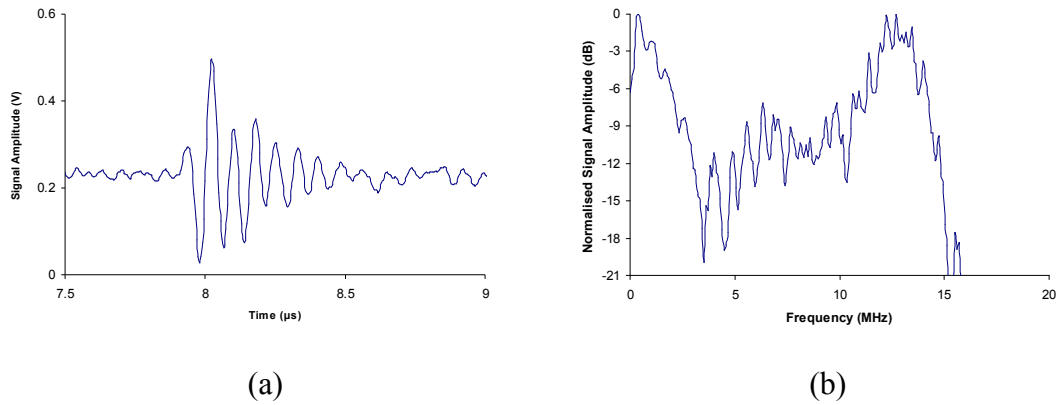


Figure 5.14: Pulse-echo signal from MC1.

5.5.2. Results from MC2

A second MC, denoted MC2, was tested. This composite had ceramic volume fraction of 20%, with ceramic pillars of width 20 μm. Photographs of the composite are shown in Figures 5.16a and 5.16b. The physical characteristics of MC2 are given in Table 5.12, simulated and experimental electrical impedance magnitude and phase data are shown in Figure 5.17 and corresponding piezoelectric properties are given in Table 5.13.

TABLE 5.12: PHYSICAL CHARACTERISTICS OF MC2

Parameter	Value
Area (m ²) / Dimensions (mm)	3.13 x 10 ⁻⁶ / 1.77 x 1.77
Thickness (μm)	75
Piezoelectric Material	PZT 5H (TRS600FG)
Polymer	RX771
Volume Fraction	0.2
Pillar shape	Square
Pillar Size (μm) / Aspect ratio	20 / 3.8
Electrodes	Cr-Au Thin film

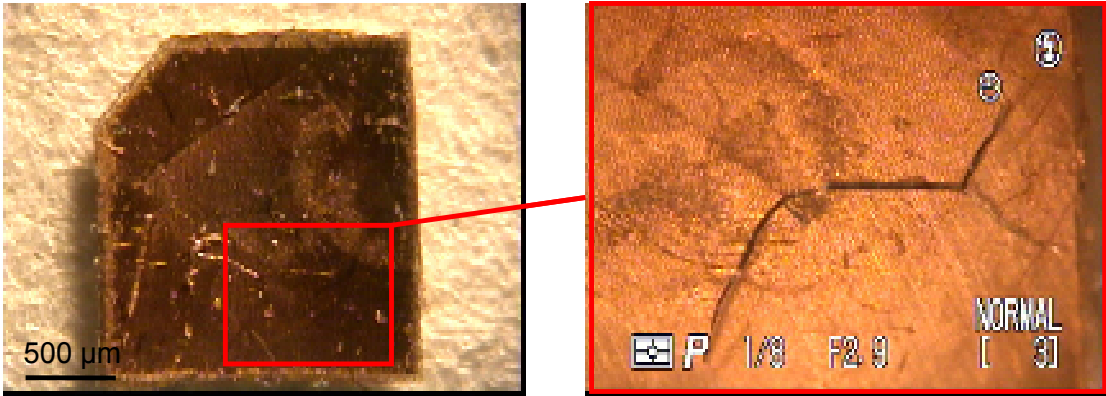


Figure 5. 15: Photographs of Composite MC2, including close up of small crack.

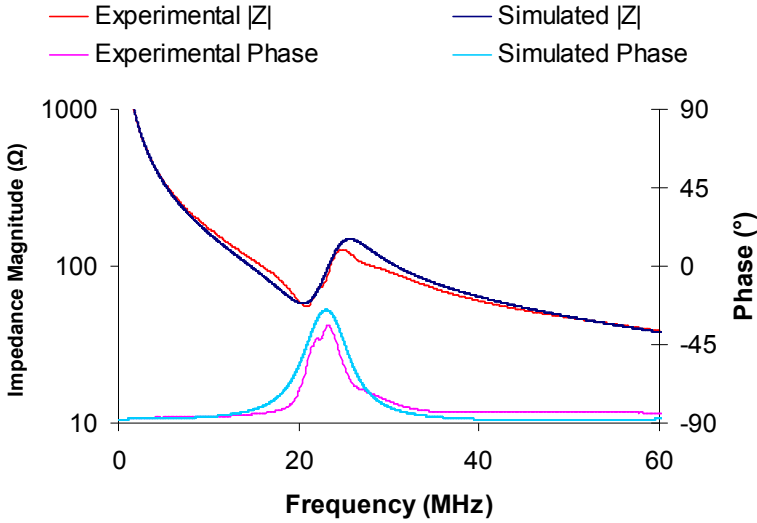


Figure 5. 16: Electrical impedance spectroscopy measurement and simulation for MC2

TABLE 5. 13: CALCULATED PIEZOELECTRIC PARAMETERS OF MC2

Parameter	Measured Value	Fitted Value	% difference	Nominal Value (TRS600 23%)	% difference
ρ (kg m ⁻³)	2700	2700	0	2700	0
v (ms ⁻¹)	3720	3730	<1	3710	<1
Z (MRayl)	10.0	10.1	1	10.0	0
c_{33}^D (Nm ⁻²)	3.73×10^{10}	3.75×10^{10}	<1	3.72×10^{10}	<1
c_{33}^E (Nm ⁻²)	2.49×10^{10}	2.7×10^{10}	9	2.02×10^{10}	19
ϵ_R^S	181	181	0	320	76
e_{33} (Cm ⁻¹)	4.46	4.1	8	6.94	56
h_{33} (Vm ⁻¹)	2.79×10^9	2.56×10^9	8	2.45×10^9	13
d_{33} (mV ⁻¹)	1.20×10^{-10}	1.09×10^{-10}	9	1.87×10^{-10}	55
k_T	0.58	0.52	10	0.68	18
α (dB cm ⁻¹) @ 1 MHz	N/M	15	N/M	3.07	N/M

The fit of theoretical impedance data to experimentally obtained data is reasonably good. All parameters used in the fitted model match to within 10% of the experimentally measured parameters, with k_T slightly lower than measured and associated reductions in e_{33} and h_{33} and a larger c_{33}^E .

The experimental parameters differ more significantly from nominal parameters calculated for an equivalent dice-and-fill composite, in this case assumed to have volume fraction 23%. The values of k_T , h_{33} and c_{33}^E measured experimentally for this sample differ by between 10-20%. ϵ_R^S and e_{33} are significantly lower however, by 76% and 56% respectively, with the value of ϵ_R^S , 181, significantly lower than expected for a composite of this volume fraction. e_{33} is calculated from measurement of permittivity and so would be expected to be lower too.

As discussed previously, ceramic pillars fabricated by micromoulding do not necessarily have identical properties to those made from bulk materials by dice-and-fill. However, as shown in Figure 5.16, sample MC2 was cracked, which made estimation of active area difficult because it was difficult to tell whether a section of the composite had become electrically isolated. This may have compromised the determination of ϵ_R^S for this sample. The value of attenuation used for the fitted model is significantly higher than the nominal value, as has been seen in most previous cases. Pulse-echo signals were also successfully acquired for this sample as shown in Figure 5.18.

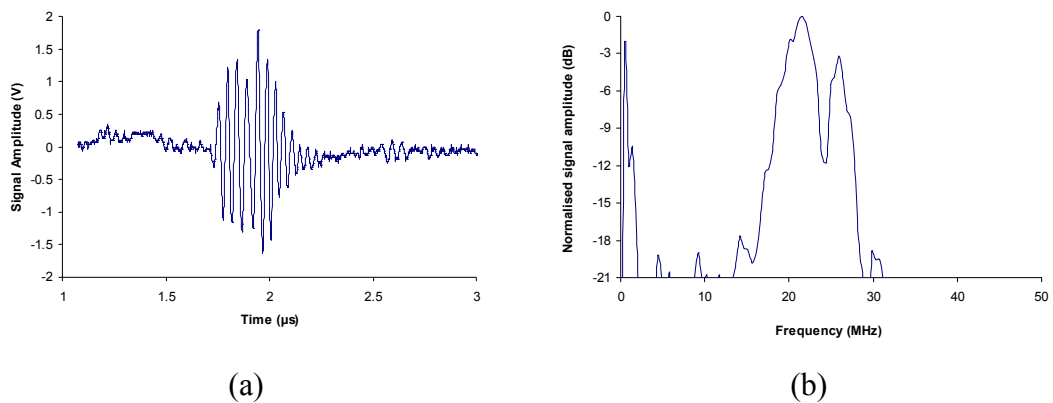


Figure 5. 17: Pulse-echo signal from MC2 in (a) time domain and (b) frequency domain.

There is a clear pulse echo signal received from MC2. The frequency spectrum shows two peaks around the main resonance at 20-25 MHz: this can also be seen in the impedance spectra. Again this may be due to the crack in the sample.

5.5.3. Results from MC3

A further composite was tested, denoted MC3, and is shown in Figure 5.19. This composite had volume fraction of around 20%, with ceramic pillar diameter of approximately 18 μm . The physical characteristics of MC3 are given in Table 5.14, simulated and experimental electrical impedance magnitude and phase data are shown in Figure 5.20 and corresponding piezoelectric properties are given in Table 5.15.

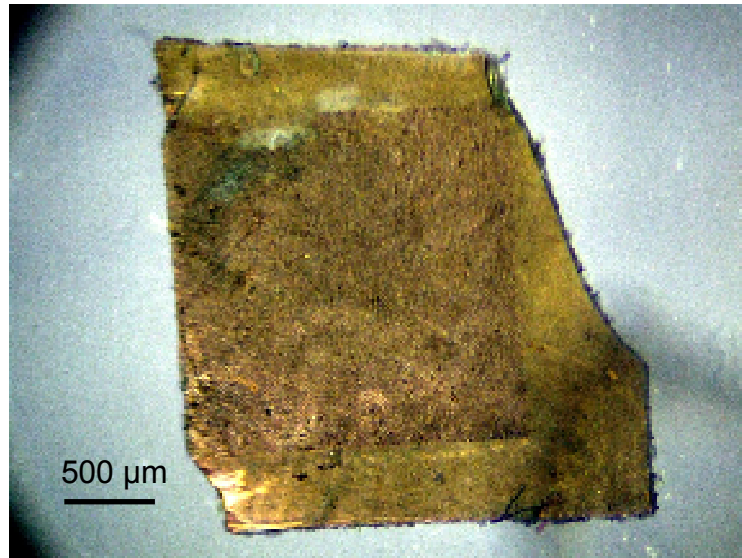


Figure 5. 18: Microscope photograph of MC3

TABLE 5. 14: PHYSICAL CHARACTERISTICS OF MC3

Parameter	Value
Area (m ²) / Dimensions (mm)	6.25 x 10 ⁻⁶ / 2.5 x 2.5
Thickness (μm)	115
Piezoelectric Material	PZT 5H (TRS600FG)
Polymer	RX771
Volume Fraction	0.2
Pillar shape	Circular
Pillar Size (μm) / Aspect ratio	18 / 6.4
Electrodes	Cr-Au Thin film

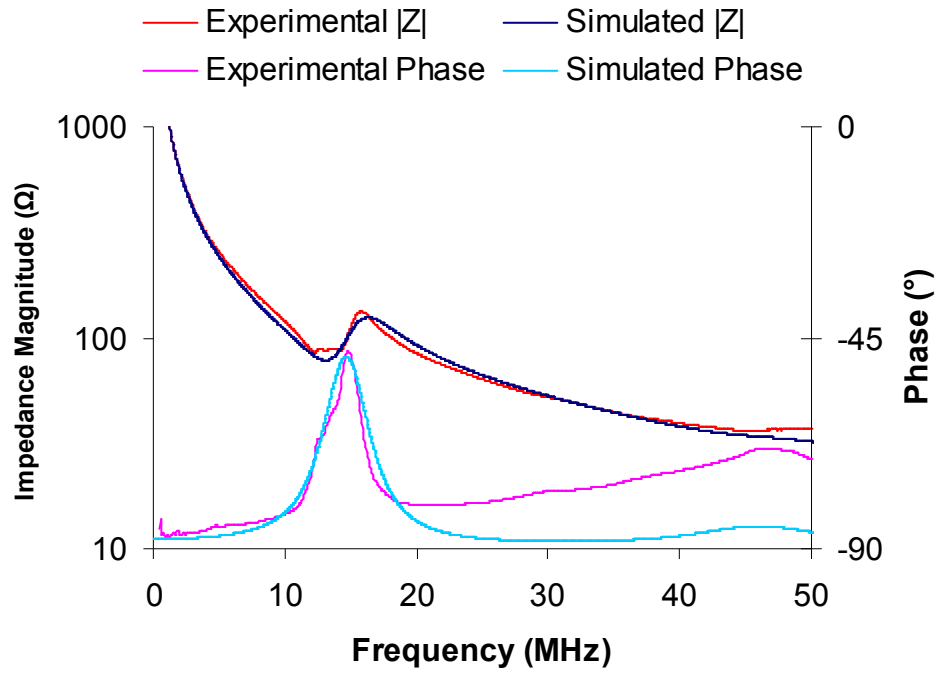


Figure 5. 19: Electrical impedance spectroscopy experimental measurement and simulation for MC3

TABLE 5. 15: CALCULATED PIEZOELECTRIC PARAMETERS OF MC3

Parameter	Measured Value	Fitted Value	% difference	Nominal Value (TRS600)	% difference
ρ (kg m ⁻³)	2350	2350	0	2360	<1
v (ms ⁻¹)	3630	3610	<1	3660	1
Z (MRayl)	8.53	8.48	<1	8.57	<1
c_{33}^D (Nm ⁻²)	3.10×10^{10}	3.06×10^{10}	1	3.11×10^{10}	<1
c_{33}^E (Nm ⁻²)	2.30×10^{10}	2.40×10^{10}	4	1.78×10^{10}	22
ϵ_R^S	205	210	2	251	22
e_{33} (Cm ⁻¹)	3.7	3.5	5	5.43	47
h_{33} (Vm ⁻¹)	2.04×10^9	1.88×10^9	8	2.45×10^9	20
d_{33} (mV ⁻¹)	1.21×10^{-10}	1.14×10^{-10}	6	1.75×10^{-10}	44
k_T	0.49	0.46	6	0.65	33
α (dB cm ⁻¹ @ 1 MHz)	N/M	20	N/M	5.44	N/M

As with MC2, the theoretical data for electrical impedance matches the experimental measurement well, and the parameters used for this model are all within 10% of the values measured. As before k_T , e_{33} and h_{33} are slightly lower than for the theoretical model.

When compared to nominal values for this composite, k_T is again lower than might be expected, by around 30%, and c_{33}^E , h_{33} , and ϵ_R^S all differ by around 20-25%. As was the case with MC2, e_{33} is around 50% lower than predicted by nominal values. However, the values measured for MC3 are approximately consistent with MC2. Attenuation is also very different to the nominal value, as was the case with previously tested composites.

5.5.4. Results from MC4

Sample MC4 was made with ceramic pillars of approximately 20 μm diameter, and had overall volume fraction of around 13 %. The low overall volume fraction in this case was caused by part of the sample missing pillars: this can be seen on Figure 5.21. This sample was used for the investigation into UPG, as discussed in Section 5.2.2. The physical characteristics of MC4 are given in Table 5.16, simulated and experimental electrical impedance magnitude and phase data is shown in Figure 5.22 and corresponding piezoelectric properties are given in Table 5.17.

TABLE 5. 16: PHYSICAL CHARACTERISTICS OF MC4

Parameter	Value
Area (m^2) / Dimensions (mm)	6.72×10^{-6} / 2.4 x 2.8
Thickness (μm)	79
Piezoelectric Material	PZT 5H (TRS600FG)
Polymer	RX771
Volume Fraction	0.13
Pillar shape	Hexagonal
Pillar Size (μm) /Aspect ratio	20 / 4
Electrodes	Cr-Au Thin film

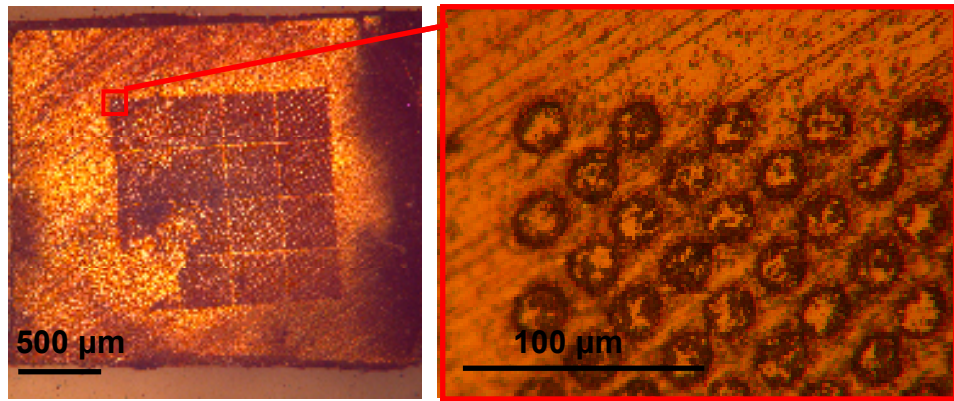


Figure 5. 20: Microscope photographs showing MC4 and close-up of a section of pillars.

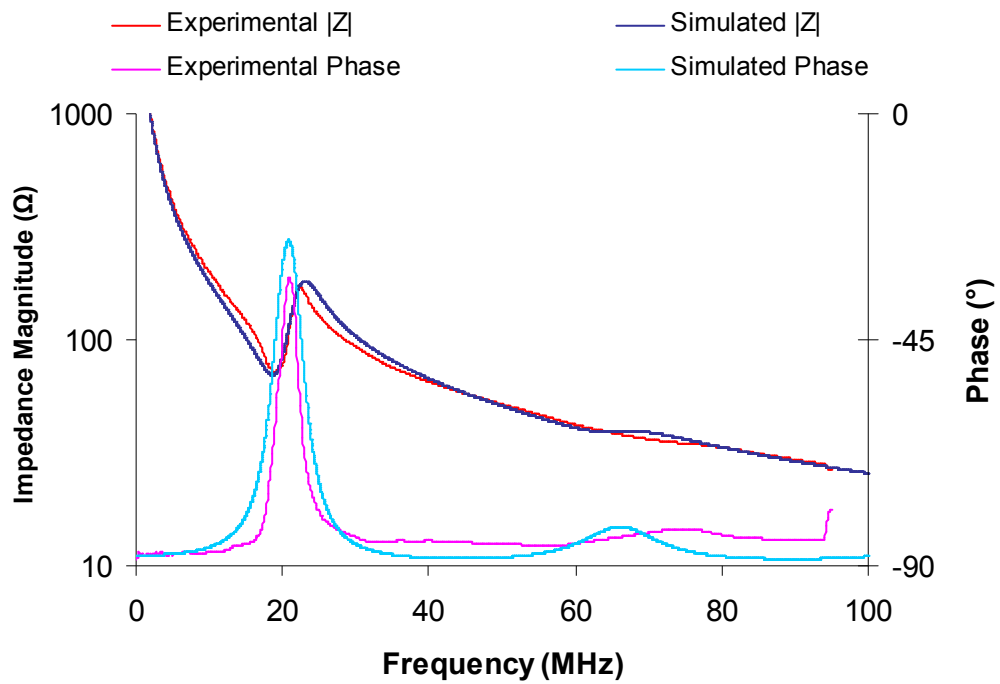


Figure 5. 21: Electrical impedance spectroscopy experimental measurement and simulation for MC4

TABLE 5. 17: CALCULATED PIEZOELECTRIC PARAMETERS OF MC4

Parameter	Measured value	Fitted value	% Difference	Nominal value	% Difference
ρ (kg m ⁻³)	2020	2020	0	2020	0
v (ms ⁻¹)	3530	3540	<1	3530	0
Z (MRayl)	7.12	7.14	<1	7.12	0
c_{33}^D (Nm ⁻²)	2.51×10^{10}	2.52×10^{10}	<1	2.51×10^{10}	0
c_{33}^E (Nm ⁻²)	1.75×10^{10}	1.85×10^{10}	6	1.55×10^{10}	11
ϵ_R^S	81.1	81.1	0	181	123
e_{33} (Cm ⁻¹)	2.34	2.20	6	3.93	68
h_{33} (Vm ⁻¹)	3.26×10^9	3.06×10^9	6	2.45×10^9	25
d_{33} (mV ⁻¹)	9.31×10^{-11}	8.7×10^{-11}	7	1.56×10^{-10}	67
k_T	0.55	0.52	5	0.62	13
α (dB cm ⁻¹ @ 1 MHz)	N/M	15	N/M	3.6	N/M

The simulated electrical impedance data fits well to experimental data and, as with the majority of other composites tested, experimentally derived properties match well to those used in the simulation of MC4, to within 10% in all cases. Nominal values for the composite differ significantly however. k_T is lower than expected for a standard composite of this volume fraction, while c_{33}^E and h_{33} are lower and higher, respectively. Measurements of e_{33} and ϵ_R^S differ most significantly, being less than 60% and 50% of the respective nominal values calculated, although the measured values correspond reasonably well to measurements of other composites of low volume fraction. The value of attenuation used for the model is significantly lower than the nominal value, as has been seen previously.

5.5.5. Results from MC6

The final composite made and tested is denoted MC6. This composite was of volume fraction just under 0.5 and contained circular pillars of around 25 μm width. The sample had thickness of 53 μm , and resonant frequency of around 38 MHz.

Photographs of MC6 are given in Figure 5.23. The physical characteristics of MC6 are given in Table 5.18, simulated and experimental electrical impedance magnitude and phase data are shown in Figure 5.24 and corresponding piezoelectric properties are given in Table 5.19.

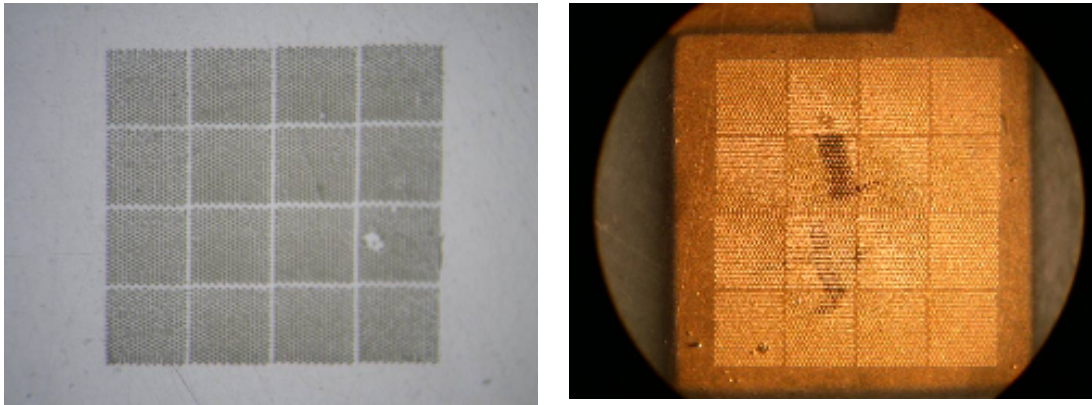


Figure 5. 22: Microscope photographs of MC6.

TABLE 5. 18: PHYSICAL CHARACTERISTICS OF MC6

Parameter	Value
Area (m ²) / Dimensions	3.02 x 10 ⁻⁶ / 1.81 x 1.67 mm
Thickness (μm)	53
Piezoelectric Material	PZT 5H (TRS600FG)
Polymer	Epofix
Volume Fraction	0.46
Pillar shape	Circular
Pillar Size (μm) / Aspect ratio	25 / 1.8
Electrodes	Cr-Au Thin film

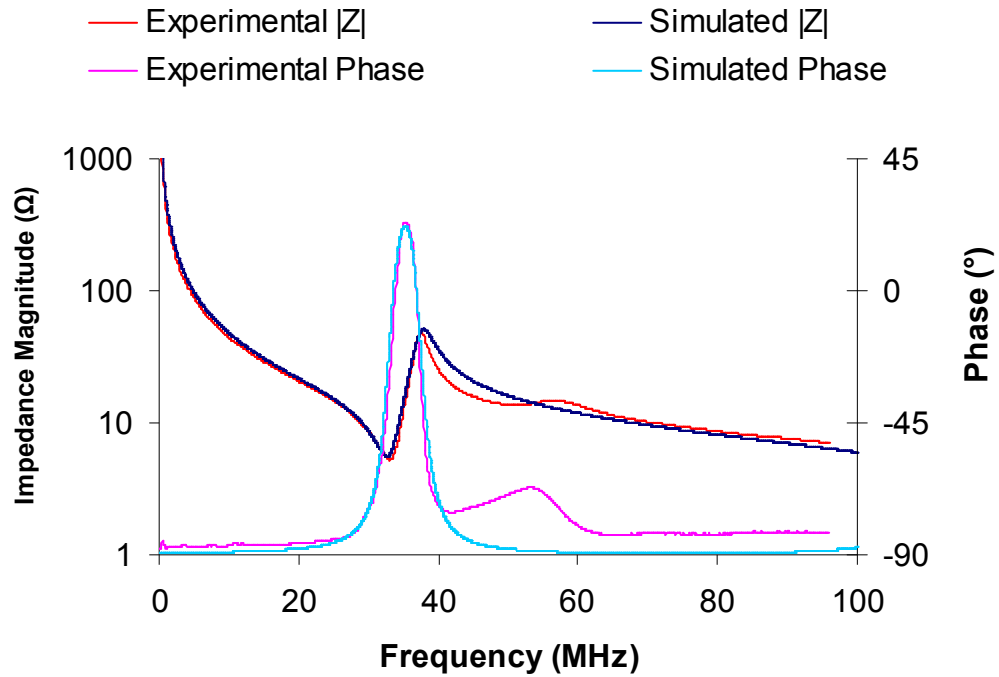


Figure 5. 23: Electrical impedance spectroscopy measurement and simulation for MC6

Figure 5.24 shows there is a good fit between experimentally derived and simulated impedance data. It can also be seen that the resonance characteristics for this composite are significantly more distinct than for previously measured composites, suggesting this composite is much less attenuative. The value of attenuation used for the one dimensional model, 5.5 dB/cm is much closer to the nominal value, 2.11 dB/cm, than was found to be the case in other composite samples. The values of piezoelectric parameters used for the one-dimensional model are all very well matched to the measured values, to within no more than 2-3% error in all cases. When measured values are compared to nominal values for a standard composite of this volume fraction, similar discrepancies are observed to previously tested composites. Once more, the nominal value of k_T , 0.71, is around 40% higher than the measured value of 0.51. The nominal values of h_{33} , ϵ_R^S and e_{33} are also higher than was measured for MC6, by around 16%, 40% and 60% respectively while the nominal value of c_{33}^E is lower than the measured value.

TABLE 5. 19: CALCULATED PIEZOELECTRIC PARAMETERS OF MC6

Parameter	Measured	Fitted	%	Nominal	%
-----------	----------	--------	---	---------	---

	Value	Value	Difference	Value (50% TRS600)	Difference
ρ (kg m ⁻³)	4280	4280	0	4250	1
v (ms ⁻¹)	3970	3980	<1	3920	1
Z (MRayl)	17.0	17.0	0	16.7	2
c_{33}^D (Nm ⁻²)	6.76×10^{10}	6.77×10^{10}	<1	6.54×10^{10}	3
c_{33}^E (Nm ⁻²)	5.00×10^{10}	5.00×10^{10}	0	3.18×10^{10}	36
ϵ_R^S	447	460	3	640	43
e_{33} (Cm ⁻¹)	8.35	8.50	2	13.8	65
h_{33} (Vm ⁻¹)	2.11×10^9	2.09×10^9	1	2.44×10^9	16
d_{33} (mV ⁻¹)	1.24×10^{-10}	1.25×10^{-10}	1	2.11×10^{-10}	70
k_T	0.51	0.51	0	0.72	40
α (dB cm ⁻¹ @ 1 MHz)	N/M	5.50	N/M	2.11	N/M

5.6. Summary

This chapter presented results from HFUS characterisation of W-epoxy, a material used to make passive backing layers in ultrasound transducers including TH13 and TH16 reported here, and results from tests of a novel method of piezocomposite finishing, UPG. These results are discussed in detail in Section 7.1. This was followed by results from experimental characterisation of a number of PZT composite samples, in the form of standard dice-and-fill composite, VPP fibre composite and micromoulded VPP composite. Further discussion of these results is in Section 7.2-7.3.

The next chapter presents results from ultrasonic characterisation of single element transducers made with VPP composites. Results from characterisation of a PZT dice-

and-fill composite transducer and a lithium niobate transducer and are also presented for purposes of comparison.

5.7. References

Carey S.J., Gregory C.M, Brewin M.P., Birch M.J., Ng S., Hatfield J.V. (2004) PVDF Array Characterisation for High Frequency Ultrasonic Imaging Proceedings of IEEE Ultrasonics Symposium, pp. 1930-1933

Nelson L.J. Bowen C.R., Stevens R., Cain M., Stewart M., (2003). High field behaviour of piezoelectric fibre composites. Proc. SPIE Int. Soc. Opt. Eng. 5053, pp. 544-55

Nelson L.J. Bowen C.R., Stevens R., Cain M., Stewart M., (2003) Modelling and measurement of piezoelectric fibres and interdigitated electrodes for the optimisation of piezofibre composites. Proc. SPIE Int. Soc. Opt. Eng. 5053, pp.556-67

Webster R.A., Cochran S., MacLennan D., Meggs C., Button T.W. (2007) Passive Materials for High Frequency Ultrasound Components *Proceedings of 2007 IEEE International Ultrasonics Symposium* pp. 1925-1928

6. Transducer testing and applications testing

6.1. Introduction

This chapter outlines basic characterisation measurements taken from seven prototype transducers. These are:

- unfocussed micromoulded composite transducer TH10 of frequency 26 MHz;
- focussed micromoulded composite transducers TH09, TH16 and TH13, of frequencies 36, 43 and 32 MHz respectively.
- a focussed 51 MHz transducer, JB1, fabricated by Jeremy Brown (Dalhousie University, Nova Scotia) from standard dice-and-fill CTS3203HD PZT piezocomposite
- a 60 MHz unfocussed Lithium Niobate transducer, LNO60;

JB1, TH09, TH16 and TH13 were spherically focussed by mechanically shaping the active element, using the technique reported by Lockwood et al. (1994). All transducers, except JB1, were fabricated by AFM Ltd. Index numbers used for each transducer are as supplied by AFM Ltd. Transducers TH9, TH10, LNO60 and JB1 were all encased in standard SMA casings with silver-loaded epoxy backing layer. TH13 and TH16 were encased in commercial grade packaging with W-loaded epoxy backing layers.

Electrical impedance magnitude and phase data is shown for each transducer alongside simulated data from the one-dimensional model. Pulse shapes and axial resolution were determined for all transducers and depth of field measurements and lateral resolution measurements were taken for all focussed transducers, using the procedures described in Section 4.9. Basic measurements were performed in water but for the purpose of calculations the medium is assumed to be tissue ($v_l = 1540$ m/s).

Representative 2D B-scan images are also presented for the transducers. As transducer and characterisation equipment availability both varied and evolved during the period of the study, it was not always possible to carry out testing in a

systematic and methodical manner. The data presented is thus intended to be illustrative of the nature and performance of these transducers

6.2. Basic testing: Transducers made with standard materials

6.2.1. Results from JB1

The primary reason for testing of JB1 was to provide comparative data for the prototype transducers being tested in this investigation. Although not a commercial device, JB1 was fabricated using well-established fabrication methods, in terms of both composite and transducer manufacture. Physical characteristics of JB1 are given in Table 6.1.

TABLE 6. 1: PHYSICAL CHARACTERISTICS OF JB1

Parameter	Value
Piezoelectric material	Diced PZT (CTS3203HD) Composite
Element diameter (mm)	3.3
Element thickness (μm)	30
Operational frequency (MHz)	51
Focal distance (mm)	9.1
f-number	2.8

Shown here are data measured experimentally from JB1. Electrical impedance magnitude and phase are shown in Figure 6.1. Experimental pulse-echo responses are shown in Figure 6.2 at the transducer focal point, 9.1 mm. Figure 6.3 shows a line spread function from the focal depth of the transducer and the depth of field measurement is shown in Figure 6.4.

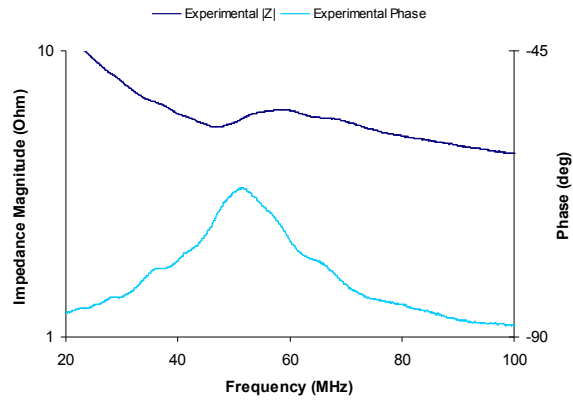


Figure 6. 1:Experimental measurement of impedance magnitude and phase of JB1

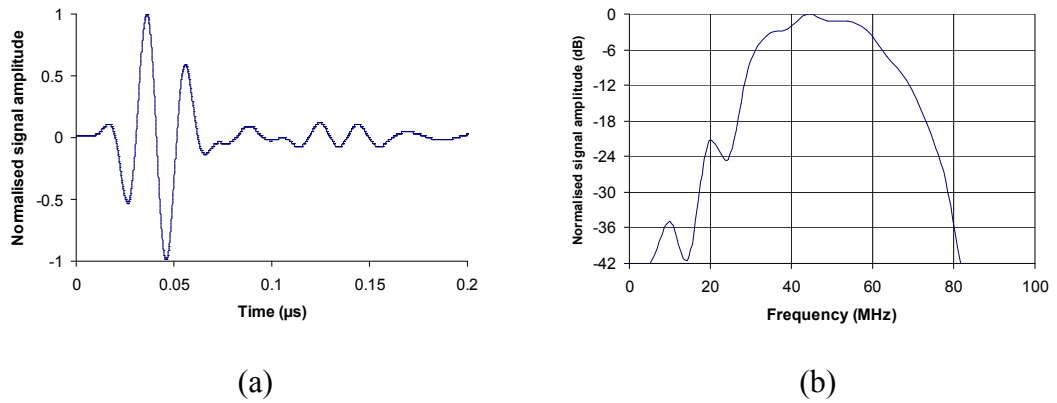


Figure 6. 2: Pulse-echo from stainless steel flat surface from JB1 in (a) time and (b) frequency domains.

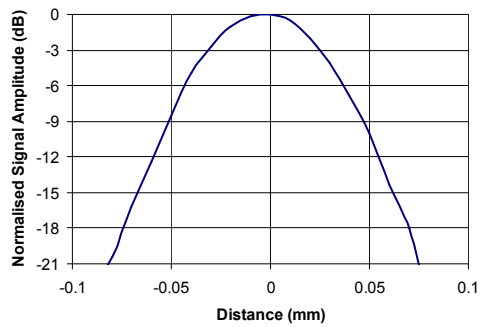


Figure 6. 3: Line spread function from transducer JB1

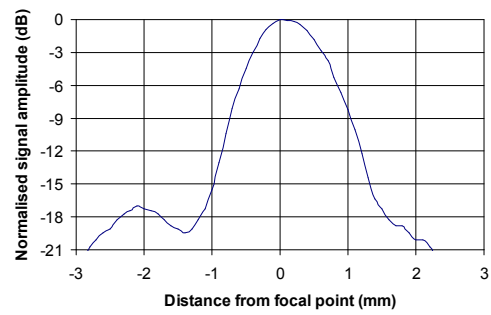
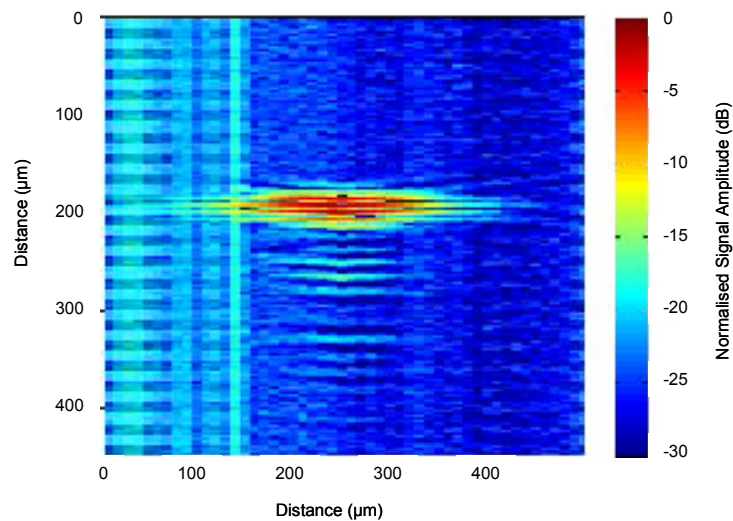


Figure 6. 4: Depth of field measurement for JB1.

TABLE 6. 2: STATISTICS FOR JB1 PULSE-ECHO MODE

Parameter	Threshold	-3dB	-6 dB	-20 dB
Bandwidth (MHz)	Experimental	23	31	48
Q	Experimental	-	1.6	-
Pulse Length (ns)	Experimental	39	48	59
Axial Resolution (μm)	Experimental	30	37	45
Lateral Resolution (μm)	Theoretical	-	85	-
	Experimental	55	80	155
Depth of Field (mm)	Theoretical	-	1.63	-
	Experimental	1.0	1.5	2.7

Figure 6. 5: B-scan image of single 5 μm Tungsten wire at focus of JB1

Measurements of bandwidth and resolution for this transducer are outlined in Table 6.2. The -6 dB bandwidth of this transducer is 31 MHz, giving Q of 1.5. The axial resolution of the transducer is 37 μm at -6 dB; lateral resolution is 80 μm and depth of field 1.5 mm. In all cases, experimental measurements are reasonably close to theoretically calculated values.

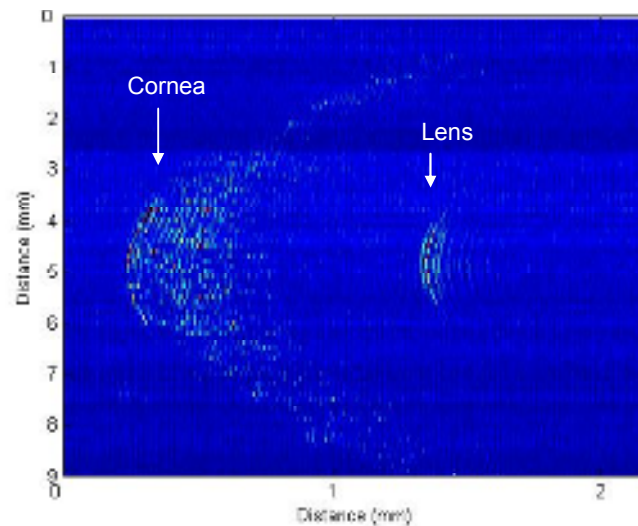


Figure 6. 6: B-scan image of porcine eye from JB1.

Figure 6.6 shows a B-scan of a porcine eye generated using JB1. The image shows good resolution, as expected from basic measurements, and anatomical features of the eye – the cornea and lens, can be clearly seen. Nevertheless, the low sensitivity and relatively large focal distance of JB1 (~ 1 cm) lead to a rather poor SNR in the image.

6.2.2. Results from LNO60

LNO60 is a flat (unfocussed) single element transducer of diameter 1.3 mm, with operational frequency of approximately 60 MHz. The primary reason for testing this transducer was again to provide comparative data for the transducers made using MC. Although this transducer was made using a different material, the transducer fabrication processes were the same as for the MC transducers. Physical characteristics of LNO60 are given in Table 6.3. Figure 6.7 shows experimental and simulated impedance magnitudes and phases of the transducer and the resultant simulated pulse-echo response and measured pulse-echo response are shown in the time and frequency domains in Figures 6.8 and 6.9 respectively.

TABLE 6. 3: PHYSICAL CHARACTERISTICS OF LNO60

Parameter	Value
Piezoelectric Material	y36° Lithium Niobate
Element Diameter	1.3 mm
Element Thickness	57 μm
Operational Frequency	60 MHz

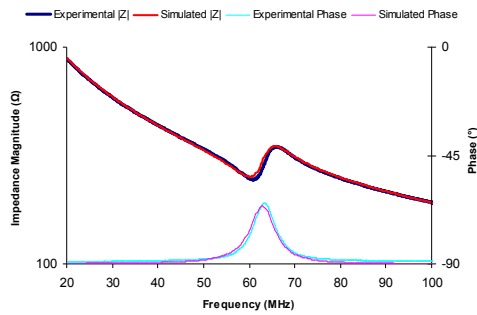


Figure 6. 7: Impedance Magnitude and Phase of LNO60

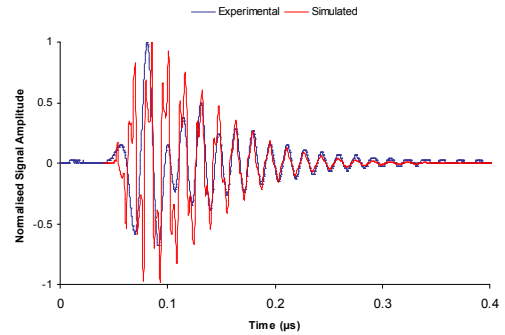


Figure 6. 8: Pulse-echo measurement of LNO60 from stainless steel block at 20.5 mm

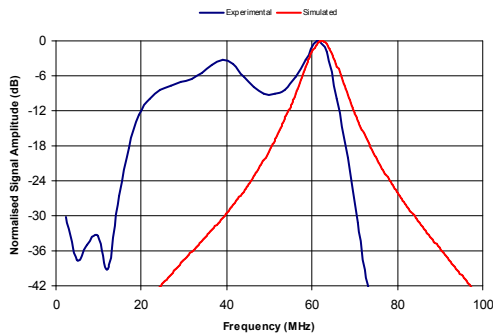


Figure 6. 9: FFT of pulse in Figure 6.8

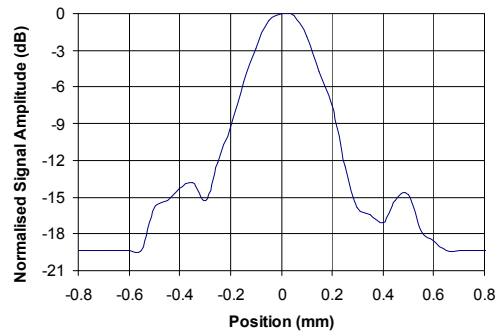


Figure 6. 10: Line spread function from LNO 60 MHz transducer, taken using pulse-echo on 5 μm Tungsten wire

TABLE 6. 4: STATISTICS FOR LNO60 PULSE-ECHO MODE

Parameter	Threshold	-3 dB	-6 dB	-20 dB
Bandwidth (MHz)	1D Simulation	6	9	26
	Experimental	5	9	51
Q	1D Simulation	10.6	6.7	2.4
	Experimental	12.3	6.7	0.8
Pulse Length (ns)	1D Simulation	77	100	179
	Experimental	40	50	185
Axial Resolution (μm)	1D Simulation	56	73	130
	Experimental	31	39	142

It can be seen that the simulated impedance fits very well to the experimentally measured impedance. The fit of the simulated pulse to the experimentally measured pulse is reasonably good, although some unexpected lower frequency content is present in the measured pulse. Conversely, the simulated pulse also shows high frequency content, due to the 3rd harmonic of the fundamental resonance. This is likely to have been attenuated during transmission so is not seen in the experimental measurement.

Bandwidth and resolution for this transducer are given in Table 6.4. The -6 dB bandwidth of this transducer is relatively small, at 9 MHz, giving Q of 6.7, significantly greater than that of JB1 as expected. Axial resolution, 39 μm at -6 dB, is comparable to JB1 although at -20 dB it is significantly more, 142 μm compared to 45 μm .

6.3. Basic Testing: Unfocussed MC Transducers

Two unfocussed single element transducers, TH10 and TH17, were made using MC composites and subjected to the testing procedures described above. The results of this are now presented.

6.3.1. Results from TH10

TH10 is a transducer made from flat (unfocussed) micromoulded composite, with a rectangular active layer of dimensions 1.2 mm x 0.8 mm and centre frequency of 26 MHz. In this case both through-transmission measurements, with a membrane hydrophone as receiver, and pulse-echo measurements were taken. Experimental and simulated impedance magnitude and phase for this transducer are shown in Figure 6.11. Simulated and experimentally measured pulses in the time and frequency domains are shown in Figure 6.12 for through-transmission and in Figure 6.13 for pulse-echo mode.

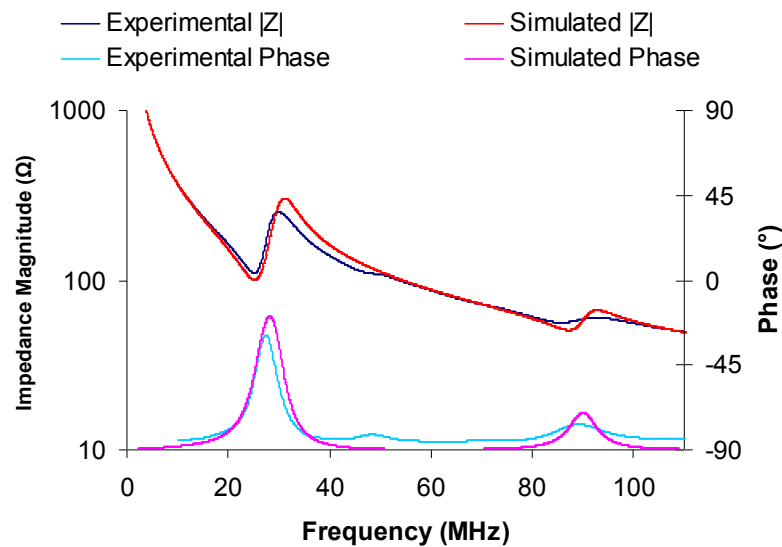


Figure 6. 11: Electrical impedance magnitude and phase measurement for TH10.

TABLE 6. 5: PHYSICAL CHARACTERISTICS OF TH10

Parameter	Value
Piezoelectric Material	VPP PZT MC with 25 μm diameter pillars and VF 42%
Element size	1.2 x 0.8 mm
Element Thickness	73 μm
Operational Frequency	26 MHz

Through-transmission

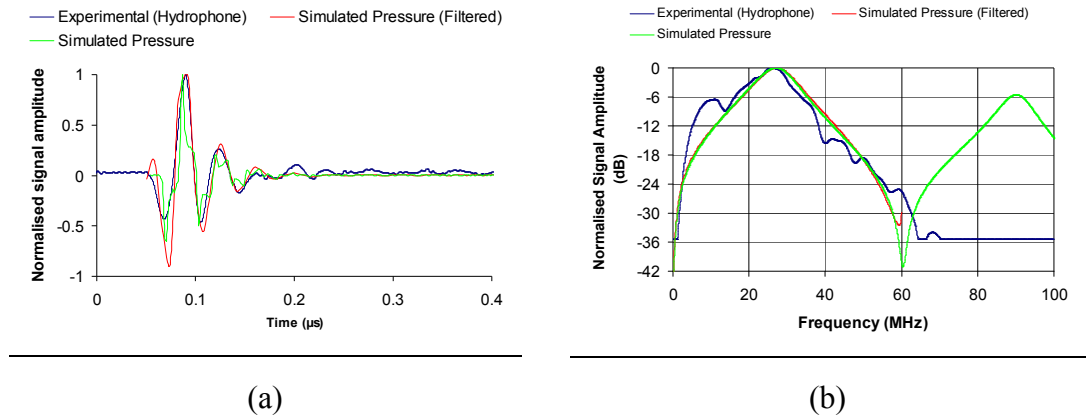


Figure 6. 12: Pulse shape from TH10 through-transmission (at 10 mm distance) in (a) time and (b) frequency domains.

TABLE 6. 6: STATISTICS FOR TH10 THROUGH-TRANSMISSION MODE

Parameter	Data Source	Threshold		
		-3 dB	-6 dB	-20 dB
Bandwidth (MHz)	1D Simulation	11	17	47
	Experimental	10	17	49
Q	1D Simulation	-	1.5	-
	Experimental	-	1.4	-
Pulse Length (ns)	1D Simulation	34	58	94
	Experimental	41	52	150
Axial Resolution (µm)	1D Simulation	52	90	144
	Experimental	63	80	231

Pulse-echo

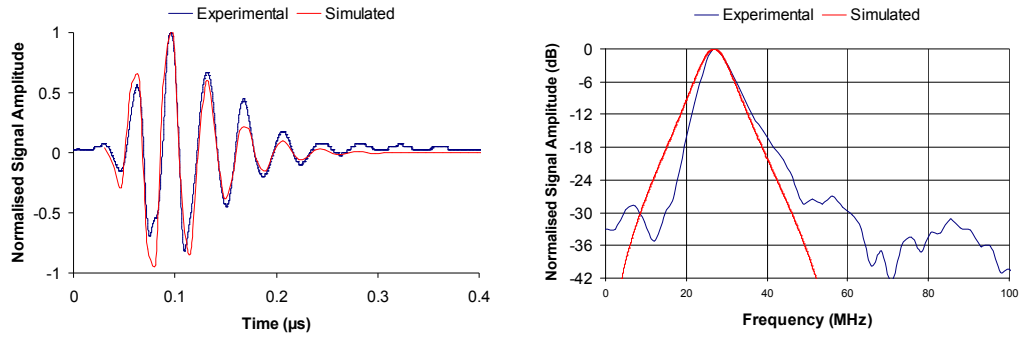


Figure 6. 13: Pulse-echo measurement from TH10 on stainless steel at distance of 11.5 mm, shown in time and frequency domains.

TABLE 6. 7: STATISTICS FOR TH10 PULSE-ECHO MODE

Parameter	Data Source	Threshold		
		-3 dB	-6 dB	-20 dB
Bandwidth	1D Simulation	6.5	10	26
	Experimental	6.0	9.0	25
Q	1D Simulation	-	2.7	-
	Experimental	-	3.1	-
Pulse Length (ns)	1D Simulation	94	112	154
	Experimental	81	101	192
Axial Resolution (µm)	1D Simulation	72	86	119
	Experimental	62	78	148

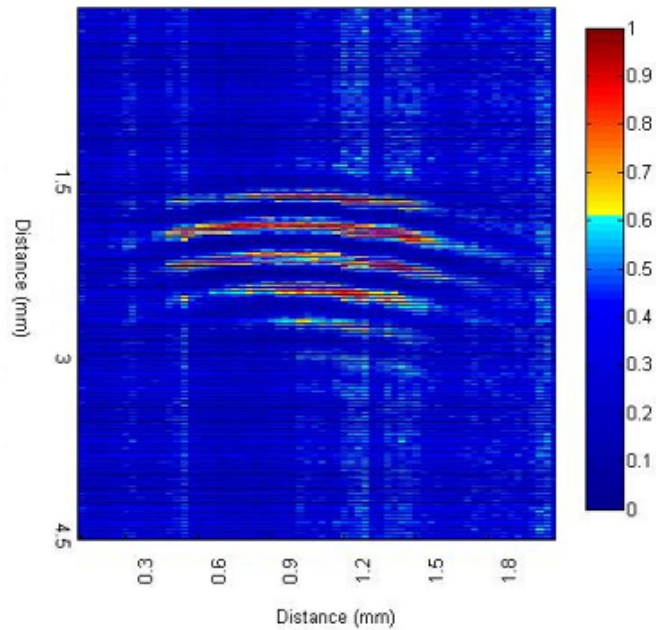


Figure 6. 14: Single scan of 5 μm Tungsten wire at distance of 11.5 mm from TH10.

The simulated electrical impedance data fit reasonably well to the experimentally measured data shown in Figure 6.11. This is also the case for the pulse measurements, both through-transmission (Figure 6.12) and pulse-echo modes (Figure 6.13).

Pulse bandwidth and resolution measurements for TH10 are outlined in Tables 6.6 and 6.7 for through-transmission and pulse-echo respectively. For through-transmission the -6 dB bandwidth of TH10 is 17 MHz, corresponding to $Q = 1.4$, and axial resolution is 80 μm . These values match closely to the values generated by simulations. For pulse-echo mode, the -6 dB bandwidth is 10 MHz, giving Q of 3.1. Axial resolution is 78 μm . Both are reasonably well matched to theory for this transducer. A B-scan of a single 5 μm tungsten wire is shown in Figure 6.14, showing relatively wide beam width as expected from a unfocused transducer.

6.4. Basic Testing: Focussed MC Transducers

Finally, three focussed single element transducers, TH09, TH16 and TH13, were made using MC composites. Results from acoustic tests performed on these are now presented.

6.4.1. Results from TH09

TH09 was the first prototype focussed transducer to be fabricated. It has an active element of diameter 1.7 mm, with operational frequency of 36 MHz. The active element is spherically focussed to a focal distance of 6.5 mm ($f\# = 4$). Surface profiling was undertaken of TH09 – this is shown in Figures 6.15 in 3D and Figure 6.16 in 2D. It can be seen that the transducer element was misaligned with respect to the front face of the transducer during assembly.

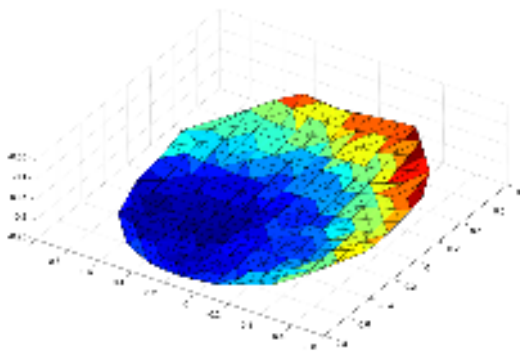


Figure 6.15: Surface profile of TH09 in 3D

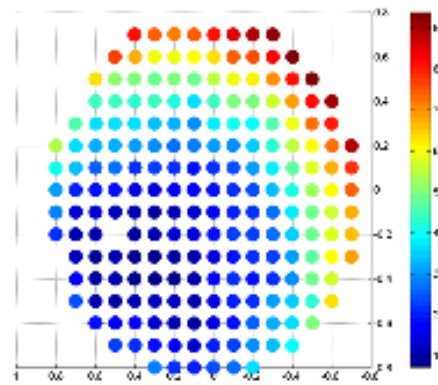


Figure 6.16: Surface profile of TH09 in 2D

Experimental and simulated impedance magnitude and phase data is shown in Figure 6.17. A lateral mode can be seen to exist at around 50 MHz. This is because the pillar width in this composite is not of sufficiently large aspect ratio. The same frequency of lateral mode can be seen in AFMTH10 which was made from the same composite design. It is less of an issue in AFMTH10 as the active layer thickness is greater than AFMTH09, and therefore the thickness mode frequency is lower and not close to the lateral mode frequency.

A measurement of one-way pulse from TH09 is shown in Figure 6.18, in both time and frequency domain, alongside accompanying simulations. During the course of the work, TH09 ceased to be operational and no useful pulse-echo measurement was collected. However, an ‘experimental’ pulse-echo response has been generated by convolution of the one-way measurement. This is shown in Figure 6.19 alongside corresponding one-dimensional simulation.

TABLE 6. 8: PHYSICAL CHARACTERISTICS OF TH09

Parameter	Value
Piezoelectric Material	VPP PZT MC with 25 μm diameter pillars and VF 42%
Element Diameter (mm)	1.7
Element Thickness (μm)	53
Operational Frequency (MHz)	36
Focal Point (mm)	6.5
f-number	3.8

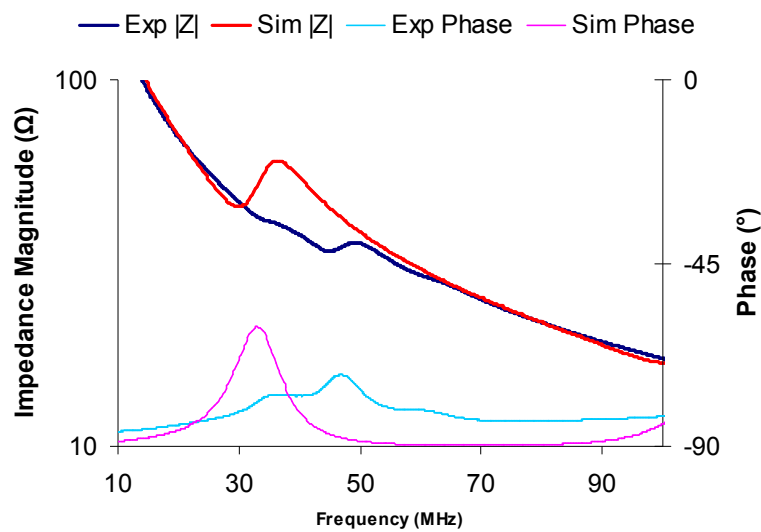


Figure 6. 17: Electrical impedance magnitude and phase measurement for TH09, and associated piezoelectric properties.

Through-transmission

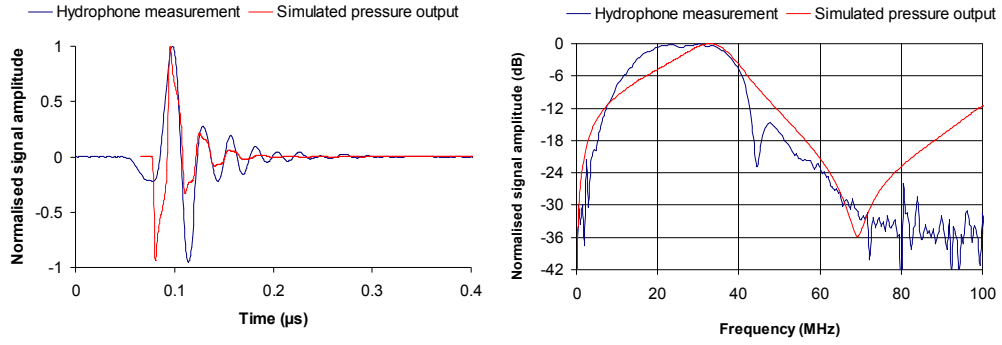


Figure 6. 18: Through measurement of pulse from TH09 from membrane hydrophone, taken at 11 mm, in time domain and frequency domain

TABLE 6. 9: STATISTICS FOR TH09 THROUGH-TRANSMISSION MODE

Parameter	Threshold	-3 dB	-6 dB	-20 dB
Bandwidth (MHz)	1D Simulation	15	25	56
	Experimental	23	29	40
Q	1D Simulation	-	1.2	-
	Experimental	-	0.9	-
Pulse Length (ns)	1D Simulation	34	39	69
	Experimental	68	70	123
Axial Resolution (μm)	1D Simulation	26	29	53
	Experimental	52	54	95

Pulse-echo Transmission

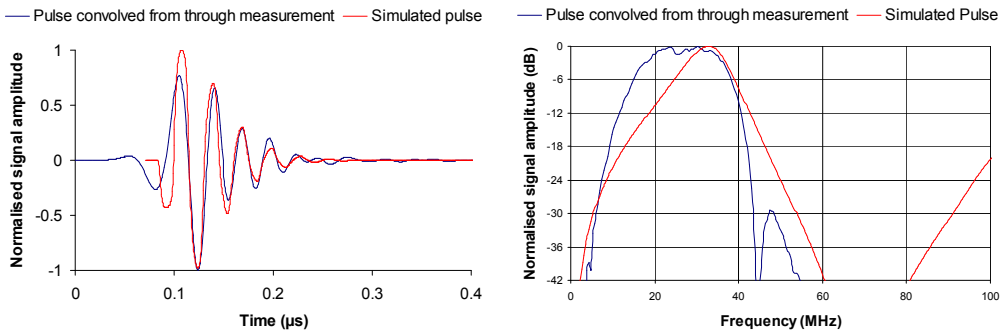


Figure 6. 19: Pulse-echo from TH09, in time domain and frequency domain.

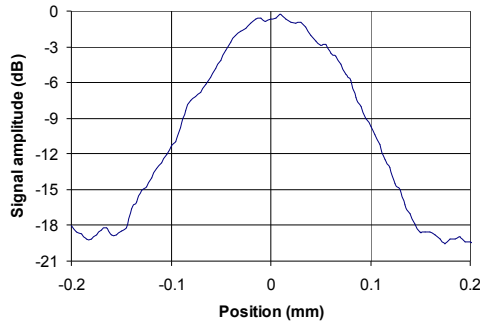


Figure 6. 20: Line spread function of TH09 at focus, taken from pulse-echo measurements on 5 μm Tungsten wire.

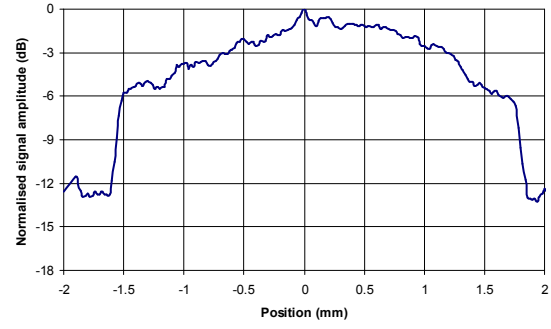


Figure 6. 21: Depth of field of Transducer TH09, taken by pulse-echo measurements from 5 μm Tungsten wire.

TABLE 6. 10: STATISTICS FOR TH09 PULSE-ECHO MODE

Parameter	Threshold	-3 dB	-6 dB	-20 dB
Bandwidth	1D Simulation	9	14	36
	Experimental	19	23	33
Q	1D Simulation	-	2.2	-
	Experimental	-	1.2	-
Pulse Length (ns)	1D Simulation	69	72	129
	Experimental	90	105	172
Axial Resolution (μm)	1D Simulation	50	52	93
	Experimental	69	81	132
Lateral Resolution (μm)	Theoretical	N/M	165	N/M
	Experimental	105	145	360
Depth of Field (mm)	Theoretical	N/M	4.39	N/M
	Experimental	2.24	3.30	N/M

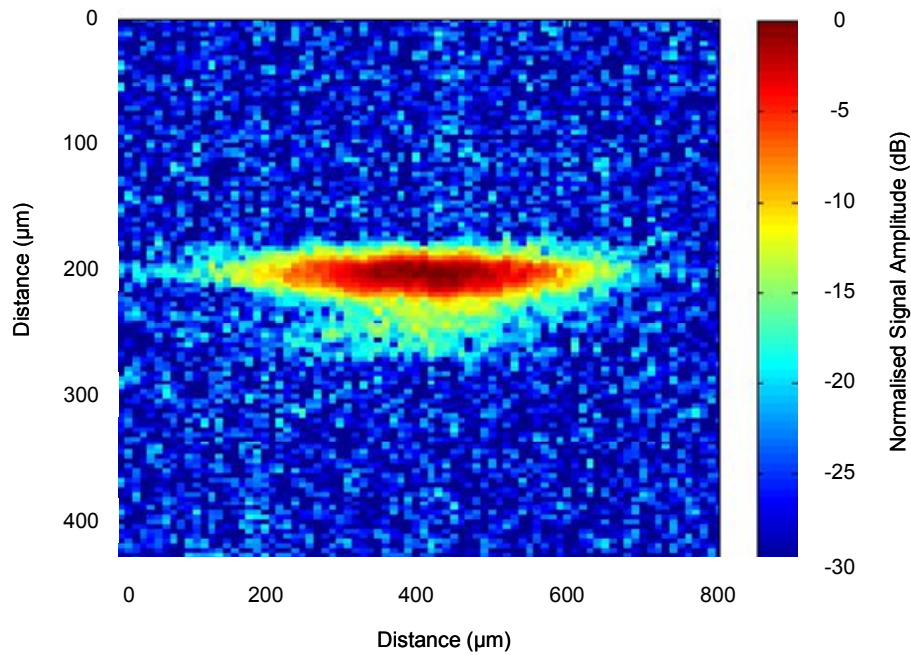


Figure 6. 22: B-scan image of single 5 μm Tungsten wire at focus of TH09

It can be seen from the Figure 6.17 that TH09 has a significant lateral mode present at around 50 MHz, relatively close to the fundamental thickness mode resonance. The backing material within the transducer may preferentially damp thickness mode resonance, contributing to the dominance of the lateral mode. This cannot be modelled using ODM, and therefore the simulated impedance does not fit well to the experimental data in this case. The performance of the transducer does not seem to be diminished to a great degree, and a clear pulse can be seen in Figure 6.18, which fits reasonably well to the simulated data. There is some low frequency content at the beginning of the pulse (in time), but the frequency domain shows a flatter, broader response than most of the other VPP composite transducers tested.

Bandwidth and resolution data for TH09 are shown in Table 6.9 for one-way transmission and Table 6.10 for pulse-echo response: as expected these data correspond to one another, being from the same measurement. The -6 dB bandwidth of 23 MHz, corresponding to a Q of 1.5, is somewhat larger than expected from simulations of TH09. -6 dB axial resolution of 81 μm is approximately twice what is expected from simulations but -6 dB lateral resolution of 145 μm corresponds well to the theoretical calculation. The experimentally measured depth of field of this

transducer was less than predicted by theoretical calculation, but this is to be expected as lateral resolution was smaller than predicted also. A B-scan taken of a single 5 μm tungsten wire at the focus of TH09 is shown in Figure 6.22, and appears as expected from the calculations discussed here. Figure 6.23 shows a series of images taken at distances between the transducer and the wire of 5 mm to 13 mm, in 1 mm steps.

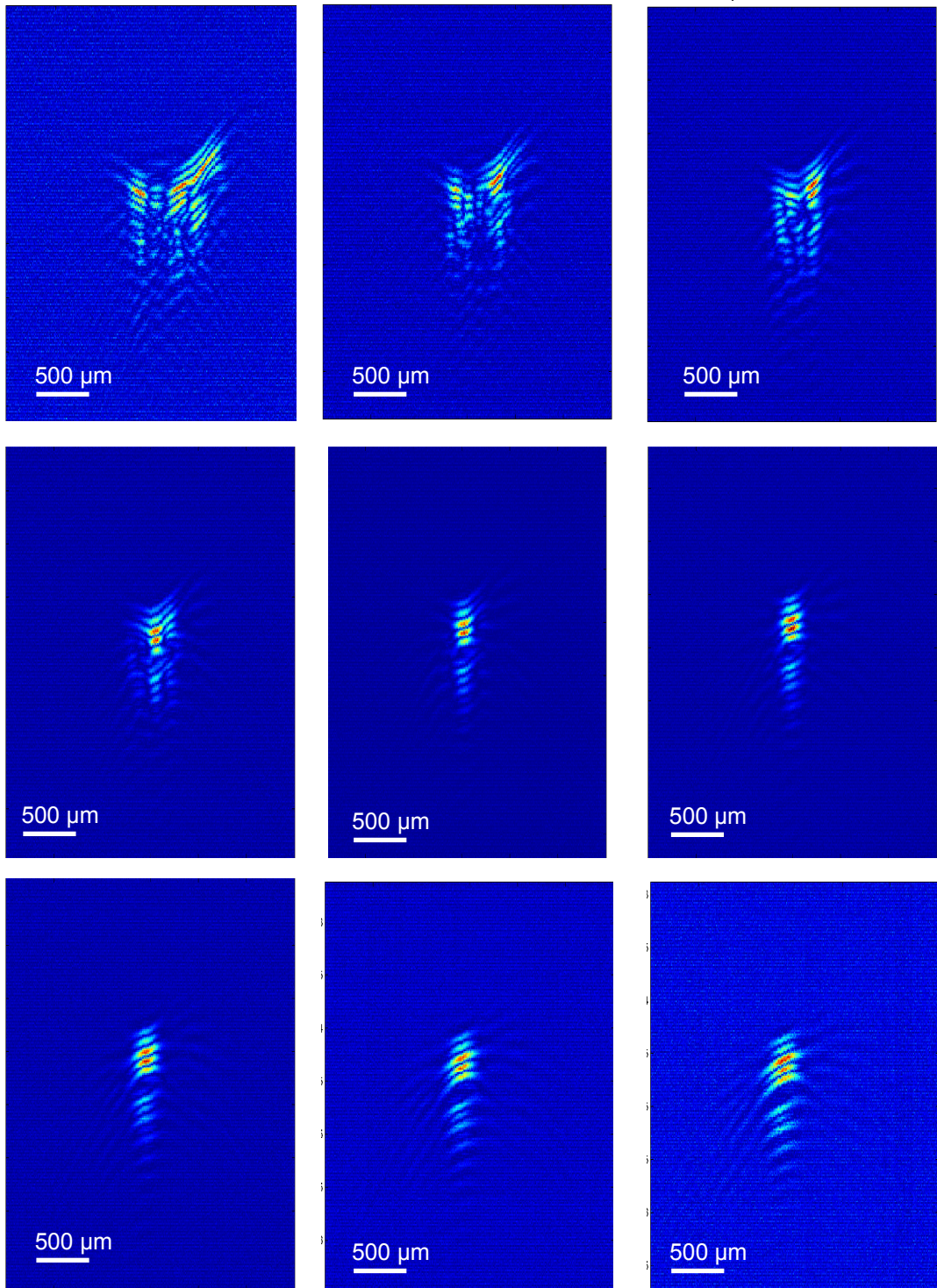


Figure 6. 23: B-scans of single 5 μm wire at varying distances from the transducer. Wire was at distances of (top row, l-r) 2 mm, 3 mm, 4 mm; (middle row, l-r) 5 mm, 6 mm, 7 mm and (bottom row, l-r) 8 mm, 9 mm, 10 mm from the transducer in 1 mm increments.

Image of ovine eye

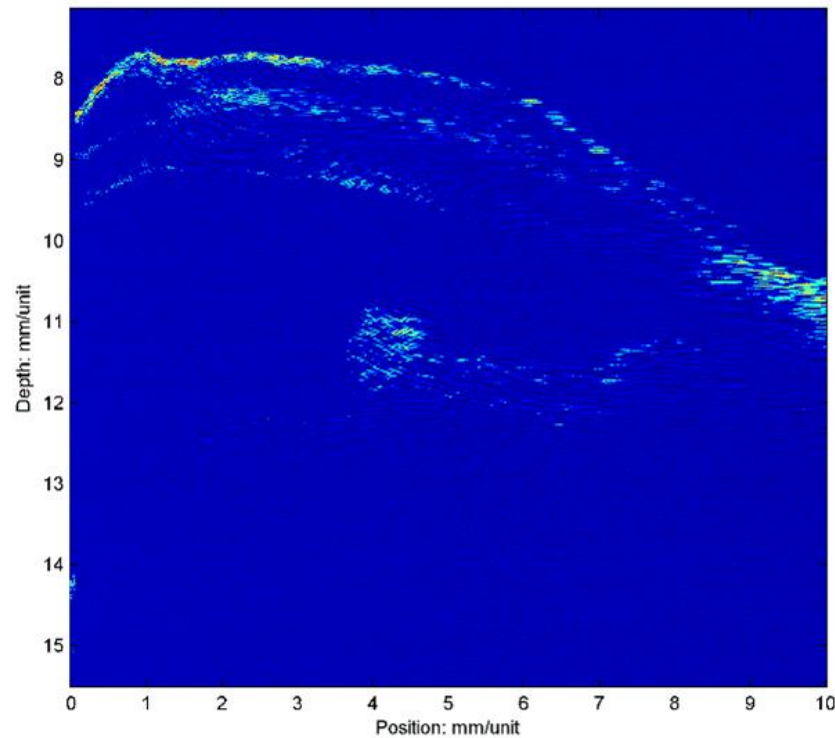


Figure 6. 24: B-scan of ovine eye generated using TH09

Figure 6.24 is a B-scan of an ovine eye collected using TH09. This image has good resolution and low noise. Anatomical features can be clearly seen. It is worth noting in particular, that the profile of the cornea is clear. This B-scan was collected using a scanning system with automated ‘Z-axis’ adjustment, as described in Section 4.10 and is in fact a composite of 5 B-scans taken at different distances from the eye. This has allowed anatomical details to be visualised over a larger depth of field. All other images presented are B-scans taken at a single distance from the imaging subject.

6.4.2. Results from TH16

A second spherically focussed MC transducer, TH16 was fabricated, of diameter 1.6 mm and operational frequency 43 MHz. The focal length of this transducer was 3.5 mm, corresponding to f-number of 2.2. Experimentally measured and simulated electrical impedance magnitude and phase are shown in Figure 6.25 and pulse-echo responses are shown in the time domain and frequency domain in Figure 6.26. A line

spread function, taking from a 5 μm tungsten wire at the focus of TH16, is shown in Figure 6.27 and depth of field measurement in Figure 6.28.

TABLE 6. 11: PHYSICAL CHARACTERISTICS OF TH16

Parameter	Value
Piezoelectric Material	VPP PZT MC with hexagonal packed 20 μm diameter pillars at 29 μm pitch.
Element Diameter	1.6 mm
Element Thickness	48 μm
Operational Frequency	43 MHz
Focal Point	3.5 mm
f-number	2.2

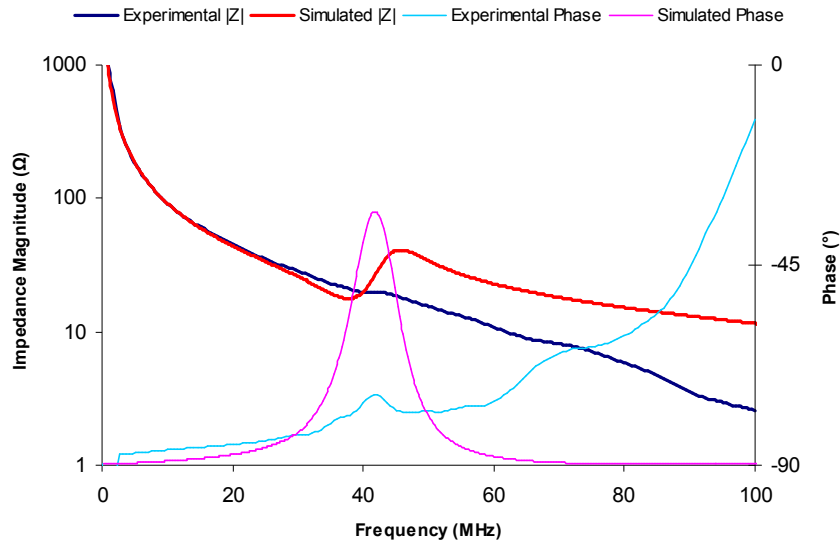


Figure 6. 25: Impedance magnitude and phase measurement and 1D simulation from TH16

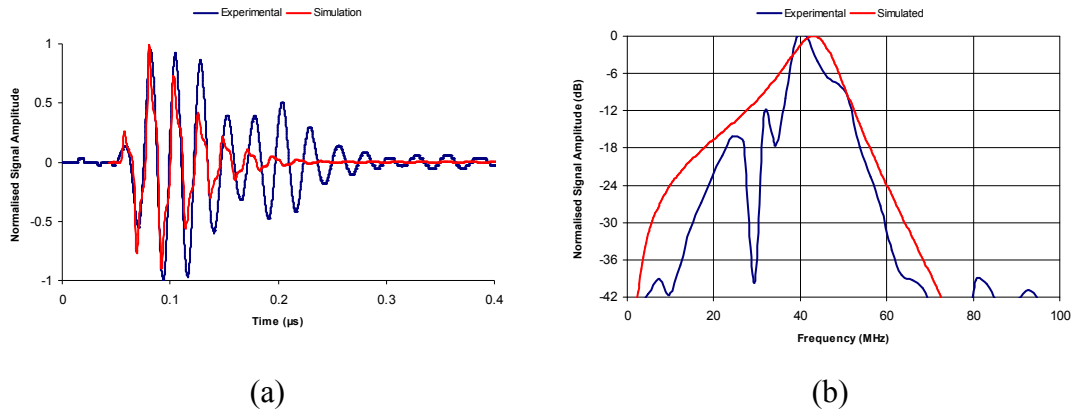


Figure 6. 26: Pulse-echo measurement from TH16 at focus in (a) time and (b) frequency domains.

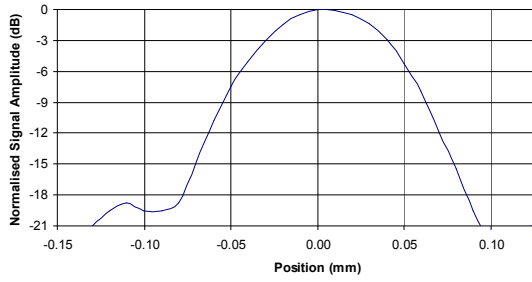


Figure 6. 27: Line spread function for TH16 by pulse-echo from 5 µm W wire at focus.

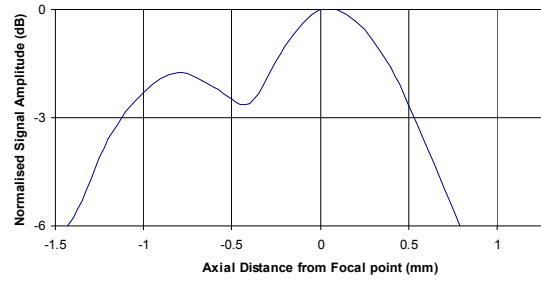


Figure 6. 28: Depth of field measurement of TH16 taken by pulse-echo on stainless steel.

TABLE 6. 12: STATISTICS FOR TH16 PULSE-ECHO MODE

Parameter	Threshold	-3 dB	-6 dB	-20 dB
Bandwidth	1D Simulation	9	14	45
	Experimental	5	8	24
Q	1D Simulation	-	3.1	-
	Experimental	-	4.9	-
Pulse Length (ns)	1D Simulation	61	73	129
	Experimental	79	91	219
Axial Resolution (µm)	1D Simulation	47	56	99
	Experimental	61	70	168
Lateral Resolution (µm)	Theoretical	N/A	77	N/M
	Experimental	70	100	185
Depth of Field (mm)	Theoretical	N/M	1.18	N/M
	Experimental	1.8	2.4	N/M

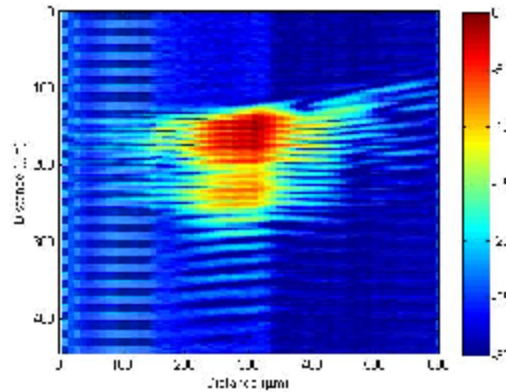


Figure 6. 29: B-scan image of single 5 μm Tungsten wire at focus of TH16

The experimentally measured impedance does not show clear resonance peaks, and also suffers from incomplete calibration at higher frequencies. As such the simulated impedance magnitude and phase do not fit particularly well to experimental data. The experimental pulse response shows low frequency content, and also shows unusual amplitude decay characteristics. This can be seen clearly in the frequency domain, with nulls at approximately 30 MHz and 35 MHz. Measurements were repeated to ensure that this was not caused by misalignment or saturation of the reception equipment, but this was not the case.

Table 6.12 outlines the bandwidth and resolution characteristics of TH16. The experimentally measured -6 dB bandwidths are just over half of what is predicted by one dimensional simulation, at 8 MHz ($Q = 4.9$) and 14 MHz ($Q = 3.1$) respectively. The measured -6 dB axial resolution of 70 μm is worse than predicted by theory (56 μm) by around 25%. Experimentally measured lateral resolution at -6 dB of 100 μm is reasonably close to theoretical calculation, of 77 μm . The experimentally measured depth of field is twice that predicted by theoretical calculations, which is unexpected as the theoretical and experimental lateral resolutions are relatively close. Finally, Figure 6.29 shows a B-scan of a single 5 μm tungsten wire at the focus of TH16. The wire image is reasonably symmetrical, although there does appear to be some evidence of slight misalignment of the transducer with respect to the wire. The unusual pulse shape observed from Figure 6.26 can be clearly seen to cause an aberration in the B-scan also.

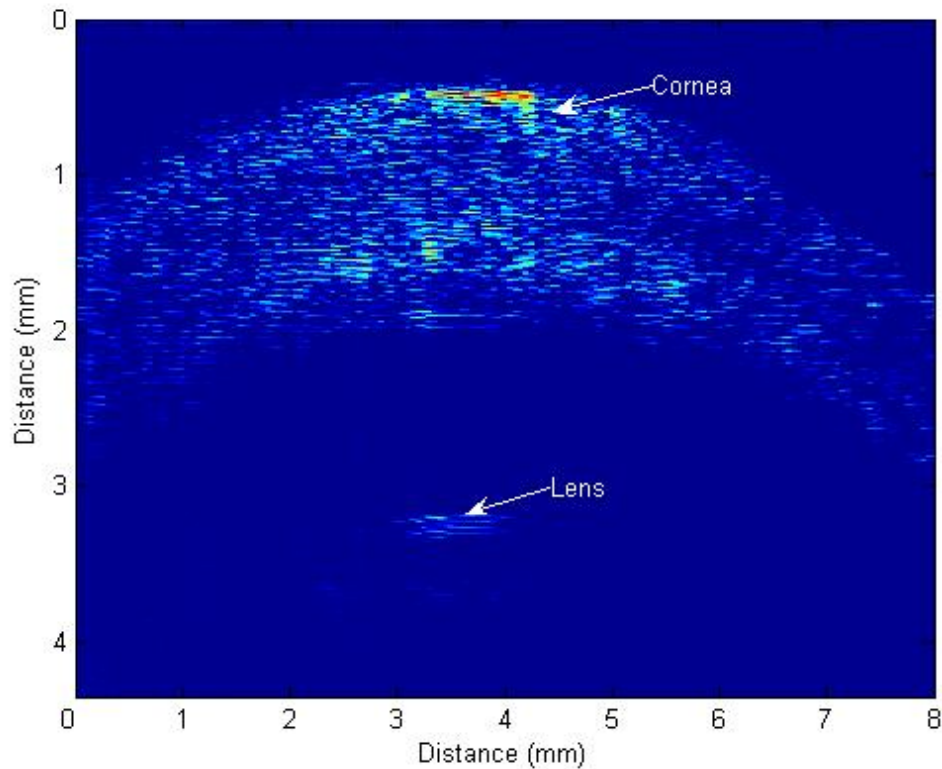


Figure 6. 30: B-scan of porcine eye generated by TH16

Figure 6.30 is a B-scan of a porcine eye collected using TH16. This image shows reasonable resolution, with the outline of the cornea very clear, but is of lesser quality than images produced by TH09. The image is relatively noise-free, showing the transducer to have good sensitivity, although the lens of the eye in this image is not clear, suggesting limited penetration.

6.4.3. Results from TH13

The final focussed MC transducer tested is TH13, with diameter of 1.6 mm and operational frequency 32 MHz. The focal length of this transducer is 3 mm, corresponding to $f\# = 1.9$. Experimentally measured and simulated data are shown for electrical impedance magnitude in Figure 6.31 and for pulse-echo response in the time and frequency domain in Figure 6.32.

TABLE 6. 13: PHYSICAL CHARACTERISTICS OF TH13

Parameter	Value
Piezoelectric Material	VPP PZT MC with hexagonal packed 20 μm pillars at 29 μm pitch.
Element Diameter	1.6 mm
Element Thickness	54 μm
Operational Frequency	32 MHz
Focal distance	3 mm
f-number	1.9

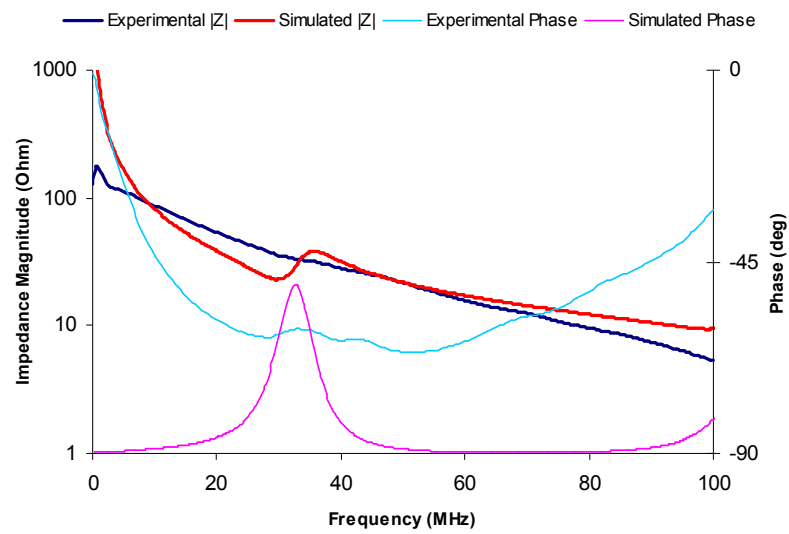


Figure 6. 31: Experimental measurements and 1D simulation of impedance magnitude and phase from TH13

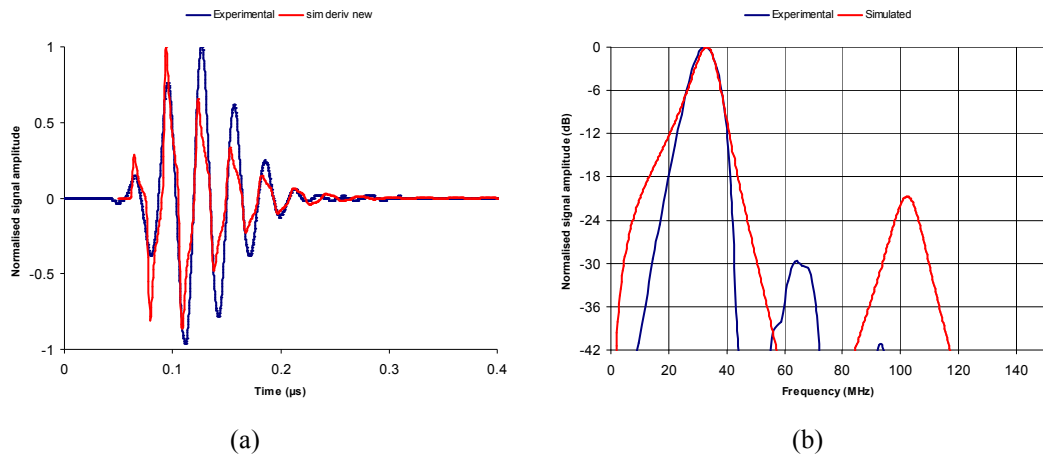


Figure 6. 32: Pulse-echo measurement from TH13 on stainless steel at focus in (a) time and (b) frequency domains.

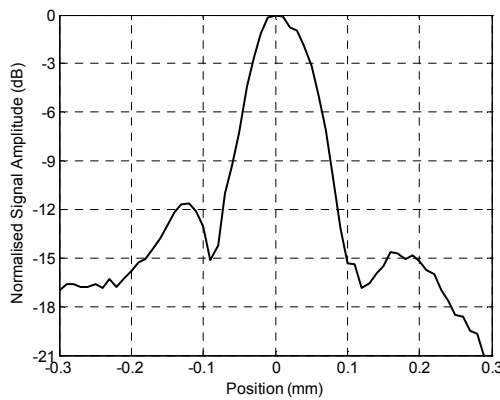


Figure 6. 33: Line spread function from TH13 by pulse-echo from 5 µm W wire.

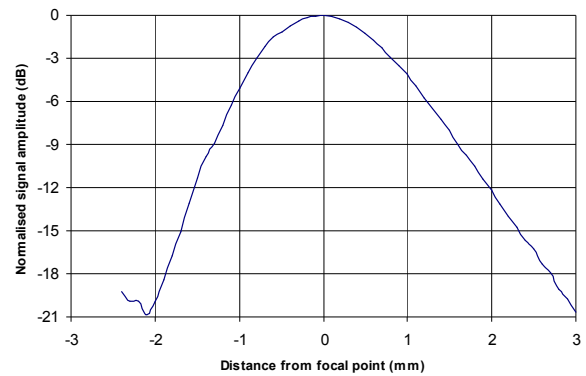


Figure 6. 34: Depth of field measurement for TH13.

TABLE 6. 14: STATISTICS FOR TH13 PULSE-ECHO MODE

Parameter	Threshold	-3 dB	-6 dB	-20 dB
Bandwidth (MHz)	1D Simulation	8	12	34
	Experimental	9	12	23
Q	1D Simulation	4.3	2.8	0.8
	Experimental	3.6	2.7	1.3
Pulse Length (ns)	1D Simulation	61	76	148
	Experimental	100	115	157
Axial Resolution (µm)	1D Simulation	47	59	114
	Experimental	77	89	121
Lateral Resolution (µm)	Theoretical	N/M	93	N/M
	Experimental	80	120	600
Depth of Field	Theoretical	N/M	1.20	N/M
	Experimental	1.6	2.30	4.9

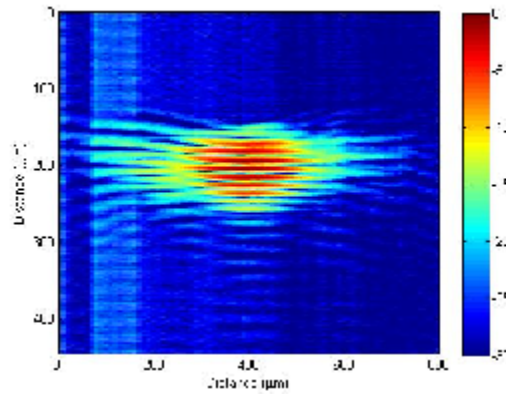


Figure 6. 35: B-scan image of single 5 μm Tungsten wire at focus of TH13

Experimentally measured impedance data does not show clear resonances and also appears to show incomplete calibration, as seen previously. Simulated data does not, therefore, fit well. However, simulated data for pulse-echo response fits closely. The frequency domain representation of pulse-echo data shows some activity at around 60 – 70 MHz; this can also be seen in the impedance data, though it is less clear due to the incomplete calibration of the machine.

Bandwidth and resolution data for TH13 are given in Table 6.14. As can be seen, values for bandwidth and Q match well to those predicted by simulation. Measured axial resolutions are around 50% greater than predicted from one-dimensional simulations: 59 μm compared to 89 μm at -6 dB, Experimental lateral resolution at -6 dB, 120 μm , is also larger than the theoretically calculated value, 93 μm , though by only around 20% in this case. The depth of field measured for this transducer is almost twice the predicted value; 2.3 mm compared to 1.3 mm. Figure 6.35 shows a B-scan of a single 5 μm tungsten wire at the focus of TH13. It can be observed that this image corresponds well to the statistics measured above, and indicates the output of this transducer is satisfactorily symmetrical and does not produce image aberrations.

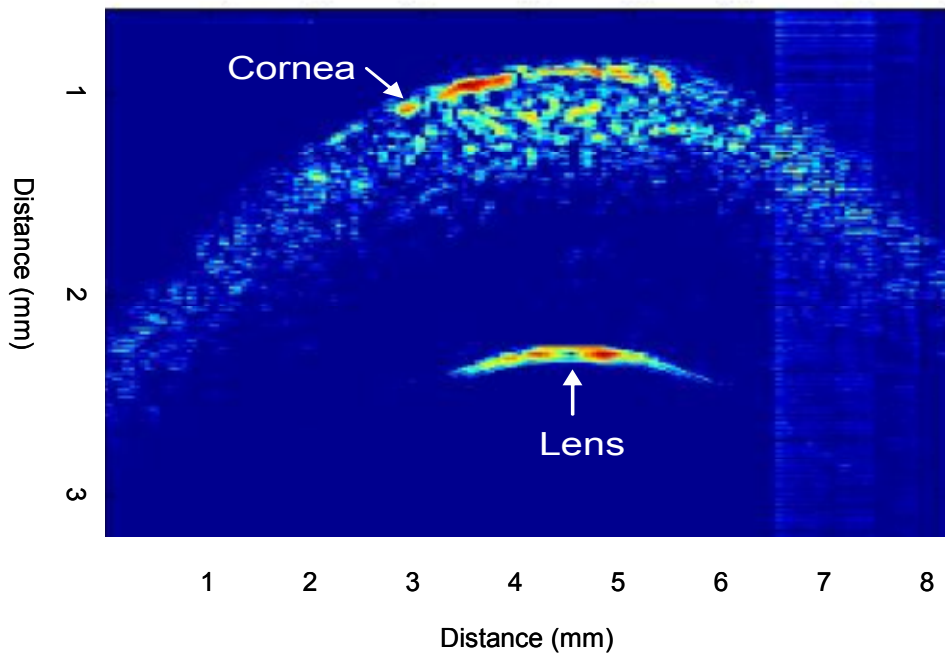


Figure 6. 36: B-scan of porcine eye from TH13

A B-scan of a porcine eye generated using TH13 is shown in Figure 6.36. This image clearly shows the anatomical features of the eye, with the cornea well defined and the lens also clearly visualised. This image is also relatively noise free. There is an unusual band on the right side of the image, but this is caused by the scan system rather than the transducer itself.

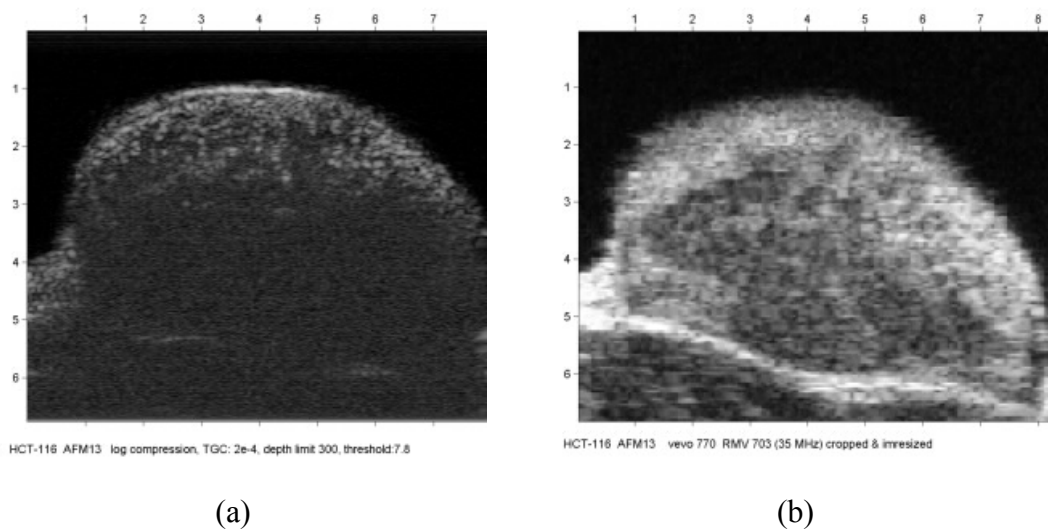


Figure 6. 37: Mouse tumour imaged using (a) TH13 and (b) a Visualsonics Vevo system. Dimension markers are in mm.

A mouse tumour was also imaged using TH13. Two images are shown in Figure 6.37. Figure 6.37 (a) was generated using the DPR500 pulser receiver as before and Figure 6.37 (b) generated using a commercial Visualsonics Vevo 770 scanning system. It can be seen that the tumours are well defined within the image. It is also worth noting that the image quality is better in Figure 6.37 (b) than 6.37 (a), illustrating the benefits of having a good quality imaging system as well as a good transducer.

6.5. Summary

This chapter presented results from acoustic characterisation of four VPP micromoulded composite transducers, including data on bandwidth, resolution and depth of field of each of the devices. Data from a dice-and-fill composite transducer and a LNO transducer were also presented for purposes of comparison. The lateral resolution of JB1 is better than the MC transducers, TH09, TH16 and TH13, by 80%, 50% and 25% respectively. Although from theory TH09 is expected to have better lateral resolution, TH16 and TH13 would be expected to be closer to JB1 than they are. JB1 does have the smallest depth of field of the focused transducers, which could be expected given smaller lateral resolution goes with in smaller depth of field. The axial resolution of JB1 is also better than that of the MC transducers, by around a factor of 2-2.5 in all cases.

Images of ex-vivo animal tissue produced using these transducers were also presented, and finally an image of a mouse tumour. The image produced by JB1 was of similar clarity to the MC transducers; although JB1 has better resolution, it has rather poor sensitivity because of its long focal distance, which detracts from image quality. These results are discussed further in Section 7.4 in the next chapter.

6.6. References

Lockwood G.R., Turnbull D.H., Foster F.S. (1994) Fabrication of High Frequency Spherically Shaped Ceramic Transducers *IEEE Transactions on Ultrasonics, Ferroelectrics and Frequency Control*, Vol. 41, No. 2 pp. 231-235

7. Discussion

Piezocomposites are the material of choice for ultrasonic transducers because of their favourable piezoelectric performance and acoustic properties. This has been discussed in detail throughout this thesis and is demonstrated by results of one-dimensional modelling undertaken and presented in Section 2.7. Results are discussed further in this chapter.

In Sections 7.2 and 7.3, results from fundamental characterisation of bare piezocomposite material, as presented in Chapter 5, are discussed. Electrical impedance measurements were taken from bare composite and used to calculate piezoelectric properties of the composites, using constitutive equations. These were then compared to one-dimensional simulations. Where required, properties were fitted to impedance measurements. These results were compared, with the aims of determining whether this method can be used to derive fundamental properties of the materials accurately and whether the micromoulded piezocomposites offer performance benefits over materials more commonly used in HFUS transducer fabrication.

In Section 7.4, results presented in Chapter 6 from acoustic testing of piezocomposite after inclusion in transducer casing are discussed. As before, electrical impedance has been measured and used to predict the effective piezoelectric properties of these transducers. From this, simulations of acoustic output were generated, and these were compared to experimental measurements of acoustic output. Within this chapter, these results are analysed to determine the accuracy of one-dimensional simulation in predicting the acoustic performance of a transducer. Prototype transducers have also been compared with those reported in the literature, to gauge performance and potential for future development.

7.1. Transducer design and fabrication

7.1.1. Passive materials

Knowledge of the acoustic properties of the materials used in passive components of ultrasound transducers, primarily the matching and backing layers, is crucial to device design and in particular to modelling of transducers. The key parameters are acoustic impedance and attenuation, and elastic properties such as stiffness and Poisson's ratio. Matching layers must be of particular acoustic impedance for optimum transmission and reception and the value of acoustic impedance of a backing layer is crucial in optimising the sensitivity and bandwidth of a transducer. Only backing layers were used in the work reported here; matching layers were not.

In general, a backing layer of slightly lower acoustic impedance than the active layer is desired. This is because when a wave incident on the boundary of a material with higher acoustic impedance is reflected, the phase of the wave remains the same, whereas a 180° phase shift is usually considered a prerequisite for $\lambda/2$ resonance. A backing layer should also be relatively lossy to ensure that minimal energy is reflected from its back face. The tungsten-loaded epoxy tested for the work of this thesis fulfils these characteristics, having specific acoustic impedance for longitudinal waves in the range 3-15 MRayl and relatively high losses, at approximately 30 dB/mm (at 36 MHz). It has also been shown that it can be reliably characterised, with velocity, and acoustic impedance varying with volume fraction as expected from theory. This material was used in the fabrication of TH13 and TH16.

7.1.2. UPG

Work was also undertaken to investigate surface finishing of composite materials with UPG. UPG is known to produce excellent surface flatness and planarity, and could be capable of bulk production of high frequency composites. The work for this thesis showed this to be true. Measurements of surface profile using a DekTak 3ST surface profiler (Veeco, Cambridge, UK) showed surface deviation not exceeding $\pm 3 \mu\text{m}$ on a standard dice-and-fill composite and $\pm 1 \mu\text{m}$ on a micromoulded

composite made with VPP PZT. This was better than the surface deviation measured from samples prepared using a standard lapping process: $\pm 2 \mu\text{m}$ on a micromoulded composite and over $\pm 15 \mu\text{m}$ on a standard dice-and-fill composite. Discontinuities at the boundary between the polymer matrix and ceramic pillar were also less with UPG.

Optimisation of the lapping process can significantly improve the surface finish of piezocomposites compared to standard lapping. Bernassau et al. (2007) used a glass lapping plate with $3 \mu\text{m Al}_2\text{O}_3$ and subsequent polishing using an alkaline colloidal silica solution on a dice-and-fill composite made with PZ27 (Ferroperm, Kvistgaard, Denmark) for the ceramic phase and Epofix epoxy (Struers, Solihull, UK) for the polymer phase. Surface deviation of around $\pm 50 \text{ nm}$ was achieved. This is a significant improvement in surface finish, even compared to UPG. Lapping equipment has a further advantage in that it is significantly less expensive, and smaller, than UPG equipment. However, while the ultra precision grinder is specifically designed for bulk fabrication, producing high quality surface finishes with lapping is presently labour-intensive and is unlikely to be able to produce high frequency composites on a large scale.

7.2. Active materials: standard materials

7.2.1. One dimensional simulation of standard materials

One-dimensional simulations were presented in Section 2.7 for transducer geometries corresponding to a typical 40 MHz single element transducer and one element of a 40 MHz array using a range of materials commonly used for high frequency transducer fabrication: LNO, PVDF, PZT, PZT-polymer composite, PMN-PT and PMN-PT polymer composite. It is useful to recap on this to provide some context for the discussion on piezocomposites that follows.

The low permittivity of LNO and PVDF means typical single element transducer apertures have electrical impedance well matched to 50Ω instrumentation. The

converse is true for the other materials considered. PZT in particular has very high permittivity. This makes it suited to fabrication of array elements. LNO has the highest propagation velocity of these materials, which makes HFUS fabrication easier because the active layer will be thicker for a given frequency. PVDF is easily formable, allowing mechanical focusing of single elements. The latter property is also the case for piezoceramic-polymer composite materials. PVDF has the acoustic impedance most closely matched to tissue, but piezocomposites are also relatively well matched. PMN-PT composite has the highest value of k_T of these materials. PZT composite also has excellent k_T . Low k_T is a significant disadvantage of PVDF, although it is known to have excellent reception characteristics and large receive bandwidth.

Assessing the results it is clear that each of these materials has specific advantages. However, in terms of overall performance, composite materials are extremely attractive, as is widely acknowledged in the literature. While not performing best in terms of individual parameters, composites can generally be regarded as offering excellent piezoelectric properties and relatively close acoustic impedance match to tissue. They also typically provide convenient electrical impedance, both for single element transducers and arrays; this may be optimised by tailoring of composite volume fraction, although this will also affect piezoelectric properties of the material, for example k_T , as shown in Figure 2.17.

7.2.2. Testing and characterisation of PZT-5A / RX771 composite

Traditional material characterisation was not possible for the micromoulded composites studied for the work of this thesis. An alternative method was adopted, where piezoelectric properties were derived from electrical impedance spectroscopy measurements and verified by comparison to simulations from a one-dimensional model.

To test this, firstly, a composite material was fabricated from well-understood materials, Ferroperm PZ27 (PZT-5A) and epoxy (RX771) using dice-and-fill techniques then characterised. It was shown that piezoelectric parameters produced

experimentally were well matched to the theoretical values. Secondly, simulations produced from direct measurements of composite materials were well matched to models produced from Smith and Auld equations for composite homogeneity. This confirmed that the characterisation procedure proposed was suitable. The piezoelectric properties of this piezocomposite also provide a useful comparison for properties measured with VPP composites.

7.3. Novel materials: fabrication and characterisation

7.3.1. Fibre composite

A novel design for composite manufacture is to use extruded small diameter fibres, which are then packed together and bonded in a polymer matrix, as described in Section 4.1.3. If fibres could be made with sufficiently small diameter they could be used for high frequency composite manufacture. Fibre composites have some key advantages. The fibres may be packed tightly giving high volume fraction, and the semi-random nature of their distribution in lateral directions reduces the influence of inter-pillar lateral modes. A further advantage is that it is a cost effective method of producing piezocomposites (Rödig et al., 2005)

In the present work, two fibre composite samples were made using 250 μm diameter VPP fibres and one with 100 μm diameter VPP fibres. These were characterised with the primary motivation of testing the VPP material as opposed to development of HFUS fibre composites. In general, electrical impedance data fitted reasonably well to simulated data, to within 10% or less. A high frequency fibre composite was fabricated and pulse-echo signals were recorded from this. However, as the fibres used to make this composite were of far larger diameter than ideal for a high frequency composite, full characterisation was not possible. The piezoelectric properties measured for the fibre composite samples at low frequency are discussed further in Section 7.3.3, and compared to the standard composite described in Section 7.2.1.

7.3.2. Micromoulded composites

The work for this thesis was centred on characterisation and testing of piezoceramic composites made from VPP PZT by a novel micromoulding technique, as described in Section 4.1.3. A total of six micromoulded composites (MCs) were tested. MCs 1 – 4 were made using an early generation process, while MC6 was made with a refined process. It is therefore to be expected that the piezoelectric properties are best in MC6, and this is the case. The match between the experimentally generated piezoelectric properties and theoretical data varied between samples but was much closer for MC6 than for the other MCs, suggesting that this late sample was closer to performing optimally. Across the range of MCs, the experimentally-derived theoretical properties matched those generated by simulations from direct impedance measurements to within around 10%. The piezoelectric properties of each composite were also compared to those generated by one-dimensional simulations using nominal properties of a TRS600 / RX771 composite of the same volume fraction. In this case the difference was as much as 70%. This could be expected due to the differences in material and fabrication processes. In general, the MC had higher c_{33} , e_{33} and h_{33} and lower k_T and ϵ_R^S than the nominal piezocomposite values.

7.3.3. Comparison of composite materials

TABLE 7. 1: LIST OF COMPOSITE SAMPLES TESTED

Composite Type	Composite Name	Mechanical Resonant Frequency (MHz)
PZ27 Dice-and-fill Composite	SC1	5.6
VPP PZT Fibre Composite	FC1	1.9
	FC2	8.0
	FC3	9.0
VPP PZT Micromoulded Composite	MC1	11.8
	MC2	24.9
	MC3	15.7
	MC4	22.4
	MC6	37.6

As described in the preceding sections of this chapter, several composite materials were tested: dice-and-fill composite made with PZ27, fibre composites made with VPP PZT fibres, and micromoulded composites made from VPP PZT. These samples are listed in Table 7.1, and operational frequencies for each are given.

It is instructive to compare the piezoelectric properties of the fibre composites and micromoulded composites with properties of the standard dice-and-fill composite. Nine parameters were compared for all of the samples. These can be split conveniently into related properties: ultrasonic: v_l , Z ; mechanical: c_{33}^D , c_{33}^E ; electrical ϵ_R^S ; and piezoelectric h_{33} , d_{33} and k_T .

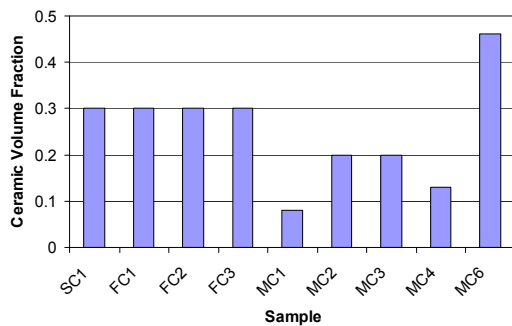


Figure 7. 1: Summary showing ceramic volume fractions of all composites tested.

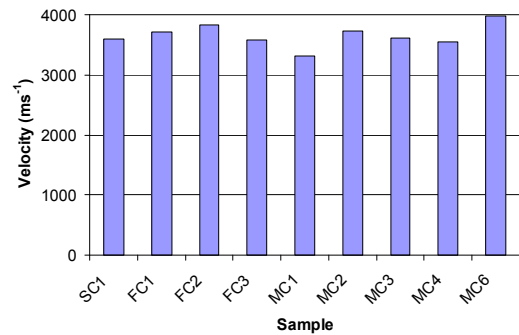


Figure 7. 2: Summary showing velocities of all composites tested.

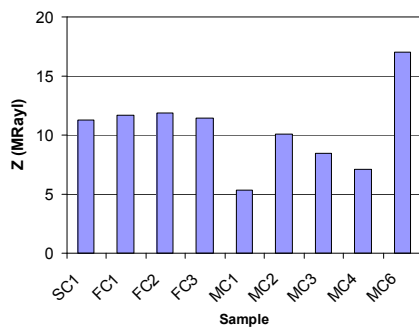


Figure 7. 3: Summary showing acoustic impedance of all composites tested.

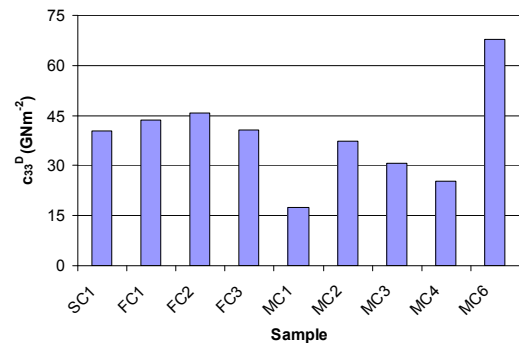


Figure 7. 4: Summary showing c_{33}^D of all composites tested.

The velocities, v , of the composites (shown in Figure 7.2) are all relatively similar, and can be linked to volume fraction of the composite: a higher volume fraction of ceramic will lead to an increased thickness mode velocity because the piezoceramic

phase of a piezocomposite has far greater velocity than the polymer phase. Similarly, the density, ρ , of a composite is increased when volume fraction of piezoceramic is increased, so acoustic impedance, $Z = \rho v$ will increase.

As c_{33}^D is also directly linked to ρ and v by:

$$c_{33}^D = \rho v^2 \quad 7.1$$

this also corresponds to volume fraction. The values of Z and c_{33}^D measured across the range of composites are shown in Figures 7.3 and 7.4 respectively. It can be seen that piezocomposite samples with higher volume fraction also have increased Z and c_{33}^D , as expected.

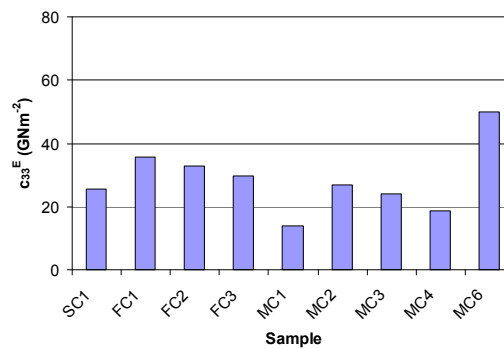


Figure 7. 5: Summary showing c_{33}^E of all composites tested.

The values of c_{33}^E also appear to correspond approximately with ceramic volume fraction across the range of composites tested. c_{33}^E is lower in the standard composite than the majority of other composites tested: this is due to the standard composite being made from lower permittivity ceramic material.

The values of ϵ_R^S for each composite are shown in Figure 7.6. These values vary quite considerably over the samples tested. This can be partly attributed to ϵ_R^S increasing with increasing volume fraction. However, it can also be seen that the fibre composite samples, FC1, FC2 and FC3 show relatively high ϵ_R^S , significantly greater than the standard composite SC1.

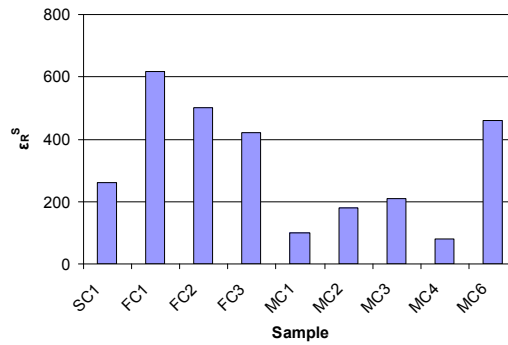


Figure 7. 6: Summary showing ϵ_R^S of all composites tested.

The micromoulded samples generally show varying permittivity approximately in line with volume fraction. MC6 has ϵ_R^S almost twice that of the other MC samples tested, but is also of much greater volume fraction than the other MC samples so this is to be expected.. Comparison of the ϵ_R^S results for MCs with the standard composite, SC1, show that MC1 - MC4 are of slightly lower permittivity than SC1, though not substantially lower. MC6, conversely, has much greater permittivity. This is to be expected for two reasons: firstly, MC1 - MC4 are lower volume fraction than SC1, while MC6 is of higher volume fraction, and secondly, the standard composite was fabricated from PZT-5A, which is of medium permittivity, and the MCs from PZT-5H (TRS600), which is of high permittivity.

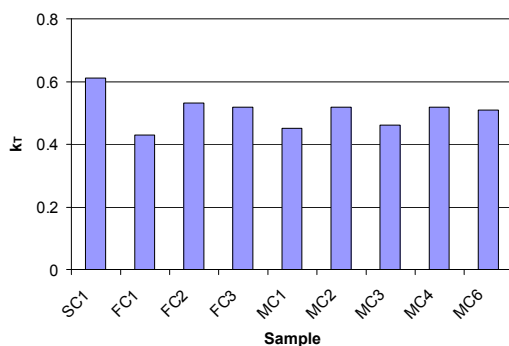


Figure 7. 7: Summary showing k_T of all composites tested.

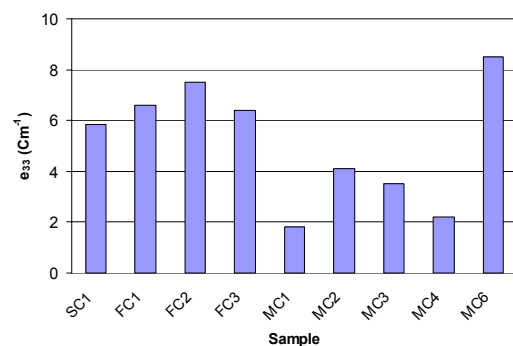


Figure 7. 8: Summary showing e_{33} of all composites tested.

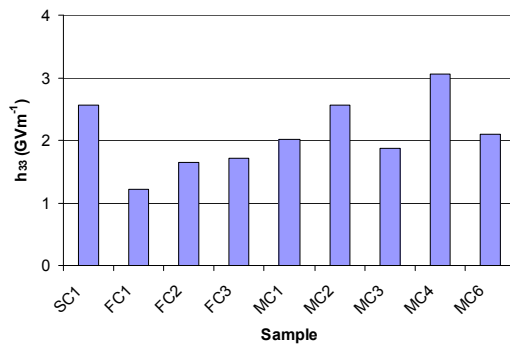


Figure 7. 9: Summary showing h_{33} of all composites tested.

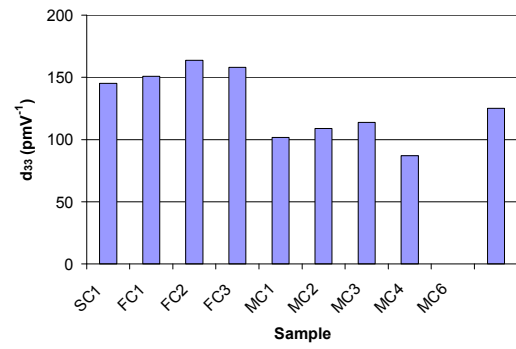


Figure 7. 10: Summary showing d_{33} of all composites tested.

The values of k_T calculated for each of the composites tested are shown in Figure 7.7. As can be seen, the value of k_T in the standard composite, 0.61 is around 10 - 15% higher than the FCs and MCs tested. The value of k_T is generally consistent across the FC and MC samples, in the range 0.43 – 0.52.

The value of h_{33} would not be expected to change markedly across composites of different volume fraction but the values for h_{33} in the composites tested, shown in Figure 7.9, fluctuate considerably. The value of h_{33} is calculated from:

$$h_{33} = \sqrt{\frac{k_T^2 c_{33}^D}{\epsilon_0 \epsilon_R^S}} \quad 7.2$$

so errors in k_T , c_{33}^D and ϵ_R^S , which are themselves derived indirectly from other measurements, lead to systematic errors in determination of h_{33} . It should also be noted that the values of c_{33}^E , e_{33} and d_{33} are also calculated from other properties and so could be subject to the same effect.

Values of e_{33} , as shown in Figure 7.8 are also generally consistent when similar samples are compared. e_{33} is high in the fibre composite samples, when compared to the standard composite and also the MC. This is to be expected as ϵ_R^S is higher in the fibre composite samples than the other samples, and this is proportional to e_{33} according to the relationship:

$$e_{33} = \varepsilon_0 \varepsilon_R^S h_{33} \quad 7.3$$

d_{33} also shows a degree of uniformity broadly across the range of samples but particularly when the types of composite are compared. In the case of both fibre composites and micromoulded composites, the values are the same to within 20%.

7.4. Transducer applications results

7.4.1. Basic testing

The results generated from fundamental characterisation suggest that MC could be used to fabricate HFUS transducers for use in medical imaging. Further investigation of the performance characteristics of the MC was undertaken in the form of ultrasonic testing. Five MC samples were incorporated into casings to make single element transducers, with a tungsten-loaded epoxy backing layer but no matching or protective front layer. Two of the transducers were unfocussed and three were spherically focussed by mechanical shaping of the active element.

For each of these transducers, electrical impedance magnitude and phase measurements were taken and one dimensional simulation fitted to these in the same way as for the bare material. The piezoelectric properties of each transducer were then used to generate the impedance simulation and to produce simulations of the pulse-echo response of each transducer. These were compared to pulse-echo responses measured experimentally. For purposes of comparison, identical measurements were also taken from two transducers made by similar fabrication processes but with alternative piezoelectric materials. The first of these was a PZT (CTS3203HD) dice-and-fill composite transducer and the second a LNO transducer.

The performance characteristics of these transducers were set out in detail in Chapter 6. The following paragraphs are a general analysis. Performance figures for the transducers tested are summarised in Table 7.2. $f\#$ is f-number (spherically

focussed transducers only), f_m is centre frequency, Q is -6 dB quality factor, R_A and R_L are axial and lateral resolution at -6 dB, respectively, DOF is depth of field at -6 dB and IL is insertion loss.

TABLE 7. 2: SUMMARY OF MEASURED PULSE-ECHO PERFORMANCE CHARACTERISTICS OF ALL TRANSDUCERS TESTED.

Name	Active material	f#	f_m (MHz)	Q	R_A (μm)	R_L (μm)	DOF (mm)	IL (dB)
JB1	Dice-and-fill PZT composite	2.8	51	1.6	37	80	1.5	-48
LNO60	LNO	Flat	60	6.7	39	N/M	N/M	-93
TH10	MC	Flat	26	3.1	78	N/M	N/M	-44
TH09	MC	3.8	36	1.2	81	145	3.30	N/M
TH16	MC	2.2	43	4.9	70	100	2.4	-60
TH13	MC	1.9	32	2.7	89	120	2.3	-58

Broadband response, i.e. *low* Q , is an essential characteristic for high resolution medical imaging transducers, and so an active material which can contribute to this is extremely useful. Examples in the literature are up to $Q = 3$ for PZT (Lockwood et al., 1994), and $Q < 1$ for PVDF (Foster et al., 2000).

Tests on LNO60 and JB1 indicate they have Q of 6.7 and 1.6 respectively. BW is a function not only of the active material of the transducer, but also of the properties of any backing layers, matching layers and acoustic impedance mismatch between transducer and imaging media. This makes explicit comparison between active materials difficult, but these figures at least give some context to those measured for the MC transducers.

TH16 has relatively high $Q = 4.9$, which is less than LNO60 but can be considered poor in the context of figures quoted for other materials. TH10 and TH13 are better, having comparable Q to PZT. TH9 has the lowest Q of the MC transducers, close to that of the standard composite transducer, JB1. This is greater than the figure quoted

for PVDF, but the acoustic impedance mismatch between PVDF and water is much less than between piezocomposite and water. Q of the MC transducers could be improved by addition of a matching layer (Goll and Auld, 1975).

The MC transducers have R_A at -6 dB in the range 70 – 89 μm . From the figures presented in Section 6.2 and 6.3 it can be seen that this is greater than expected from theoretical pulse simulations but there is reasonable consistency across the MC transducers. R_L is 100 μm for TH16 and 120 μm for TH13, greater than expected from theoretical calculations based on $f\#$ and frequency. The DOF measured for these transducers is greater than predicted from theory, but this is to be expected as R_L is also larger. R_L for TH9 is 145 μm , which is smaller than expected from theory but DOF is also smaller than predicted from theory.

The final figures compared in Table 7.2 are for insertion loss. For the MC transducer this is in the range -44 dB to -62 dB which is approximately the same as measured for JB1 (-48 dB) and compares favourably to LNO60 (-93 dB). This is desirable as low insertion loss is key to achieving good sensitivity for a transducer without having to use high drive voltages.

R_A , R_L , DOF and insertion loss are heavily dependent on the geometrical design and fabrication of the transducer, so are not necessarily indicative of the performance of the active material itself. The work reported in this thesis focussed on assessing the potential for MCs to be used for HFUS transducer and array fabrication. Optimisation of the prototype MC transducers was not within the scope of this work, and as such a number of design and fabrication issues were not examined. For example, the transducers did not incorporate matching layers, and backing layers were not well optimised. Fabrication and loading of active elements into transducer casings was also not an optimised process, leading to misalignment with casings, particularly in the case of TH09. However, it is worth noting that the axial and lateral resolutions measured for the MC transducers are commensurate with high frequency operation, despite lack of optimisation in the transducer fabrication process. This suggests that MC is indeed a viable route to HFUS transducer fabrication.

7.4.2. Imaging performance

The fundamental motivation for this research is to show that MC can be used to make transducers suitable for high resolution medical ultrasound diagnostics. To address this, basic imaging procedures were undertaken with the MC transducers. B-scans of ex-vivo tissue samples were produced of ovine and porcine eyes. Despite the relatively simple imaging hardware system that was used, and minimal processing of raw RF data, useful images were generated. Key structures within the eyes were clearly visualised, such as the cornea and lens. Clear images of a mouse tumour were also generated using an MC transducer with a standard pulse- receiver set-up and compared with a sophisticated commercial system. This suggests that transducers made with MC have potential as high resolution ultrasound imaging devices.

7.5. Summary

A number of MCs have been intensively characterised and it has been found that MCs have good potential for use in HFUS devices and their performance compares well with other piezoelectric materials commonly used in HFUS devices. The results discussed here indicate that transducers made with the MC have reasonable high frequency ultrasonic properties and that MC transducers can be incorporated into an imaging system and produce high resolution images of anatomy.

7.6. References

Bernassau A.L., McKay S., Hutson D., Démoré C.E.M., Garcia-Gancedo L., Button T.W., McAneny J.J. and Cochran S. (2007) Surface Preparation of 1-3 Piezocomposite Material for Microfabrication of High Frequency Transducer Arrays. *Proceedings of 2007 IEEE Ultrasonics Symposium* pp. 96-99

Foster F.S., Harasiewicz K.A., Sherar M.D. (2000) A History of Medical and Biological Imaging With Polyvinylidene Fluoride (PVDF) Transducers. *IEEE*

Transactions on Ultrasonics, Ferroelectrics, and Frequency Control, Vol. 47, No. 6, pp. 1363-1371

Goll J.H. and Auld, B.A. (1975) Multilayer Impedance Matching Schemes for Broadbanding of Water Loaded Piezoelectric Transducers and High Q Electric Resonators *IEEE Transactions on Sonics and Ultrasonics* Vol. SU-22, No.1. pp.52-53

Lockwood G.R., Turnbull D.H., Foster F.S. (1994) Fabrication of High Frequency Spherically Shaped Ceramic Transducers *IEEE Transactions on Ultrasonics, Ferroelectrics and Frequency Control, Vol. 41, No. 2 pp. 231-235*

Rödig T., Schönecker A., Hladky A.C. (2005) Design and Characterisation of 1-3 Ultrasonic Composites using ATILA and Ultra Fast Laser Measurements (20 MHz) *Proceedings of 2005 IEEE Ultrasonics Symposium* pp. 353-356

8. Conclusions

The results presented in this thesis suggest that MCs exhibit good piezoelectric properties; that transducers made with MCs have reasonable high frequency ultrasonic properties; and that incorporation of MC transducers into a high-resolution medical imaging system is feasible. Thorough investigation and characterisation of the MCs supports the following conclusion:

8.1. Micromoulded piezocomposites provide a route to production of high resolution ultrasound transducers

Micromoulded PZT-polymer composites (MC) have been extensively characterised, both in the form of bare coupons and after incorporation in transducer casings. Fundamental characterisation of these MCs has shown that the piezoelectric properties of these materials are comparable to, and in some cases superior to other materials used for high frequency transducer manufacture: e.g. LNO, PVDF and bulk PZT. Each of these materials has key advantages and disadvantages. In terms of overall performance, MCs appear desirable. MCs exhibit many of the advantages associated with piezocomposites, which are widely accepted as the material of choice for ultrasonic transducers at lower frequencies.

Comparison of the material properties of MC to those of a standard dice-and-fill piezocomposite of similar volume fraction, found them to be comparable for most properties. However, key parameters k_T and d_{33} are smaller. This is a clear disadvantage of MC and is likely to be a fundamental issue unless further ceramic processing optimisation is performed. The value of ϵ_R^S measured for the MCs was greater than for the standard piezocomposite, although this was with a different PZT. The relatively high ϵ_R^S of the MCs is a major advantage when looking toward development of high frequency arrays.

The key advantage of MCs is that they offer a route to higher frequency piezocomposites than are currently possible with dice-and-fill fabrication techniques. Although transducer design is aimed at meeting clinical needs it has traditionally

been held back by lack of suitable active materials. To gain the benefits of 1-3 connectivity piezocomposite materials, they require volume fraction of at least 30% and pillars of aspect ratio of three. Increasing the frequency of dice-and-fill piezocomposites is dependent on thinner saw blades being produced. Currently the smallest available saw blade width is 9 μm , meaning minimum active layer thickness of around 45 μm . This corresponds to a maximum achievable frequency of little more than 40 MHz.

Micromoulded PZT structures can be made with smaller pillars, and smaller kerfs, than possible with dice-and-fill fabrication giving piezocomposites of sufficiently high ceramic volume fraction to be capable of working at frequencies previously unattainable with piezocomposite transducers. When considering frequencies of 40 MHz and upward, it becomes clear that MCs do in fact offer improved properties to other materials which can be fabricated for transducers at these frequencies. A further advantage of MC pillars is that they may be shaped in non-standard geometries (Cochran et al., 2004). Dice-and-fill piezocomposite pillar shapes are limited to rectangles, hexagons and triangles, periodic structures that may encourage lateral modes. This is often solved by use of pseudo random pillar structures at lower frequencies, but fabrication of these to the small scale dimensions required for high frequency piezocomposites is challenging (Brown et al., 2009).

Functional transducers, both focussed and unfocussed, have been successfully produced using MCs. It was shown that MCs work well after mechanical focussing. The performance of these transducers has been shown to vary, and was not as good as a transducer made from dice-and-fill piezocomposite in terms of imaging resolution. This may be improved with further refinement of the transducer manufacturing process. However, the transducers do show good sensitivity despite having no acoustic matching layer or electrical matching. Images have been produced of reasonably high resolution and SNR; further improvement may be possible with optimisation of both the transducer fabrication process and the imaging system into which it is incorporated.

It has been shown that high frequency ultrasound devices made with MCs are capable of generating 2D images of ex-vivo tissue. Images have been made of ex-vivo ovine and porcine eyes, and in-vivo mouse tumours. Structures within the eyes, such as the cornea and lens could be distinguished, and the mouse tumour was clearly defined, suggesting that these HFUS transducers may be useful diagnostic tools.

8.2. Further conclusions

Although the work described in this thesis was primarily intended to assess the potential for MCs to be used as the active layer in HFUS devices, a number of other conclusions may also be drawn from the results presented in this thesis. These are as follows:

Piezocomposite materials may be characterised using impedance measurements and one dimensional modelling

Electrical impedance spectroscopy can be used in conjunction with one dimensional modelling, based on the one-dimensional wave equation, to characterise active materials. This procedure was tested using a well-defined dice-and-fill piezocomposite. Simulations based on direct electrical impedance measurements matched well to those generated using the piezocomposite homogeneity principles of Smith and Auld (1991). The properties of MCs cannot be determined from traditional experimental measurements of the properties of the constituent materials. Fitting of experimentally derived properties to one-dimensional models has been shown to be an effective method of material characterisation (Maréchal et al., 2006), and results presented here suggest this is an effective method of characterising MC (MacLennan et al., 2008).

It should be noted, however, that in the context of piezocomposites, one-dimensional modelling is limited to samples where the pillar aspect ratio is sufficiently large that the frequency of lateral modes generated within the composite is not close to the thickness mode frequency. In practice, this means that one-dimensional modelling should ideally be restricted to piezocomposites where pillar height is at least three

times the pillar width. This rule also applies when designing a composite to work efficiently: composites with lesser aspect ratio have been shown to have reduced k_T (Hayward and Bennett, 1996), as discussed in Section 2.8.3.

PZT-fibre composites have potential for use as the active material for high frequency transducers

Piezofibres made using VPP have historically exhibited better piezoelectric properties than comparable commercially produced fibres (Dent et al., 2005) and piezocomposites have been successfully fabricated from these (MacLennan et al., 2006). Fibre composites offer other benefits including ease of handling and reduced manufacturing costs due to a reduction in the number of fabrication steps required. The piezoelectric properties measured for these composites are comparable with alternative active materials and, provided VPP fibres of small enough diameters can be produced, thinner, higher frequency active elements could be produced without the pillar aspect ratio problems described above. This arrangement also has other advantages. Although the fibres are aligned to one another in the thickness direction, they can be randomly positioned, laterally, within this composite. This can significantly reduce interpillar lateral mode coupling. Further practical benefits of use of piezofibres in this way are the relatively easy handling of the material, and the removal of the ‘dice-and-fill’ step, so less ceramic waste product.

Passive materials can be tailored for use in high frequency ultrasound transducers and accurately characterised

Results presented here verify that tungsten loaded epoxy can be fabricated reliably to design requirements, and that the through-transmission measurement technique described in this thesis can be used to determine parameters of passive materials at high frequencies for theoretical transducer modelling. This has been undertaken in the one dimensional modelling used for the work of this thesis (Webster et al., 2007).

UPG may provide a route to bulk production of piezocomposite for high frequency transducers

Work in this thesis has shown that UPG could provide a practical method to aid bulk production of high frequency piezocomposites for ultrasonic transducers (MacLennan et al., 2006). Piezocomposite layers have been produced of less than 100 μm in thickness, with surface roughnesses of approximately $\pm 1 \mu\text{m}$. It can also be seen that UPG produces an improved surface finish when compared to conventional lapping and less indication of discontinuity between ceramic pillars and binding polymer. Work undertaken by Bernassau et al. (2007) showed surface roughnesses of significantly less than $\pm 1 \mu\text{m}$ can be achieved using an optimised lapping procedure but, unlike UPG, this procedure cannot easily produce large numbers of piezocomposite samples.

8.3. Further Work

As well as drawing conclusions from the work described in this thesis, strands of future work may also be considered.

Micromoulded composites for HFUS transducers

Characterisation of the MCs showed this material has good potential for use in HFUS devices. The composite structures tested here had pillar diameters of 20 μm and greater. To retain a pillar aspect ratio of three, an MC with pillar diameter 20 μm can be no thinner than 60 μm , meaning that the highest frequency for this piezocomposite is around 30 MHz. As discussed above, it is possible to fabricate piezocomposites of frequency up to 40 MHz with dice-and-fill technology. For a 0.3 volume fraction piezocomposite, this corresponds to pillars of width 14 μm . The key goal in the development of MC is therefore to produce pillar structures of less than 14 μm width.

The piezoelectric properties of the MCs are comparable with other materials used for HFUS transducers but key properties k_T and d_{33} are lower than would be expected for a PZT piezocomposite. Further optimisation of the material production process to increase k_T and d_{33} would be highly beneficial. This is particularly important, as advances in RIE for single crystal materials have indicated that very high performance piezocomposites can be made, meaning it is possible to fabricate higher

frequency piezocomposites than previously was possible. MCs will not present a viable alternative to RIE single crystal piezocomposites without the material properties being at least comparable.

HFUS Arrays

Results presented here also suggest that the MCs are a viable active material for array fabrication and these are currently under development. Figure 8.1 shows a prototype linear array made with a MC (Bernassau et al, 2009). The array pattern has 20 elements with 15 μm inter-element pitch and 7.5 μm wide electrodes. Assuming inter-element pitch of one wavelength is required, this array pattern would be suitable for a linear array operating at up to approximately 100 MHz. It is suitable for a phased array, which requires half-wavelength inter-element pitch, operating at up to 50 MHz.

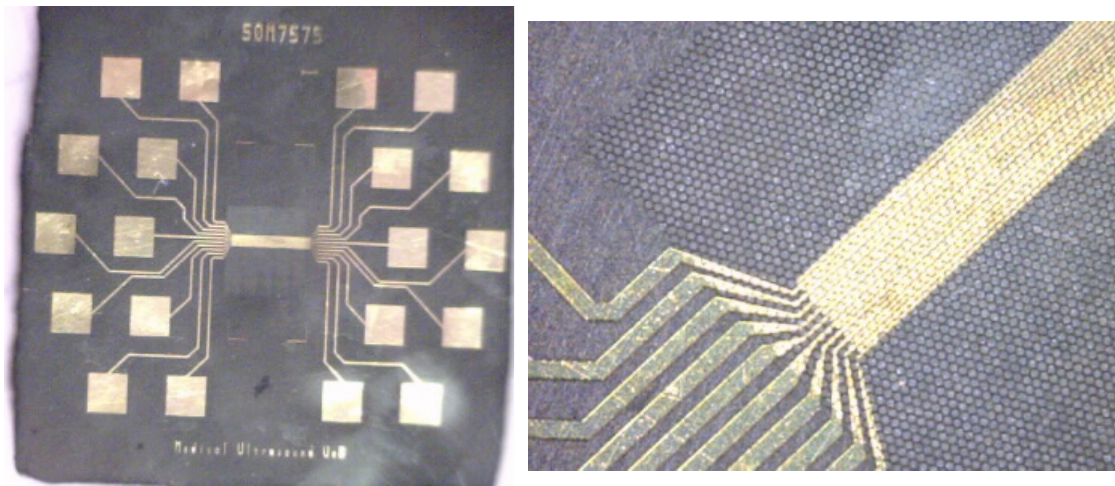


Figure 8. 1: Prototype linear array made with MC

The piezocomposite has circular pillars of diameter 20 μm in a hexagonal configuration with 9 μm kerf. As discussed, the upper frequency of this composite would be limited to 30 MHz. However, the volume fraction of this piezocomposite is 0.43, which is higher than the minimum 0.3 required. The pillar diameter could be reduced while maintaining acceptable volume fraction, allowing the upper limit of operational frequency to be increased.

Fibre Composites

The diameter of fibre required for fabrication of high frequency fibre composite layers is significantly smaller than was tested in the work described here. The upper frequency limit for ultrasound transducers made with fibre composites may be limited, however. When PZT fibres become very thin, they are likely to be too fragile to handle. As such the minimum thickness, and therefore maximum frequency of an active layer made from PZT composite would be limited. A 50 MHz fibre composite active layer would need to be a thickness of 35 – 40 μm . The accepted minimum aspect ratio of three corresponds to fibre diameter of approximately 11-13 μm , which may not be practical for piezocomposite manufacture. Another limitation of fibre composites is that due to the random positioning of the fibres they are not suitable for making arrays. However, as fibre composites are cost effective to produce, further development may be useful for single element transducers in the 20-30 MHz range.

8.4. References

Bernassau A, University of Dundee, Photo of array, personal communication.

Bernassau A.L., McKay S., Hutson D., Démoré C.E.M., Garcia-Gancedo L., Button T.W., McAneny J.J. and Cochran S. (2007) Surface Preparation of 1-3 Piezocomposite Material for Microfabrication of High Frequency Transducer Arrays. *Proceedings of 2007 IEEE Ultrasonics Symposium* pp. 96-99

Brown J.A., Chérin E., Yin J., and Foster F.S. (2009) Fabrication and Performance of High-Frequency Composite Transducers with Triangular-Pillar Geometry. *IEEE Transactions on Ultrasonics, Ferroelectrics, and Frequency Control*, Vol. 56, No. 4 pp.827-836

Cochran S., Abrar A., Kirk K.J., Zhang D., Button T.W., Su B., Meggs C., Porch N. (2004) Net-Shape Ceramic Processing as a Route to Ultrafine Scale 1-3 Connectivity Piezoelectric Ceramic-Polymer Composite Transducers *Proceedings of 2004 IEEE Ultrasonics Symposium* pp. 1682-1685

Dent A.C. Nelson L.J., Bowen C.R., Stevens R., Cain M., Stewart M. (2005) Characterisation and properties of fine scale PZT fibres. *J. Euro. Ceram. Soc.*, 25, 2387-91

Hayward G, Bennett J (1996) Assessing the Influence of Pillar Aspect Ratio on the Behavior of 1-3 Connectivity Composite Transducers. *IEEE Transactions on Ultrasonics, Ferroelectrics, and Frequency Control*, Vol. 43, No.1 pp.98-108

Jiang X., Snook K., Cheng A., Hackenberger W.S., Geng X. (2008) Micromachined PMN-PT Single Crystal Composite Transducers: 15-75 MHz PC-MUT *Proceedings of 2004 IEEE Ultrasonics Symposium* pp. 164-167

MacLennan D., Zhang D., Cochran S., Button T.W., Kirk K. *Piezofibre-Polymer Composite Material for High-frequency Ultrasound*, 2006 POLECER International Conference, Lillehammer.

MacLennan D., Cochran S., Button T.W., Hughes H., Ponting M. and Sweet J. (2006) Ultra Precision Grinding in the Fabrication of High Frequency Piezocomposite Ultrasonic Transducers *Proceedings of 2006 IEEE International Ultrasonics Symposium* pp. 2353-2356

MacLennan D., Elgoyhen J., Button T. W., Démoré C. E. M., Hughes H., Meggs C. and Cochran S. (2007) Properties and Application-oriented Performance of High Frequency Piezocomposite Ultrasonic Transducers. *Proceedings of 2007 IEEE International Ultrasonics Symposium* pp. 100-103

MacLennan D., Button T.W., Elgoyhen J., Hughes H., Meggs C. Corner G., Démoré C.E.M., Zhang D., Cochran S. (2008) Fundamental Performance Characterisation of High Frequency Piezocomposites made with Net-shape Viscous Polymer Processing for Medical Ultrasound Transducers. *Proceedings of 2008 IEEE International Ultrasonics Symposium* pp. 58-61

Maréchal P., Levassort F., Holc J., Tran-Huu-Hue L.P., Kosec M., and Lethiecq M. (2006) High-Frequency Transducers Based on Integrated Piezoelectric Thick Films for Medical Imaging. *IEEE Transactions on Ultrasonics, Ferroelectrics, and Frequency Control*, Vol. 53, no. 8, pp.1524-1533

Webster R.A., Cochran S., MacLennan D., Meggs C., Button T.W. (2007) Passive Materials for High Frequency Ultrasound Components *Proceedings of 2007 IEEE International Ultrasonics Symposium* pp. 1925-1928

9. Appendices

9.1. Appendix A: Calculation sheet for piezoelectric properties from electrical impedance spectroscopy measurements

Information Sheet for Transducer Properties	
AFM confidential	
Composite:	Transducer:
Date:	Date:
Serial No:	Serial No:
Notes:	

Composite Information

Piezoelectric Material:	
Epoxy:	
Electrodes:	
Volume Fraction:	
Pillar Shape:	

Width		m
Length		m
Diameter		m
Thickness		m
Mass		kg

Impedance Analyser measurements

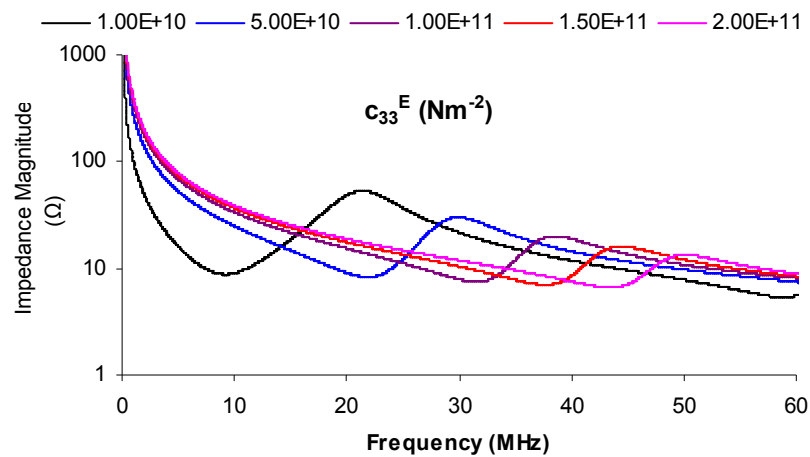
f_r (Hz)		f_a (Hz)	
Parameter	At 1kHz	At 2fm	
Z			Ω
Phase			$^\circ$
R			Ω
X			Ω
Cp			F
G			S

Calculated Parameters

Surface Area		m^2
Volume		m^3
Speed		ms^{-1}
Density		kgm^{-3}
Z		MRayl
K_t		
ϵ_R^T		
ϵ_R^S		
C_{33}^E		Nm^{-2}
e_{33}		Cm^{-1}

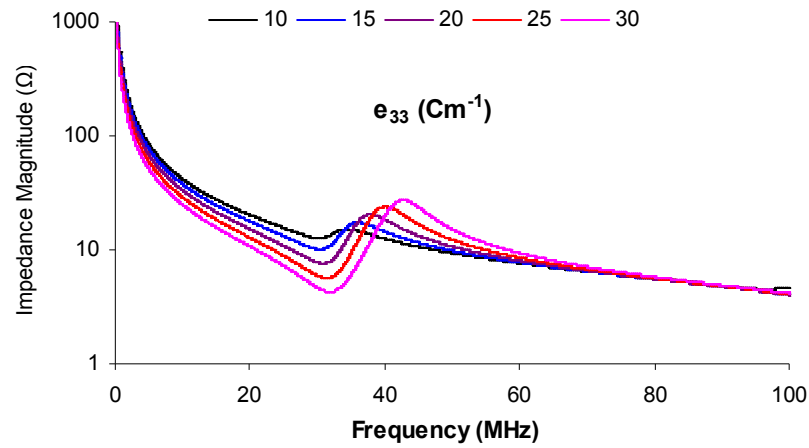
9.2. Appendix B: Effect of varying ODM input parameters on calculated electrical impedance spectrum

To facilitate understanding of the effect of changing parameters within the one-dimensional model on electrical impedance spectra, a number of simulations were undertaken with only a single parameter changing. This was done for c_{33}^E , e_{33} , ϵ_R^T and ϵ_R^S .



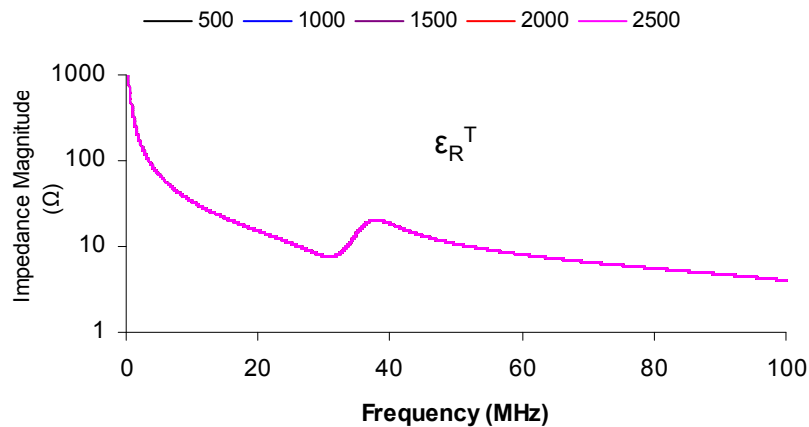
Graph B. 1: Effect on electrical impedance spectra of changing c_{33}^E .

As can be seen from Graph B.1, increasing the value of c_{33}^E causes changes to the impedance, notably: increased resonance frequency because the model assumes increased velocity; flattening of the impedance curve, because of dampening at resonance; and reduction in the value of k_T .



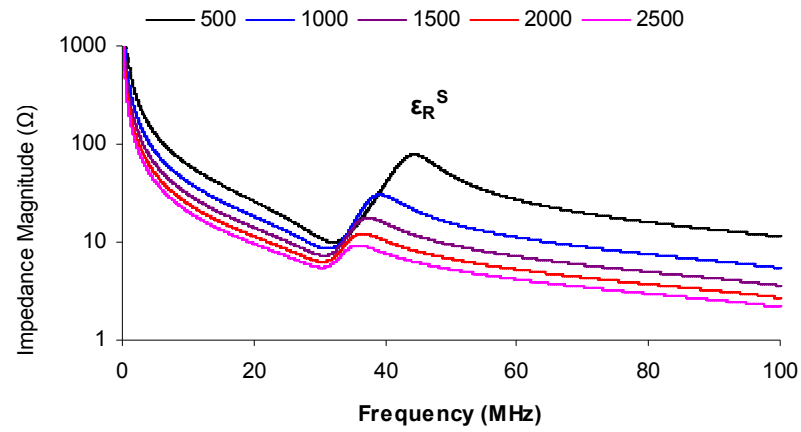
Graph B. 2: Effect on electrical impedance spectra of changing e_{33} .

From Graph B.2 it can be seen that changes in e_{33} also changes the shape of the impedance curve significantly. Increasing the value of e_{33} leads to greater prominence of resonance peaks and an increase in the value of k_T , due to an increase in f_a .



Graph B. 3: Effect on electrical impedance spectra with changing ϵ_R^T

Graph B.3 shows that changing the value of ϵ_R^T does not noticeably affect the impedance spectra.



Graph B. 4: Effect on electrical impedance spectra with changing ϵ_R^S

Graph B.4 shows, however, that changing of ϵ_R^S does affect the impedance curve. Increasing the value of ϵ_R^S leads to decreased f_a and f_r and reduced k_T while the resonant peaks at f_a and f_r are more highly attenuated.

9.3. Appendix C: Description of LabVIEW B-scan collection program

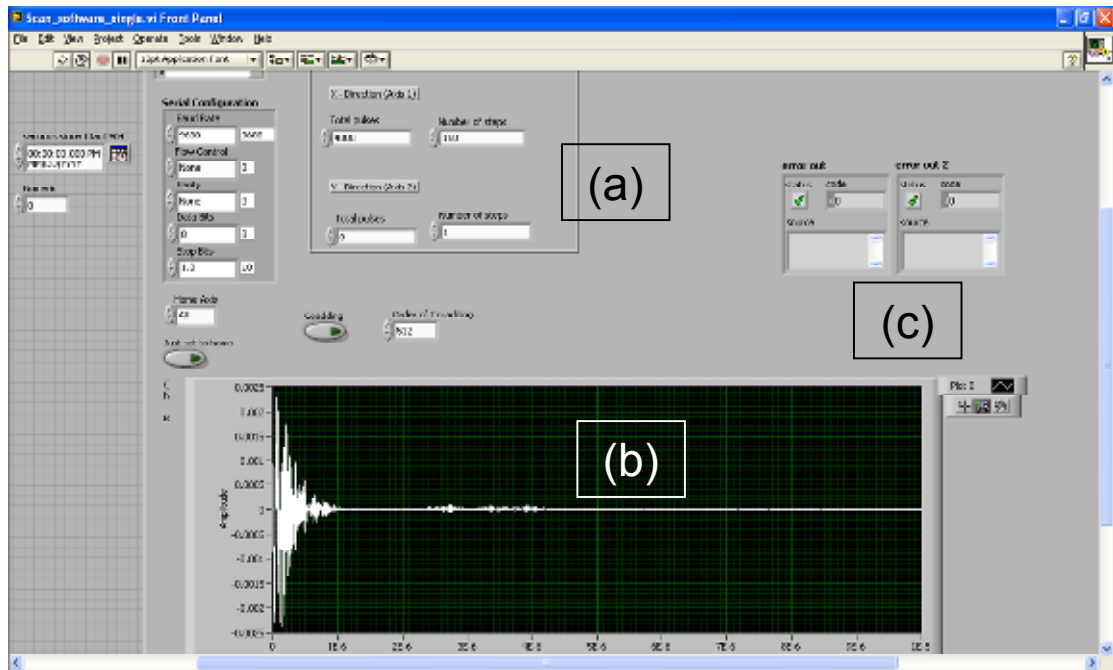


Figure C.1: Screen shot of LabVIEW showing scan system user interface (a) fields for user-entered scan parameters, (b) individual A-scans and (c) error markers.

The LabVIEW programme requires the following parameters to be set before a scan is performed:

X-direction: The stage operates by ‘pulses’, which equate to movements of $2\ \mu\text{m}$ each. The scan length is entered as a number of pulses: e.g. 1 mm is 500 pulses. The number of steps required over the scan length in the x-direction is also set at this point.

Y-direction: The length of scan in the y-direction and the number of steps required over the scan length are set. This is only used if several B-scans are to be collected. If only one B-scan is required, the scan length is set to ‘zero’ and the number of steps to ‘one’.

Averaging: The scan system can be instructed to collect several data sets at each point in space and average these, to increase the SNR. The number of repeated data collections is generally set to 512.

Sampling rate: To obtain the best possible time resolution, the sampling rate of the Picoscope was always set at 500 MHz, the maximum achievable.

Number of data points: The number of points, N , collected by each scan is set according to the sampling rate, f_s , and time period of interest, T , over which data is to be collected using the relationship $N = f_s \times T$